Photoionization and Excitation of Free Variable Size van der Waals Clusters in the Inner Shell Regime

Dissertation

vorgelegt von

Ioana Lavinia Bradeanu

aus Bucharest

Würzburg 2005

Eingereicht am:

bei der Fakultät für Chemie und Pharmazie

1. Gutachter:

2. Gutachter:

der Dissertation

1. Prüfer:

2. Prüfer:

3. Prüfer:

des Öffentlichen Promotionskolloquiums

Tag der mündlichen Prüfung:

Doktorurkunde ausgehändigt am:

Abstract

Photoionization from core levels provides element-specific information on the electronic structure of atoms, molecules, and condensed matter. Post-collision interaction (PCI) is investigated in free, variable size krypton and argon clusters near the Kr $3d$- and Ar $2p$-ionization energies. Photoionization of free Van der Waals clusters is reported using zero kinetic energy (ZEKE) photoelectron spectroscopy in the Ar $2p$, Ne $1s$, Kr $3d$ and N $1s$ excitation regime. ZEKE photoelectron spectroscopy is used as an experimental technique for investigating the core ionization process as a function of cluster size. It is found that the asymmetry, which is a consequence of PCI, is characteristically smaller for clusters than for isolated atoms. Moreover, there is less asymmetry for bulk-sites than for surface-sites in variable size rare gas clusters.

The emission of ultraviolet fluorescence from variable size argon clusters is investigated in the Ar $2p$-excitation regime (240–270 eV). The results are assigned in terms of plausible relaxation processes occurring in the $2p$-excitation regime. This implies that charge separation mechanisms are active, which occur after electronic relaxation of the core hole. Besides electron impact ionization within clusters caused by Auger electrons, the interatomic Coulombic decay (ICD) mechanism appears to be a plausible way to rationalize the experimental findings.

Cluster size effects in core excitons below the N $1s$ ionization energy of nitrogen clusters are investigated in the energy regime 405-410 eV. These results are compared to the molecular Rydberg states as well as the corresponding bulk excitons of condensed nitrogen. The experimental results are compared with ab initio calculations, providing an improved spectral assignment of core exciton states in weakly bound molecular clusters and the corresponding condensed phase.

To my Parents

"Run rabbit run
  Dig that hole, forget the sun
  And when at last the work is done
  Don't sit down
  It's time to start another one"

List of Publications

I) I.L. Bradeanu, H. Setoyama, T. Hatsui, N. Kosugi and E. Rühl,
   "Post Collision Interaction of Free Van der Waals Clusters"
   In manuscript

II) I.L. Bradeanu, H. Setoyama, T. Hatsui, N. Kosugi and E. Rühl,
   "Photoelectron Profiles of Free Variable Size van der Waals Clusters"
   In manuscript

III) I.L. Bradeanu, R. Flesch and E. Rühl,
   "ZEKE Photoelectron spectroscopy of free Van der Waals clusters"
   In manuscript

IV) T. Hatsui, H. Setoyama, N. Kosugi, B. Wassermann, I.L. Bradeanu and E. Rühl,
   "Photoionization of Small Krypton Clusters: Evidence for Site-Specific Photoemission"
   J. Chem. Phys. **123**, 154304 (2005)

V) I. L. Bradeanu, R. Flesch, M. Meyer, H.-W. Jochims and E. Rühl,
   "Radiative Relaxation of 2p-Excited Argon Clusters: Evidence for the Interatomic Coulombic Decay Mechanism"
   Eur. J. Phys. D, 173–178 (2005).

VI) R. Flesch, N. Kosugi, I. Bradeanu, J.J. Neville and E. Rühl,
   "Cluster Size Effects in Core Excitons of 1s-Excited Nitrogen"
   J. Chem. Phys. **121**, 8343-8350 (2004).

The following are papers to which I have contributed but they are not discussed in the thesis.

I.L. Bradeanu, R. Flesch, N. Kosugi and E. Rühl,
"Core (C 1s and N 1s) $\rightarrow \pi^*$ transition in pyridine clusters
In manuscript

I.L. Bradeanu, R. Flesch, N. Kosugi, A.A. Pavlychev and E. Rühl,
"C 1s $\rightarrow \pi^*$ transitions in benzene clusters"
Submitted to Phys. Chem. Chem. Phys.

Participation at International Conferences

I) **7–9 September 2005**
International Workshop on Free Clusters and Nanoparticles using Short Wavelength Radiation, Bad Honnef, Germany
contributed talk: <u>I.L. Bradeanu</u> *"Photoelectron profiles of free variable size van der Waals clusters"*

II) **27 July—1 August 2005**
International Workshop on Photoionization, IWP2005, Campinas, Brazil
poster contribution: <u>I.L. Bradeanu</u>, H. Setoyama, T. Hatsui, N. Kosugi and E. Rühl *"Post Collision Interaction of Free Van der Waals Clusters"*
poster contribution: <u>I.L. Bradeanu</u>, R. Flesch, M. Meyer, H.-W. Jochims and E. Rühl *"Radiative Relaxation of 2p-Excited Argon Clusters: Evidence for the Interatomic Coulombic Decay Mechanism"*

III) **8–9 October 2004**
Studiecentrum Soeterbeeck, Ravenstein, The Nethelands
Invited talk: <u>I.L. Bradeanu</u> *"Spectral shifts in core-to-valence transitions of molecular van der Waals clusters"*

IV) **3–5 September 2003**
Workshop on free, neutral clusters studied by synchrotron radiation, Sigtuna, Sweden
Invited talk: <u>I.L. Bradeanu</u> *"Zero kinetic energy photoelectron spectroscopy of free Van der Waals clusters"*

Comments on my own participation

All papers in this thesis are the result of teamwork as is necessary in experimental physics. My contribution to these papers always lies in the theoretical, experimental and data analysis side. My contribution to papers I and II covers the performance of the theoretical model of post collision interaction in clusters, of the experimental data analysis and the preparation of the manuscript. In paper III my contribution lies in the experiment and data analysis, theoretical calculations and preparation of the manuscript. In paper IV my contribution is the data analysis and the preparation of Fig. 2 and Table 1, and the text around them in the manuscript. In paper V, I have participated in the experimental work, data analysis and the discussion of the manuscript. For paper VI, my contribution consists of preparing figure 4.

Contents

Chapter 1

Introduction

Core levels have properties which make them interesting for the study of variable size matter: they are atomic-like and localized even in molecules and solids, and are very short-lived. This means that core level spectroscopy can give information not only about which atoms are present in the sample, but also the number and the type of different sites which these occupy, and how the local electronic and geometric structure depends on the type of site. The short lifetime of core holes enables studies of the dynamics development occurring during their lifetime, i.e. a few femtoseconds (10^{-15} s).

This thesis is dedicated to the study of core level excitation of clusters – which is a unique approach to probe element and site specific size-dependent properties of free clusters in the gas phase. Clusters are aggregates of a finite number of atoms or molecules that bridge the gap between an isolated atom/molecule and an infinite solid [1]. It is therefore of primary interest to be able to follow size dependent changes of properties of matter by specific experimental and theoretical approaches in order to understand whether changes of cluster size occur gradually, in distinct steps, or if there are size regimes with unique properties.

Free clusters produced in specially prepared gas beams give a possibility of following the gradual development of the size-dependent properties with cluster size. Information about the atom-to-solid evolution obtained from free cluster investigations have the additional advantage that the density of states is low in comparison to studies of outer valence shells. As clusters are small objects, a large and size dependent fraction of their constituent atoms are located at their surface. The properties of clusters are thus to a high degree determined by the surface electronic and geometric structure. It is thus desirable to be able to separately probe the atoms located at the surface and those in the bulk interior. Spectroscopic methods focusing on the core electronic levels allow such surface and bulk specific studies to be made. These experimental methods have proven to be powerful tools for the investigations of the electronic and geometric structure of the conventional forms of matter: gas-phase atoms and molecules, solids, and surfaces [2, 3]. Core-level spectroscopy has an obvious advantage: in contrast to valence levels, the localized nature of core orbitals makes it possible to separate the response of atoms of the same element at different sites and to study these sites selectively [2, 3].

Substantial progress in the field of surface and bulk resolving spectroscopies has been made due to the implementation of tunable soft X-rays provided by modern synchrotron radiation facilities [2, 3]. The field remained highly unexplored though it was clear that

free clusters were not only unique objects for studies on the atom-to-solid evolution, but they could in many cases be preferable for obtaining information on the undisturbed properties of the solids themselves.

The investigation of radiative or non-radiative decay processes in atoms, molecules and clusters following a primary electronic excitation to an empty bound level – empty molecular orbital or Rydberg state – below a core ionization threshold provides information on the nature of both the intermediate core excited and the final valence ionized states, as well as on the dynamics of the entire relaxation process.

Information on core-excited states is given by X-ray absorption spectroscopy. With this method studies of core level excitation electronic states are performed, which allows to study size effects in electronic structure. When the excitation energy is lowered and reaches the regime near the core absorption edge, one observes significant and asymmetric line broadening in photoelectron and Auger spectra. This phenomenon is called post-collision interaction (PCI), which concerns the energy transfer between the low kinetic energy photoelectron and Auger electron. The photoelectron may then be retained in the ionic core, even though the photon energy exceeds the core ionization energy. This situation changes deeper in core ionization continua where the photoelectron has sufficient kinetic energy to be emitted, so that doubly charged final products are formed, according to the normal Auger decay. The resonant Auger decays occurring in the pre-edge regime lead to the formation of singly charged products, if the primarily excited core-electron remains as a spectator in an excited electronic state. The variety of processes, involving resonant excitation below core-edges, and direct photoemission in core ionization continua leads to strong variations in charge states of the cations that are formed.

Core-excited clusters may undergo radiative relaxation, if electronically excited species are formed. The emission of fluorescence photons may either occur in the soft X-ray regime or at considerably larger wavelengths, i.e., in the ultraviolet or vacuum ultraviolet regime. The emission of low energy photons has been extensively studied in free van der Waals clusters for the outer-shell excitation regime [4, 5]. There is considerably less information on radiative relaxation processes of core-excited van der Waals clusters. This is the primary motivation for this work.

To get some perspective on the enormous progress in cluster physics science, I would like to end this introduction and to invite you to see what is inside of the thesis.

Chapter 2

Core Level Photoelectron Spectroscopy

The purpose of this chapter is to give a brief overview of different photon-matter interactions that render an ionized final state. Typically one distinguishes between resonant and non-resonant processes and depending on the photon energy involved one may distinguish between a wealth of different techniques.

Usually, one does not directly measure the amount of photons absorbed by the target but instead the photoabsorption is measured via the yields of secondary particles, such as electrons or ions, produced by the photoabsorption process. For this reason one often distinguishes between electron yields, where the electron is measured as a function of photon energy, and ion yield, where the yield of ions is measured as a function of photon energy. For instance, a common denotation used for higher photon energies is X-ray absorption spectroscopy (XAS). However, if the spectrum is measured close the threshold, the denotation near edge X-ray absorption fine structure (NEXAFS) may be encountered and accordingly, spectra measured far from the threshold are often denoted extended X-ray absorption fine structure (EXAFS). Central to all these techniques is the measurement of transitions into or from core orbitals, as shown in the schematic drawing on the electronic processes involved in Figure 2.1. This allows us to measure the electronic structure in the close vicinity of a given atom due to the localized nature of the core orbitals.

The principle of X-ray photoelectron spectroscopy (XPS)

When the $h\nu$ of the incident photon exceeds the ionization threshold, the atom/molecule is ionized. The photoelectron spectrometer detects the emitted electron with certain energy and in certain direction. The change of the angle between the polarization vector e and the photoelectron momentum k allows to study the anisotropy of photoionization. Photoelectron spectroscopy gives direct information about occupied molecular levels. If the incident photon has high energy (x-ray photons), the photoelectron spectroscopy is designated as x-ray photoelectron spectroscopy (XPS). When the electron spectrometer detects photoelectrons with the binding $E_B = h\nu - E_{kin}$ near the core ionization potential IP one talks about core level XPS. The XPS spectrum has resonances when $E_B = IP$. In molecules the ionization potential of the core electron experiences chemical shifts which are different for different atoms or atoms of the same chemical element but which are not equivalent chemically.
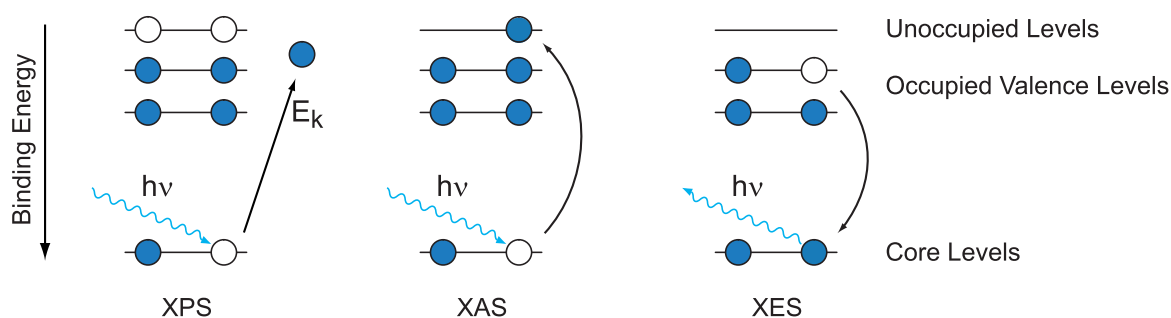
Figure 2.1: Schematic picture of the processes involved in XPS, XAS and XES.

The principle of X-ray absorption spectroscopy (XAS)

XAS measures the cross section of the transition of a core electron into the unoccupied density of states as a function of the photon energy. Since the core orbital is localized around the nucleus of the atom, the orbitals into which the electron can be excited with the largest probability are those which have a large contribution close to the same nucleus as the core orbital. This means we can locally probe the unoccupied electronic structure of an atom in the presence of the core hole. The XAS transition follows the dipole selection rules, so assuming we excite an electron from an orbital of atomic s-symmetry, we will only probe the atomic p character. Furthermore, the transitions with the final state p orbital pointing in the perpendicular direction to the electric field vector of the exciting light will have a vanishing matrix element. A useful consequence of this is that if we use linearly polarized light and perform angular resolved measurements we can selectively probe p states along a given direction. The reverse is also true. If the direction of an orbital is known in the molecular reference system, angular resolved XAS can be used to deduce the orientation of adsorbates relative to the surface.

The Principle of NEXAFS

When X-rays pass through a sample the intensity of the incident beam is reduced due to photoabsorption. The X-ray photons excite core electrons to an unoccupied molecular orbital when the photon energy is smaller than the core ionization potential (Fig. 2.2). Near the photoionization threshold one can also observe weak transitions to so-called Rydberg levels. When the photon energy exceeds the ionization threshold, the core electron is excited to continuum states. These states differ qualitatively going from atoms to molecules. Due to the multiple scattering of the photoelectron on the surrounding atoms in a molecule, resonances then appear also in the continuum [6, 7].

Such resonances are known as shape resonances. The alternative interpretation of the shape resonances is related to the effective barrier [8] which creates the quasi-stationary state (see Fig. 2.2), the barrier is shaped by the molecular potential. Quite often the X-ray absorption profile is disturbed by weak two-electron transitions. Both near edge (NEXAFS) and extended X-ray absorption fine structure (EXAFS) spectroscopies are widely used in materials science to study structure of compounds. As NEXAFS spectra are formed by transitions of core electrons of specific atoms to vacant orbitals which are very sensitive to inter- and intra-molecular interactions, NEXAFS has become one of the
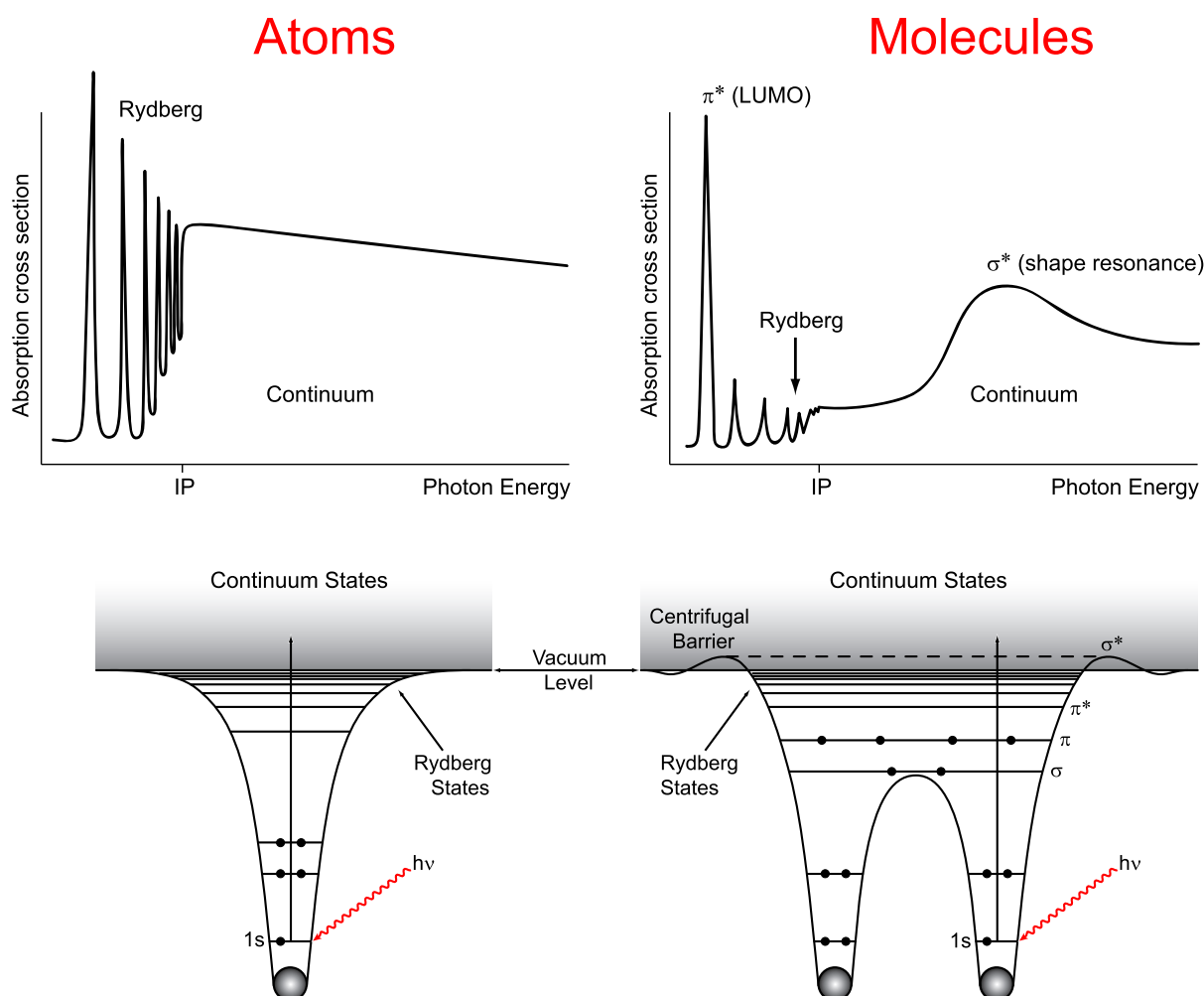
Figure 2.2: Formation of x-ray absorption spectra in atoms (left) and molecules (right).

most powerful tools in studies of molecular interactions as well as molecular structure.

The principle of X-ray emission spectroscopy (XES)

In XES the occupied electronic states are probed locally by measuring the energy distribution of emitted photons from core hole decay processes. To produce a core hole, electrons are excited from a core orbital into the unoccupied valence or continuum. This can be done using electrons or photons. For adsorbates it is typically better to use photons for the excitation process as this reduces problems with sample damage and allows selective excitation into a specific orbital, which can select out only one species to be probed on the surface. A few femtoseconds after the excitation, the core excited state decays.

XES can be measured both in resonant or non-resonant mode. In the resonant case, additional selection rules will apply, resulting in an excitation energy dependence of the intensity distribution. In order to accurately treat this effect one has to take into account the intermediate states, whereas in the non-resonant case, this effect can be neglected. Non-resonant XES has the same final state as valence band photoemission, i.e. one

valence hole, and can be interpreted without taking the core hole into account other than as localizing the transitions to a given atom [9].

2.1   Direct photoionization

Direct photoionization implies that an electron is excited out into the continuum via an interaction with the electromagnetic field of the incoming photon. To remove an electron from the molecule/atom out into the continuum requires, for photon energies well above the threshold energy, a constant amount of energy which is given by the energy difference between the ground and the ionized state. This constant amount of photon energy is commonly referred to as either binding energy (E_B), ionization or threshold energy. Well above threshold, the binding energy is photon energy independent, and from the requirement of energy conservation, the kinetic energy of photoelectron (E_{kin}) is given by the difference between the photon energy and the binding energy; $E_{kin} = h\nu - E_B$. With knowledge of the incoming photon energy, this relation implies that the binding energy of a certain electronic level can be extracted by measuring the kinetic energy distribution of the photoelectrons.

Occupied molecular orbitals are commonly divided into core-orbitals that are predominantly associated with a specific atom and do not take place in the molecular bonding, and valence orbitals, diffuse orbitals which are forming the molecular bond. The binding energy of a valence level is typically order of magnitudes smaller than the binding energy of a core level.

2.2   Auger electron spectroscopy

A core-ionized or core-excited state is far from energy equilibrium and will eventually decay (de-excite) – the average lifetime of a core-hole is typically only a few femtoseconds. A common denotation for core-excited and core-ionized states is intermediate states; reflecting that from a truly two step description of the Auger process, the core-ionized or the core-excited state can be thought of as intermediate between the ground and the final state. Eventually, the core-hole is filled by an electron from a higher orbital (valence); the energy released by this process will be carried away by either an electron or by a photon.

The first case is known as Auger decay [10] whereas the second case is known as X-ray emission or radiative decay; a common denotation is secondary processes, and a state populated by a secondary process is generally known as a final state. For photon energies in the soft X-ray region, the Auger decay process is by order of magnitudes more common than the X-ray emission process.

Depending upon whether the intermediate state is a core-to-valence/Rydberg excited or a core-ionized state, one distinguishes between resonant Auger – populating two-hole one-electron ($2h1e$) or one-hole ($1h$) final states – and non-resonant Auger decays – populating two-hole ($2h$) final states. The core-ionized state has a fixed energy independent of the photon energy and, therefore, the Auger electron is found at a fixed kinetic energy as well; the Auger electron energy is photon energy independent and all photon energy in excess of the energy needed to create the core-hole is carried away by the photoelectron, as shown in Fig. 2.3.
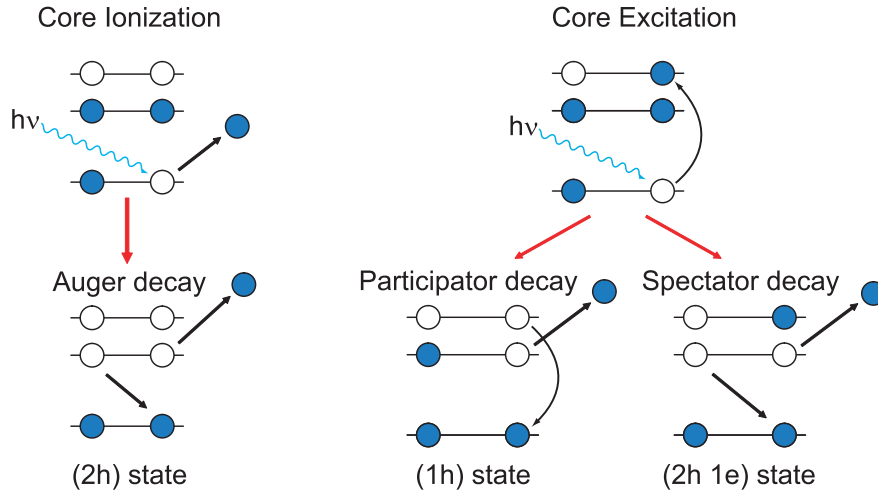
Figure 2.3: Resonant and non-resonant excitations.

This also implies that the energy resolution in the non-resonant Auger decay spectrum is independent of the photon energy resolution. The kinetic energy of the Auger electron is given by

$$E_B = E_{B,2h} + E_{K,\text{Auger}}$$

where $E_{B,2h}$ is the binding energy of the $(2h)$ final state, $E_{K,\text{Auger}}$ is the kinetic energy of the Auger electron, and E_B is the binding energy of the core-ionized state. However, in the case of resonant Auger decay, the energy of the core-excited state is photon energy dependent, and hence also the kinetic energy of the Auger electron is photon energy dependent.

As for direct photoionization, the kinetic energy of the resonant Auger decay is given by

$$h\nu = E_{B,2h1e,1h} + E_{K,\text{Auger}}$$

where $E_{B,2h1e,1h}$ is the binding energy of the $(2h1e)$ or $(1h)$ final states, respectively. It should be mentioned that different resonances usually populate different final states, and, therefore, there is no simple relation between the Auger electron kinetic energy and the photon energy in the case of resonant Auger decay measured at different resonances. Strictly, it is only when tuning the energy over a specific resonance with completely monochromatic light that this simple relation is valid. Compared to the Auger decay from a core-ionized state, the resonant Auger decay is modified by the additional electron in the valence/Rydberg level.

2.3   In vicinity of the core-ionization threshold

All the studies presented in this thesis have one common factor: some kind of core-excited state is involved. Either the study has been focused on the creation of the core-excited state itself or the secondary de-excitation of the core-excited state. The definition of a core-excited state is that an electron is missing in one of the core-orbitals. This core-excited state is far from any energy equilibrium and therefore energy has to be added

from the outside to create it. This added energy can be sufficient to either promote the core-electron to one of the unoccupied valence-orbitals or to remove the electron entirely from the system, i.e. out in the continuum. The latter is also known as a core-ionized state. The creation of the core-ionized state requires a minimum amount of energy; a core-ionization threshold can be defined. The energy of the core-excited state is greater than the energy of the neutral or ionic ground state and will eventually decay. The process by which it decays is generally denoted the secondary process.

2.3.1   Below the threshold; resonant Auger decay

The cross section of valence hole states is usually small at higher photon energies. However, within small photon energy regions, the cross section of valence hole states may be raised by several order of magnitudes. The reason for this dramatic enhancement is the opening of resonant channels, channels which usually are found just below the core-ionization threshold. A resonant channel is opened if a core-excited state is acting as a scattering agent. In a simplified two-step description this could be explained as a core-electron is promoted to an empty valence or Rydberg orbital; a one-hole one-electron $(1h1e)$ core-excited state is created. Subsequently this excited state will decay. In the Auger process one valence electron fills the empty core-hole and another carries the released energy out in the continuum; a valence ionized $(2h1e)$ final state is created. However, due to the limited lifetime of the core-hole, typically only a few femtoseconds, this "two-step" description is too crude and in a more correct description of the Auger process, such as the one presented in the earlier section, the core-excited state should only be regarded as a scattering agent.

2.3.2   Rydberg vs. valence and participator vs. spectator

One usually distinguishes between core-to-valence and core-to-Rydberg excitation (see for example Flesch *et al.* [11]). The distinction is typically such that the Rydberg orbital should be described within the hydrogenic model, and is thus non-bonding, whereas the valence orbital is severely distorted from this model and is either of bonding or antibonding type. The hydrogen model implies that an electron in a Rydberg orbital is treated as a strict spectator. Thus, the complicated Rydberg-valence or Rydberg-core hole interaction can be approximated by a much simpler Rydberg orbital–point charge interaction. According to this model, the Rydberg electron acts as an even screening of the ionic molecule, and the $(1h1e)$ core-hole excited states or the $(2h1e)$ valence-holes final states may be assigned from the corresponding $(1h)$ core-ionized or $(2h)$ valence holes final states. Therefore, the Rydberg resonant Auger decay spectrum can be assigned by comparison to the corresponding core-ionized Auger decay spectrum.

Whether the core-excited electron takes part in the resonant Auger process or not gives a first distinction of an Auger decay spectrum. A $(1h)$ final state is created if the electron takes part in the Auger decay, and the process is denoted participator decay. A $(2h1e)$ final state is created if the electron does not take part; this process is denoted spectator decay. The participator $(1h)$ final states are usually found at a lower binding energy than the spectator $(2h1e)$ final states. Participator decay is the denotation of Auger decay that results in $(1h)$ final states. However, core-excited electrons may take part by other

means. one example is the Auger shake process. Because of the Auger decay, the central potential experienced by the core-excited electron undergoes a sudden increase. Due to the suddenness of the Auger decay process, the electron in the Rydberg/valence orbitals may not be able to adjust accordingly. Therefore, the Rydberg electron may be "shaken" to a higher or lower orbital.

2.3.3   Above the threshold; non-resonant Auger

High photon energy implies that a core electron can be removed from an atom or molecule in the continuum. The minimum photon energy required to core-ionize the molecule sets the core-ionization threshold energy. For large photon energies, can be extracted as the difference between the photon energy and the kinetic energy of the photoelectron. Provide that the core-hole decays via the Auger process, at least two electrons are promoted to the continuum; the Auger process and the photoelectron. The photoelectron may interact with the Auger electron for photon energies just above the threshold. This interaction in the continuum is generally known as post collision interaction (PCI), and will be subject of the chapter 9.

After first sharp increase, the probability for core-ionization drops constantly with increasing photon energy from the core-ionization threshold. However, just above threshold, wiggles in the core-photoionization cross section are often found. These continuum resonances are usually separated into shape and double excitation resonances.

2.4   At the threshold

As the photon energy increases from the low photon energy side of the threshold, both the energy spacing between adjacent core to Rydberg resonances and the cross section for photon excitation decrease. Therefore, as a consequence of the natural broadening due to the core hole lifetime, the core-excited states cannot be selectively excited. Also the probability for Auger shakeup/shakedown increases and the resonant Auger decay grows increasingly rich of structures for photon energy just below the core ionization threshold. On the other hand, for decreasing photon energy above the threshold, the PCI causes an intensity redistribution of the Auger decay line profile. Also very close to threshold, the kinetic energy of the outgoing photoelectron may be so small that the overtake by the Auger electron causes a recapture of the photoelectron by the ionic molecule/atom. In that case a $(2h1e)$ final state is populates; as for resonant Auger below threshold. These arguments suggest a continuous link between the resonant Auger precess below threshold populating $(2h1e)$ final states, and the Auger process above threshold, populating $(2h)$ final state. PCI at the threshold is investigated in the chapter 11.

Chapter 3

From Atoms to Clusters

The physics of clusters, with its many facets covering free as well embedded or deposited clusters, addresses an impressive set of problems, ranging from fundamental to applied ones. In all that, clusters are a species of their own asking for specific understanding of their properties. A specific feature is, e.g., that cluster size can be varied systematically between atoms and bulk: they are, so to say, "scalable" objects. Clusters play an important role from a fundamental physical point of view. Bear in mind that solid state physics deals with virtually infinite samples while in molecular physics the systems never contain more than a few hundreds of constituents. Clusters bridge the gap. But the interest in them is not purely fundamental. The most striking property of clusters for applications in physics is their size. Indeed, because clusters may be quite small, but not too small, they can exhibit a large surface to volume ratio.

For atoms which have only a few electrons in the outer shells, the valence shells, such as alkali atoms, the valence electrons are highly localized upon condensation, forming a collective electron gas which is smeared out over the entire crystal. In the case of closed-shell atoms or molecules, neither covalent nor ionic bonding is possible. However an electrical dipole-dipole interaction occurs between the atoms or molecules, which is either due to already existing dipole moments, as can be found for many molecules, or there are fluctuations in the electron cloud, giving rise to induced dipole moments in atoms or molecules. This is known as van der Waals bonding. All bonding mechanisms have something in common; they depend on the electronic distribution.

3.1   Clusters as finite objects

Clusters are, by definition, aggregates of atoms or molecules with regular and arbitrarily scalable repetition of a basic building block. Their size is intermediate between atoms and bulk. The definition of bulk may vary from one observable to another, namely a given physical property may reach its bulk value for a size different from another observable [12].

Molecules usually have a well defined composition and structure. Think, e.g., of the well known molecules such as benzene (C_6H_6). Such systems have only a small number of isomers, a few units at most, even if they are themselves not small molecules. This is different for clusters, which often possess a large number of energetically close isomers and in which the number of isomers grows huge with increasing cluster size. For example,

in such a small cluster as Ar_{13}, one has found hundreds of isomers, the actual number slightly depending on the detail of the interatomic potential used in the calculations, while less than 10 isomers were identified in Ar_8 [13].

An aspect where clusters are distinguished from bulk (and from molecules) are finite size effects in terms of surface to volume ratio. Most clusters are large enough such that one can speak about a surface zone. On the other hand, they are sufficiently small such that a sizeable fraction of the constituents lie on the surface of the system, while this is not true in bulk. Let us take as example the Ar_{55} cluster. It has 32 atoms on its surface. Now consider a piece of bulk material of 1 mm^3 volume. Taking an order of magnitude for the bond of 1 Å tells us that there are about 10^{18} atoms in the sample, out of which about 10^{12} lie on the surface of the system. The ratio of surface atoms to total is thus 32/55=0.6 in Ar_{55} as compared to about 10^{-6} in the bulk sample. Even taking a smaller sample of micrometer size the ratio would only increase to about 10^{-4}. There is thus a huge difference in the fraction of surface atoms when passing from clusters to bulk. And it turns out that this ratio constitutes a simple and efficient way to classify clusters. See for details calculations in Chapter 7.

As is obvious from the above discussion, clusters interpolate between atoms/molecules and bulk. But they are more than just trivial emanations of these two extremes cases. Of course, very small clusters look like molecules, though, and can thus be studied with chemistry methods, while very large clusters can be attacked with techniques stemming from solid state physics. In between, more specific techniques have to be developed for accessing clusters. Already here, we can note that size is obviously a key parameter in cluster physics. Following the argument developed just above, a classification in terms of size can be given by considering the fraction of surface atoms to volume. The question of size effects will be recurrent throughout this thesis, first, because clusters interpolate between atom and bulk with largely variable size, and second, because it turns out that most cluster properties do indeed strongly depend on size. But as already stressed above, convergence towards the bulk value with increasing cluster size essentially depends on the nature of the observable and on the resolution with which one looks at it.

Van-der-Waals binding prevails in rare-gas clusters, as e.g. for Ar. Rare gas clusters play an important role as a "model system" for clusters of more practical use. Both van der Waals bonds, formed in rare gas clusters, and metallic bonds are non-directional and clusters of both types exhibit related size-dependent structural transitions. Size effects of matter have been of considerable interest in the past [1, 14, 15, 16, 17]. This is on one hand due to the fundamental interest in structural changes by going from the gas to macroscopic condensed matter. The strongest changes in electronic structure of variable size matter are found when the isolated atom is compared to small clusters [1, 18].

3.2   Bonding rare gas dimers

There is a significant change in bonding upon removing an electron from a rare gas cluster. This can be best understood by considering the differences between the electronic structures of the neutral (Rg_2) and singly charged (Rg_2^+) dimers. For the heavier rare gas elements, the lowest energy electronic state ($^2\Sigma_2^+$) of Rg_2^+ is generated by removing an electron from the high-lying σ_u^* (np) antibonding orbital formed by out-of-phase combination of atomic np orbitals, oriented along the interatomic (bond) vector. Removal of
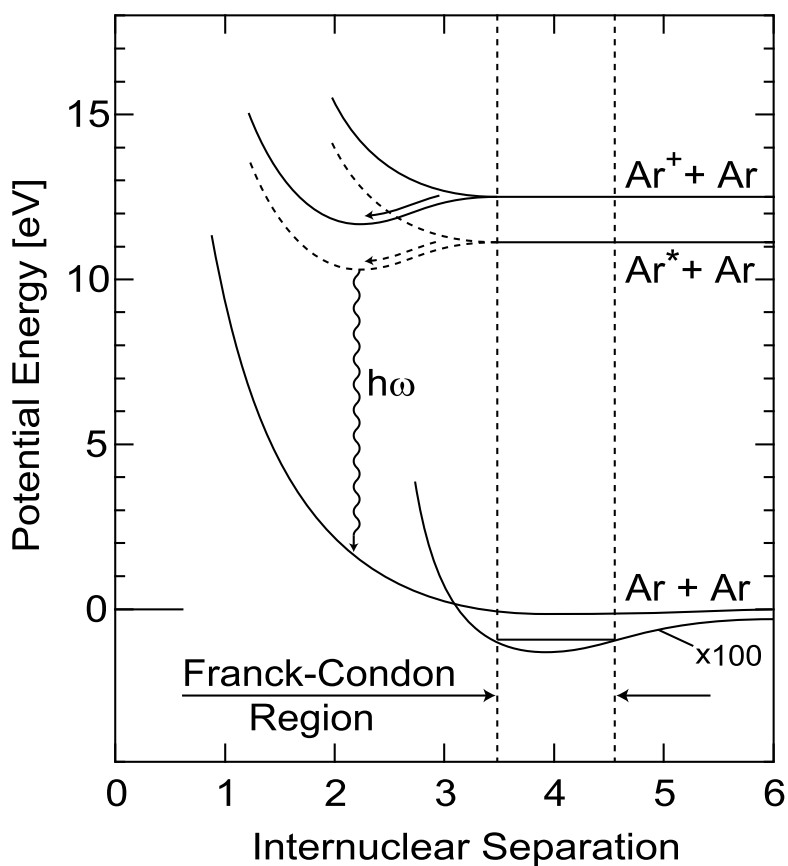
Figure 3.1: Potential energy curves for neutral, charged, and excited Ar_2.

this electron again leads to a formal covalent bond order of 1/2. In the case of argon, as shown in Figure 3.1, the binding energy of Ar_2^+ is 1.5 eV, compared with a value of 12 meV for the neutral dimer. The smaller increase in binding energy on ionization observed for argon, compared with helium, is because the argon $3p$ orbitals overlap less efficiently than the helium $1s$ orbitals [1].

As shown in Figure 3.1, the large increase in binding energy upon ionization of the rare gas dimer is accompanied by a decrease in the equilibrium Rg–Rg distance, reflecting the presence of partial covalent bonding. In the case of the argon dimer, there is a 30% decrease in the Ar–Ar bond length on going from Ar_2 to Ar_2^+. The stability of the Ar_2^+ ion is confirmed by mass spectral measurements (using a 70 eV electron beam for ionization) of a beam of neutral Ar clusters, mass selected by momentum transfer from a beam of helium atoms. In this experiment, the Ar_2^+ peak is much larger than those due to Ar_3^+–Ar_5^+, indicating that Ar_2^+ is the dominant fragment channel when small argon clusters are ionized.

3.3   Rare gas clusters

After double/multiple ionization, the Coulomb forces tend to fission the clusters. Due to efficient charge migration mechanisms in competition with the Coulomb forces, the fission

results in the formation of singly charged fragments. The photon energy mainly determines the degree of ionization and no direct dependence is expected. For each ionization degree, the multiply charged species get stable (within a 10^{-6} s time scale), when a critical size (N_c) is reached [1, 19]. Thus the cluster fission varies gradually with the degree of the ionization of the cluster. In Fig. 3.2 an illustration of the sequence of processes is shown. The absorption process is photon energy dependent. The hole produced by photoabsorption is primarily stabilized by either electronic or radiative relaxation. Assuming the localization of the electronic relaxation process in rare-gas clusters we expect a doubly-charged atom to be formed within the cluster, also triply and higher charged atoms can be formed by more autoionization steps. The cluster can also be further ionized if the electrons emitted in the electronic relaxation processes interact with a neutral atom in the cluster. The probability for this is considered to be quite low but increases with cluster size and varies with the energy (mean free path) of the electron. This effect is not included in the figure. The charges are delocalized in the cluster by formation of charge transfer excimers, thus the charges are delocalized before fission.

For very small clusters $\langle N \rangle < N_c$ the fragmentation dynamics has been satisfactorily described by a model based on fast "Coulombic explosion" with charge separation [20, 21]. The charge separation takes place prior to neutral evaporations for very small clusters, while for large clusters neutral evaporations occur at any time [22]. Due to the weakly bound nature of van der Waals clusters, the critical size N_c is always high (> 50 atoms) and a "liquid droplet" model can be used to described the fragmentation of the large clusters [23]. The term "Coulomb explosion" is frequently used to describe the overall charge separation process. Indeed for doubly charged dimers the kinetic energy imparted to the fragment can be too high for a pure "Coulombic explosion" model [24], while for the largest clusters massive neutral evaporation promote the fission [22].

Fig. 3.2 shows a common scheme that has been developed from results on $2p$ excited Ar clusters. It includes all processes that follow primary photoabsorption of a soft X-ray photon by an atom that is located near the surface of a cluster. This includes: core-hole formation, photoionization, relaxation, and finally, fragmentation. In the case of molecular clusters, additional fragmentation processes are known to occur besides van der Waals fragmentation, yielding interacting molecular moieties that are either neutral or singly charged, chemical fragmentation occur.

In the above description it is assumed that only electrons at the excited atom take part in the decay process. Thus the environment of the initially excited atom is assumed only to modify the Auger energy spectrum via its influence on the energy levels. In contrast to that is Cederbaum's model who predicted a non radiative decay process for weakly bound aggregates such as hydrogen bonded systems [25, 26] and van der Waals clusters [27, 28], which is only possible due to the presence of neighboring atoms. In this process, named Interatomic Coulombic Decay or Intermolecular Coulombic Decay (ICD), a vacancy in an inner–valence shell is filled by an outer valence electron and the energy released is transferred to a neighboring atom because of an efficient Coulombic mechanism. This energy is used to emit a valence electron into the continuum. As seen in Fig. 3.3 the final state after ICD has two positive charges (holes) distributed at two different atoms / molecules of the aggregate. Thus the total energy of the system is lowered by shielding of the Coulomb repulsion; this explains why these electronic decay channels are energetically accessible.
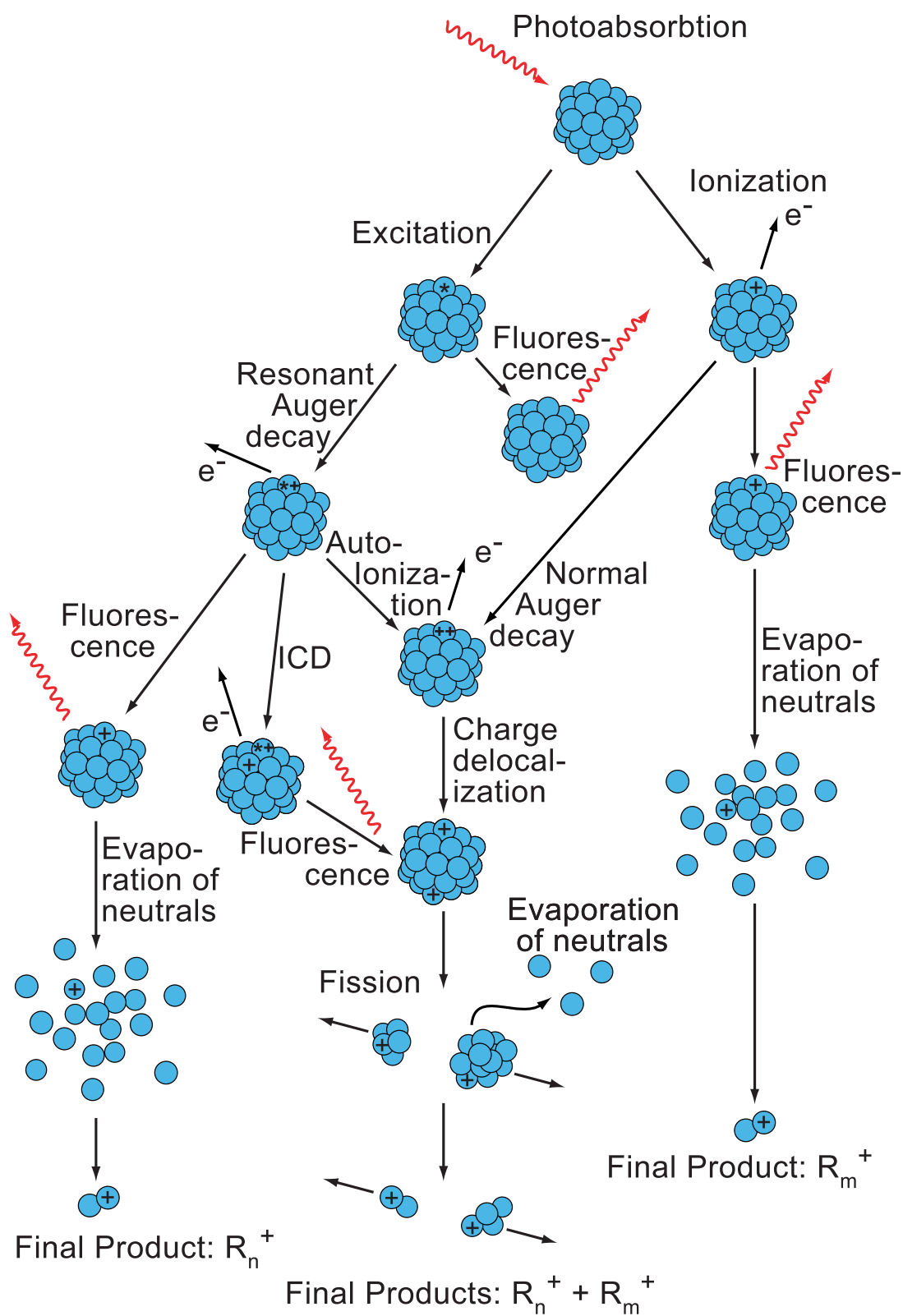
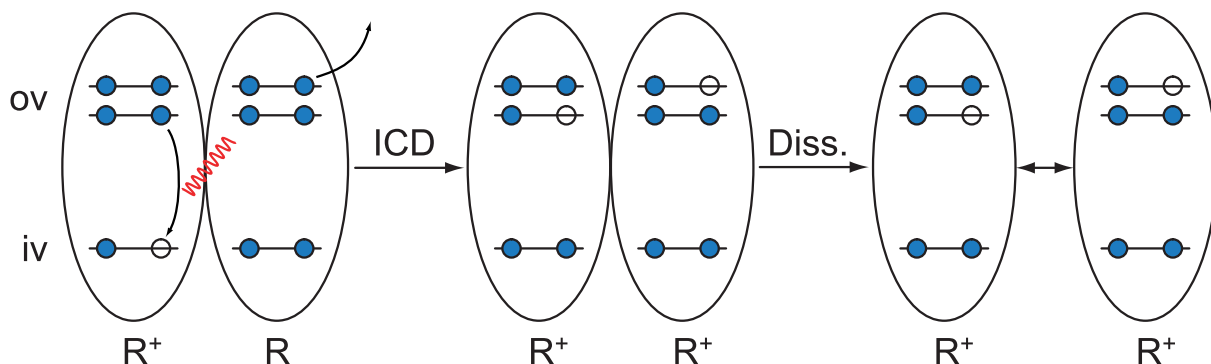Figure 3.2: De-excitation routes of core-excited clusters.

Figure 3.3: An inner valence (iv) vacancy is filled by an outer valence (ov) electron and the excess energy is transferred to a neighboring atom/molecule by a Coulombic mechanism causing the ejection of one of its outer valence electrons. This excess energy is transferred to a neighboring atom or molecule, leading to the ejection of a valence electron [29]. Finally, the doubly charged system dissociates due to electrostatic repulsion. In the core excited clusters ICD will follow the Auger decay which is localized to the excited atom. The ICD lifetime is expected to drop with the number of the nearest neighbors of the excited center [27, 30] implying that bulk sites are more sensitive to the ultrafast process.

3.4 UV/Vis Fluorescence decay

Due to the nature of the free emitted electron, any amount of energy can be absorbed and transformed into kinetic energy in the photoionization process. Below the orbital binding energy (threshold energy) the photon can be absorbed to lift the electron from an inner occupied orbital to a partially filled or to an unoccupied orbital. The transition is possible only when the photon energy exactly matches the energy difference between both states. The event is called resonant excitation. The schematic illustration of photoionization and resonant excitation processes yielding either emission or excitation of an Ar $2p_{3/2}$ electron is presented in Fig. 3.4.

The Auger decay is the dominant electronic relaxation route of the Ar $2p$ core hole. Resonant Auger processes are known to occur below the $2p$-ionization threshold as a result of $2p^{-1}nl$ excitations [31]. This leads efficiently to Ar$^+$ formation since the primarily excited electron acts preferentially as a spectator. However, high-resolution Auger spectra reveal limitations of the spectator model [31, 32, 33, 34, 35]. This is particularly true for the $2p_{3/2}^{-1}3d$ and $2p_{1/2}^{-1}3d$ states that are dominated by shake processes. As a result, various cationic states with excited electronic configurations, such as $3p^44d$ or $3p^45d$, are observed as a result of shake-up processes [34]. Many of these excited states decay via the emission of fluorescence light in the ultraviolet-visible (UV-VIS) regime.

As an example, normal Auger decay starts by photoemission of a $2p$ electron by radiation above the ionization threshold, i.e., for example, 260 eV. Resulting configuration:

$1s^22s^22p^53s^23p^6$
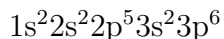
Auger relaxation leads to the doubly charged cation

$1s^22s^22p^63s^23p^4$
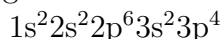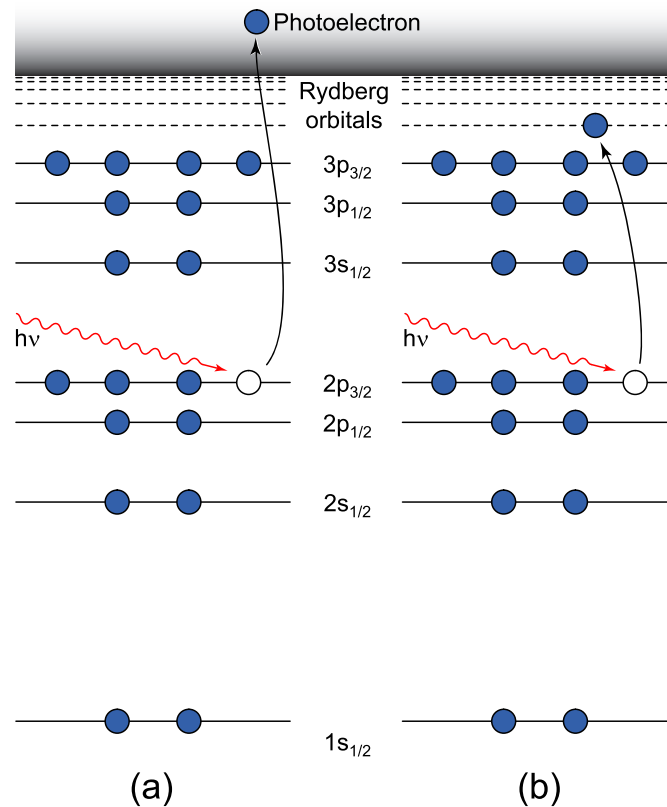
Now consider resonant excitation at 244.4 eV. This leads to
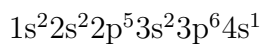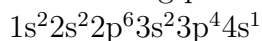
Figure 3.4: Schematic illustration of (a) photoionization and (b) resonant excitation of an Ar $2p_{3/2}$ electron.

$$1s^2 2s^2 2p^5 3s^2 3p^6 4s^1$$

The $4s$ Rydberg electron acts, during Auger decay, as a spectator, i.e., it is not involved in the following processes. In this way we end up in

$$1s^2 2s^2 2p^6 3s^2 3p^4 4s^1$$

Thus, we have Ar^+ instead of Ar^{++}, and this Ar^+ is a Rydberg atom. Now we come to the important issue. There is a certain probability for the $4s$ Rydberg electron to act in the process as a participator rather than solely spectator. It may gain (shake-up) or loose (shake-down) energy, so that it undergoes a transition into another stationary state during the Auger process. We might come up with

$$1s^2 2s^2 2p^6 3s^2 3p^4 3d^1$$
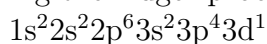
as the final state. That means the energy of the final ion is somewhat higher. Consequently, the energy of the Auger electron is somewhat lower. Therefore, when doing Auger electron spectroscopy, we see a peak that is shifted by the energy difference between the $4s$ and the $3d$ state. Actually, there are many states, which are due to spin-orbit coupling etc; Argon has a very complicated intermediate coupling scheme that is traditionally described in terms of LS coupling. As a result, a $3d$ state is born even though a $4s$ electron was originally excited, this happens not only after excitation of the $4s$ state. It may happen after excitation of other primary states as well.

Flesch *et al.* [36] obtained results on UV-VIS fluorescence of $2p$-excited argon by using monochromatic synchrotron radiation allowing them to excite the argon selectively

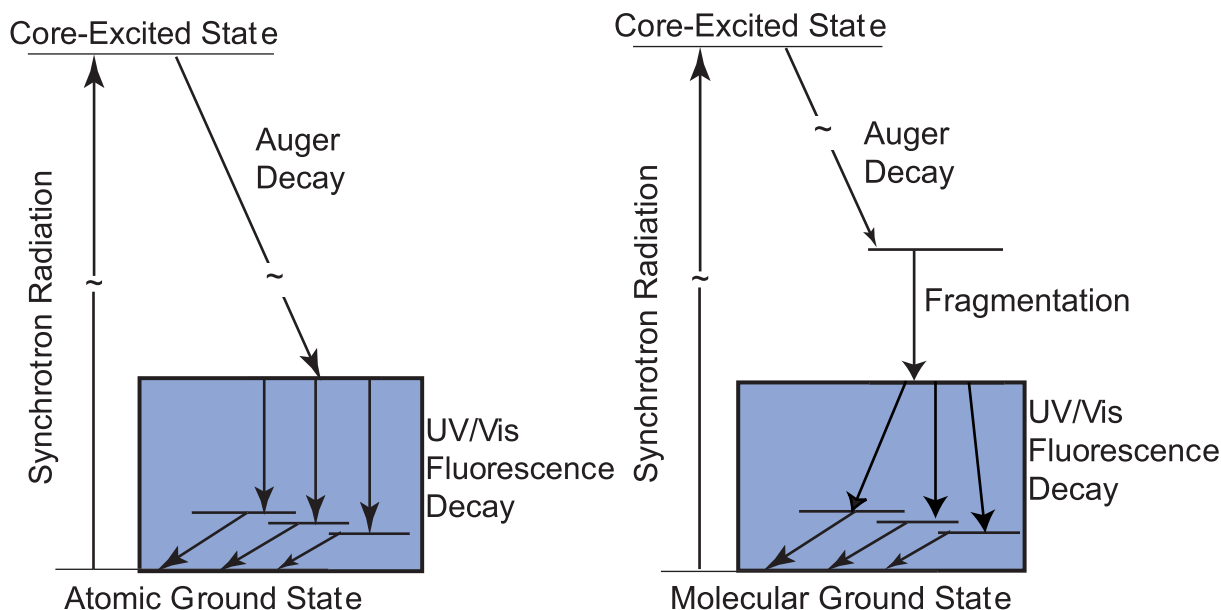**Figure 3.5:** De-excitation scheme including UV/Vis emission of atoms and molecules. The Auger decay leads to the formation of electronically excited photofragments which give rise to fluorescence photons.

into specific core-excited configurations. Therefore, state-selective dispersed fluorescence spectra could be recorded. The results were compared to high-resolution Auger-electron spectroscopy experiments [32, 33, 34, 35, 37], since the final states of Auger transitions act as a start for relaxation processes via the emission of fluorescence light. In addition, time-resolved experiments were reported. As a result, fluorescence that comes directly from ions that are formed by resonant Auger shake processes is clearly distinguished from secondary fluorescence processes occurring in radiative cascades of Ar^+.

The excitation of a core electron in atoms and molecules induces very complex relaxation processes, which are governed by the competition between emission of electrons and photons as well as the fragmentation of the molecules (see Fig. 3.5). Various experimental techniques have been applied to a large number of systems for studying different aspects of various mechanisms [38].

The relaxation processes for a core-excitation in atoms and molecules are illustrated schematically in Fig. 3.5. After excitation of a strongly bound core electron, the electronic decay via autoionization or Auger transition leads to singly or doubly charged ionic states. Most of the highly excited states are not stable against dissociation and lead to the fragmentation of the molecule. De-excitation by emission of x-ray photons represents a minor relaxation channel, but has nonetheless been studied experimentally [39]. More common techniques applied to investigate the excitation and relaxation processes are absorption and electron spectroscopy and electron-ion coincidence methods [40, 41, 42, 43, 44]. Information about the initial core-excited state, the fragmentation process, and the final ionic states has been obtained by these methods and provides already a rather large basis for the theoretical analysis [45, 46].

Chapter 4

Synchrotron Radiation

In this chapter I will present the basics of the synchrotron radiation production and the beam lines where I have performed by experiments (BESSY-II and UVSOR-II). Firstly the generation of synchrotron radiation as well as different types of time of flight technique and electron energy analyzers can be found thoroughly described in other publications [47]. Secondly this thesis is mainly devoted to clusters physics; synchrotron radiation, time of flight techniques, and photoelectron spectrometer are the techniques which we have chosen to study this area of cluster physics. For this reason, it is believed that a detailed description of synchrotron facilities is necessary. A brief introduction is given, since the main part of this experimental work has been carried out at synchrotron radiation facilities, and the summary of the thesis should in some way reflect the experimental work including the equipment.

4.1   The synchrotron as a light source

This chapter deals with basic properties of the synchrotron radiation. Synchrotron radiation is electromagnetic radiation that is emitted by charged particles traveling in a curved trajectory at velocities close to the speed of light. When a charged particle encounters a magnetic field, it is subject to centripetal acceleration due to the Lorentz force and some of the kinetic energy of the electron is transformed to synchrotron radiation.

4.1.1   Synchrotron light generation

A synchrotron radiation facility consists basically of three different components: The electron (positron) storage ring, the insertion devices, and the beamlines (see Fig. 4.1). The same storage ring can be alternatively used to store electrons or positrons, since both particles have the same mass and obey the same physics. In the electron storage ring, electrons (positrons) are circulating with kinetic energy in the order of 1–5 GeV, corresponding to 99.999% of the speed of light. At non-straight paths of the electron storage ring, the electrons are deflected by dipole magnets. To compensate for energy losses, the stored electrons are accelerated by a microwave cavity. An accelerated charged particle, such as an electron in a storage ring, emits radiation. Thus, depending on the device used to bend their trajectories, synchrotron radiation is produced. The simplest devices generating synchrotron light are bending magnets (BM). They are located in the non-straight
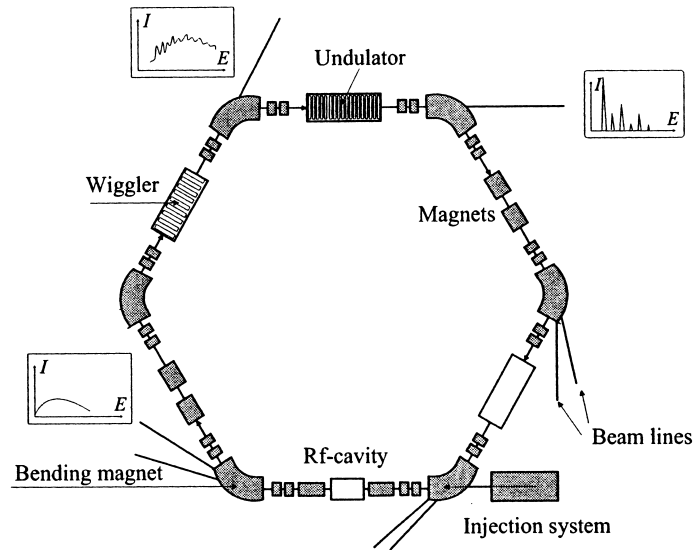
Figure 4.1: Schematic diagram of a storage ring

paths of the storage ring where the electrons are deflected. The radiation is emitted at the bending pointing in forward direction. This radiation is highly polarized with the electric field vector **E** confined to the orbital plane and it emerges highly collimated in the direction of the instantaneous acceleration.

At a synchrotron facility the stored electron undergoes centrifugal acceleration at the bending magnets or at special insertion devices. The centrifugal acceleration of the stored electrons is highly relativistic. Both wigglers and undulators are located at the straight sections of the electron storage ring, and consist usually of arrays of permanent magnets; one array is located above the electron trajectory and the other below. The period of the magnets is such that the magnetic field is of alternating direction, for this reason the electrons wiggle their way through the undulator/wiggler.

The main difference between wigglers and undulators is that in undulators there is constructive interference of the emitted radiation, whereas in wigglers no interference occurs. Compared to undulators the period length of a wiggler is generally smaller and the strength of magnetic field is larger and therefore one can use wigglers to generate photons with energy above 2 keV whereas undulators often are used in the photon energy region between 50 eV and 1.5 keV. Constructive interference takes place when the period of the sinusoidal movement of the electron when passing through the undulator coincides with the wavelength of the radiation. This implies that the spectrum obtained from an undulator is not smooth, it has sharp interference maxima of harmonics spread over a wide energy range. The position of these maxima may be changed by varying the strength of the magnetic field; in practice this is done by changing the distance (gap) between the two arrays of permanent magnets.

The width of a harmonic in an undulator spectrum is not narrow enough for high-resolution spectroscopy so that a monochromator is needed to perform spectroscopy experiments. To improve the photon energy resolution in the soft X-ray region is a challenge. Below the soft X-ray region normal incidence gratings and mirrors can be used, but in
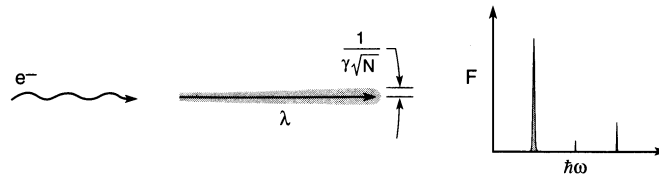
Figure 4.2: Characteristics of undulator radiation [48].

the soft X-ray region are limited to grazing incidence optical elements. For this reason and since there is commonly a requirement for a small photon spot in the experimental setup, the photon energy dispersive part is usually an extended device. Most often, the beamline incorporates both pre-focusing optics, a monochromator, and re-focusing optics. Although the radiation generated in the BM and ID has the basic characteristic to be useful in experiments it needs several optical components to be transmitted to the experimental region with proper focusing and spot size conditions [47].

4.1.2 Insertion devices

The most simple insertion device, the wavelength shifter, has only three magnetic poles; one with higher field strength and two weaker ones. The shape of the photon distribution is similar to bending magnet radiation, but the spectrum is shifted to higher energies and it has higher intensity. Undulators are periodic magnetic structures with relatively weak magnetic fields. The periodicity causes the electrons to experience harmonic oscillations as they move in the axial direction, as in the figure 4.2. The weak magnetic fields cause the amplitude of this undulation to be small, hence the resultant radiation cone is narrow. Undulator radiation is generated as a highly relativistic electron traverses a periodic magnetic field. In the undulator limit the resultant angular deviations of the electron are smaller than the angular width of the natural radiation cone, $1/\gamma$, normally associated with synchrotron radiation. The frequency spread of undulator radiation can be very narrow and the radiation can be extremely bright and partially coherent under certain circumstances. The characteristic emission angle is narrowed by a factor $\sqrt{N}$, where N is the number of magnetic periods. Typically, N is of the order of 100. Depending on magnet strength, harmonic radiation may be generated.

Wigglers are a strong magnetic field version of undulators. Due to the stronger fields the oscillation amplitude and radiated power are larger. The radiation cone is broader in both, space and angle. The radiation spectrum is similar to a bending magnet, but characterized by a much larger photon flux and shift to harder X-rays (shorter wavelengths), as in the figure 4.3. Wiggler radiation is also generated from a periodic magnetic structure, but in the strong magnetic field limit, at least in one plane the angular deviation is significantly greater than the natural $(1/\gamma)$ radiation cone. Although more power is radiated, wiggler radiation is less bright because of the substantially increased radiation cone.

Undulators and wigglers have different characteristics in their magnetic arrays. Namely, wigglers have higher magnetic fields and less magnetic poles than undulators. The so-called K-parameter can be used to determine if the insertion device acts as a wiggler or
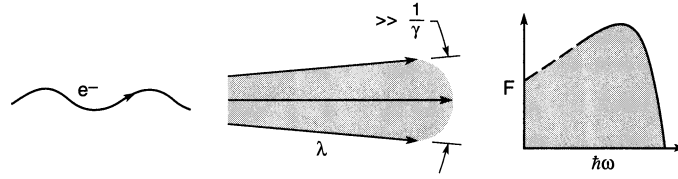
Figure 4.3: Characteristics of wiggler radiation [49].

as an undulator

$$K = \frac{eB_0\lambda_0}{2\pi m_0 c} \simeq 0.934 B_0[T]\lambda_0(\text{cm}), \tag{4.1}$$

where B_0 is the amplitude of the magnetic field and λ_0 is the period length of the magnetic array.

The physical meaning of the K-value corresponds to the ratio between the maximum deflection angle α in the insertion device and the natural angular spread of photon emission of one electron, see fig. 4.4. When $K \gg 1$, the deflection is bigger than the angular spread of the emission. In this case, the insertion device is a wiggler and the energy distribution of the radiation resembles that of bending magnet radiation. However, due to the multiple structure, the emitted intensity is proportional to number of the periods $\simeq 2N_m$, causing higher intensity [50].

For K values close to unity, the insertion device behaves as an undulator. The major difference from the wiggler is that constructive interference occurs more strongly in the undulator. This causes the spectral intensity to concentrate on certain frequencies (harmonics)

$$\nu_n \simeq n \left(\frac{2c\gamma^2}{\lambda_0}\right) \left(1 + \frac{K^2}{2} + \gamma^2\theta^2\right)^{-1} ; n = 1, 2, 3 \ldots, \tag{4.2}$$

where θ is the observation angle with respect to the undulator axis and n is the number of the harmonics. When the K-value is below unity, the spectrum is composed mainly of the strong peak at the fundamental frequency ν_1. With $K < 1$, the relative intensity of the higher harmonics n ν_1 is increased. The K-value also affects the frequency of the harmonics; when K is increased, the undulator spectrum shifts toward lower photon energies. Because the K-value depends on the magnetic field in the undulator, it is conveniently varied by changing the distance between the magnets, i.e. by changing the gap.

The undulator spectrum contains narrow, well separated peaks, and thus the intensity can be 2–4 decades higher at the peak maximum compared to the continuous spectrum of a bending magnet. The intensity of an undulator harmonic depends on how narrow the peak naturally is, i.e how concentrated the energy distribution is around the harmonic energy. There are several factors that contribute to the energy width of the harmonics. The natural width for the nth harmonic at the angle $\theta = 0°$ depends on the number of undulator periods N_m as $\Delta\nu/\nu \simeq (nM_m)^{-1}$.

By increasing the number of periods, the peak width becomes narrower. The peak width is also affected by the accepted angular cone $2\Delta\theta$ of the radiation as
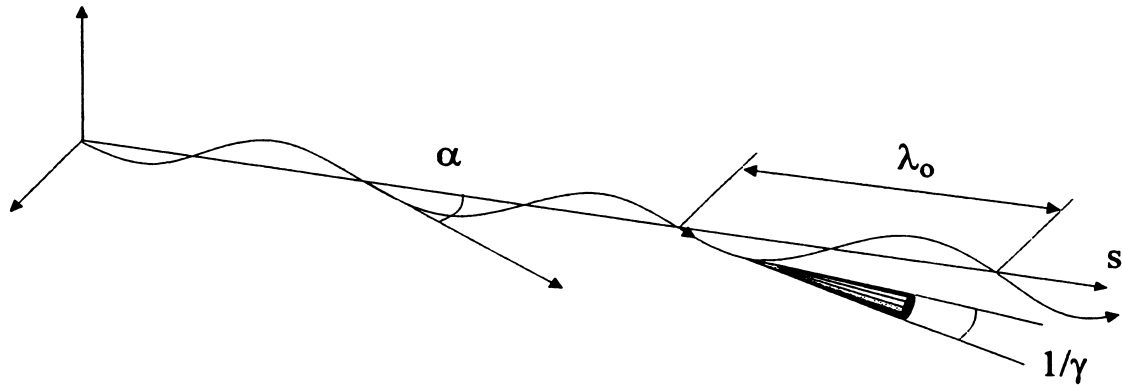
Figure 4.4: Electron beam trajectory in a planar insertion device.

$$\Delta\nu/\nu \simeq \frac{\gamma^2 \Delta\theta^2}{1 + K^2/2}. \tag{4.3}$$

The accepted angular range of the beamline is usually limited by apertures or baffles. However, while the apertures make harmonics narrower, they also cut out some of the intensity. Other factors that cause line broadening are magnetic field errors in the undulator and the energy spread of the electrons, which is described by

$$\Delta\nu/\nu \simeq 2\Delta E/E \tag{4.4}$$

Undulator radiation also possesses full polarization of the light. For a basic planar undulator and an axis of the magnetic poles perpendicular to the storage ring plane, the light is usually $\sim 100\%$ linearly polarized in the horizontal plane. In addition, there are various undulator designs (e.g. APPLE type) that are used to produce elliptically or circularly polarized light. After the undulator has been placed in the storage ring and has become operational, some of its characteristics such as period length and number of magnetic poles are fixed. However, there are still variables that can be used to modify the undulator spectrum. The gap between the magnets can be changed in order to change the harmonic energy, or the magnetic arrays can be shifted with respect to each other in order to change the polarization properties. The distance between the magnets does not have to be uniform through out the undulator, (tapering) which can be used to produce broadening of the harmonics.

4.2   Beamline

The radiation that comes from a bending magnet or from an insertion device is usually not directly usable for spectroscopic experiments even though synchrotron radiation is already collimated and in the case of undulators, also partly monochromatic. In order to maximize the brilliance, the photon beam size should be of same size as, or smaller than the source size. On the other hand, the existence of a large variety of different energies in the incoming radiation would complicate the spectra, broaden resonant structures

and disguise selective excitations. It is necessary to supply the soft X-ray beamlines with reflection optics that are used to focus the radiation into the experimental setup. The beamlines are maintained under ultra-high-vacuum (UHV) in the soft X-ray regime, because the soft X-ray radiation is heavily absorbed when it encounters a gas or solid. Even more important is that very low pressure reduces the contamination rate of mirrors and grating surfaces. The heart of a beamline is the monochromator because it selects the usable photon energy range, the spectral resolution, and photon flux that is delivered to the experiment. In principle, the monochromator contains mirrors, gratings, and slits. Diffraction grating monochromators are used in the soft X-ray regime, whereas crystal monochromators are used in the hard X-ray regime. The dispersion of radiation is based on the grating equation

$$\sin \theta_i + \sin \theta_d = m\lambda N \qquad (4.5)$$

where θ_i and θ_d are the incidence and diffraction angles, m is a integer number that specifies the order of the diffraction. The number of lines per millimeter on the grating is given by N. Depending on the wavelength the radiation is diffracted into different angles and thus it is possible to choose the desired energy that passes the monochromator. An important parameter that describes the relative energy width ΔE around the center energy E is the energy resolving power $R = E/\Delta E$.

After monochromatization and focusing the radiation is used for measurements at the end station. In addition to optics and the monochromator, the beamline consists of a large number of other essential parts. Some of them are described here: The UHV in the beamline and at the experimental chamber is usually maintained using ion, turbo molecular, and sublimation pumps. Pressure gauges give signals to an interlock system that closes the beamline in the case of unexpected pressure changes. Gate valves separate the beamline in isolated sections. They are also used to separate some of the pumps from the beamline or from the end station. A beam shutter closes the beamline and absorbs γ radiation that is created during the injection. Water cooling, which can also be connected to the beamline safety system, cools the optics and other parts in the beamline and the experiment. The photon flux can be measured by detecting the current from a gold mesh or a photo diode. Apertures, baffles, and slits can be used to modify the size and shape of the photon beam. They can affect the polarization resolution and the amount of stray light from the storage ring. Finally, a beamline control system works as an interface between users and the beamline. It takes care of the safe and reliable operation of the beamline.

Chapter 5

Experimental setup

This chapter gives a short overview over the experimental resources where I have performed my measurements. I have investigated free clusters by using several spectroscopy methods. I will describe cluster production techniques, then time-of-flight (TOF) mass spectrometry, zero kinetic energy photoelectron (ZEKE) spectroscopy, fluorescence and finally electron spectroscopy. Most of the experiments have been carried out at BESSY II, Berlin and UVSOR, Okazaki.

5.1 Clusters production in supersonic jets

It is important to note that progress in cluster science has followed closely on the development of new experimental techniques, in particular the development of molecular beam techniques have enabled the study of free clusters in an interaction free environment. The study of clusters requires a proper understanding and management of their production and bundling. As for many other physical systems, production conditions strongly limit the level of details accessible in experiments. It is thus of importance to discuss production mechanisms in order to better understand what is measurable and how. It is thus the first aim of this chapter to make a brief presentation of cluster production mechanisms, in terms of cluster sources.

We shall here illustrate this by several examples from ongoing cluster research. Cluster production and analysis are intimately linked. Usually, an experimental set up integrates all elements from the source to the collection of data. Such a complete chain of production/measurements/data storage is made possible by the relative compactness of all the elements in the experimental set up. All in all, cluster physics experiments can be performed in modestly sized rooms of a few tens of square meters at most. A schematic picture of a typical experimental set up is shown in Figure 5.1. It demonstrates the case of the widely used supersonic jet source associated with a mass spectrometer for cluster selection. Let us briefly discuss the various components of such an apparatus.

Once produced in the source, clusters are ionized either by electron or photon impact. The non-zero net charge thus acquired allows mass selection in the mass spectrometer, an essential step in order to identify the clusters on which experiments are performed. The third compartment contains the analysis apparatus itself.

The last compartment on the right, sketches electronic devices to store accumulated data. Not shown in the sketch is the very last step of the chain, the data analysis.
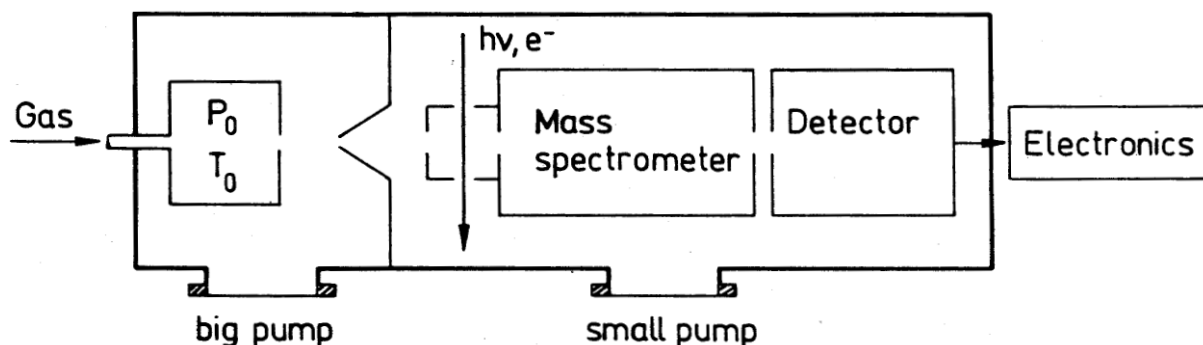
Figure 5.1: Schematic view of an experimental setup [1].

It is usually done off line. Because this chain is continuous, from production up to data storage, and because it is usually operated as a whole, the production phase is of particular importance as it directly affects experimental outcomes.

Variable size clusters are efficiently produced by adiabatic expansion of neat gases or gas mixtures into the vacuum. This method is well-known since decades [1]. It makes use of a small nozzle of typically 10–100 μm diameter and a skimmer, which separates the expansion chamber from the detection chamber, where the clusters are analyzed.

Cluster production is a key step in cluster studies. As mentioned above, cluster physics, in particular the study of free clusters, really started in the 1970s with the increasing availability of cluster sources. Without proper and controlled means of production, cluster physics was bound to the study of embedded, or at best deposited, systems. In such cases observed phenomena mix in a complex manner the effects of cluster and substrate or matrix. The start of studies on clusters themselves is thus directly related to progress made at the level of production sources. Not surprisingly, many types of sources have been developed to produce clusters of various sizes and properties. Clusters are finite objects, finite pieces of material. In order to produce them, one can thus either aggregate smaller systems (atoms, molecules, small clusters) or break larger systems (bulk typically). Cluster sources hence basically rely either on condensation/aggregation or on break up, and sometimes on both.

One can thus sort cluster production sources into three main classes [51]. In supersonic jets, a gas is expanded into vacuum from a high pressure through a small nozzle. The subsequent adiabatic expansion and cooling leads to cluster formation by condensation. In gas aggregation sources, atoms are injected into a stationary or streaming gas and cluster formation again proceeds via condensation due to cooling of a gas of atoms. In surface sources, on the contrary, clusterization primarily proceeds via break up, in the sense that "proto"-clusters are stripped from a surface by particle or photon impact or by a high electric field, even if some condensation follows.

There remains to detail how to activate efficiently these basic production mechanisms. We shall briefly present various types of frequently used cluster sources. One type of source will be discussed in somewhat more detail, namely the supersonic jet sources. This should serve to exemplify the experimental difficulties raised by cluster production, in particular in terms of cluster identification and properties such as size, charge, and temperature. A more detailed discussion of the various sources and their advantages and
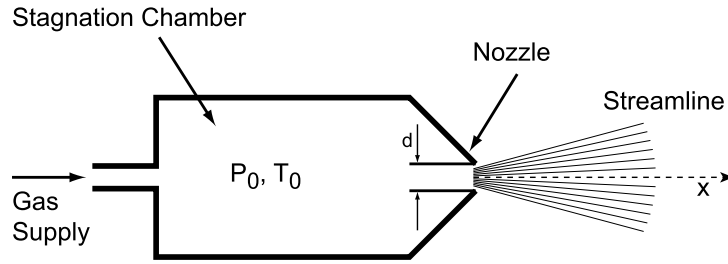
Figure 5.2: Free jet expansion from a sonic nozzle into vacuum.

disadvantages can be found in the review [52] or in the books [53, 54].

5.1.1   Seeded supersonic nozzle sources

The widely used supersonic jets are among the best understood cluster sources. They thus offer an ideal tool to analyze the difficulties encountered in cluster production and identification. The basic idea in such sources is cluster formation by condensation of an expanding gas of atoms [55]. A highly compressed gas (typical total pressure $P \sim 10$ bar) with atoms of the material to be aggregated is allowed to expand through a small nozzle. The ensuing adiabatic expansion slows down the atoms up to a point at which binding between neighboring atoms becomes energetically favorable. This leads to the successive aggregation of the atoms in clusters.

Free jets expanding into vacuum (see Fig. 5.2) are widely used for supersonic flow fields and as a source for nozzle and cluster beams. Their properties are well understood and documented in the literature [51]. The following brief discussion gives the main results for monatomic gases.

In the initial collision-dominated regime the expansion is isentropic with flow velocity increasing up to its limit ω_∞:

$$\omega_\infty = 1.581\sqrt{\frac{2kT_0}{m}} = 204\sqrt{\frac{T_0[\text{K}]}{m[\text{amu}]}}\left[\frac{\text{m}}{\text{s}}\right], \tag{5.1}$$

with 1 amu = atomic mass unit = 1.660×10^{-27} kg. The streamlines of the flow resemble those of a source flow, and thus number density n drops as the inverse square of distance. The result for density n and temperature T on the jet axis is, for $\delta = x/d > 4$:

$$n(\delta)/n_0 = 0.156\delta^{-2}; \quad T(\delta)/T_0 = 0.282\delta^{-4/3}. \tag{5.2}$$

Note that the flow field variables depend only on the reduced nozzle distance δ. The absolute values of n_0, T_0, and d determine, however, the range of the effective expansion, i.e., the range of δ, beyond which the flow has reached the terminal temperature T_∞, and passes into the collisionless molecular flow regime. This transition depends on the scaling parameter Ψ, [56]

$$\Psi = n_0 d T_0^{-1.25}. \tag{5.3}$$

For hard-sphere molecules T_∞, and Ψ, are related by

$$T_\infty = K\Psi^{-4/5}, \tag{5.4}$$

the constant K depending on the respective gas. Considering that nozzle mass flow J_0 is proportional to $n_0 d^2 \sqrt{T_0}$, Ψ is proportional to $J_0 d^{-1} T^{-1.75}$: For $J_0 = \text{const.}$ small nozzles and low temperatures T_0 increase Ψ and thus lead to lower terminal temperatures. This explains the tendency to use smaller nozzles operated at higher pressures/densities.

Seeded supersonic nozzle sources are mostly used to produce intense, cold, and "directed" cluster beams with acceptably narrow speed distributions. They allow the formation of clusters with hundreds, even thousands of atoms per cluster with reasonable abundance.

5.1.2 Expansion

One starts with an initial gas of atoms at a given temperature T_0. Before atoms are expanded through the nozzle their velocities are random; the high pressure implies a small mean free path (much smaller than the nozzle diameter) and thus a highly collisional regime, which can be typically understood in terms of hydrodynamics. The adiabatic expansion through the will occur, as we shall see. With proceeding expansion, one reaches a point beyond which the picture of a continuous medium breaks down, and so does the hydrodynamical approach. From then on, each formed particle will more or less follow its own path. The basic properties of the further expanding gas are essentially frozen beyond this instant of "decoupling" of the system. The velocity profiles of the expanding gas, for example, turns out to be essentially Maxwellian from then on, with temperature as given by the one at the end of the "hydrodynamical" phase of the expansion [57].

5.1.3 Cluster formation and size distribution

Cluster formation during the expansion proceeds by condensation. It is a complex process which is not yet fully quantitatively understood. The basic condensation mechanism, though, is simple. When atoms in the jet become sufficiently cold, they can bind together to form a dimer (this corresponds to a temperature smaller than the binding energy of the dimer). These dimers (some of them being possibly already present even in the original vapor) constitute seeds for further clusterization. It should be noted here that the kinematics of the expansion process, with only a small spread of atomic velocities, tends to favor this clustering mechanism by keeping atoms in the vicinity of each other. The actual evolution of the system towards the formation of large or small clusters depends on the thermodynamical properties of the jet itself. When the pressure in the jet is small, cluster growth mostly proceeds on the basis of monomer aggregation, basically leading to low mass clusters. A high pressure p in the jet, in turn, allows growth of clusters by cluster aggregation which leads to the production of large clusters. Not surprisingly, the initial pressure p_0 of the gas of atoms is hence directly linked to the actual size distribution of the produced clusters and thus to the abundance spectrum.

One important property of adiabatic expansions is, that they give size distributions, so that the average cluster size, often denoted as $\langle N \rangle$, characterizes the maximum of the size distribution of neutrals that are produced in jet expansions. The average cluster size can be easily obtained from scaling parameters, which have been introduced by Hagena [56, 57]. The advantage of scaling parameters is, that they reduce various experimental quantities that affect the gas expansion, such as the temperature and pressure in the high

pressure reservoir (stagnation temperature T_0 and stagnation pressure p_0), the nozzle diameter D, and properties of the expanded gas. The reduced scaling parameter Γ^* is defined as follows [57]:

$$\Gamma^* = \frac{\Gamma}{\Gamma_{\text{ch}}} = \Gamma R_{\text{ch}}^{3-q} T_{\text{ch}}^{1.5-0.15q} \tag{5.5}$$

where q is an experimental parameter, which is for argon 0.85, T_{ch} is the characteristic temperature: $T_{\text{ch}} = \Delta h_0^0 / K$, where Δh_0^0 is the sublimation enthalpy at $T = 0$ K, k is the Boltzmann constant; R_{ch} is the characteristic distance: $R_{\text{ch}} = (m/\rho)^{1/3}$, where m is the atomic mass and ρ is the density of the solid; Γ is the scaling parameter, with $\Gamma = n_0 D T_0^{0.25q-1.5}$, where n_0 is the number density in the high pressure volume. Typical values for argon are: $R_{\text{ch}} = 3.39$ Å and $T_{\text{ch}} = 927$ K. This yields for argon the simple formula [58]:

$$\Gamma^* = \frac{1646 p_0 [\text{mbar}] d^{0.85}[\mu\text{m}]}{T^{2.29}[\text{K}]} \tag{5.6}$$

The reduced scaling parameter Γ^* can be used in combination with experimental observations in order to obtain a first qualitative estimate on the cluster size in the jet [57]: if $\Gamma^* < 200$ no clusters are formed while if $200 < \Gamma^* < 1000$ then small clusters are formed. If $\Gamma^* > 1000$ then large clusters are formed.

$$\begin{array}{ll} \Gamma^* < 200 & \text{no clusters} \\ 200 < \Gamma^* < 1000 & \text{small clusters} \\ \Gamma^* > 1000 & \text{large clusters} \end{array}$$

Various experimental approaches have been used in the past to correlate Γ^* with $\langle N \rangle$. These include electron diffraction [59], mass spectrometry [60], and molecular beam scattering experiments [61]. The latter approach is especially suitable for the low $\langle N \rangle$-regime. The typical value range that is available for core level excitation on krypton clusters in our experiment is $\langle N \rangle < 1700$ [62], if the correlation of Farges *et al.* is used [59]. Somewhat lower values are obtained, if the more recent, but likely more realistic calibration of Karnbach *et al.* is applied (cf. Table 5.1) [60].

The typical $\langle N \rangle$-range that is covered by most experiments devoted to core level excitation, reaches from the isolated gas phase up to several thousand atoms per cluster. Table 5.2 gives an overview on the correlation of Γ^* with $\langle N \rangle$.

5.1.4 Temperature effects and handling of supersonic jet sources

The poor mass selection of primary clusters (just behind the source) is however not the single difficulty to overcome. The whole production mechanism involves temperature. The expanding gas cools down; its temperature thus depends on the expansion stage.

Clustering hence takes place at different temperatures corresponding to different instants of the expansion. Even more delicate is a proper control of the formation heat involved in the clustering process. In other words, clusters are formed at finite temperature. And this temperature results from the decreasing global temperature of the collectively expanding system and from the formation heat in each aggregation mechanism, making it specific to the history of each cluster. The problem looks even more complex when realizing that clusters in the jet may also cool down, for example by collisions inside the jet, or by monomer evaporation (basically due to the fact that clusters

Table 5.1: Average cluster size $\langle N \rangle$ of krypton clusters for typical experimental expansion conditions using a nozzle diameter of 50 μm. The correlation of Γ^* with $\langle N \rangle$ is obtained from Ref. 60.

P_0	T_0[K]	Γ^*	$\langle N \rangle$
1	298	180	2
2	298	370	4
3	298	550	12
4	298	730	18
5	298	920	30
5	273	1120	40
5	243	1460	90
5	213	1970	140
5	183	2800	350
5	163	3640	1000
5	158	3910	1250

have a finite temperature). In order to understand the thermal behavior of the clusters during the aggregation phase, one has thus to account for all these competing processes, for example by employing a statistical model when the temperature is high enough. But all the details of these models, in particular at the level of evaporation rates, are not known, rendering these approaches not fully predictable.

The population of clusters formed in the jet will thus exhibit a temperature distribution which is obviously not easy to predict precisely. One might wonder, though, whether this cluster temperature is likely to affect cluster properties. Roughly speaking, the temperatures attained may be comparable to the clusters dissociation energies which obviously make them crucial, even for the existence of the clusters themselves. We shall see below that even moderate temperatures may have an important impact. All that makes a better control over temperature desirable. This can be achieved by mixing the cluster beam for a while with an inert-gas beam of well defined temperature [63]. Heat exchange by collisions brings the clusters into thermal equilibrium with the cooler-gas. This allows one to tune temperature over a broad range and in particular to cool down the cluster beam, when necessary.

All in all, this brief overview of cluster production in supersonic jets clearly points out the difficulties one faces in the identification and characterization of formed species. The proper tuning of source parameters thus turns out to be an essential ingredient of any experimental program. As we have seen above, there are no definite models to handle these parameters precisely, although one understands basic underlying physical mechanisms. And of course, experience in the handling of sources becomes essential. In the case of supersonic jets, there thus exist scaling laws for cluster formation involving the initial pressure p_0 and temperature T_0 of the atom gas, as well as the diameter D of the nozzle. For example, it is known that cluster size increases with increasing p_0 or D and decreasing T_0. Usually the distribution of formed clusters is broad. It should also be noted that, in such a condensation process, impurities in the gas play a big role. They

Table 5.2: Correlation of Γ^* with $\langle N \rangle$ for argon clusters, when $p_0 = 5$ bar of argon are expanded through a 50 μm nozzle. The stagnation temperature T_0 is measured at the nozzle tip. Γ^* is calculated according to [57]. The correlation of Γ^* with $\langle N \rangle$ is obtained from [60] and [59], respectively.

T_0 (°C)	Γ^*	$\langle N \rangle$ (Ref. 60)	$\langle N \rangle$ (Ref. 59)
30	490	10	10
0	620	15	20
-10	675	18	30
-20	740	20	50
-30	810	22	80
-40	900	25	105
-50	990	35	140
-60	1100	40	175
-70	1230	50	225
-80	1380	60	270
-90	1570	70	340
-100	1790	80	430
-110	2050	120	530
-120	2380	200	750

may constitute condensation germs and lead to an increase of average cluster sizes.

The clusters are detected by a mass spectrometer after ionization. Observed mass spectra are generally not uniform, giving some peaks at certain numbers which are called *magic numbers*. In the case of rare gas clusters observed magic numbers, 13, 55, 147, . . . , correspond to the series N_{magic} given by:

$$N_{\mathrm{magic}}(n) = 1 + \sum_{k=1}^{n} \left(10k^2 + 2\right)$$

where atoms are built up layer by layer to a total of n layers of an icosahedron.

Some other series of numbers due to polyicosahedral and partially closed icosahedral clusters are also observed. These typical magic number peaks are observed for Xe and Kr clusters and for very large Ar clusters [64]. Since small Ar clusters are generated from the stable core Ar_2^+, different magic numbers are observed.

The experiments, that have been carried out in the field of core level excitation, made use of compact portable jet expansion setups. These are flexible in use and easy to mount in short time periods at storage ring facilities [65, 66, 67, 68]. This is different from earlier approaches, where large molecular beam end stations were permanently installed at normal incidence or grazing incidence beam lines, which gave numerous results on outer-shell excitation of clusters [69, 70]. Compact experimental setups are required for these experiments, since there is only limited access to synchrotron radiation light sources. As a result, table top expansions, which make use of high throughput turbomolecular pumps and relatively small nozzle diameters $D < 100$ μm, stagnation pressures $p_0 <$

10 bar, and stagnation temperatures ranging between room temperature and 70 K were preferentially used in the past. Moreover, it turns out that the requirements that make these experiments extremely flexible have no severe drawbacks, since the $\langle N \rangle$-regime that is accessible reaches from purely atomic conditions up to several thousands of atoms per clusters. This is sufficient for investigations on size effects of clusters.

In conclusion variable size clusters in the gas phase are efficiently produced in adiabatic expansions of neat gases or gas mixtures into the vacuum [1]. A small nozzle is used to expand the gases. The size distribution of neutral clusters that are formed in jet expansions is reflected by log-normal distributions [71]. They are characterized by the average cluster size $\langle N \rangle$, which can be estimated from scaling laws. These contain scaling parameters, which were introduced for atomic clusters by Hagena [57]. Later work also allowed to estimate the average cluster size of molecular van der Waals clusters [72].

5.2 Detection methods

Core level excitation leads after photoabsorption of an X-ray photon to photoemission of a core-electron, if the photon energy exceeds the core-electron binding energy. The core hole is stabilized by electronic or radiative relaxation. As a result, double or multiple ionization processes govern core ionization continua. Therefore, the detection of charged products, such as electrons or cations, is the most straightforward way to investigate size effects in variable size clusters by core level spectroscopies.

5.2.1 Time-of-flight techniques

Figure 5.3 shows schematically a typical experimental setup, where all vacuum equipment is not shown for clarity. Jet experiments require high vacuum, whereas in beam lines and X-ray monochromators ultrahigh vacuum is needed. Therefore, an efficient differential pumping stage is essential between the jet experiment and the beam line. The jet experiment consists of

- a continuous jet expansion for cluster production,

- the beam of monochromatic X-rays provided by the storage ring facility,

- a time-of-flight mass spectrometer for cation detection, and

- an electron detector.

Time-of-flight mass spectrometry is among various methods of mass spectrometry the most suitable approach in the regime of core level excitation of free clusters. This technique has the advantage that the transmission function of the mass spectrometer is high, typically of the order of 30% [73]. The cation extraction conditions can be optimized so that even high kinetic energy fragments, that are formed by Coulomb explosion are efficiently detected. Another advantage is that all cations of interest are measured simultaneously. Individual masses are selected by applying proper time gates. This allows to measure simultaneously electronic properties of isolated and clustered species. Small energy shifts of resonant excitations, which can be as small as a few meV in the regime of core-level excitation have been reliably identified in this way [74, 75].
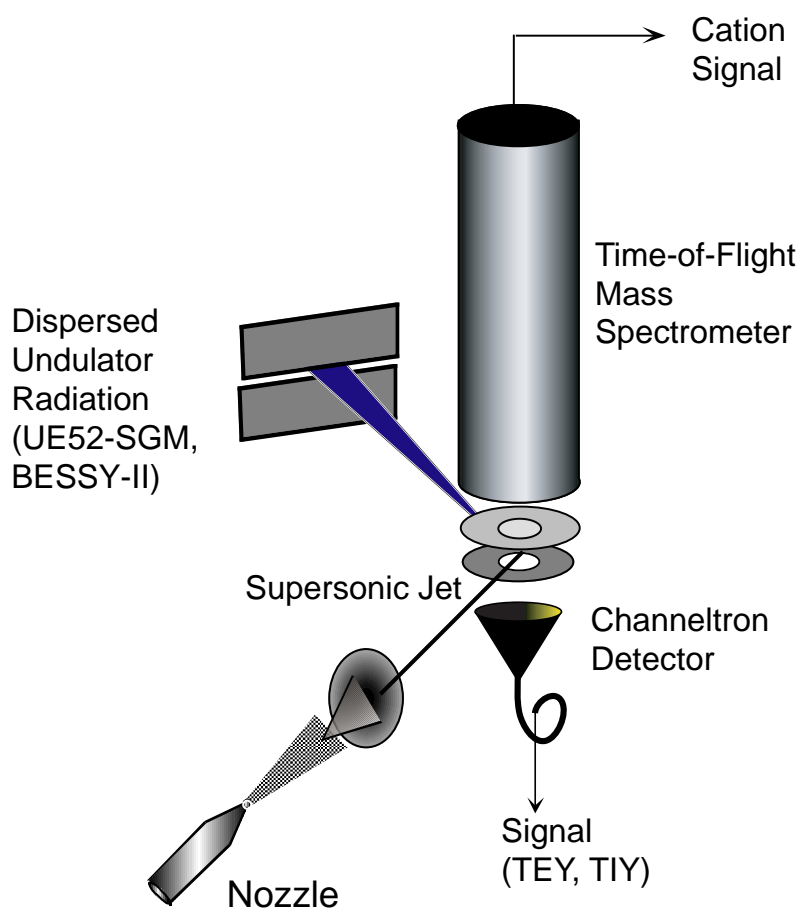
Figure 5.3: Experimental setup for TOF spectrometry on clusters jets. The jet is skimmed, so that the clusters are reaching the adjacent detection chamber. There, it is intersected with a beam of monochromatic synchrotron radiation. The interaction region is typically located in the ionization region of a time-of-flight mass spectrometer or a photoelectron spectrometer.

However, time-of-flight mass spectrometry requires a defined time structure. This is either accomplished by pulsing the cation drawout field (typically 100–2000 V/cm, 10–100 kHz repetition rate) [21], or by using directly the time structure of the storage ring [76]. Especially large circumference storage rings, which are characterized by relatively low repetition rates (typically 1 MHz) in the single bunch mode, can be used in combination with continuous extraction voltages for direct cation flight time measurements. This method turns out to be extremely efficient for cation detection of mass-selected cluster ions, since dead times are minimized [76]. It is noted that this approach requires the use of a short time-of-flight mass spectrometer, so that the cation flight times are kept as short as possible. Then, high electric field strengths for cation extraction are required to obtain proper space focusing of the cation masses at the detector [77].

The standard pulses start a time-to-amplitude convertor (TAC), which is stopped by the delay trigger signal. The TAC output pulse having an amplitude which is proportional to the time between start and stop, is digitized in the fast analog-to-digital convertor of
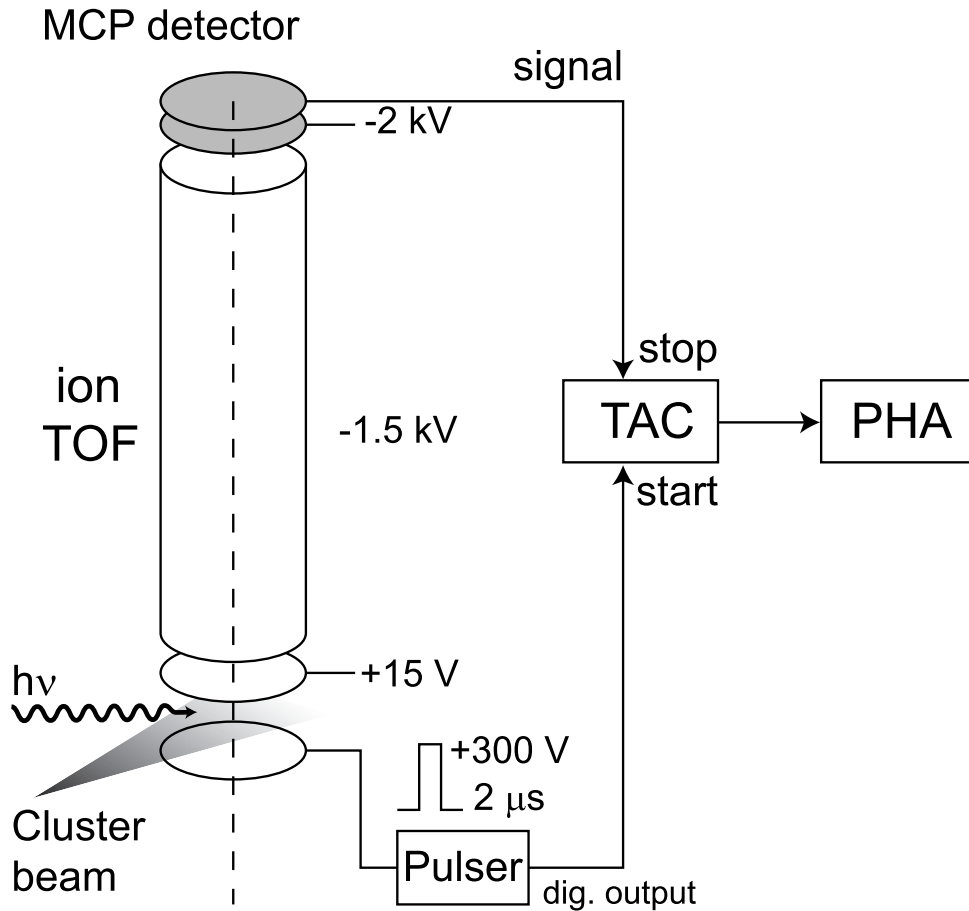
Figure 5.4: Setup used for TOF mass spectrometer. The voltages applied to the TOF and MCP are indicated in the figure.

a multichannel analyzer and stored in the corresponding channel. In contrast to this inverted time configuration it would probably easier to understand to start the TAC with a trigger signal and stop it with the detector signal. The TAC would be more often started than stopped. It would be necessary to stop the TAC internally after a time corresponding to the lowest observed flight time. This would drastically increase the deadtime of the time-of-flight spectrometer. Instead of a TAC one uses for multicoincidence spectroscopies multi-hit time-to-digital converters (TDC).

Electrons are most efficiently detected using total electron yield detectors. These consist either of a channeltron multiplier or a stack of micro channelplates, that are mounted close to the ionization region, where the photon beam crosses the cluster jet. The amplified electron current of "all" electrons is measured as a function of the incident photon energy. Total electron yield spectra may be regarded as pseudo-absorption spectra, but there are distinct differences in physical processes compared to photoabsorption, especially since one X-ray photon may lead to the emission of several electrons.

In order to understand what portion of the cluster distribution contributes to a given yield spectrum, we have investigated the sensitivity of the various detection techniques. This include total electron yield, partial ion yield, total ion yield detection both with
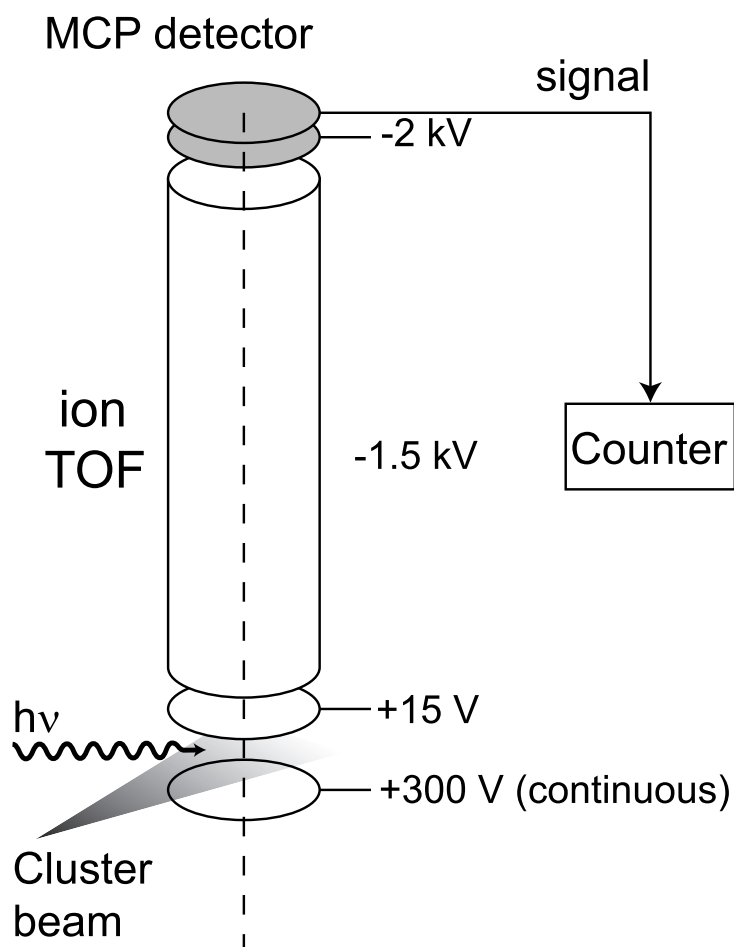
Figure 5.5: Setup used for total ion yield detection (TIY). The voltages are indicated in the figure.

channeltron directly adjacent to the ionization region and with the channelplate detector at the end of the time-of-flight mass spectrometer (see Fig. 5.4). If there is no selectivity among the detection channels all the spectra recorded with these techniques would appear the same. It is clear that mass selected ions can be very beneficial at investigating the absorption spectra of specific a component of a multicomponent beam. Total ion signals are more atomic-like, indicating that the proportion of the atomic signal is artificially enhanced because of discrimination against heavy cluster ions (see Fig. 5.5).

If the beam contained as high a proportion of atoms as either of the total ion yield spectra appear to indicate, then the TEY spectrum would have a much larger atomic contribution, since this detection channel has the least discrimination and thus best represent the spectrum integrated over the distribution of species in the beam. In addition to detection mode dependence, particularly those based on ion detection, were also dependent on the extraction voltages employed. In all cases the conditions were chosen to optimize the sensitivity to high mass components of the beam.

Further development of the excitation creates ionized species with the electrons removed from the valence levels. By scanning the photon energy in the region of interest
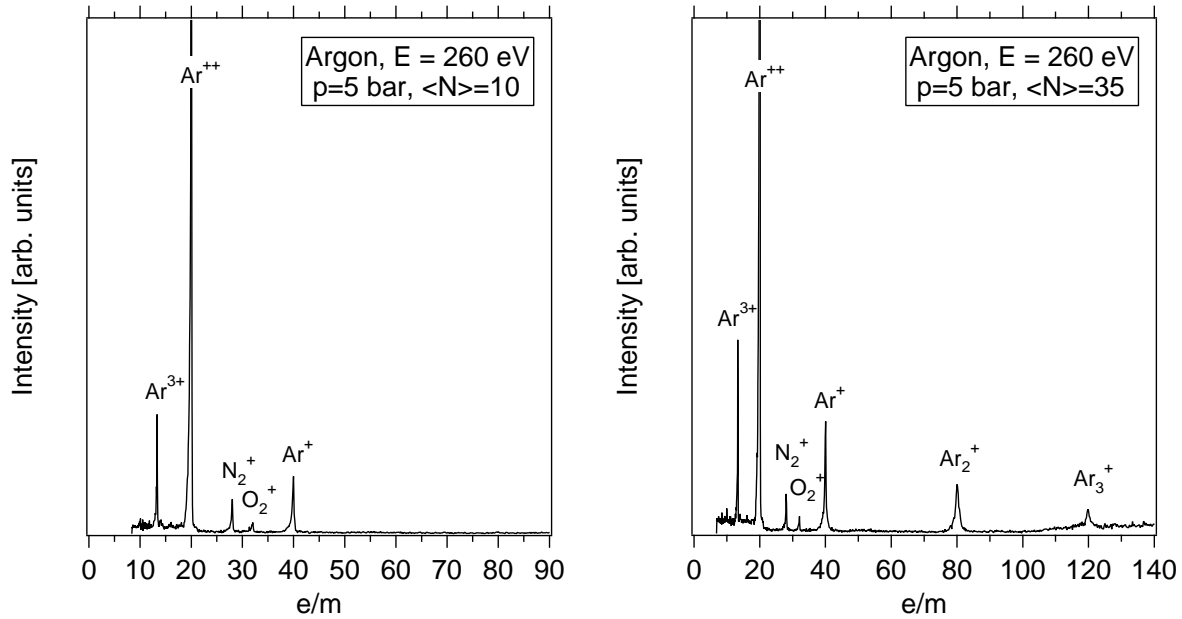
Figure 5.6: Time-of-flight mass spectrum of argon clusters. The mass spectrum on the left has been measured at room temperature while the spectrum on the right at -50 °C. They were recorded using 260 eV photon energy and 300 V, 2 μs extraction pulse.

and collecting the resulting ions (total ion yield, TIY) or the electrons ejected from the valence levels as the result of the excitation decay (total electron yield, TEY) the photoabsorption spectrum is indirectly measured. It provides information on the core-excited states, but when performed by TIY or TEY. In the case of free cluster beams an additional complexity arises as the beam always contains a certain fraction of "uncondensed" atoms. The resulting TEY spectrum is then a superposition of the atomic, cluster surface and cluster "bulk" contributions. PIY is recorded by monitoring the intensity of the cluster fragments, most common of the dimers. Then the response of the uncondensed atoms is excluded from the absorption spectrum. For free argon clusters – one of the most typical object of studies – surface and "bulk" features were identified in TEY and TIY and interpreted in terms of the electronic and geometric structure of the excited and otherwise unoccupied energy levels [65, 68, 75, 78]. In the case of TEY and TIY of free krypton clusters the features could even be correlated to different types of surface sites [78].

Mass spectra of cluster beams generated by supersonic expansion show non-monotonic size distribution. The stability and structure of such atomic and molecular clusters has remained a controversial issue, discussing centering on the consideration of whether the intensity fluctuations found in the mass spectra reflect the size distribution of neutral or ionic clusters. As mass spectroscopy of clusters provides information about the size distribution of the ionic clusters rather that of the neutral species, the question of the effect of the ionization processes on neutral clusters arises.

The example displayed in Figure 5.6 exemplifies a basic difficulty in cluster production, namely the fact that one produces a large variety of clusters in the jet. And it is obvious that clusters with very different sizes will exhibit different physical properties. In other
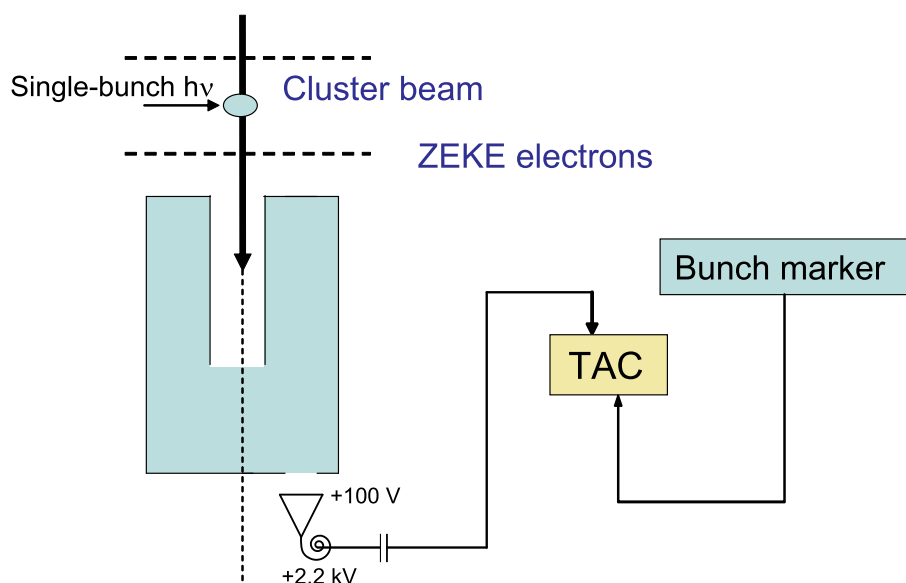
Figure 5.7: ZEKE electrons are extracted by a delayed, weak voltage pulse into the electron spectrometer, where they are identified by their flight time.

words, it is likely that one cannot exploit the cluster beam as is directly formed in a source. Fig. 5.6 presents a selection of time-of-flight (TOF) mass spectra over the range of cluster conditions employed. They were recorded using 360 eV photon energy (above the Ar $2p$ ionization potential) and a 300 V, 2 μs extraction pulse with the TOF potentials chosen to match the Wiley-McLaren space focusing conditions [77]. Focussing conditions compensating for finite size of the source volume to preserve time resolution. Achieved by appropriate choice of geometry and electric fields on time-of-flight mass spectrometer. With an expansion condition of $T_0 = 20°C$, $p_0 = 5$ bar, $\Gamma^* = 500$, corresponding to $\langle N \rangle = 10$.

The largest cluster ion observed in the mass spectral features can be associated with the large proportion of unclustered atoms present in the beam. At 260 eV the mass spectrum of atomic Ar is dominated by Ar^{++} with appreciable Ar^{3+} and very little Ar^+ [79, 80]. The multiple ionization is associated with the Auger decay of the initial Ar $2p$ ionized state.

5.2.2 ZEKE spectroscopy

The experiments have been carried out at the undulator UE52-SGM, BESSY II. The main advantage of this beamline is the access to lower photon energies, down to 30 eV. There is state-of-the-art setup for high resolution photoelectron spectroscopy using synchrotron radiation.

Partial electron yields are also useful for investigations on clusters. Techniques that have been applied in the past were:

(i) energy selected electron yields [68, 81] and

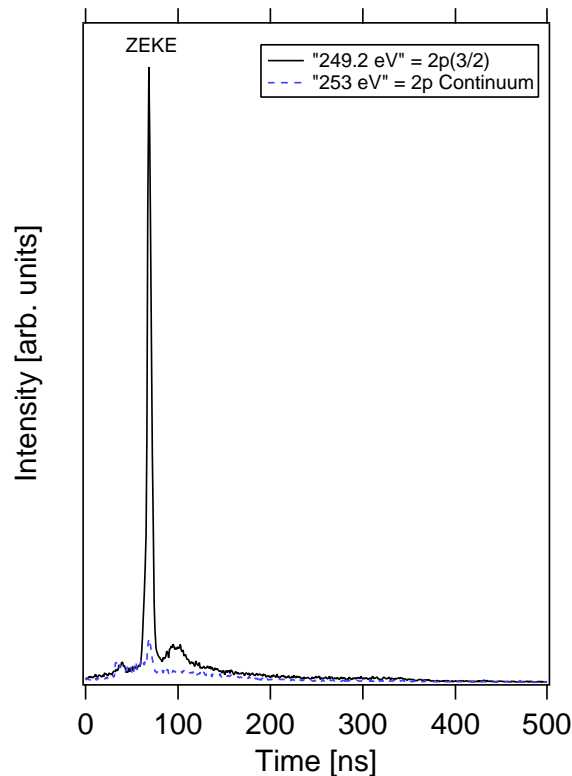(ii) zero kinetic energy (ZEKE) photoelectron spectroscopy [82].

Figure 5.8: ZEKE at 1 eV above the ionization threshold of Ar $2p_{3/2}$.

Energy-selected electrons are obtained by using e.g. electrostatic energy analyzers, such as cylindrical mirror analyzers (CMA) [83, 84] or electron time-of-flight analyzers [68]. These devices allow the detection of both photoelectrons and Auger-electrons.

Zero kinetic energy (ZEKE) photoelectrons are those electrons that do not carry any or very little kinetic energy [85]. These electrons are selected by using the time structure of the storage ring, mostly when a single electron bunch is stored in a storage ring [82]. The general idea of selecting ZEKE photoelectrons is straightforward: If the photoionization process occurs in a field free region, then the ZEKE photoelectrons will be at rest, whereas other energetic electrons leave the ionization region as a result of their considerable kinetic energy. A very low drawout voltage pulse, of typically 5–10 V/cm, extracts the ZEKE photoelectrons into the ZEKE photoelectron spectrometer.

Discrimination of energetic electrons is fourfold 5.7.

(i) The device consists of a narrow flight tube with a length-to-diameter ratio of ≥ 10. Therefore, energetic electrons cannot efficiently penetrate to the detector because of angular discrimination [86, 87];

(ii) The electron detector is mounted off the line-of-sight, so that straight into the detector flying electrons are not detected;

(iii) The voltage pulse for extracting ZEKE photoelectrons is properly delayed after photoionization, it is applied after the energetic electrons have disappeared;
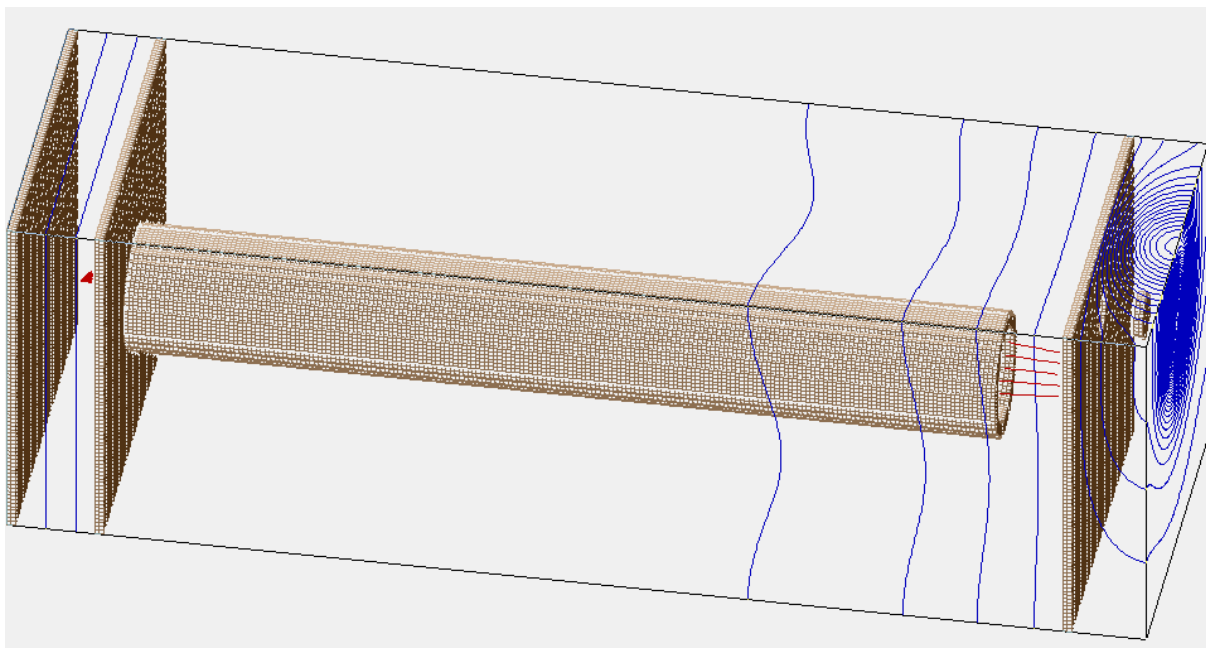
Figure 5.9: 3D view of the ZEKE detector as modeled with SimIon. Constant potential curves are shown with thin continuous lines.

(iv) The electron flight time is used as an additional way to suppress the detection of energetic electrons [82].

The ZEKE spectrometer consists of an ionization region and a narrow drift tube (length: 12 cm, diameter: 1.2 cm) for angular discrimination of energetic electrons (stera-diancy analyzer [86, 87]). A channeltron is mounted off-axis 1.25 cm, behind an aperture at the end of the flight tube. Field penetration of the cone voltage of the channeltron pulls the zero-kinetic-energy photoelectrons into the detector.

The ZEKE spectrometer can be operated in two different modes: (i) continuous extraction using exclusively angular discrimination of energetic electrons; (ii) a pulsed mode, whereby a weak extraction pulse (6 V/cm and 10 ns fwhm provided by a pulse generator) is synchronized with the BESSY-II bunchmarker pulse. In our experiments continuous extraction voltages were used. Under typical conditions the overall energy resolution of the ZEKE spectrometer is $\approx$0.30 eV as measured by the fwhm of the Ar($2p_{3/2}$) zero kinetic energy ionization signal shown in Fig. 5.8.

I have modeled the ZEKE detector theoretically in order to determine it's efficiency for zero kinetic energy electron detection. The geometry of the detector is shown in Fig. 5.9. I have used the SimIon program [88] to simulate the paths of electrons inside the ZEKE spectrometer (see Fig.5.10 for some of the possible trajectories). The dimensions of the simulated detector and the voltages applied were identical to those of the actual device used in the experiments.

A large number of trial electrons were generated, with the initial velocities randomly oriented in space, and having kinetic energies in the interval 0–0.6 eV. I then recorded the number of events when an electron was detected, and plotted it as function of initial kinetic energy. The curve so obtained resembles a Lorentzian shape, with a FWHM of
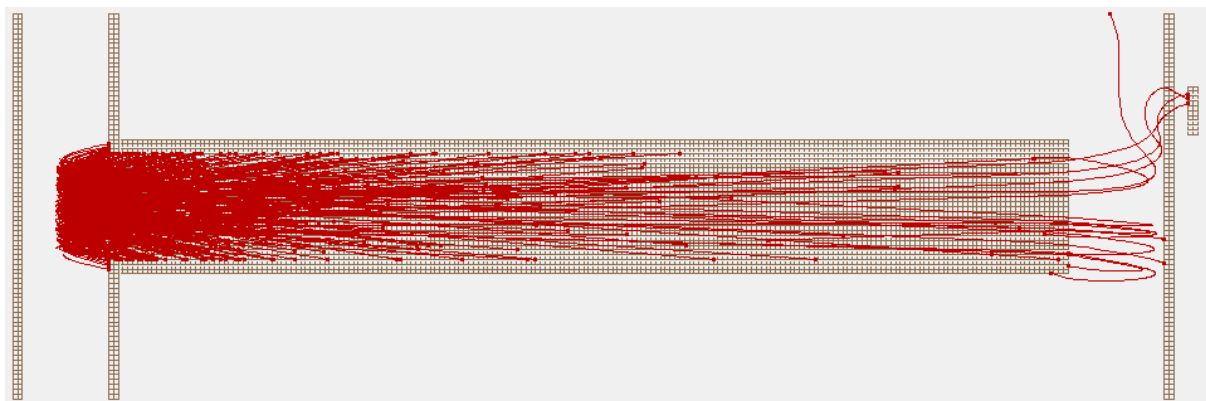
Figure 5.10: Axial section of the ZEKE detector as modeled with SimIon. Electrons trajectories are shown with thin lines. Electrons are generated in the left side, where an uniform electric field extracts them into the detector tube. When the electrons emerge on the right side of the tube, some of them are captured by a channeltron, situated in the upper-right of the figure.

0.25 eV.

5.2.3 Fluorescence spectroscopy

Fluorescence spectroscopy has also been used in core level excitation experiments on clusters. Electronically excited fragments are formed, so that radiative relaxation in the ultraviolet or vacuum ultraviolet (VUV) regime can be detected [89], similar to experiments on valence shell excitation [60]. Fluorescence excitation spectra as well as dispersed fluorescence spectra at constant excitation energy can be measured with such setups.

The first harmonic of the U49-PGM1 undulator is used and the monochromator is operated with a 600 ℓ/mm plane grating. The total fluorescence in the ultraviolet regime is detected by a cooled photomultiplier tube, which is mounted behind a quartz window (EMI 9789QB), similar to previous work [89]. This set-up is also used to measure fluorescence excitation spectra.

The dispersed fluorescence is collected in the ultraviolet/visible regime by a spherical mirror and a UV silica lens(see Fig. 5.11). It is focused onto the entrance slit of a secondary Czerny-Turner monochromator with a focal length of 460 mm (HRS-460, Jobin-Yvon, f/5.3). This device is equipped with a 300 ℓ/mm grating providing an ultimate wavelength resolution of 0.2 nm [90]. The resolution is set during the experiments to 1.5 nm, as established from the atomic argon transitions. The fluorescence light is detected by a liquid nitrogen cooled CCD-detector with a chip size of 800×2000 pixels (Lumogen&VISAR, SITe (Tektronix)).
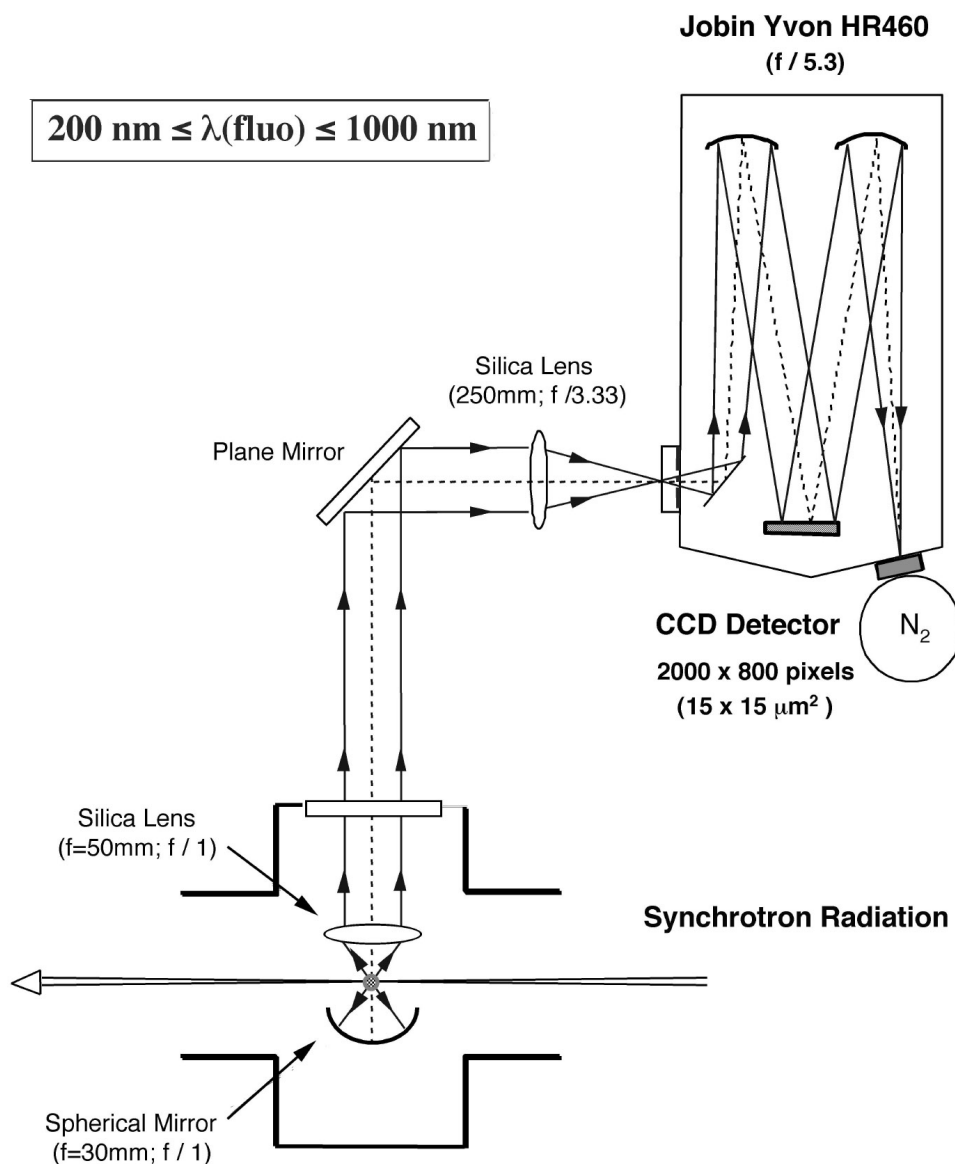
Figure 5.11: A schematic representation of the fluorescence setup. A biconcave lens ($f_1 = 50$ mm) and a spherical mirror ($f_2 = 30$ mm) collect the fluorescence photons produced in the so-defined interaction region, providing a collection efficiency of about 15% of 4π steradians. The collimated fluorescence is extracted from the vacuum chamber through a flat window and is matched to the entrance slit of a secondary monochromator by a large focal lens ($f_3 = 250$ mm). All optical components have been chosen in UV-fused silica to ensure a good transmission down to $\lambda_{\text{fluo}} \approx 200$ nm. The polarization vector of the synchrotron radiation is parallel to the axis of observation, so the measurements are not sensitive to the alignment of the excited fluorescing states [90].

The spectral detection covers the range from 200 nm to 1000 nm with a quantum efficiency of the order of 25% in the ultraviolet regime. The transmission function of the spectrograph is estimated to be low at wavelengths below 250 nm. It reaches $\sim$10% at 300 nm and increases to $\sim$50% at 500 nm [90]. The energy scale of the spectrograph is calibrated using the known fluorescence transitions of atomic argon [36] and the molecular nitrogen cation (B-X-transitions) [68, 91], respectively. This allows us to calibrate the absolute wavelength scale with an accuracy of smaller than 1 nm. The dispersed fluorescence signal is weak. Therefore, the signal strength is substantially increased by tuning the undulator gap to the appropriate photon energy (245–265 eV), while leaving the X-ray monochromator in zeroth order.

The harmonic of the undulator radiation is found to have a slightly asymmetric profile as a function of the photon energy with a typical band width of photon energy in the Ar $2p$ excitation regime of 6 eV for the full width half maximum. This is sufficient for experiments in the Ar $2p$-continuum of variable size clusters, where only broad continuum features are observed [65, 68]. Total and partial cation yields are measured using a time-of-flight mass spectrometer, which has been described before in greater detail [21, 65].

5.2.4 Electron spectroscopy

Fig. 5.12 shows a schematic view of the Scienta electron analyzer. The setup works in a crossed beam configuration where the cluster source, the axis of the Scienta electrons spectrometer lens, and the direction of propagation of the synchrotron light form an orthogonal set.

The measurements at BL3U beamline UVSOR were done at the magic angle, 54.7° at which the electron intensity is proportional to the case where electrons are collected over all angles. The electron spectrometer consists of two main parts, the electron lens and the analyzer. The electron lens is a complex five element system made to collect electrons, transporting and focusing them on the entrance slit of the analyzer, and also to accelerate/retad the electrons to a preset kinetic energy before entering the analyzer, the pass energy.

The analyzer is composed of one inner and one outer metal hemisphere with 200 mm mean radius (as shown schematically in Fig. 5.12), hereby the name SES-200, where SES stands for Scienta Electron Spectrometer. Electrons with kinetic energy equal to the pass energy at the entrance fulfill the half-turn between the hemispheres, and hit the center of a multi-channel plate (MCP) detector on the other side of the analyzer. Electrons with less or more kinetic energy are detected on a smaller or larger radius relative to the center of the MCP.

The electrons enter the hemisphere at different angles. Electrons with identical kinetic energy but different entrance angles are focused onto the detection plane (MCP). The MCP detector amplifies the impact of the photoelectron to a measurable pulse. A phosphor screen on the back side of the MCP detector transforms the MCP pulse to a visible dot. The position of the phosphor screen dot is monitored by a charge coupled device (CCD) camera, and the corresponding kinetic energy is calculated by the computer. The energy resolution is dependent on the entrance slit size and pass energy. At 10 eV pass energy and 0.5 mm curved slit it is $\Delta E = 15$ meV.
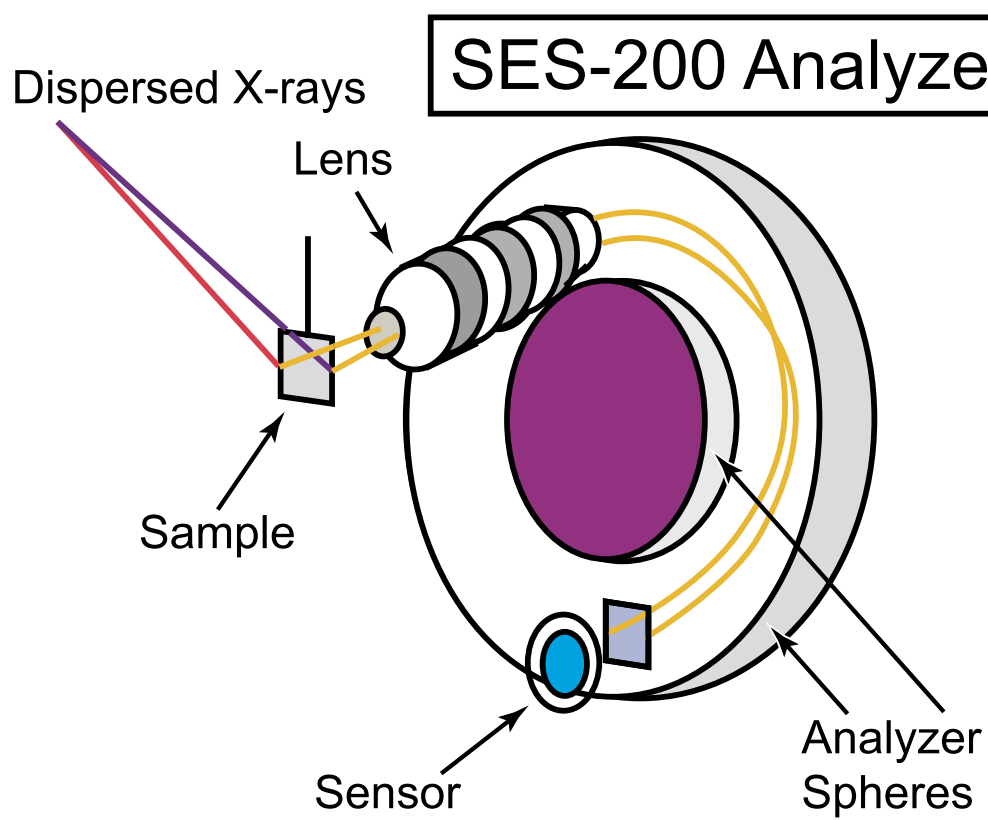
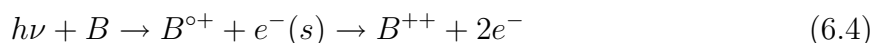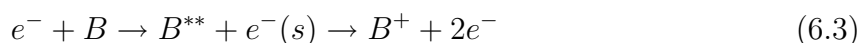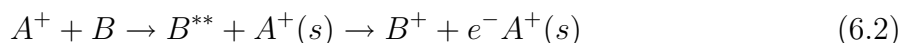Figure 5.12: SES-200 electron spectrometer.

Chapter 6

Post Collision Interaction

When charged particles emerge from an atomic process they interact over long distances by the Coulomb force. For more than two charged particles these long range interactions pose problems to the theoretical description, and effects, due to these interactions, and observed in various experiments.

The effects which arise when an atomic process proceeds can be viewed as two well separated steps: In a first step the atomic system is excited to an unstable state with respect to electron emission, with one charged particle receding from it, and in a second step an electron is ejected, which now interacts with the other charged particle and with the ion, leading to exchange of energy and angular momentum among the three particles. Effects of these interactions – which are called Post Collision Interactions (PCI) – are observed when the charged particle from the first step of the process has traveled not too far during the lifetime (τ) of the unstable state. One can give a rather general criterion for the observable occurrence of PCI effects: Since the partitioning of the kinetic energy among the particles is uncertain at least by the amount (in atomic units) $\Delta E = \tau^{-1}$, for PCI to become observable the Coulomb interaction energy between the atomic system at the instance of electron ejection and the receding charged particle must be larger or equal to this amount. With the velocity $v = \sqrt{(2/m)\epsilon}$ of the receding charged particle. We therefore have the condition

$$\frac{1}{v\tau} \geq \frac{1}{\tau}; \quad v \leq 1; \quad \epsilon \leq m/2 \tag{6.1}$$

Observed PCI effects for the following processes will be discussed

$$A^+ + B \rightarrow B^{**} + A^+(s) \rightarrow B^+ + e^- A^+(s) \tag{6.2}$$

$$e^- + B \rightarrow B^{**} + e^-(s) \rightarrow B^+ + 2e^- \tag{6.3}$$

$$h\nu + B \rightarrow B^{\circ+} + e^-(s) \rightarrow B^{++} + 2e^- \tag{6.4}$$

where B** is a neutral atom in an auto-ionizing state, and B$^{\circ+}$ an inner shell ionized atom capable of Auger ionization. The "slow" particle whose velocity is subject to condition 6.1 is marked by (s). PCI-effects for process 6.3 have been the discussed by Read [92] and PCI following inner shell photoionization 6.4 were discussed by van der Wiel *et al.* [93]. The observed phenomena were only partly and qualitatively understood.

In a series of papers [94, 95] it was shown that all so far observed PCI-phenomena are well described and understood in terms of a semi-classical theory. It was first developed

to describe newly observed oscillatory structures in electron energy spectra of process 6.2 [94], and then found to describe also the PCI-effects in reactions 6.3 [95, 96] and 6.4 [96] after introducing the appropriate modifications. A great advantage of this description is that it yields analytical expressions for the experimentally determined quantities, and is therefore readily applicable to the analysis of experimental data. It was shown that also the so called "shake down" model [97], proposed earlier to explain PCI effects for reaction 6.3 [98, 99], is able to account quantitatively for structures in the ejected electron spectra from process 6.3. It was also found that the "shake-down" model is the quantum mechanical analogue to the semi-classical description [96].

In the following I will review the existing theories of PCI, starting from the classical approach, presenting then the quantum mechanical approaches, and finally an attempt to treat PCI in clusters and solids. All of these theories have been applied in the analysis of my experimental data.

6.1   Inner-shell photoionization

Along the same line of thought as used by Read and coworkers [99], it was already realized earlier [79] that inner-shell photoionization near threshold is another process to produce the ingredients needed for PCI: an excited core which rapidly emits a fast Auger electron, and a slowly receding photoelectron still in the vicinity of the atom. Here we should actually be dealing with an as nearly ideal case of PCI as possible. Instead of having a still relatively slow incident electron, the moment of the collision can now be narrowed down to the event of photoabsorption proper, to be followed by the evolution of the excited complex on a much longer time scale.

The differences with the electron impact cases referred to in the introduction, are the following:

- the slow electron is not a decelerated projectile, but it originates from the atomic volume ("half-scattering" process).

- the remaining ion has at least double charge

- a core-excited atom usually has a large number of possible decay channels, among which the "double" Auger-process [100], leading to a triply charged ion and an additional, slow ejected electron.

Let's discuss the simplest case of normal Auger decay in more detail. The usual description is based on a time-separation between excitation and decay (see diagram in Fig. 6.1(a). First, a photoelectron is ejected with well-defined energy $\epsilon_1 = h\nu - \mathrm{IP}_{i(\mathrm{inner})}$; subsequently, Auger emission occurs of an electron of energy $\epsilon_2 = \mathrm{IP}_i - \mathrm{IP}_{2+}$. Such a picture is suggested by the observation of sharp photoelectron and Auger lines at well-defined energies, while moreover the presence of sharp shake-up lines indicates that outer-shell relaxation precedes the Auger transition.

However, for $h\nu$ only slightly in excess of IP_i, we have to allow for PCI, i.e. an additional "final state" interaction. Since the fast Auger electron escapes from a dication still partially screened by the slow photoelectron, it gains energy ($\epsilon_2 \to \epsilon_2 - \delta$) at the expense of the latter ($\epsilon_1 \to \epsilon_1 - \delta$). Thus, the effects of PCI can be observed in a variety of ways (see Fig. 6.1(b)) as deviations from the "normal" behavior:
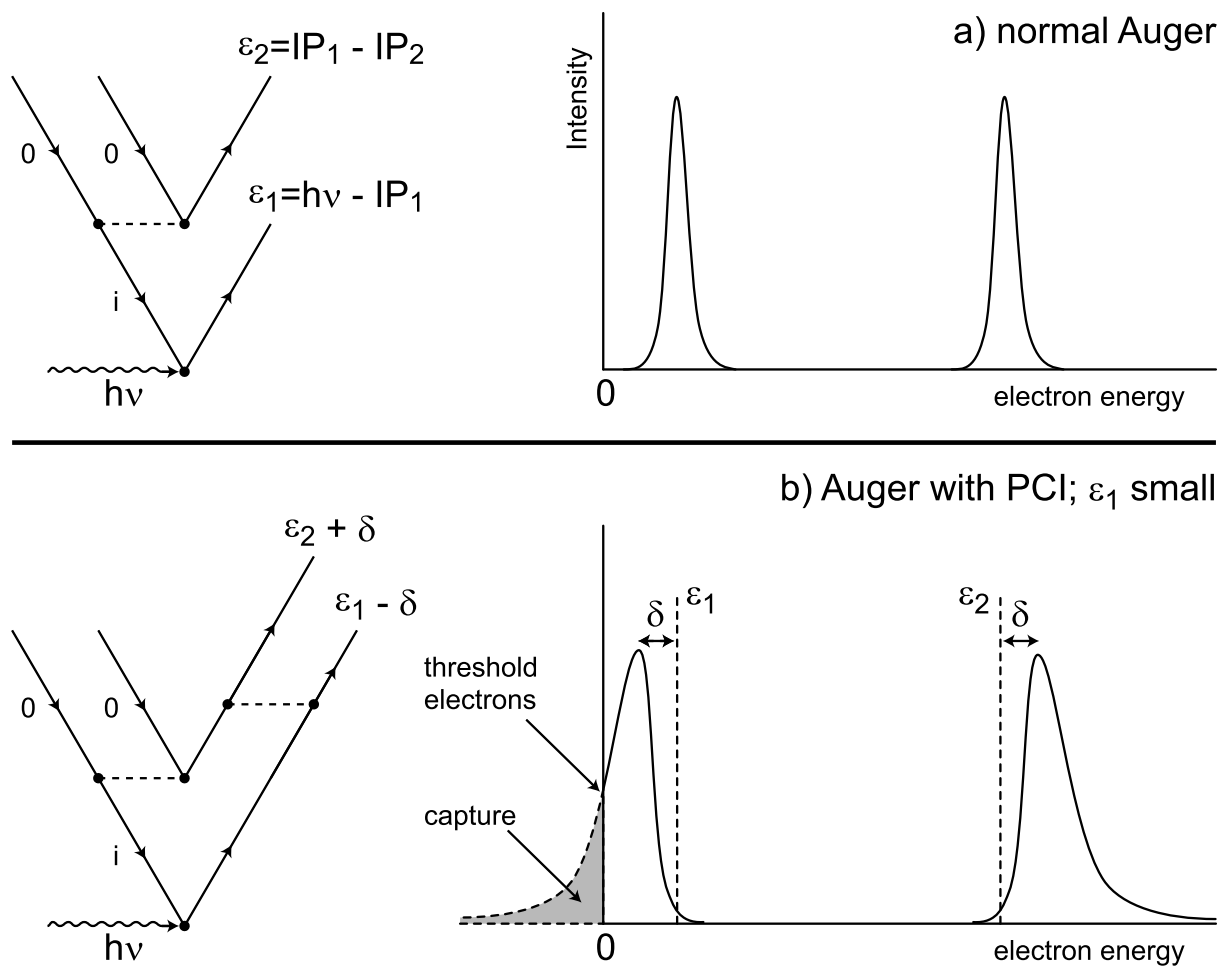
Figure 6.1: (a) Diagram for the normal Auger process, which results in ejection of two electrons with well-defined energies. (b) Diagram for the case of small excess energy of the photon. Additional interaction (PCI) takes place between the two outgoing electrons. As a consequence the electron lines shift and are broadened, such that threshold electron formation or capture into an excited singly charged ion occurs.

i. One obvious consequence of PCI is that the Auger electron appears at higher energy than normally is the case.

ii. As regards the photoelectron, a shift of a low-energy electron to even lower energies may be hard to observe. However, a convenient and efficient way of detecting PCI is to observe formation of threshold electrons ($\epsilon_1 - \delta = 0$) at incident photon energies above threshold.

iii. Moreover, ($\epsilon_1 - \delta$) might even become negative, which means that the "photoelectron" does not escape but eventually remains bound by the atom. Hence, instead of a dication a singly charged ion is formed in a (highly) excited state. Evidence for such "capture" should be found in structure in the rate of production of excited singly charged ions near the inner threshold.

iv. For the same reason, one may expect the absence of a sharp discontinuity at threshold in the total production of singly charged ions (ground-plus excited states) relative to that of dications via the normal Auger decay.

v. Without PCI, the fraction of Auger transitions, in which two electrons share the available excess energy (double Auger [100]), should be uniquely determined by atomic dynamics and be a constant. A dependence of the ratio 2+/3+ on ϵ_1 again gives evidence of PCI.

Convincing evidence of recapture was reported by Samson *et al.* [101], again for photo-ionization near the Ar $L_{2,3}$ ionization threshold. In this work the recapture model of Tulkki *et al.* [102] was extended to higher excess energies and an approximate relation between the recapture probability $P(E_{\mathrm{ex}})$ and the energy E_{ex} of the slow photo-electron ejected in the initial inner-shell ionization was found to be

$$P(E_{\mathrm{ex}}) = 1 - \exp(-\Gamma E_{\mathrm{ex}}); \qquad (6.5)$$

where Γ is the line width of the Auger transition. Reasonable agreement was obtained with observed Ar^{2+} and Ar^{3+} ion yield spectra, however the model was not applied closer than 0.25 eV above threshold due to computational difficulties.

The question of what happens to the recaptured electron was discussed at about the same time by Samson *et al.* [101] who noted that contrary to the observation of a finite Ar^{2+} yield at the L_3 threshold, if all zero-energy electrons were recaptured at the threshold, no Ar^{2+} would be observed. To account for the finite Ar^{2+} yield they reasoned that electrons could be recaptured into high-lying Rydberg states forming Ar^{+*} and that some of the states would subsequently autoionize back into the Ar^{2+} continuum. They found that about 33% of the recaptured electrons remain captured and a similar fraction, about 26%, remains captured at the L_2 threshold. They also calculated that about 15% of electrons recaptured by Ar^{3+} remain captured, compared with only about 5% permanently recaptured by Ar^{4+}. Recently Lu *et al.* [103] examined the role of recapture in production of the Ar $(^1D)6d$ final state, thought to be the only suitable candidate for the two-step auto-ionization model proposed by Hayaishi *et al.* [104] discussed earlier. They found that inclusion of a recapture contribution was essential for a proper description of the production of near-zero-energy electrons in the decay of all Ar $2p^{-1}$ ns and nd resonances.

Further evidence for recapture above threshold was provided by Eberhardt *et al.* [105] in the photo-ionization Ar^{2+} and Ar^{3+} yields near the $2p$ threshold. They observed a steady variation in the ion branching ratio, which they ascribed to PCI effects in the Auger decay of the $2p$ hole. By applying the semi-classical model of Russek and Mehlhorn [106] they were able to predict the variation of the recapture probability near threshold. Better agreement was obtained by Tulkki *et al.* [102] with a quantum-mechanical model that predicted the recapture probability as a function of the excess energy of the slow photo-electron, assuming that the probability of recapture for a zero-energy electron was unity. Following similar coincidence studies Levin *et al.* [107] suggested that recapture induced by post-collision interaction was a suitable link between below threshold resonant excitation to bound np levels with subsequent Rydberg shake-off, and above-threshold energy-dependent shake-off and double-Auger effects.

6.2 ZEKE line shape

The quantum-mechanical escape probability distribution reproduces a scaling with excess energy and width expected from semi-classical models, rather than one previously suggested [102]. We find that, in general, the threshold must be exceeded by an amount proportional to $\Gamma^{2/3}$ before escape becomes the dominant mechanism. The general features of the quantum ZEKE distributions are also explored as a function of Γ and l. These distributions peak at excess photon energies that are also proportional to $\Gamma^{2/3}$ and widen and become more symmetric as Γ increases. The connection with semi-classical ZEKE distributions is investigated and the question raised by Thomas *et al.* [108] concerning additional lifetime convolution in semi-classical models is addressed in light of present results.

The production of zero-energy electrons at photon energies near an inner-shell threshold constitutes a very straightforward proof of the occurrence of PCI. Such measurements, which require the use of a continuous photon source such as synchrotron radiation, have been performed recently [109]. We have performed experiments near the threshold on free van der Waals clusters. The results are presented in Chapter 11.

We shall try to investigate the insight gained from classical arguments. The recapture process can be investigated along the lines described by Russek and Mehlhorn [106] in their treatment of the PCI effect on Auger line shapes. The following derivation is essentially that of Eberhardt *et al.* [105], with some analytic features of the problem emphasized for the later discussion.

At time $t = 0$, a photoelectron is ejected with an energy $E_{\text{exc}} = \omega - I_i$, where I_i is the binding energy of the intermediate hole state. This "slow" electron recedes from the ion, experiencing an attractive potential Z_i/r. After some time t a "fast" Auger electron is emitted with energy $\bar{\epsilon}_A$. When the Auger electron passes the slow photoelectron at radius r_{pass}, the photoelectron experiences (on average) an increase in screening charge $Z \to Z_i + 1$. The slow electron loses an amount of energy $\Delta = 1/r_{\text{pass}}$, which is gained by the Auger electron. This exchange of energy, induced by the sudden change in screening, is the origin of the PCI shift: Observed at infinity, the Auger electron has energy $\epsilon_A = \bar{\epsilon}_A + \Delta$ and the photoelectron $\epsilon_P = E_{\text{exc}} - \Delta$.

However, if the ejected photoelectron is sufficiently slow there is a probability that the passing radius is small enough ($r_{\text{pass}} < 1/E_{\text{exc}}$) so that the photoelectron cannot escape the ion, remaining in a bound classical orbit of energy $E_{\text{exc}} - \Delta < 0$. For a given excess energy there is a critical radius $r_C = 1/E_{\text{exc}}$ such that the slow electron is "recaptured" if passed at any radius $r \leq r_C$. There is thus a critical time T_C such that Auger emission at any earlier time results in recapture.

Taking the probability per unit time for Auger emission as $\mathrm{d}P = \Gamma \exp(-\Gamma t)\mathrm{d}t$, the probability of photoelectron recapture is

$$P_{\text{recap}} = \int_0^{T_C} \mathrm{d}P = 1 - e^{\Gamma T_C}. \tag{6.6}$$

For ejection energies near threshold, where $E_{\text{exc}} \ll \bar{\epsilon}_A$, the "catch-up" time between Auger emission and passing the photoelectron is negligible [106, 110]. This approximation was not imposed by Eberhardt *et al.* [105]. With this simplification, the critical time can then be solved by straightforward integration
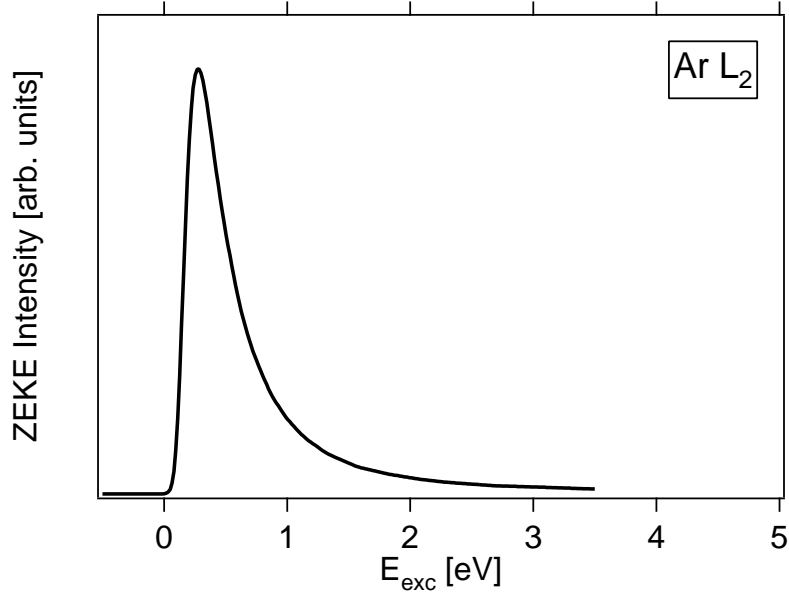
Figure 6.2: Yield of zero-kinetic-energy electrons as a function of photon excess energy for the Ar L_2 ($\Gamma = 0.12$ eV, $l = 2$). The ZEKE line distribution was computed from the classical model.

$$T_C = \int_{r_0}^{r_C} \frac{\mathrm{d}r}{v}, \tag{6.7}$$

where v is the photoelectron velocity and r_0 the starting radius.

Assuming rectilinear motion ($v = \sqrt{2E_{\mathrm{exc}}}$) and $r_0 = 0$ the critical time becomes $T_C = 1/\sqrt{2}E^{3/2}$, a result pointed out by Tulkki *et al.* [102]. The recapture probability becomes $P_{\mathrm{recap}} = -\exp(-\Gamma/\sqrt{2}E^{3/2})$. A convenient reference point is the delay energy E_D, the excess energy at which the recapture probability equals that of escape ($P_{\mathrm{esc}} \equiv 1 - P_{\mathrm{recap}}$). This occurs when $P_{\mathrm{esc}}(E_D) = P_{\mathrm{recap}}(E_D) = \frac{1}{2}$ and for free-electron trajectories $E_D = (\Gamma/\sqrt{2}\ln 2)^{2/3}$.

The model can be extended to the Coulomb ($Z_i = 1$) case by considering trajectories for which $v^2/2 = E_{\mathrm{exc}} + 1/r - \gamma/r^2$, where the angular momentum can be quantized as $\gamma = l(l+1)/2$. The extension adds some complications to the model: The initial radius r_0 at which the liberated photoelectron first appears cannot be chosen arbitrarily and is taken here as the classical minimum. For $\gamma \neq 0$ there is a nonzero starting radius and so there is no recapture for large enough ejection energy, the critical radius becoming less than r_0. With this model, the escape probability becomes

$$P_{\mathrm{esc}}(E_{\mathrm{exc}}) = \begin{cases} \exp\left(-\frac{\Gamma}{E_{\mathrm{exc}}^{3/2}}\beta\right) & \text{for} \quad E_{\mathrm{exc}} \leq 2/\gamma \\ 1 & \text{for} \quad E_{\mathrm{exc}} > 2/\gamma, \end{cases} \tag{6.8}$$

where β is a slowly varying function of energy

$$\beta = \sqrt{1 - \frac{\gamma E_{\mathrm{exc}}}{2}} + \frac{1}{2\sqrt{2}} ln\left[\frac{\sqrt{4\gamma E_{\mathrm{exc}} + 1}}{2\sqrt{2 - \gamma E_{\mathrm{exc}}} + 3}\right]. \tag{6.9}$$

I have found that the line shape, which is equal to the derivative of $P_{\mathrm{esc}}(E_{\mathrm{exc}})$ is expressed as:

$$P'_{\mathrm{esc}}(E_{\mathrm{exc}}) = \begin{cases} exp\left(-\frac{\Gamma}{E_{\mathrm{exc}}^{3/2}}\beta\right)\left(\frac{3}{2}\frac{\Gamma}{E_{\mathrm{exc}}^{5/2}}\beta - \frac{\Gamma}{E_{\mathrm{exc}}^{3/2}}\beta'\right) & \text{for} \quad E_{\mathrm{exc}} \leq 2/\gamma \\ 0 & \text{for} \quad E_{\mathrm{exc}} > 2/\gamma, \end{cases} \tag{6.10}$$

where

$$\beta' = \frac{\sqrt{2}\gamma(1 - 2\gamma E_{\mathrm{exc}})}{2\sqrt{2 - \gamma E_{\mathrm{exc}}}(4\gamma E_{\mathrm{exc}} + 1)} \tag{6.11}$$

This ZEKE line shape is plotted in Fig. 6.2, corresponding to a core-hole lifetime of Ar $2p$ (118 meV). For s-wave ($\gamma = 0$) excitation β is energy independent, $\beta_0 \approx 0.377$. For $\gamma \neq 0$, β increases from β_0 as E_{exc} increases from zero, reaching a maximum value of $\beta_{\max} \approx 0.461$ at approximately $E_{\mathrm{exc}} \approx 0.251(2/\gamma)$. Thereafter β decreases slowly to zero as $E_{\mathrm{exc}} \to 2/\gamma$, passing through β_0 again at $E_{\mathrm{exc}} \approx 0.633(2/\gamma)$.

The use of a Coulomb trajectory is thus similar to the free-particle result, but with an energy-dependent multiplier β replacing the factor of $2^{-1/2} \approx 0.707$. This factor is always smaller than the free-electron factor; a Coulomb particle moves faster than a free particle of the same energy in regions where the potential is negative. The delay energy at which escape and recapture probabilities become equal is $E_D = (\Gamma\beta/\ln 2)^{2/3}$, which occurs at smaller excess energy than in the free-particle case.

The classical model outlined above can be tinkered with by employing a more realistic potential and starting radius for specific cases. In such a model, the screened charge seen by the photoelectron would be much larger than unity near r_0. The critical time would then be reduced, resulting in smaller values of β and thus E_D. However, such elaboration, while straightforward in practice, cannot be evaluated analytically. The simple model outlined above suffices for present purposes, providing an easily visualized picture with which quantum-mechanical results can be loosely interpreted.

While Tulkki *et al.* [102] pointed out the classical $E_{\mathrm{exc}}^{-3/2}$ scaling of the critical time, they returned to Eq. 6.6 with a quantum argument: They reasoned that the critical time should, through the uncertainty principle, be related to the inverse of the spread of energy, so that $T_C \approx 1/\Delta\epsilon \approx 1/E_{\mathrm{exc}}$. Thus they predicted on quantum-mechanical grounds that the escape distribution should go as $P_{\mathrm{esc}}(E_{\mathrm{exc}}) = \exp(2\Gamma/E_{\mathrm{exc}})$, and this functional form is still invoked [101]. If this is so, the delay energy E_D is proportional to Γ rather than to the classical $\Gamma^{2/3}$ result.

6.3   Semi-classical approach

The post-collision Coulombic interactions between particles after inner-shell ionization with associated Auger electron emission can be thought of in the following way. The pre-collision system contains an atom and either a projectile photon or electron that ionizes

a) Inelastic collision (photoionization)   b) Ionized atom
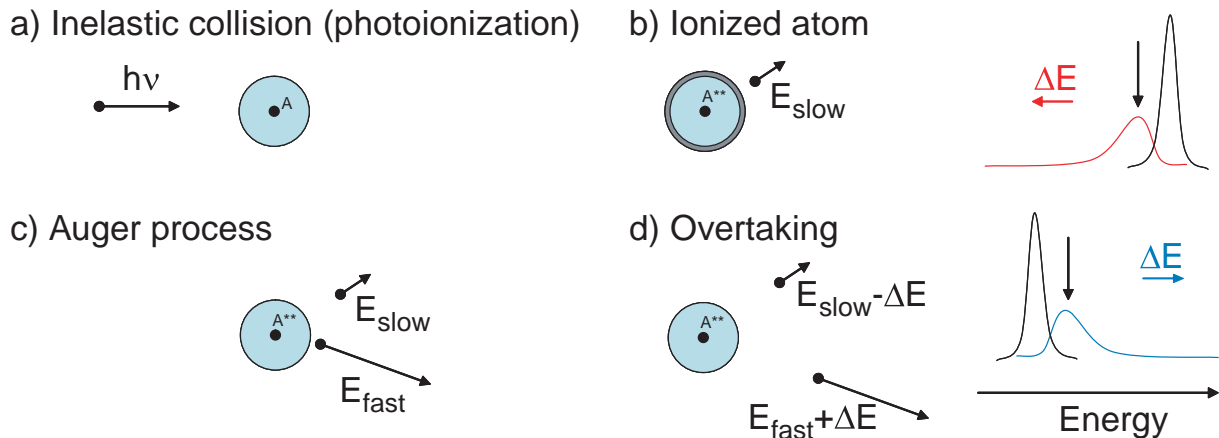
c) Auger process   d) Overtaking

Energy

Figure 6.3: Schematic representation of the PCI process. An atom is excited by X-rays, core electron is ionized. After photoionization, the photoelectron moves in the field of the singly ionized atom. A subsequent decay of the vacancy by an Auger process produces a fast Auger electron. If the lifetime of the inner-shell vacancy is sufficiently short the fast Auger electron can overtake the photoelectron, which is then exposed to a doubly charged ion core. The photoelectron will be slowed down losing a certain amount of energy, where as the Auger electron (now exposed to a singly charged core) gains energy. This exchange of energy results in a distorted line shape and a shift in peak energy of both electrons. In fact, even the ionization threshold the short lifetime of the Auger decay, allows the Auger electron to interact with the primary excited photoelectron.

an electron from an inner shell of the atom. The ejected electron has a given energy, called the excess energy, which may be close to zero. During the collision the atom relaxes by dropping an electron from an outer orbital into the inner-shell vacancy and the additional energy (characteristic of the particular re-arrangement that takes place) made available by the relaxation process is transferred to an Auger electron that is emitted from the atom. In the post-collision state an ejected electron from the initial inner-shell ionization (assumed here to have lower energy than the Auger electron) sees a singly-charged ion until it is passed by the Auger electron. The slow electron then sees a doubly-charged ion and slows in the stronger potential. The Auger electron initially sees a doubly-charged ion until it passes the slow ejected electron, and the subsequent shielding allows the Auger electron to gain energy, as shown in Fig. 6.3.

It is clear however that PCI between the Auger electron and the slow ejected electron violates the assumption in the classical model of complete independence of inner-shell ionization and Auger emission. This is not surprising, and means for example that the Auger transition anisotropy predicted by Sheinerman *et al.* [111], and others, cannot be attributed solely to alignment of the intermediate ion state, thus preventing interpretation of the angular distributions in terms of a pure alignment tensor. However, models based upon the two-step approach, including the eikonal model of Sheinerman *et al.*, are in agreement with most aspects of the PCI effects.

The PCI effect in an Auger spectrum mainly manifests itself as an energy shift to higher kinetic energy and a pronounced asymmetry in the shape of the Auger lines. The

energy shift is usually studied as a function of the excess energy E_1, where E_1 is defined as the difference between the kinetic energy of the incident particle and the binding energy of the electron to be expelled. The notations $E_1^{h\nu}$ and E_1^{e-} will be used in contexts where there is risk for confusion whether photon or electron excitation is meant [112, 113].

When the incident particle is a photon the photo-electron is ejected with the energy E_1, but in the case of an incident electron the excess energy is shared between the ejected and scattered electron. Therefore the energy shift, in the case of electron ionization, will also depend on the energy distribution between the two electrons. Because of this energy distribution the PCI effect is much more pronounced in electron ionization than in photon ionization at the same excess energy. However, the theoretical problems encountered when attempting to account for this energy distribution, makes the development of a strict quantum mechanical PCI model for electron-impact ionization considerably more difficult.

The energy shift and the asymmetric line shape can qualitatively be understood if PCI is interpreted as a dynamic screening of the ion by the slow receding electron(s). The Auger electron will then move in the field of an effectively smaller attractive potential, than would be the case if there was no dynamic screening. The asymmetry is caused by a combination of dynamic screening and the lifetime of the core-hole. If the lifetime is long, the slow electron(s) will be further away at the time of the decay, giving a smaller screening. Hence, the PCI will be smaller. Shorter lifetimes will give larger PCI effects [114].

PCI can be described by a transition of the initially excited state Φ_i to the final state Φ_f of ionized target plus emitted electron. (Atomic units will be used in all theoretical expressions.)

$$a(\epsilon) = \left(\frac{\Gamma}{2\pi}\right)^2 \langle \Phi_f(R)|\Phi(R)\rangle. \tag{6.12}$$

The wave-functions $\phi_n(R)$ of the emitted electrons be described by outgoing JKWB wave-functions.

$$\phi_n(R) = k_n^{-\frac{1}{2}} \exp\left(i \int_{R_n}^{R} k_n dr\right) \tag{6.13}$$

with R_n ($n = i, f$) the radii at which slow and Auger electron respectively start out.

The influence of the PCI-inducer is reflected the wave-numbers k_i and k_f.

$$\tfrac{1}{2}k_i^2 = E_1 + \tfrac{1}{2}i\Gamma + V_i(R) \tag{6.14}$$

$$\tfrac{1}{2}k_f^2 = E_1 - \epsilon + V_f(R) \tag{6.15}$$

The energy ϵ is the difference between the electron energy E and the Auger-energy E_A, and E_1 is the excess energy of the photo electron. The potential $V_i(R)$ is simply the Coulomb potential $1/R$ between PCI-inducer and target. The imaginary part of the initial state energy, $\Gamma/2$, accounts for the finite life time $\tau = 1/\Gamma$ of the system in this state. The potential V_f consists of the Coulomb potential $2/R$ between PCI inducer and doubly ionized target and a part, describing the interaction between PCI-inducer and electron. This part has been neglected in earlier theories assuming that the electron travels instantaneously to infinity. In the potential diagram (Fig. 6.4) the transition is drawn vertical. In reality it takes some time for the electron to escape from the field of the PCI-inducer. The transition can therefore not longer be represented by a vertical line.
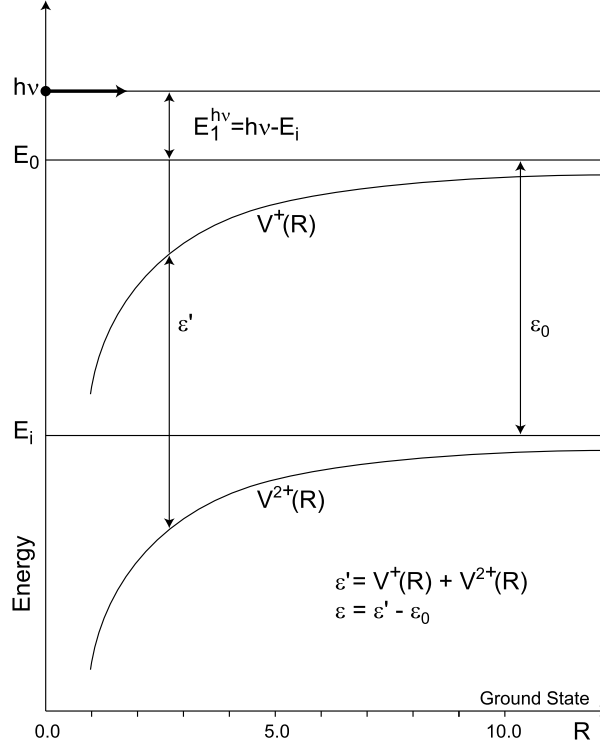
Figure 6.4: Coulomb potential curve diagram showing the influence of the slow electron on the energy, ϵ', of the Auger electron. The Auger decay is described by vertical transitions $V^+(R) \to V^{2+}(R)$. The relative energy is defined as the difference $\epsilon = \epsilon' - \epsilon_0$ where ϵ_0 is the nominal Auger energy, $E_i - E_f$

Auger energy, and $1/\Gamma$ is the lifetime of the core hole. The wave functions of the initial state (outgoing wave) and final state (ingoing wave), are now given by:

$$\phi_i(R) = k_i^{-1/2} \exp\left(\mathrm{i} \int^R k_i \mathrm{d}R'\right) \tag{6.16}$$

$$\phi_f(R) = k_f^{-1/2} \exp\left(-\mathrm{i} \int^R k_f \mathrm{d}R'\right) \tag{6.17}$$

If only outgoing waves were used to describe the initial and final states, an unphysical transition probability would be obtained. The transition probability thus obtained would go to infinity at $\epsilon = 0$ and be zero elsewhere, when E_1 goes to infinity. This is the case in the semi-classical model by Niehaus which does not give the right asymptotic behavior when going to high excess energies, i.e., a Lorentzian distribution is not obtained. (For discussion of the use of outgoing and ingoing waves in the calculation of matrix elements see [115, 116].

The transition amplitude with these wave functions becomes:

$$
\begin{aligned}
a_{if}(\epsilon) &= C \int_0^\infty \mathrm{d}R (k_i \overline{k}_f)^{-1/2} \exp\left\{\mathrm{i}\left(\int_0^R k_i \mathrm{d}R' + \overline{\int_0^R k_f \mathrm{d}R'}\right)\right\} \\
&= \int_0^\infty f(R) e^{i\Phi(R)} \mathrm{d}R
\end{aligned}
\tag{6.18}
$$

With the transformation $z = 1/(R + \delta)$ and $E_a = 1/\delta$, the phase can be written as

$$
\begin{aligned}
\phi(z') &= \sqrt{2}i \int_0^\infty z^{-2} \left(E_1 + i\frac{\Gamma}{2} + z \right)^{1/2} dz \\
&+ \sqrt{2} \overline{\left\{ \int_{z'}^{E_a} z^{-2} \left(E_1 - \epsilon + 2z \right)^{1/2} dz \right\}}
\end{aligned}
\tag{6.19}
$$

where $z = \epsilon_r/(R + \delta)$, $\varepsilon_r = 1.61$ is the dielectric constant of solid argon [117], $E_a = 1/\delta$, E_a is the Auger electron energy, E_1 is the energy of the slow electron, R is the overtaking distance, δ is expectation value of the ionized orbital, Γ is the core hole lifetime, and ϵ is the relative energy at the nominal Auger energy. The changing in the formula considering the dielectric constant of the solid argon has been performed by myself. The stationary point,

$$
z^* = \frac{1}{R^*} = \frac{\epsilon + i(\Gamma/2)}{C}
\tag{6.20}
$$

is obtained by solving the equation:

$$
z^2 \frac{\partial}{\partial z} \left(\frac{\phi + \overline{\phi}}{2} \right) = 0
\tag{6.21}
$$

In Eq. 6.20 we used the abbreviation:

$$
\frac{C}{\varepsilon_r} = 1 - \frac{v_1}{|\mathbf{v}_e - \mathbf{v}_1|}
\tag{6.22}
$$

where ε_r is the is the dielectric constant of solid argon. This stationary point is to be compared with the one obtained by Niehaus, $z^* = \epsilon$. This latter stationary point is the cause of the singularity at $\epsilon = -E_1$ in his semiclassical model. The singularity is avoided by choosing the path of integration in the complex plane. Actually $z^* = \epsilon$ is obtained in this model if one makes the approximation $\Gamma/2 \gg E_1 + z$, i.e.,

$$
\left(E_1 + i\frac{\Gamma}{2} + z \right) \simeq (E_1 + z)^{1/2} + i\frac{\Gamma}{4}(E_1 + z)^{-1/2}
\tag{6.23}
$$

This latter approximation makes it possible to divide $\phi(z)$ explicitly into real and imaginary parts before applying the stationary phase approximation [114, 118]. The consequence of this is that it will not be possible to get any dependence on Γ in the second derivative of the real part of the phase and this leads to the fact that the Lorentzian line shape is not obtained at high excess energies.

Finally we arrive at the following result

$$
P(\epsilon) = |a(\epsilon)|^2 \alpha \cdot \frac{\exp[2\sqrt{2}\mathrm{Im}(\phi(z^*))]}{\left\{ \left(E_1 + \frac{\epsilon \varepsilon_r}{C} \right)^2 \frac{\Gamma}{4} \left(1 + \frac{\varepsilon_r}{C} \right)^2 \right\}^{\frac{1}{4}} \left(\epsilon^2 + \left(\frac{\Gamma^2}{2} \right)^2 \right)}
\tag{6.24}
$$

with

$$
\begin{aligned}
\phi(z^*) &= I\left(E_i, E_1 + i\frac{\Gamma}{2}, 1 \right) - I\left(z^*, E_1 + i\frac{\Gamma}{2}, 1 \right) \\
&- I\left(E_i, E_1 - \epsilon, 1 + c \right) + I\left(z^*, E_1 - \epsilon, 1 + c \right)
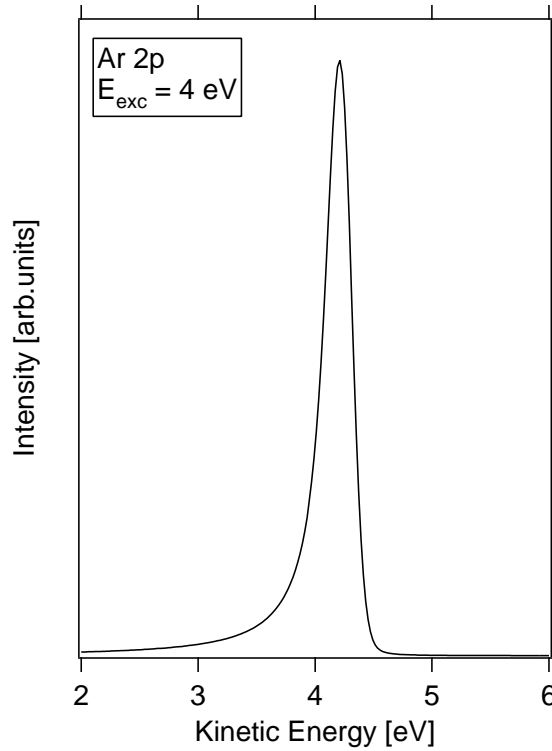\end{aligned}
\tag{6.25}
$$

Figure 6.5:   Calculated line shape of the Ar $2p$ photoelectron at $E_A = 201$ eV and $\Gamma = 118$ meV. The excess energy of the incoming photon is 4 eV.

and

$$I(z, E, x) = \frac{\sqrt{E + xz}}{z} - \frac{x}{2\sqrt{E}} \ln\left(\frac{\sqrt{E + xz} - \sqrt{E}}{\sqrt{E + xz} + \sqrt{E}}\right) \qquad (6.26)$$

E_i is the potential energy of the electron at the radius R_i of escape and does not influence the line shape. The theoretical line shape by using the above theory is shown in Fig.6.5. The line shape was computed for the case of an excess energy of 4 eV and a core-hole lifetime of Ar $2p$ core-hole (118 meV). The Auger energy is that of Ar $2p$ (200 eV).

Schmidt [119] discussed advances in photo-ionization studies using synchrotron radiation and suggested that near threshold PCI-induced energy exchanges might be so large that the slow photoelectron would be recaptured by the ion into a bound orbital. Schmidt proposed that a suitable recapture mechanism would provide a natural link between inner-shell ionization followed by Auger decay and outer-shell ionization with simultaneous excitation. The challenge was to obtain well-resolved data spanning the ionization threshold, and then to search for indications of recapture effects.

An elegant non-coincidence photon impact experiment by Čubric *et al.* [120] was the first to address the challenge. They recorded electron energy-loss data from Xe around the $4d$ ionization threshold. The incident photon energy was increased in small steps and the electron spectra were sequentially recorded and presented a two-dimensional view of Auger electron energy and incident photon energy. The data showed the PCI region above threshold, a shake-modified resonant Auger emission area below threshold and the quasi-continuum region in-between. In a small energy range just above threshold

the slow photoelectron could lose enough energy via PCI to be recaptured by the ion. Within the region where recapture could occur two pathways to the same final state were identified, one direct and another involving the PCI-induced recapture event. The two pathways would not be distinguishable and given sufficient resolution it was thought that interference effects would be observed in the form of discrete structure, particularly on the high-energy side of the Auger line.

The boundary region was again studied in detail by de Gouw *et al.* [121], with the aim of developing a model to explain how PCI phenomena above threshold evolved into the resonance Auger effect below threshold. They presented a time-dependent semi-classical model based upon the trajectory of a Rydberg electron moving in the Coulomb potential of the core ion. The model was in reasonable agreement with their data. Below threshold the trajectory of the Rydberg electron contained a turning point thus indicating the possibility of recapture but this was not explicitly discussed. Consequently, the Rydberg electron would be at the same radius R twice in its trajectory, once when receding from the ion and once when returning. In both instances the subsequently emitted Auger electron would suffer an identical PCI effect, leading to interference in the Auger electron line shape. The model then implies that for excess energies below threshold the Auger line shape would contain oscillatory structure on the high-energy side of the line shape. Their model indicated that further below threshold the interference tends to make the Auger line shape appear almost Lorentzian, but with low amplitude oscillations extending on the high energy side of the line shape. However, their energy resolution was insufficient to resolve such structure and they noted deficiencies in the model, including the lack of quantization of the final state.

In resonant Auger emission just below threshold the photoelectron remains bound to the residual ion core in a "spectator" nd orbital, while in diagram Auger processes the photoelectron enters the continuum. Armen *et al.* [122] examined suppression of the Xe L_3–$M_{4,5}M_{4,5}$ diagram Auger intensity observed for excess energies up to about 4 eV above threshold, and found that the observed near-threshold intensity was actually due to PCI-induced photo-electron recapture into large-n bound spectator nd orbitals. The possibility of interference effects was not explored but the necessity of coincidence experiments to partition the observed near-threshold intensity into spectator and diagram contributions was noted, as was the inherent difficulty of observing the boundary region.

6.4 Dynamics of PCI in clusters

A complete theory for PCI in clusters would have to take into account processes which are neglected in this section, i.e. elastic and inelastic scattering of the electrons, different mean free path for Auger an photoelectrons.

We can start from the time-independent quantum mechanical considerations based on asymptotic Coulomb wave functions [123] in association with an effective charge concept [110] account for the most salient features of the PCI effect in non-coincidence experiments [110, 123, 124, 125]. The approach [110, 123] is related to the semiclassical model of Kuchiev and Sheinerman [126]. Their angle dependent PCI line shape formula is used for qualitative predictions of the Auger electron line shape in the case where the Auger electron and photoelectron are observed in coincidence [110, 125].

The Auger process is treated as a resonance in double photoionization. The starting

point is thus a generalization of the conventional resonant multichannel scattering theory to allow for two electrons, the photoelectron and the Auger electron, in the outgoing channel [124]. As a consequence the influence of the lifetime of the initial inner-shell hole state on the PCI effect is correctly taken into account. If we exclude all irrelevant factors and limit myself to a description of the angle-averaged Auger electron line shape $P_Q(\epsilon)$ we have

$$P_Q(\epsilon) = (\Gamma + \mathrm{i}/2\pi)|\langle E - \epsilon|\tau'\rangle| \tag{6.27}$$

where

$$|\tau'\rangle = \int_0^\infty |\tau\rangle \, (E_{\mathrm{exc}} - \tau + \mathrm{i}\Gamma_i/2)^{-1}\mathrm{d}\tau \tag{6.28}$$

In Eqs. 6.27 and 6.28

$$|E - \epsilon\rangle = (2/\pi k)^{1/2} \sin\left[kr + \frac{Q}{k}\log 2kr + \arg\Gamma(1 - \mathrm{i}Q/k)\right] \tag{6.29}$$

and

$$|\tau\rangle = (2/\pi k')^{1/2} \sin kr' \tag{6.30}$$

are asymptotic s-waves, without a short range phase-shift [110, 123] In the non-Lorentzian Coulomb line shape $P_Q(\epsilon)$ which can be expressed in closed form [123] $E = E_{\mathrm{exc}} + \epsilon_A$, where $E_{\mathrm{exc}} = \omega - I_i$ and $\epsilon_A = I_i - I_{ff'}$. Here ω is the incident photon energy and ϵ_A the Auger electron energy for the transition from an initial one-hole state $[i]$ with the lifetime $T_i = \Gamma_i^{-1}$ to a final double-hole state $[ff']$. In Eq. 6.29 $E - \epsilon = \frac{1}{2}k^2$, and in Eq. 6.30 $\tau = \frac{1}{2}k'^2$. Besides the excess energy E_{exc} and the width Γ_i, $P_q(\epsilon)$ depends according to Eq. 6.29 only on one additional parameter, namely the effective charge Q, which may depend on k. If $P_Q(\epsilon)$ is expressed as a function of $\epsilon_p = E - \epsilon$ rather than ϵ it describes the shape of the corresponding photoelectron line. Since Q only appears in the final-state wave function 6.29 it implicitly implies that the photoelectron sees the charge $Q_i = 0$ rather than $Q_i = 1$ prior to the Auger decay. As shown below this assumption is justified by a proper choice of Q. In order to obtain the calculated spectrum we have to calculate the real and imaginary part. The results are given in Fig. 6.6.

The overlap amplitude $\langle\epsilon_p|\tau'\rangle$ may be expressed as a superposition of Lorentz amplitudes, weighted by the coefficients $A(k, k')$ of the free spherical waves in Eq. 6.30 in the expansion of the final-state Coulomb wave function in Eq. 6.29 [110]. The result

$$\langle\epsilon_p|\tau'\rangle = (\Gamma_i/2\pi)\int_0^\infty A(k, k')\frac{2}{k' - \beta'}\mathrm{d}k' \tag{6.31}$$

where $\beta^2 = 2E_{\mathrm{exc}} + \mathrm{i}\Gamma_i$, shows that independently of the magnitude of the lifetime T_i the photo-electron "shakes down" during the Auger decay into various final states corresponding to a given Q. As Fig. 6.6 shows the real and imaginary parts of the PCI function for argon. The influence of T_i is embedded in $|\tau'\rangle$ which describes how far the photoelectron escapes from the atom before it experiences the change in the potential due to the Auger decay. In this particular case ($E_{\mathrm{exc}} = 15$ eV, $\Gamma_i = 0.11$ eV) the average distance is about 10^3 a.u.

If $Q \approx 0$ in Eq. 6.29 $A(k, k') = \delta(k - k')$ in Eq. 6.31 and $P_Q(\epsilon)$ reduces to the normalized Lorentzian profile. If $Q = 1$ the Auger electron and photoelectron line shapes become distorted such that $P_q(\epsilon)$ peaks at $\epsilon = \epsilon_A + \Delta$, where Δ is a positive PCI shift.
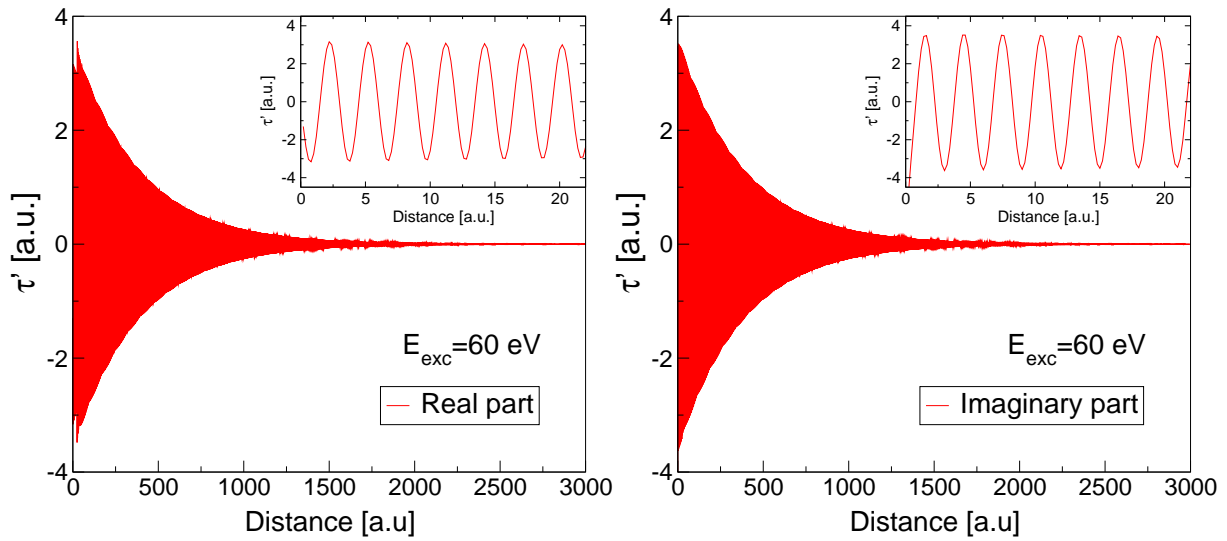
Figure 6.6: Real and imaginary parts of the PCI function $|\tau'\rangle$ as a function of radial distance, for Ar $2p$. The integration over τ was limited to the $j = 3/2$ state. It is constructed using the superposition of 10000 central-field continuum wave functions $|\tau\rangle$ and by taking into account the dipole interaction between the ground state and the $2p$ hole states into account.

The photoelectron line shape which is the mirror image of $P_Q(\epsilon)$ peaks at $\epsilon_p = E_{\text{exc}} - \Delta$. The choice $Q = 1$ accounts for the response of the photoelectron to the change of the ionic core potential produced by the Auger decay but neglects the screening of the ionic charge by the Auger electron. In this approximation, the Auger line shape has also been evaluated using Dirac-Fock central-field continuum and bound state wave functions and by incorporating the dipole interaction between the ground state and the final state [123]. Actually, the quantum-mechanical as well as semiclassical calculations agree with results, based on Eq. 6.27 unless E_{exc} is very small [123]. In spite of this internal consistency the agreement with recent experiments [127, 128] is poor at high excess energies. The calculated photoelectron spectra by taking into account the dielectric constant of the solid argon is given in Fig. 6.7. First of all is shown the calculated spectra which corresponds to 60 eV kinetic energy when the dynamical charge is equal to 1. In Fig. 6.8 is shown the comparison between the dynamical charge for kinetic energy of 4 eV. I have considered the cases which have applied to the experimental data and therefore I have shown only the photoelectron spectra. Furthermore, calculation of the line shape have been performed for Auger line shape but the discussions here is about photoelectron line shape. What we can learn from the calculated spectra? We can see that the spectra is very sensitive to the dynamical charge. Moreover, the line shape becomes asymmetric when the full final state is taken into account.

In the time-dependent semiclassical approach the choice $Q = 1$ in Eq. 6.29 corresponds to the assumption that the photoelectron is exposed instantaneously to a change of ionic core potential by one unit during the Auger decay. However, as realized by Ogurtsov [129], it takes some time for the Auger electron to pass the previously emitted photoelectron. If $E_{\text{exc}} \geq \epsilon_A$ it does not pass at all with the consequence that there should practically
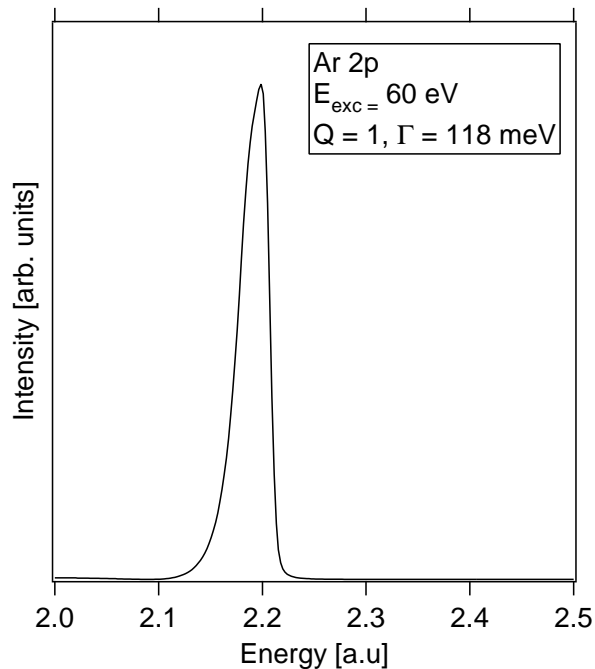
Figure 6.7: Calculated photoelectron line shapes. The excess energy is $E_{\text{exc}} = 60$ eV, and the dynamical charge is $Q_d = 1$.

be no PCI distortion at these excess energies [106, 127]. The semiclassical theory of this "no-passing" effect is in excellent agreement with recent experiments both regard to the shape [106, 127] and shifts [106, 127, 128].

In the time-independent picture the gradual time-dependent change of the screening of the core corresponds to an energy-dependent screening, i.e. $Q = Q(k)$. It is a final-state effect due to the interaction of the two escaping electrons. Since the atomic structure of the core does not matter the functional dependence $Q = Q(k)$ may be determined by requiring that the product of two Coulomb wave functions corresponding to two undetermined effective charges has the same asymptotic phase as the exact angle-dependent solution for two continuum electrons in a Coulomb field [110]. Suppose that the charge of the core is $Z + 1$. Then it follows from taking the spherical average over the necessary condition for correctly describing the two continuum electrons in terms of the Coulomb wave functions that the fast electron sees the charge Z if the slow one is unscreened. On the other hand if the fast electron is assumed to be unscreened the slow one sees the charge $Z + 1 - (k_s/k_f)$, where k_s and k_f are the wave numbers of the slow and fast electron respectively.

The PCI line shape formula, which is described above, is based on an effective charge Q, an angle independent quantity [117]. The dynamical charge Q_d in the analytical line shape formula takes the "no-passing effect" in PCI during the Auger transition following near threshold photoionization into account [106, 127]. The "no-passing effect" is caused in theory by the approximation, that the slow electron is emitted as an s-wave. The quantum mechanical treatment of the PCI effect indicates that the "no-passing effect" is a consequence of the mutual screening of the two electrons in the final state of the double photoionization like process leading to Auger electron emission [106, 127]. This result implies that the photoelectron is exposed to a change of the ionic charge during the
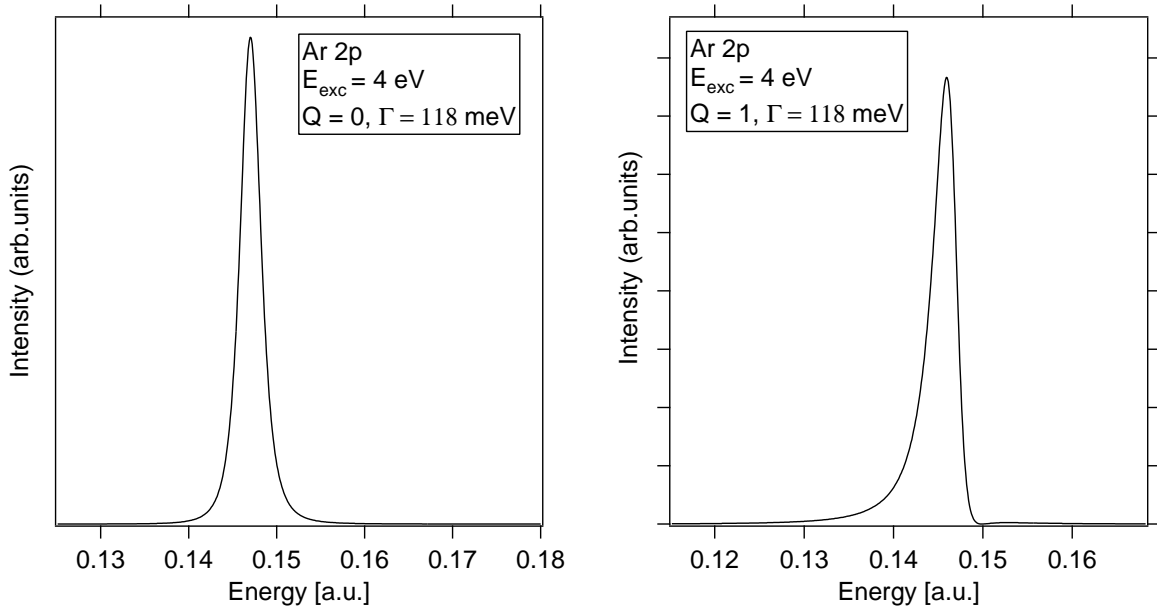
Figure 6.8:   Comparison of the calculated photoelectron line shapes for two different values of the dynamical charge, $Q_d = 0$ (left), and $Q_d = 1$ (right). The excess energy is $E_{\text{exc}} = 4$ eV.

Auger decay which is equal to

$$Q = Q_d = 1 - \sqrt{E_{\text{exc}}/\epsilon_A} \qquad (6.32)$$

if $E_{\text{exc}} \leq \epsilon_A$ and is zero if $E_{\text{exc}} > \epsilon_A$ [110]. The PCI shift becomes:

$$\Delta E \sim \frac{Q_d \Gamma_i}{2\varepsilon_r \kappa_s} \qquad (6.33)$$

and the asymmetry parameter ξ is given by

$$\xi = -\frac{Q_d}{\varepsilon_r k_s}, \qquad (6.34)$$

where k_s is $1/\sqrt{2E_1} - 1/\sqrt{2E_a}$ and E_1 is the energy of the slow photoelectron, and ε_r is the dielectric constant of the medium. The formula which takes ε_r into account, have been used to calculate the PCI shift for clusters [117].

Since Eq. 6.32 is independent of $Q_i = Z$ one may put $Q_i = 0$ as was done in Eq. 6.32. The identification of Q in Eq. 6.30 as the "dynamic" charge Q_d predicts in accordance with semiclassical models [106, 126] and the experiments [127, 128] that the PCI effect vanishes at $E_{\text{exc}} \geq \epsilon_A$. Detailed calculations show that the semiclassical line shapes [106, 126] and hence also the measured ones [129] in the Xe $4d$ case are represented very accurately by $P_{Q_d}(\epsilon)$ provided $E_{\text{exc}} > (\Gamma_i \epsilon_A)^{1/2}$ [110]. In fact this result is almost identical with a semiclassical model which assumes rectilinear trajectories [126] for the Auger electron and the photoelectron and which takes into account the energy gain of the Auger electron in a spherically average fashion.

If the averaging is not carried out the semiclassical line shape depends on the angle Θ between the directions of the emission of the Auger electron and the photoelectron and is a special case of the Kuchiev-Sheinerman formula [126]. It is given by

$$P_\Theta(\epsilon) = (\Gamma_i/2\pi)[(\epsilon_A - \epsilon)^2 + \Gamma_i^2/4]^{-1} K(\epsilon) \tag{6.35}$$

where

$$K(\epsilon) = (\pi\xi/\sinh\pi\xi)\exp[2\xi\arctan 2(\epsilon_A - \epsilon)/\Gamma_i] \tag{6.36}$$

with $\xi = \xi(\Theta) = -k_p^{-1} + |\mathbf{k}_p - \mathbf{k}_A|^{-1}$. Here $\mathbf{k}_p$ is the wave vector of the photoelectron and $\mathbf{k}_A$ is that of the Auger electron. In the spherical averaged model ξ is replaced by $\langle\xi\rangle = Q_d k_p^{-1}$, where Q_d is given by Eq. 6.32.

I have deduced the following formula for photoelectron lineshape:

$$P_Q(\epsilon) = \frac{\Gamma_i/2\pi}{(\epsilon - \epsilon_{exc})^2 - \Gamma_i^2/4}\kappa(\epsilon), \tag{6.37}$$

where

$$\kappa(\epsilon) = \frac{\pi\frac{Q_d}{\varepsilon_r k_s}}{\sinh(\pi\frac{Q_d}{\varepsilon_r k_s})}\exp\left[2\frac{Q_d}{\varepsilon_r k_s}\arctan\frac{2(\epsilon - \epsilon_{exc})}{\Gamma_i}\right], \tag{6.38}$$

This photoelectron line shape is the mirror image of the Auger line shape. In this model for PCI in clusters is possible to view the dynamic charge Q as screened by an infinite dielectric medium with permittivity ε_r. The change in potential energy is then not as large as in the vacuum case when the Auger electron overtakes the photoelectron. The PCI for surface should be close to that of the atom for all sizes, even if the dielectric constant is different for surface compared to the bulk. The value for the Ar permittivity used here is $\varepsilon_r = 1.61$ [130]. I have performed a test of the calculated lineshape with and without dielectric constant, as shown in figure 6.9. The main observation of the cluster spectra is that the PCI asymmetry is reduced for the bulk relative to the surface peak and relative to the atom near the threshold. Far away from the threshold the bulk peaks and surface peaks are identical to the atomic one. The next question will be if the size effect can give different asymmetry for bulk and surface compared to the atom and this is the subject of Chapters 9 and 11.

6.5   Dynamics of PCI in solid

The phenomenon of the Auger decay has been observed in many systems since its discovery by Auger in 1925 [10]. As is well known, its essence is rather simple: a core hole created by some reason is filled by an electron in a higher level and, accordingly, another electron is excited from another level. Here we are interested in photoexcitation. Then, the core hole is made by exciting an electron in the core level to a much higher level. When the energy of the photon is larger than the threshold energy, the electron becomes a photoelectron and propagates almost freely until it is detected. In this simplest framework, the kinetic energy of the photoelectron is uniquely determined by the photon energy, and that of the Auger electron is also fixed representing the level scheme.

In actual cases, the above framework is too simple. We must take into account the following two final-state interactions associated with the present excited states. One is
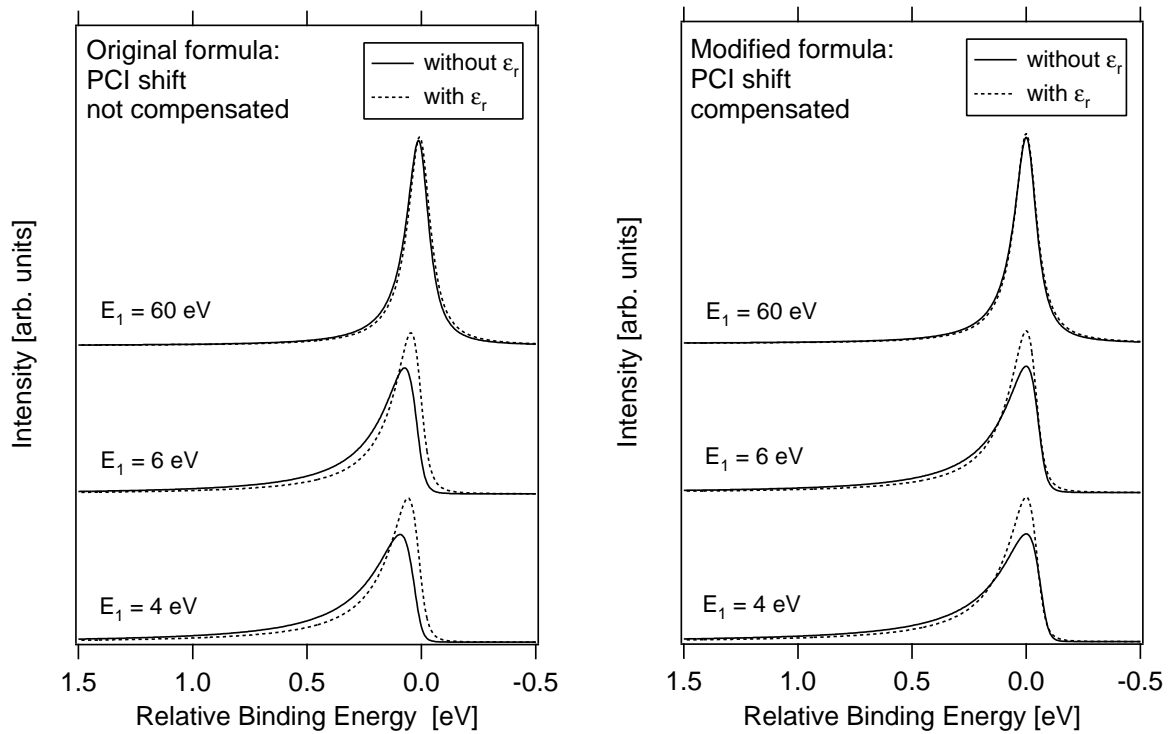
Figure 6.9:   Theoretical photoelectron lineshapes with and without taking into account the effective dielectric constant ($\Gamma = 118$ meV and $E_a = 200$ eV).

the core attraction by the core holes and the other is the Coulombic repulsion between the two propagating electrons. With these interactions, their kinetic energies are no more constant. In fact, the two electrons can share kinetic energies and a part of the energy is transferred from one to the other. Then, a new question arises, that is, in which direction the energy is transferred within the restriction of energy conservation, from the photoelectron to the Auger electron or vice versa?

From the experiments performed for atomic cases so far, we seem to have an answer: the photoelectron loses some energy and the Auger electron receives it. In particular, what is the most outstanding is the case where the energy of the former is close to the threshold. In fact, the energy loss of the former becomes largest in that case. Thus, it is one of our concerns to clarify how such asymmetry manifests itself in the dynamics of energy sharing.

In order to answer this question, we first treat each effect separately because it is too difficult to treat these entangled effects at the same time from the first. Firstly, we will show that the effect of core attraction works in such a way that the photoelectron always loses some energy and the Auger electron receives it. The physical image is as follows. The core attraction becomes enhanced when the Auger transitions occurs, because there are now two holes. The photoelectron feels such a potential change and tends to be de-excited to the lower energy, while the Auger electron is free from such a situation because the potential change is already finished when it appears. Thus, the latter electron just works as an energy source and receives the extra energy from the former one.

Next, the e–e repulsion gives an almost reverse effect, namely, a part of kinetic energy

of the Auger electron is transferred to the photoelectron. In this case, the physical picture is difficult to find. In fact, the way of sharing is determined by the sign of the two-electron resolvent. Anyway, the two effects are competing. The remaining problem is therefore determined. In order to answer this question quantitatively, we will take into account both the effects at the same time and examine the energy spectrum for propagating electrons in various cases. In solids we expect that the results will be more variable because the strengths of those two interactions are not always the same with different degrees of screening. In particular, it is possible that the Auger electron asymmetrically loses some part of its kinetic energy and the photoelectron receives it when the effect of the e–e repulsion dominates that of the core attraction.

The important part of the dynamics occurs mainly in the potential region of the excited atom. In that sense, the dynamics is essentially local. Thus, it is also expected that the local electronic structure affects the way of energy sharing.

What is important is that some new interactions which are not observed in the initial ground state can manifest themselves in those of the final states. Final state interaction is very interesting because they are deeply related to the nature of the excited state, and therefore give a special feature in the dynamics. The final state interaction in this state are the core attraction by the core-holes and the e–e repulsion working between those two electrons. I am interested to know what kind of effect each interaction gives to the dynamics. The discussion will limited to the s-wave model.

The total Hamiltonian is separated into four parts:

$$H = H_0 + H_{\text{e–ph}} + H_{\text{Auger}} + H_{\text{e–e}}. \tag{6.39}$$

The first term is the perturbed part, which is expressed by:

$$
\begin{aligned}
H_0 &= \sum_{i\sigma} \epsilon_i^{(c)} a_{i\sigma}^\dagger a_{i\sigma} + \sum_i U_i (1 - n_{i\uparrow})(1 - n_{i\downarrow}) \\
&+ \sum_{\mu\sigma} \epsilon_\mu C_{\mu\sigma}^\dagger C_{\mu\sigma} - \sum_{i\sigma} n_i V_{\mu\mu'}^{(ic)} C\mu\sigma^\dagger + \sum_\lambda \omega_{\mathbf{k}} b_\lambda^\dagger b_\lambda C_{\mu\sigma'}
\end{aligned}
\tag{6.40}
$$

Here $a_{i\sigma}^\dagger$ and $a_{i\sigma}$ are creation and annihilation operators of the ith core hole with spin σ, respectively, and $\epsilon_i^{(c)}$ is the binding energy. Throughout this study, I restrict myself to the case where only two kinds of core states are relevant. We use the convention that the state with $i = 1$ is deeper and that with $i = 2$ is shallower. The second term represents the Coulombic repulsion between the two holes in the same core level. Its strength is denoted by U_i for the ith level. The occupation numbers for the holes are written as $n_{i\sigma}$ and n_i are often used instead of $(1 - n_{i\uparrow})(1 - n_{i\downarrow})$. While, the operators of the electron in the continuum is expressed by $C_{\mu\sigma}^\dagger$ and $C_{\mu\sigma}$ if it is occupying the μth level with spin σ. Its kinetic energy is written as ϵ_μ. The forth term describes the Coulomb interaction between a hole and an electron in the continuum. Looking at the third and forth terms, we easily notice that the part for the continuum states is not diagonalized unless the numbers of the core holes are zero. Thus it is convenient to replace the basis set for the continuum, following those numbers. Here we use the two sets corresponding to the cases with (n_1, n_2) = (1,0) and $(n_1, n_2) = (0,2)$, and then denote operators as $C_{\mu\sigma}^{(1)}$ and $C_{\mu\sigma}^{(2)}$, respectively. The last term in Eq. 6.40 is for free photons, whose creation and annihilation operators are $b_\lambda^\dagger$ and b_λ, respectively. The suffix λ means $(\mathbf{k}, \mathbf{e})$, where $\mathbf{k}$ and $\mathbf{e}$ are the momentum and

the polarization, respectively. The frequency of the photon is ω_k. The next part of the total Hamiltonian is the electron-photon interaction as

$$H_\mathrm{e-ph} = \sum_{\lambda\mu i\sigma} \left(M_{\mu i}(\lambda) C_{\mu\sigma}^{(1)\dagger} a_{i\sigma}^\dagger b_\lambda + \mathrm{h.c.} \right) \tag{6.41}$$

where $M_{\mu i}(\lambda)$ is the element of the transition matrix.

The third part is related to the Auger transition, which is:

$$H_\mathrm{Auger} = \sum_{\mu\sigma} \left(V_\mu^{(a)} C_{\mu\sigma}^{(1)\dagger} a_{2\sigma}^{(1)\dagger} a_2^\dagger b_\lambda + \mathrm{h.c.} \right), \tag{6.42}$$

where the matrix element $V_\mu^{(a)}$ is related to the transition that yields two holes at the second core level and one electron at the μ th level of the continuum.

Finally, the last part describes the e–e scattering in the continuum:

$$H_\mathrm{e-e} = \frac{e^2}{2} \sum_{\mu\mu'\nu\nu'\sigma\sigma'} V_{\mu\nu\nu'\mu'}^{(\mathrm{e-e})} C_{\mu\sigma}^{(2)\dagger} C_{\nu\sigma'}^{(2)\dagger} C_{\nu'\sigma'}^{(2)} C_{\mu'\sigma}^{(2)}. \tag{6.43}$$

The matrix element $V_{\mu\nu\nu'\mu'}^{(\mathrm{e-e})}$ is to be calculated for each combination of four levels.

Although we have not written explicitly, we use screened Coulomb potentials for both the core attraction and the e–e repulsion. Such potentials are characterized by the screening length ξ as

$$V(r) = \frac{e^2}{r} exp(-\frac{r}{\xi}). \tag{6.44}$$

In actual calculations, we have to prepare electronic states, using the following two different models. In the first model, we treat a certain partial wave, assuming that spherical symmetry is good enough around the atom. In order to obtain such states, we make use of a semi-infinite and one-dimensional tight-binding Hamiltonian. Since the energy band becomes a cosine-type in that model, we only use states close to the band bottom. While, the second one is a cubic tight-binding model, in which the three-dimensional space is represented by the lattice points of a cubic. There the spherical symmetry is broken, but instead the cubic symmetry is satisfied. In this case, it is rather difficult to diagonalize the Hamiltonian directly because we need a large system size to obtain smooth spectra. We therefore make use of a method of lattice Green functions. In the present model, we do not include the scattering of electrons by the other atoms, which will make a superlattice in the original cubic lattice.

The spectrum is separated into two terms as

$$S(\epsilon) = S_1(\epsilon) + S_2(\epsilon) \tag{6.45}$$

Firstly, $S_1(\epsilon)$ is the contribution from final states with only one electron in the continuum and defined as

$$S_1(\epsilon) = \sum_{f_1} w_{f_1} \delta(\epsilon - \epsilon_\mu). \tag{6.46}$$

Here the suffix f_i means a final state with one photoelectron as

$$|f_1\rangle = C_{\mu\sigma}^{(1)\dagger} a_{1\sigma}^\dagger |g\rangle \tag{6.47}$$
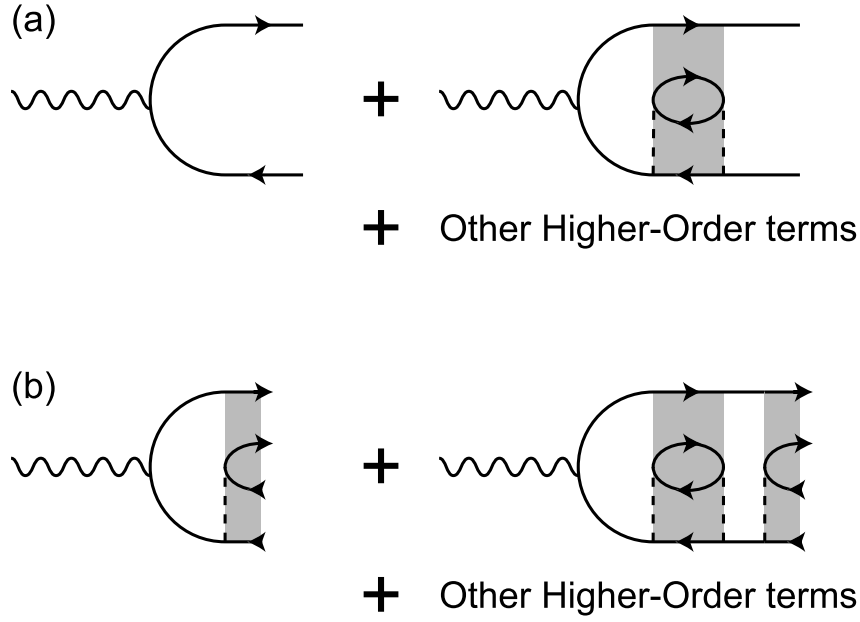
Figure 6.10:   Diagrams describing the two processes. Those related to $S_1(\epsilon)$ and $S_2(\epsilon)$ are drawn in the (a), and (b) respectively. In both figures the line with the rightward (leftward) arrow represents an electron (a hole). Adapted from [131].

and $|g\rangle$ is the electronic ground state. On the other hand, the second term gives the contribution from the channels in which both a photo-electron and an Auger electron are found in the final state and is denned as

$$S_2(\epsilon) = 2 \sum_{f_2} w_{f_2} \delta(\epsilon - \epsilon_\mu), \tag{6.48}$$

where the suffix f_2 specifies a state with two electrons in the continuum and is expressed as

$$|f_2\rangle = C^{(2)\dagger}_{\mu\uparrow} C^{(2)\dagger}_{\nu\downarrow} a^\dagger_{2\uparrow} a^\dagger_{2\downarrow} |g\rangle. \tag{6.49}$$

In both terms, the transition rate w_f is calculated for any final state f and an initial state as

$$|i\rangle = b^\dagger_\lambda |g\rangle, \tag{6.50}$$

by using the general formula

$$W_f = 2\pi|T_{f_i}|^2 \delta(E_i - E_f). \tag{6.51}$$

Here E_i and E_f are the energies of initial and final states, respectively, and the T matrix is defined as

$$T = H' + H' \frac{1}{E_i - H_0 + \mathrm{i}\gamma} + H' \frac{1}{E_i - H_0 + \mathrm{i}\gamma} H' \frac{1}{E_i - H_0 + \mathrm{i}\gamma} H' + \ldots, \tag{6.52}$$

where H' is the perturbation part, that is, $H_{\text{e–ph}} + H_{\text{Auger}} + H_{\text{e–e}}$, and γ is the positive infinitesimal. In order to specify clearly the processes to be considered, we draw the
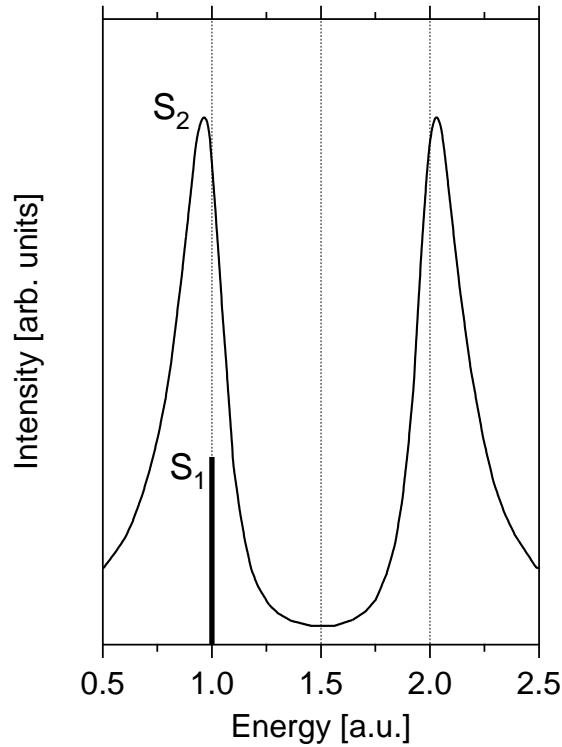
Figure 6.11: The energy distribution spectrum of a photoelectron and an Auger electron calculated from the s-wave model. The nominal energies are 1.0 and 2.0 a.u. The imaginary part of the self-energy is 0.1 a.u. Adapted from [131].

diagrams related to $S_1(\epsilon)$ and $S_2(\epsilon)$ in Figs. 6.10(a) and 6.10(b), respectively. In each diagram, the no-shaded regions correspond to the states in which only a photoelectron and a deep core hole are existing, and there the first basis set should be assigned to the continuum states. On the other hand, the shaded regions correspond to the states in which both a photoelectron and an Auger electron are existing with two shallow core holes, and there the second basis set should be assigned to the continuum states. Executing this procedure, the changing atomic valency can be automatically included as a dynamical variable.

The results obtained by Iwano *et al.* [131] using an s-wave model are given in Fig. 6.11 and 6.12. Here they used the value of 20 times the Bohr radius as the screening length for the core attraction, ξ_1. Fig.6.11 shows a spectrum in which both the two components S_1 and S_2 are drawn. Here the nominal energies are set at 1.0 and 2.0 au for the photoelectron and the Auger electron, respectively. The imaginary part of the self energy is approximated by the constant value, namely, 0.1 a.u.

The first component S_1 takes the form of a delta function because there is no other fluctuation mechanism, while S_2 shows typical features of asymmetric energy sharing, that are, the shift and distortion of each peak. It should be also mentioned that the total spectrum, namely, $S_1 + S_2$ is not symmetric around the half of the total energy because of the presence of the S_1 component.

In order to investigate the global structure, Iwano *et al.* [131] also draw a zoomed-out
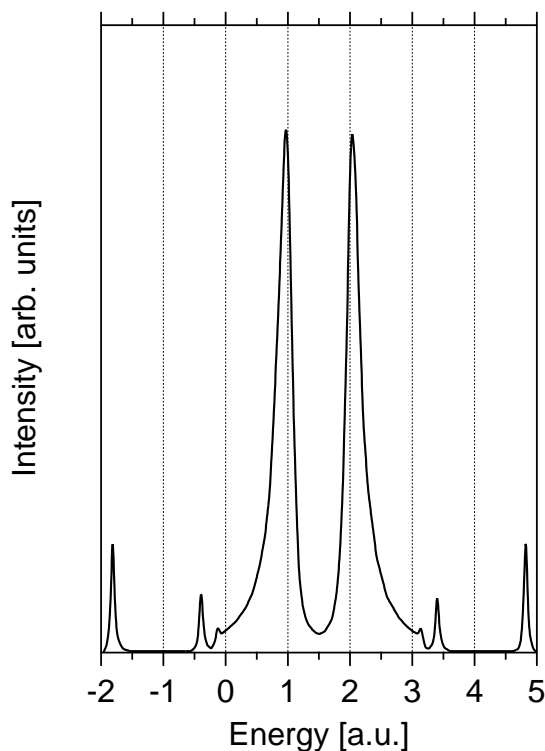
Figure 6.12: The energy distribution spectrum of a photoelectron and an Auger electron calculated from the *s*-wave model. This is a zoomed-in part of the plot from Fig. 6.11. Adapted from [131].

view of the same spectrum in Fig.6.12. They now observe several small but finite peaks on both the sides of the main peaks. As for the left-hand ones, they are associated with the photoelectrons that are once excited to the states around the nominal energy, but de-excited to bound states after that. It should be remarked that these bound states are related to the potential due to the two shallow core holes, not one deep hole. Of course, such bound electrons, which are no more photoelectrons, can not be observed, but, instead the Auger electrons can receive such energy losses (gains for the Auger electrons) and therefore can be observed. In fact, we can see such contributions in the rightmost region of the spectrum.

Summarizing these features, can be concluded that the dynamics of the PCI is very sensitive to the local electronic structure around the excited atom. If we may think that the e–e repulsion is weak enough because of the screening, it's effect against that of the core attraction, whichever the energy of the photoexcited electron is lover or higher than the Auger one. For that it is needed to use a perturbation theory taking into account terms up to the first order with respect to the e–e repulsion is not always weak. If we consider as before the *s*-wave model and fix the screening lengths at 20 times the Bohr radius for both the core attraction and the e–e repulsion then the energy of the photoelectron is lower than that of the Auger electron. Some amount of energy is transferred from the Auger electron to the photoelectron. Also can be expected that the effect of the core attraction is diminished because the attraction of the photoexcited electron is largely screened by

the Auger electron.

An experimental evidence for PCI in Cu is given Coward *et al.* [132]. They found that the magnitude of the PCI is strongly dependent on the type of atomic excitation. For electron impact excitation, the magnitude of PCI is amplified due to the presence of scattered electrons, therefore the energy distribution between the ejected and scattered electrons for electron excitation is the main factor that determines the magnitude of the PCI in Cu. In comparison, the model predicts that the photon excitation for the same Auger process produces PCI effects which are smaller in magnitude. PCI depends on the kinematics, hence, energy distribution of the emitted charges. This energy distribution is expected to be different for the solid state compared to the free atom case. But the free atom models do not take into account inelastic and elastic scattering of the emitted charges. Secondary electron emission due to the e–e inelastic scattering is one effect that may increase the magnitude of the PCI.

Another experimental evidence of the PCI in solid is given by Mikushkin *et al.* [133]. They study the post collision effect at the surface of Au solid during the scattering of fast electrons. They assumed that the anisotropic post collision effect differs from the classical one in being large at velocities characterized by cross sections close to the maximum values. The Au atom under study is part of the solid. The ejected electron and the Auger electron are emitted by the metal surface. The interaction of the slow electron and the Auger electron in Au^{2+} must therefore deal with the contribution to the PCI of these particles with the metal surface.

An interesting question arises concerning the effect of extra-relaxation on PCI in solids. Normally, extra-atomic relaxation, associated with the adjustment of neighboring atoms to the new potential produced by doubly ionized atom resulting from the photoionization followed by Auger decay, contributed to the energy of the emitted Auger electron.[134] However, when the photoelectron remains in the near vicinity during the emission of Auger electron, the extra-atomic relaxation contribution to the Auger electron energy may be expected to decrease.

The treatment of dynamic screening of Auger transitions in solids[135] is mathematically equivalent to that of PCI, and the effects on the line shape are very similar. Hence, a comparison with Auger electron line shapes of the free atom may lead to misinterpretations, if dynamic screening effects are neglected.[136]

Chapter 7

Model Calculations: Argon Clusters

Rare gas clusters can be formed by any rare gas at low temperature and they are held together by weak van der Waals interactions. Their forces have their origin in electron density fluctuation on one of the atoms, that give rise to an electric dipole. This dipole induces dipoles on the other atoms in the cluster and this dipole–dipole interaction keeps the cluster together. For an ionized cluster there are Coulombic forces between the ion and the outer atoms. The van der Waals forces holding neutral clusters together are typically very weak.

One of the most frequently asked question is that of the cluster geometry. Small clusters are believed to have icosahedral geometry, whereas large clusters have cubo-octahedral geometry built on fcc (face centered cubic) lattice [19]. For small clusters the icosahedral structure is favored over the cubo-octahedral one since the surface atoms of the former structure have at least six nearest neighbors, whereas surface atoms of cubo-octahedral structures have five nearest neighbors. The icosahedral clusters have built-in strain, resulting from the fact that this geometry does not allow for equilibrium bond lengths both within an atomic layer and between layers. At some size of the cluster this strain will be large enough to favor cubo-octahedral structure. Moreover, since the crystalline phase of the rare gases have fcc structure, and one can expect the same for the large cluster for both the above discussed geometries bulk atoms have 12 nearest neighbors.

The ionization energy of an atom in a cluster may be different compared to a single atom. For clusters the ionization potential is varying with cluster size and site within the cluster. The chemical shift can be divided into initial state effect and final state effect. The initial state effect is related to the electrostatic potential of the atom in a cluster. However, atoms in a van der Waals cluster can be considered as having no overlap between wave functions of different atoms, and hence the electrostatic potential of every atom in a cluster is the same as for the atom. Hence, there is no initials state effect. The final state effect is due to the relaxation of the final state. Upon ionization, the electron is removed from an atom in the cluster. If the core-hole is assumed to be localized on one atom, all the other electrons in the cluster will see a positive charge of $+e$ on the ionized atom.

Intra-atomic screening will cause the other electrons in the ionized atom to rearrange. The removal of a core electron will essentially result in contraction of the valence orbitals, since the nucleus will be less screened. Charge transfer means that the core-hole will attract valence electrons from the surrounding atoms and the charge will delocalize over
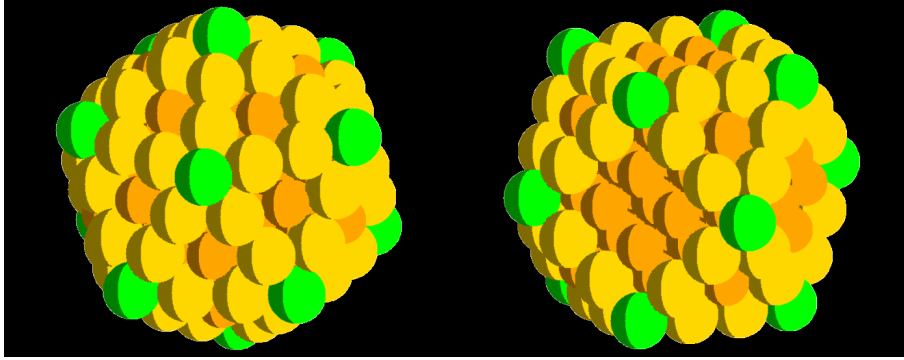
Figure 7.1: Clusters can have either icosahedral or cubo-octahedral symmetry. Left: Icosahedral cluster, 147 atoms. Right: Cubo-octahedral cluster, 147 atoms. Corner, edge and face sites are shown in different shades of grey.

the cluster. Inter-atomic screening means that the ionized atom will attract electrons from the other atoms in the cluster, but they will not leave their atoms. Instead, all atoms will have higher electron density in the direction of the ionized atom, resulting in electric dipoles. This is called charge induced dipole interaction.

This screening will lower the electrostatic energy in the final state of the cluster, leading to a lower binding energy, since the binding energy is the energy difference between the initial and final state. This process is called polarization screening of the core-hole. Core-holes will be screened to a different extent depending on their position in the cluster, and also depending on the size of the cluster. Sites near the center will have more atoms within a given radius, than atoms near the surface of the cluster. The magnitude of the induced dipole drops rapidly with distance from the ion, which means that the biggest contribution to the screening comes from the nearest neighbors.

Polarization screening can be calculated by explicit determination of the polarization of each atom in the cluster, that is induced by the ionization. The dipole strength is caused by the ionized atom, but it is also influenced by all the other dipoles in the cluster. Essentially this means solving a system of coupled system of equations. This is mathematically simple, but since the dipole strength must be calculated for all the atoms in all the spatial directions, computer requirements are increasing rapidly with increasing cluster size. For large clusters one instead uses a continuum model in which the nearest neighbors are treated as above, but the rest of the atoms are treated as a dielectric medium. Both the discrete and continuum model originated from Ref. [130].

7.1 Binding energies in Ar clusters

In clusters, the electron binding energies are substantially decreased with respect to the atomic values. These binding energy shifts arise primarily from polarization screening [130]. Calculations have been performed for several small clusters (Ar_2, Ar_3, Ar_4, Ar_5, Ar_7, Ar_{13} and Ar_{55}, see Fig. 7.2) by using the discrete model. The total energy of the
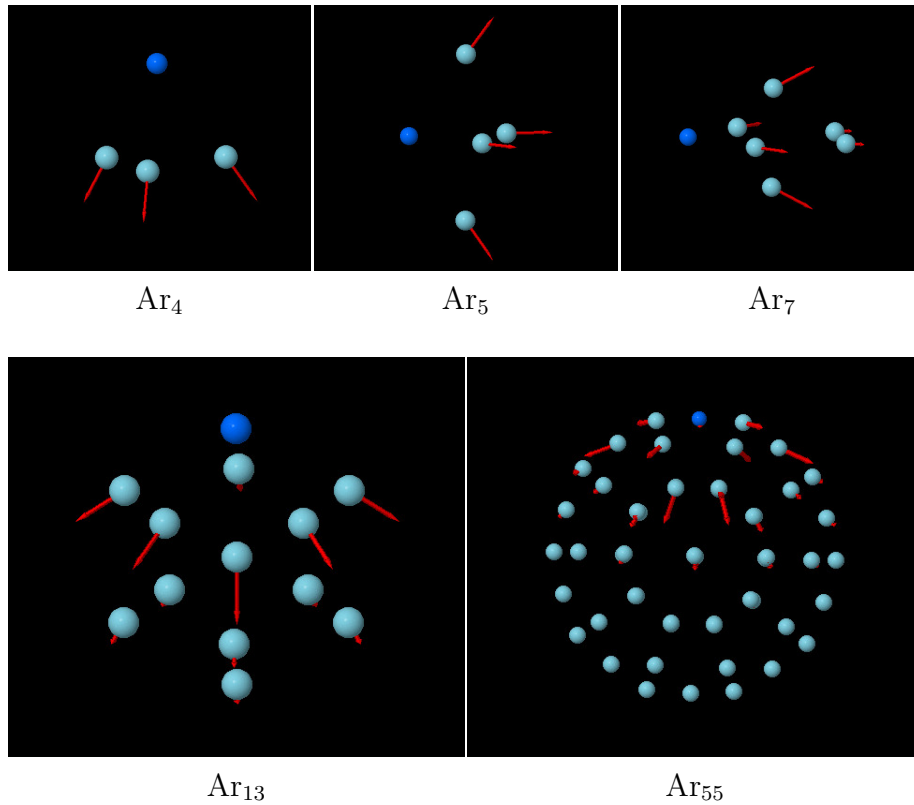
Figure 7.2: Visualization of dipole moments in several small Ar clusters by solving the discrete model. The dark grey circles represent the ionized atom, dipole moments are shown with arrows.

cluster has been derived according to Ref. 130:

$$
U_N(\mathbf{r}) = -\frac{1}{2} \sum_{\substack{i,j=1 \\ i \neq j}}^{N} \sum_{\mu,\nu=1}^{3} p_{i,\mu} \cdot \partial_\mu \partial_\nu \frac{1}{|\mathbf{R}_i - \mathbf{R}_j|} \cdot p_{j,\nu} +
$$

$$
+ \frac{1}{2} \sum_{i=1}^{N} \frac{|\mathbf{p}_i|^2}{\alpha} - \sum_{i=1}^{N} \mathbf{p}_i \cdot e \frac{\mathbf{R}_i - \mathbf{r}}{|\mathbf{R}_i - \mathbf{r}|^3}
$$

where α is the polarizability of argon, $\mathbf{R}_i$ and $\mathbf{p}_i$ are the positions and polarizations of each atom in the cluster, respectively. The ionized atom is represented by a point charge e, at the position $\mathbf{r}$. The above equations are well-known and have previously been used to calculate electron affinities of clusters [137].

The geometry of the neutral cluster was optimized for a number of cluster sizes. The computed geometries of the clusters are calculated using the Gaussian03 package with the MP2 method and a 6-31+G* basis set [138]. For Ar_2 the calculated equilibrium distance is 4.03 Å, which is somewhat larger than the experimental one (3.76 Å [139, 140]). Applying the dipole model for this Ar–Ar distance yields a calculated shift of the ionization energy relative to the atom of -45 meV. More realistically, the experimental equilibrium distance of Ar_2 is 3.76 Å and the polarizability of atomic Ar is 1.64 Å^3 [141]. Then, one obtains a slightly different shift of the ionization energy of -59 meV. This value is shown in Table

Table 7.1: Calculated shifts of the Ar $2p$ ionization energies of small clusters in meV, relative to the atomic value. [a] triangle, [b] tetrahedron, [c] pyramid, [d] pentagonal bipyramid, [e] icosahedron, [f] fcc structure, central atom plus 12 nearest neighbors, [g] fcc up to 2nd order neighbors, [h] fcc up to 3rd order neighbors, [i] fcc up to 4th order neighbors.

Cluster	Dimer	Corner	Edge	Face	Bulk
Ar_2	−59				
Ar_3 [a]		−115			
Ar_4 [b]		−167			
Ar_5 [c]		−175/−217			
Ar_7 [d]		−234/−304			
Ar_{13} [e]		−303			−578
Ar_{55} [e]		−368	−470		−680/−764
Ar_{13} [f]		−319			−576
Ar_{19} [g]		−285	−427		−628
Ar_{43} [h]		−387		−524	−660/−740
Ar_{55} [i]		−388	−491	−566	−723/−775

7.1.

From the small shift, which is calculated for the dimer (cf. Table 7.1), it also follows clearly that the dimer ionization energy cannot be visible in the raw experimental spectra, especially since the mixing ratio of dimers or small clusters is weak compared to the dominant atomic signal in the low $\langle N \rangle$ regime.

We derive for trigonal Ar_3 a shift in Ar $2p$ ionization relative to the atomic value of -115 meV, as shown in Fig. 7.2. It is increased for tetrahedral Ar_4 to -166 meV. This value corresponds to a coordination number of three and can be associated with corner sites. Ar_5 is assumed to be of trigonal bipyramidal shape. There are two kinds of corner sites, which are coordinated to 3 or 4 nearest neighbors, as shown in Fig. 7.2. These give rise to a shift in ionization energy of -175 meV and -217 meV, respectively. The Ar_7 structure is described by pentagonal bipyramid. There are two different corner sites with 4 and 6 nearest neighbor sites. These yield a shift of -234 meV and -304 meV, respectively (see Fig. 7.2).

Ar_{13} is assumed to have icosahedral structure with one atom in the center and 12 atoms in one shell at an equal distance. The repulsive part of the van der Waals interaction results from the covalent interaction between rare gas atoms. Since these are closed shell structures, the total energy will be increased for small bond distances. The most important attractive contribution comes from the basis set superposition error (BSSE) which arises due to the use of a finite basis set. Since small basis sets offer a limited representation of the true wave function, the energy can be lowered if the atom is partly represented by orbitals on the surrounding atoms. This energy gain has a maximum at some bond distance, which typically is in the same order as the experimental bond length. It is very difficult to explicitly calculate the BSSE energy. To estimate that contribution one can instead calculate the energy of a separate atom represented by two sets of basis functions, centered at two positions in space, separated by 3.7 Å and compare

to the energy of an atom with only one set of basis functions. For Ar_{13} ionization in two positions were considered in the center of the cluster and at the surface. Ionization at the center results in symmetrical contraction of the cluster and excitation of the total symmetric breathing. when ionizing at the surface of the clusters, all the other atoms are attracted to the ion in a way that pushes the ion towards to the center.

The cubo-octahedral Ar_{13} has five fold coordinated corner sites, all separated by 3.76 Å. Corner sites of the icosahedral Ar_{13} have a shift of -303 meV, which corresponds to coordination number 6, but the model results indicate that the distances are not identical for all atoms: The distance to the central atom is 3.76 Å, but the distance to the other 5 neighbors is somewhat larger, i.e. 3.95 Å (see Fig. 7.2).

Icosahedral Ar_{55} has two shells of atoms around a central atom, with the distance between the shells 3.76 Å and the distance between neighbors belonging to the same shell is 3.95 Å. There are two kinds of surface sites: six fold coordinated corner and eightfold coordinated edge sites. Further, there are two kinds of bulk sites, both have 12 nearest neighbors: inner bulk sites, consisting of the central atom, and outer bulk sites, which are located in the sub-surface layer.

The cubo-octahedral Ar_{19}, Ar_{43}, and Ar_{55} structures were obtained from the fcc nucleus Ar_{13} by adding successively argon shells. Corner-sites of small clusters (Ar_n, n=13) range from -303 meV to -388 meV, where the shift increases with cluster size. Edge sites are found in a fairly narrow regime between -470 meV and -491 meV, similar to face sites (-524 meV to -566 meV). Size distributions in the jet are expected to smear out the components of different geometrical sites. However, there are certain binding energy ranges for each given geometric sites. This will produce photoelectron spectra of clusters, where individual geometric sites can still be identified, even if there are size distributions in the jet, which is similar to recent work on Kr clusters [142]. These findings indicate that size dependent shifts in $2p$-ionization of surface-bound atoms at distinct sites are smaller than the site-dependent shifts. The widest range is covered by bulk sites, where the $2p$ ionization energies are expected to be shifted between -578 meV and -775 meV (cf. Table 7.1). This reflects a strong size dependence in $2p$ ionization energies of atoms that are either bound in sub-surface layers, or deep in the interior of a cluster. Björneholm *et al.* [68] discussed the variation of the experimental $2p_{3/2}$ binding energies of surface sites in Ar clusters as a result of cluster size dependent changes in the effective numbers of nearest neighbors in surface sites. In their model, the number of the nearest neighbors varies from 5 to 8 for surface sites, which is consistent with commonly assumed cluster geometries with icosahedral or cubo-octahedral shape [130]. However, the present work shows that different geometric sites as well as the dimer can be clearly distinguished. A comparison of these model calculations with the experimental results obtained from this work are given in chapter 9.

Chapter 8

Photoionization of Small Krypton Clusters

In this chapter we will present a study of Kr $3d$ ionization energies of small, variable size krypton clusters which are investigated by photoelectron spectroscopy, in the size regime of clusters with an average size $\langle N \rangle \leq 30$ [142]. We find evidence for photoionization of the krypton dimer. Its $3d$ ionization energy is barely shifted relative to the atomic value. Results from model calculations considering different isomers and cluster sizes as well as defect sites give evidence that the experimental results can be related to photoionization from different surface sites in variable size krypton clusters [142].

8.1 Experimental Results

Previous work in this field has been obtained from near-edge absorption or related experimental and theoretical approaches as well as photoelectron spectroscopy of variable size clusters [11, 20, 21, 65, 68, 75, 78, 130, 143, 144, 145]. Specifically, size effects of the unoccupied electronic levels in atomic clusters are studied by the conversion of Rydberg states into the corresponding core excitons [20, 65, 68, 75, 78]. For the lowest states one finds for surface excitons a considerable blueshift relative to the atomic transitions [65, 68, 75, 78]. This spectral shift is even larger for the bulk excitons [75]. The atomic Rydberg states converge to the corresponding core ionization energy, where this quantity drops significantly in clusters compared to the isolated atom [68, 130, 143, 144, 145]. This decrease in binding energy is commonly assigned in terms of final state polarization screening [130]. Additionally, attenuation of the electron signal by bulk sites in large rare gas clusters has been considered using an atomistic model [144].

The size regime of small krypton clusters has not been investigated before in the Kr $3d$ regime. It is also known from earlier near-edge spectroscopy of small clusters that the most significant changes in electronic structure are found in the regime of small clusters [68, 75]. This is the motivation for the work, where we investigate Kr $3d$ photoionization in variable size Kr clusters in the size regime $\langle N \rangle \leq 30$.

Fig. 8.1 shows the series of Kr $3d$-photoelectron spectra of atomic krypton and a variable cluster size target ranging from $4 \leq \langle N \rangle \leq 30$. These photoelectron spectra indicate that new features from clusters occur at lower binding energy than the bare atom (cf. Ref. 145). The binding energies of the atomic transitions are calibrated to
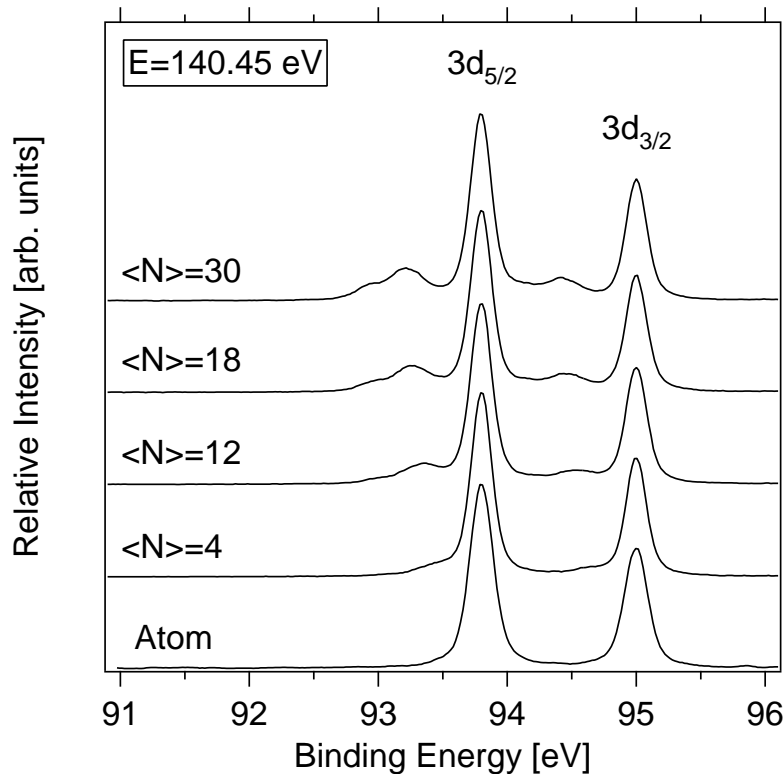
Figure 8.1: Comparison of Kr $3d$ photoelectron spectra of atomic Kr and from a cluster jet, where the average cluster size $\langle N \rangle$ of Kr clusters is varied between $\langle N \rangle = 4$ and $\langle N \rangle = 30$.

known literature values: 93.8 eV (Kr $3d_{5/2}$) and 95.0 eV (Kr $3d_{3/2}$) [145, 146].

We have carefully subtracted (see Fig. 8.2) a variable atomic portion, that depends on $\langle N \rangle$ and the mixing ratio of clusters in the jet, similar to earlier work [75]. The results are shown in Fig. 8.2. Beyond subtraction of a too large fraction of the atomic component, one observes that the remaining signal near the atomic $3d$ ionization energies starts to get slightly asymmetric or distorted. This implies that there is another component at the same energy position as the free atom. We tentatively assign this barely shifted component to dimers and discuss this point in detail below in connection with model calculations on Kr $3d$ binding energies in variable size clusters.

Knop *et al.* [75] have investigated near-edge absorption of variable size Kr clusters showing that there is a distinct dimer component that occurred with considerable intensity up to $\langle N \rangle = 150$. This component is dominant in the size regime of small clusters. Consistently, the series of spectra shown in Fig. 8.3 indicates that the ratio between dimers and larger clusters is similar to the near-edge absorption features in the Kr $3d_{5/2} \rightarrow 5p$-regime [75].

We can observe that as $\langle N \rangle$ is increased, the following systematic changes which occur in the spectra shown in Fig. 8.3:

(i) The dimer component decreases substantially in relative intensity. We do not observe any shift within the error limit observable for this component.
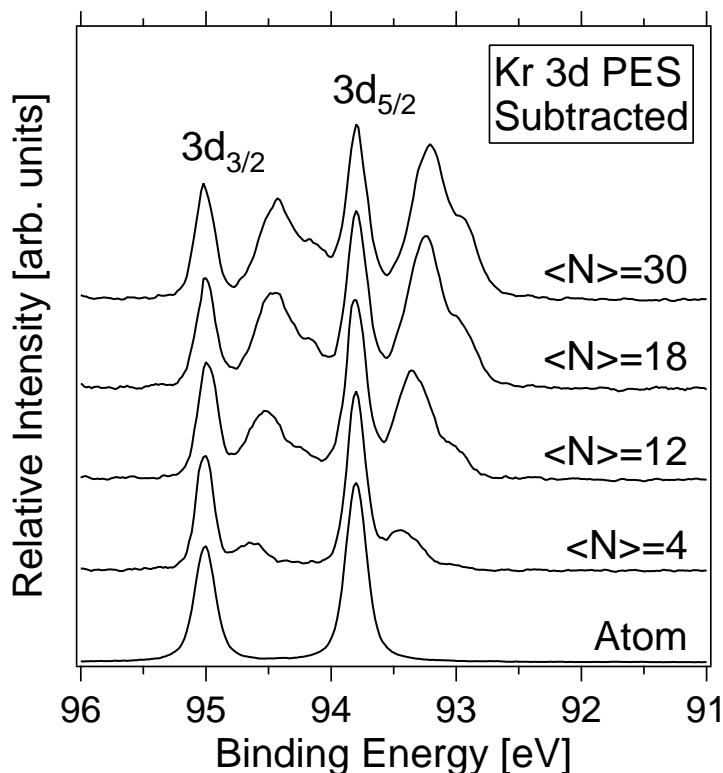
Figure 8.2: For rare gas clusters to be produced, the gas needs to be cooled down. This is usually done in the supersonic jets by adiabatic expansion by expanding highly pressurized gas through a small hole into vacuum. During the adiabatic expansion the gas cools extremely rapidly, and clusters are formed. Therefore, the subtraction of the atomic component from the raw cluster data is necessary.

(ii) Photoionization from surface sites show a characteristic size-dependent shift reaching up to $\sim$ -500 meV.

(iii) There is an energy regime, where photoionization from bulk sites should occur [145]. However, there is barely intensity in the experimental spectra, since small clusters consist essentially of surface sites.

A de-convolution of the spectral components, which contribute to the blended signals, is required, since the core ionization energies of different surface sites shown in Fig. 8.3. This is similar to recent high resolution work on large Kr clusters, where just are not visible from the raw data a single surface and bulk component was identified in larger Kr clusters ($\langle N \rangle \geq 90$) [145]. A careful inspection of the broad features indicates, however, that probably several components are blended in the experimental photoelectron bands.

We use Voigt profiles, where the Lorentzian line width is assumed to be 88 meV in all spectra, which is a result of the core-hole lifetime [146]. This implies that other processes, which may possibly affect lifetime broadening, such as short-lived final states, are not detectable. Furthermore, a 50–70 meV contribution from the spectrometer and photon-band width has to be considered by a Gaussian line shape. The total Gaussian width of the atomic and dimer component is found to be 140 meV and it is, as expected, independent

Table 8.1: Experimental shifts of the Kr $3d$ ionization energies relative to the atomic values for both spin–orbit component ((a) $3d_{5/2}$ and (b) $3d_{3/2}$). The values in parentheses correspond to the relative intensities of the photoelectron bands of clusters. Averaged values for both spin–orbit components are given. The error limits are estimated to be ± 10 meV.

a)

$\langle N \rangle$	dimer	corner	edge	Face/bulk
4	0.00 (76.5%)	-0.332 (13.7%)	-0.476 (7.8%)	-0.765 (1.9%)
12	-0.02 (51.5%)	-0.391 (22.1%)	-0.545 (18.8%)	-0.790 (7.5%)
18	-0.04 (41.7%)	-0.453 (17.4%)	-0.585 (27.7%)	-0.806 (13.2%)
30	-0.05 (41.7%)	-0.484 (17.2%)	-0.638 (25.1%)	-0.872 (15.4%)

b)

$\langle N \rangle$	dimer	corner	edge	Face/bulk
4	-0.01 (76.7%)	-0.336 (14.5%)	-0.481 (6.2%)	-0.767 (2.6%)
12	-0.02 (52.3%)	-0.409 (21.7%)	-0.560 (17.2%)	-0.794 (8.7%)
18	-0.04 (41.2%)	-0.463 (20.5%)	-0.596 (25.1%)	-0.830 (13.2%)
30	-0.05 (41.7%)	-0.497 (19.2%)	-0.652 (22.8%)	-0.875 (16.2%)

of $\langle N \rangle$. It is found to be slightly increased to 156 meV for all surface sites besides the dimer at $\langle N \rangle = 4$. This Gaussian broadening increases as a function of $\langle N \rangle$ yielding 178 meV at $\langle N \rangle = 12$, 196 meV at $\langle N \rangle = 18$, and 206 meV at $\langle N \rangle = 30$, respectively. As a result, the surface components are represented by Voigt profiles of different widths. This reflects the following size dependent contributions to line broadening in clusters:

(i) Different number of nearest neighbors to the ionized atom. This is a result of the size distribution in the jet and clusters containing defects [147, 148, 149, 150, 151].

(ii) Different isomers. These are known to exist in weakly bound van der Waals clusters [147, 148].

(iii) Vibrations/phonons. This contribution is expected to be small, i.e. ≤ 5 meV [152].

The most significant contributions to line broadening are expected to come from the size distribution and the occurrence of different isomers besides the given resolution of the photoelectron spectrometer and the band width of the photon source. The spectral components occur with different intensity and shifted energy positions as $\langle N \rangle$ is increased (cf. Table 8.1). Such shifts of spectral components are assigned to size-dependent shifts of surface components.

The dimer component is found almost unshifted as a function of $\langle N \rangle$. This appears to be reasonable since no size-dependent energy shift is expected for the dimer. However, the relative intensity of this component decreases as a function of $\langle N \rangle$, which is evidently a result of the decreasing mixing ratio of dimers in the jet. From the energy position, which is experimentally found for the dimer (cf. Table 8.1), it follows clearly, that the dimer

ionization energy cannot be visible in the raw experimental spectra, especially since the mixing ratio of dimers or small clusters is weak compared to the dominant atomic signal in the low $\langle N \rangle$ regime.

Cuboctahedra and icosahedra have been identified by experiments on rare gas clusters [59, 76]. Cuboctahedra are known to exist besides the most stable icosahedra and promote fast cluster growth in jet expansions [149]. As a result, a considerable shift in Kr $3d$ binding energy is expected to occur for corner sites, if it is assumed that polarization screening scales with the number of nearest neighbors of the core-ionized center. The component that is shifted by -334 meV (at $\langle N \rangle = 4$) to -491 meV (at $\langle N \rangle = 30$) is plausibly assigned to corner sites (see Table 8.1). The component that is found to be shifted by -479 meV to -645 meV is assigned to edge sites. The shift in binding energy is expected to be larger than for corner sites, since the number of nearest neighbors is increased to 7 in cuboctahedra and 8 in icosahedra [148]. Further, any defect in cluster geometry, such as stacking faults in larger clusters containing larger amounts of bulk sites, will lead on the surface of the cluster to additional edge sites, where face sites are converted into edge sites. The experimental findings and the spectral de-convolutions are in full agreement with this assignment. This component is indeed the strongest one at $\langle N \rangle = 18$ and $\langle N \rangle = 30$ (see Fig. 8.3 and Table 8.1).

The face component will occur with increasing cluster size. However, this can only be present, if the clusters have a sufficient size and there are no defects that lower their abundance. The number of nearest neighbors to face sites is known to be 9 independent on the structure of the clusters [148]. The shift is expected to be somewhat smaller than that of bulk sites, where the number of nearest neighbors is 12. The experimental results discussed above indicate, that the shift in Kr $3d$ binding energy will not be significantly different for face sites or sub-surface bulk sites. The number of nearest neighbors just reflects the major contribution to the shift in Kr $3d$ binding energy, but additional long-range contributions have to be considered, which further increase the binding energy shift in large clusters. This is the motivation to perform model calculations, which give a solid foundation for quantitative changes in Kr $3d$ binding energies.

8.2 Model Calculations

We have calculated the Kr $3d$ ionization energies of variable size clusters by using a model outlined in Refs. 144 and [153]. This is done by using the continuum dipole-dipole model, that describes core excitons in variable size clusters with perfect and defect cluster shapes (cf. Ref. 75).

The results are shown in Table 8.2, where it is shown that differently shaped and sized clusters have distinct shifts in Kr $3d$ ionization energy [142]. The calculations cover the most stable cluster structures in a wider size range than the experimental results in order to relate the present results to previous work [145]. Icosahedral cluster shapes as well as cuboctahedral clusters are calculated, since the latter ones are known to occur preferably in variable size rare gas clusters [76].

We have calculated Kr $3d$ ionization energies of clusters of irregular shape [142], such as Kr_{22} [149], and those containing defects, such as stacking faults, in order to estimate whether defects are of importance to the experimental results shown in Fig. 8.3.

The model calculations yield for the dimer the smallest shift in Kr $3d$ ionization energy

Table 8.2: Calculated shifts of the Kr $3d$ ionization energies relative to the atomic values in meV. [a] i: icosahedron, o: octahedron, t: tetrahedron. [b] -64 meV is calculated using the dipole approximation [130]. [c] The geometry is taken from Ref. [149]. [d] Other values in this range are: -367, -405, -452 meV.

cluster[a]	dimer	corner	edge	face	bulk
Kr_2	-19[b]	-	-	-	-
Kr_4 (t)	-	-405	-	-	-
Kr_{13}(i)	-	-410	-	-	-748
Kr_{22}[c]	-	-354 ...-470[d]	-	-	-785
Kr_{44}(o)	-	-350	-590	-	-995
Kr_{55}(i)	-	-490	-596	-	-1025
Kr_{146}(o)	-	-370	-661	-848	-1218
Kr_{147}(i)	-	-522	-586	-800	-1156

of -64 meV relative to the atomic value. In the case of small clusters and dimers one should take the electric field that is caused by the electric quadrupole moment of the Kr atom, $Q_{\alpha\alpha} \approx 18$ Debye·Å, into account. This value follows readily from Gaussian 98 *ab initio* calculations using a 6-311G* basis set. The quadrupole field $E^\alpha_{i,quadr}$ has to be added to the field of the core hole for a vertical transition $E^\alpha_{i,hole}$ in order to describe correctly the polarization caused by photoionization in clusters [142]. The resulting Cartesian component of the electric field α at the neutral atom i is given by:

$$
\begin{aligned}
E^\alpha_{i,0} &= E^\alpha_{i,hole} + E^\alpha_{i,quadr} \\
E^\alpha_{i,0} &= \frac{x^\alpha_i}{R^3_i} + \frac{5}{2}x^\alpha_i \sum_\beta \frac{Q_{\alpha\beta}(x^\beta_i)^2}{R^7_i} - \frac{Q_{\alpha\alpha}x^\alpha_i}{R^5_i},
\end{aligned}
$$

where R_i is the distance of the core hole to the corresponding neutral site, x^α_i is its Cartesian projection, and $Q_{\alpha,\beta}$ is the quadrupole tensor diagonal in the local coordinate system with one axis along the interatomic axis. This expression is substituted in eq. (4) of Ref. 144, which describes the variational condition for the minimum of the polarization energy U_N with respect to the induced dipole moment p^α_i. The solution for the induced dipole moments is obtained self-consistently. Using the equilibrium distance of Kr_2 of 4.03 Å [154], and the polarizability of atomic Kr of 2.48 Å^3 [155], one obtains a much smaller shift of -19 meV (cf. Table 8.2). By using other non-zero terms of the multipole expansion would lower the calculated shift even further so that there is excellent agreement with the experimental findings (cf. Table 8.1). Higher multipole moments will not significantly change the shifts in Kr $3d$ binding energies of larger clusters compared to the model outlined in Ref. [144]. This is because the multipole moments drop abruptly with distance from the excited center.

Also, we derive for tetrahedral Kr_4 a shift of -405 meV. This value corresponds to a coordination number of 3 and can be associated with corner sites [142]. Moreover, we have calculated the shifts in Kr $3d$ binding energy of corner sites of larger regularly shaped clusters (see Table 8.2), where both icosahedra and cuboctahedra are considered
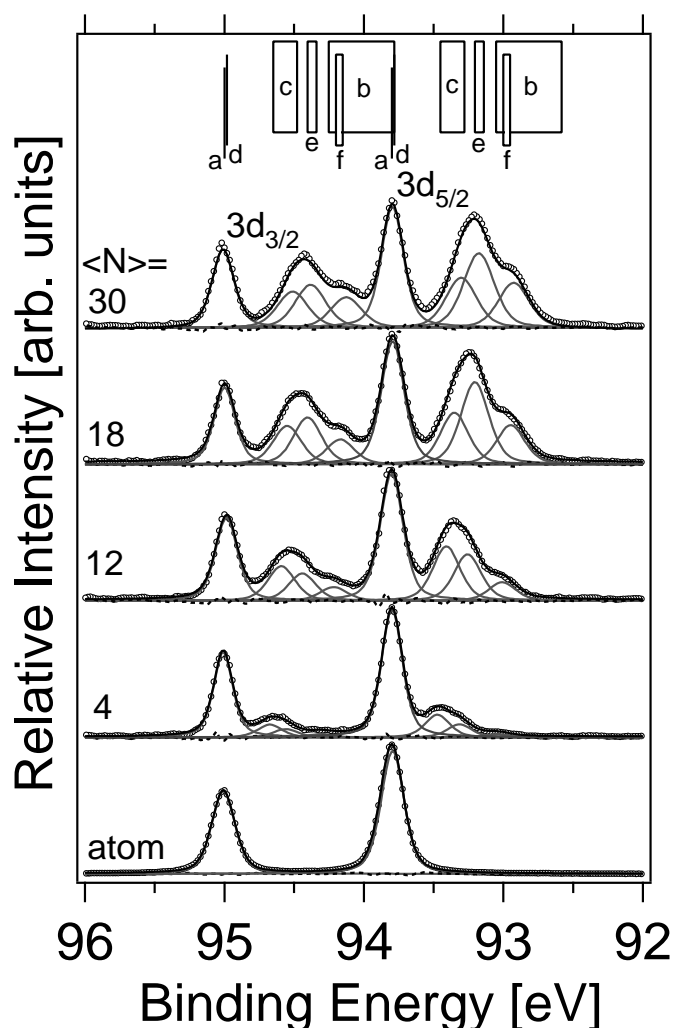
Figure 8.3: Comparison of Kr 3d photoelectron spectra of atomic Kr and variable size Kr clusters, where a variable fraction of the atomic component is subtracted (hollow circles). The sum of the spectral components (Voigt profiles, thin gray lines) is given by black lines. The difference between the fit and the experimental data is given by dashed lines near the baseline of each plot. The calculated energy regimes of different sites (a: atom, d: dimer, c: corner, e: edge, f: face, b: bulk) are shown at the top of the Figure.

as reasonable structures for modeling size and site effects in Kr clusters. These range from $\sim$ -350 meV to $\sim$ -520 meV, where the shift increases with cluster size. Such shift reflects an increase in the number of nearest neighbors around the core-ionized atom, as outlined above.

A hypothetical Kr_{22} cluster is also investigated as a prototype structure of small clusters, which is thought to represent an embryo for fast growth of fcc-moieties in jet expansions of rare gas clusters [149]. The smallest energy shifts are -354 meV and -367 meV, respectively. These are similar to the shifts in Kr 3d binding energy of corner sites with three nearest neighbors. Other values of higher coordinated sites are observed, as well, where -405 meV, -452 meV, and 470 meV are observed. This indicates that corner sites

of irregularly shaped clusters undergo characteristic energy shifts in the Kr $3d$ ionization regime.

A similar behavior is derived for edge and face sites of larger clusters, which yield narrower regimes than edge sites, ranging from $\sim$ -590 meV to $\sim$ -660 meV and $\sim$ -800 meV to $\sim$ -850 meV, respectively (see Table 8.2). Both value ranges find also resemblance in the experimental results. This is another piece of evidence that the spectral de-convolution of the experimental results is reasonable and underlines the physically meaningful assignment [142].

Size effects in the unoccupied electronic states were reported previously [75], where edge sites are found to be dominant in small clusters ($\langle N \rangle \leq 30$) and bulk sites only occur with appreciable intensity at $\langle N \rangle \geq 150$. Clusters with detects or imperfect shapes, e.g. with stacking faults, are expected to show an enhanced edge component, whereas the intensity of face sites should become weaker. This follows from the present model calculations, where surface-bound sites at stacking faults yield the same shift in $3d$ ionization energy as edge sites of perfectly shaped clusters (not included in Table 8.2).

Finally, the widest size range of variable size clusters is covered by bulk sites, where the $3d$ ionization energies are expected to be shifted between $\sim$-750 meV and $\sim$-1220 meV (see Table 8.2). This size range goes beyond the present experimental material, but clearly connects the present work to previous experimental results on large Kr clusters [145]. The results shows a strong size-dependence of $3d$ ionization energies of atoms that are either bound in a sub-surface layer or deep in the interior of a cluster. This also shows that the value ranges of face sites and bulk sites overlap, which explains the ambiguous assignment of face/bulk sites given in Table 8.1.

Bulk sites are assigned in previous work to components that are shifted by -950 meV to -1100 meV [145]. This is in full agreement with the results from the present model calculations [142].

In conclusion, we have investigated $3d$ ionization of small Kr clusters. Results from model calculations indicate that different geometric sites can be clearly distinguished from each other by their substantial shift in Kr $3d$ ionization energy, though the dimer shows almost the same Kr $3d$ ionization energy as the free atom. A comparison with the experimental results indicates that there is resemblance with the model calculations, even though close lying ionization energies are blended and require de-convolutions of the experimental spectra.

We have obtained general agreement between experiments and model calculations, which also supports the conclusion that one can investigate site-selective photoionization processes occurring in homogeneous Van der Waals clusters. The smallest of these shifts is due to corner sites of small clusters, followed by edge and face/bulk sites. This reflects qualitatively the increase in the number of nearest neighbors [148], and consequently the increase in polarization screening. However, the model calculations also indicate that there is no simple correlation between the number of nearest neighbors and core ionization energies, especially in the regime of the dimer and small clusters. This is a result of long-range contributions that lower the shift in Kr $3d$ ionization energy of the dimer. We note that face and bulk sites cannot be clearly distinguished from each other since their $3d$ ionization energies occur in the same energy regime (cf. Table 8.2 and Fig. 8.3). The occurrence of face and bulk sites goes parallel, where in large clusters the bulk component is expected to grow considerably in intensity [145].

Chapter 9

Photoelectron Line Shape of Free van der Waals Clusters

9.1   PCI in variable size Ar clusters

Post-collision interaction (PCI) is investigated in free argon clusters near the Ar $2p$ ionization energy, where the size regime of clusters with an average size ≤ 40 is investigated. We perform calculations on ionization energies of small argon clusters by using a classical dipole-dipole model. We find the occurrence of the Ar dimer in the experimental data and the $2p$ ionization energy agrees with the calculated value. The ionization energies of other surface sites are calculated as well. These are also in agreement with the experimental results. It is found that the peak shapes of the $2p$ ionizations become asymmetric in the atom and in clusters when the photon energy is set close to the Ar $2p$ ionization thresholds. The line shapes of the dimer and various surface sites in the clusters are less asymmetric than the atomic lines at a given photon energy. This behavior is rationalized using a classical PCI model. The results are compared to previous work on condensed rare gases, indicating a similar behavior.

Photoionization from core levels provides element-specific information on the electronic structure of atoms, molecules, clusters, and condensed matter. When the excitation energy is lowered and reaches the regime near the core-absorption edge, one observes significant and asymmetric line broadening in photoelectron and Auger spectra. The occurrence of asymmetric peak shapes is related to post-collision interaction (PCI) [96, 118]. In a classical description, the photoelectron is overtaken by the fast Auger electron. This leads to a change of the Coulomb interaction between the photoelectron, Auger electron, and single and double ion cores, so that the photoelectron looses kinetic energy, and the Auger electron gains energy. As a result, the lineshapes of the photoelectron spectra and Auger spectra are asymmetrically broadened. In contrast, at the higher excitation energy in the core ionization continuum, the photoelectron has sufficient kinetic energy so that the energy exchange between the Auger electron and the photoelectron is small. In this case the photoelectron lineshapes are symmetric, since the classical overtaking point is too far away from the core-excited center. This classical model has been shown to predict successfully the asymmetric broadening of photoelectron and Auger lines of atoms [118]. The interpretation of line shape in photoelectron spectra is further complicated since they contain contributions from all Auger decay channels [156].

The post-collision interaction effect in isolated atoms has been widely investigated both theoretically [114, 119, 156] and experimentally [101, 103, 108]. PCI is investigated by measuring the threshold electron yield (TPES) as a function of photon energy [108, 157, 158], or coincidences with the associated atomic cation [104, 159]. Recently, the dynamics of the slow photoelectron was investigated, where the occurrence of peaks below the inner shell threshold was explained by PCI distortions, which have been attributed to the autoionizing process [109].

A detailed theoretical model of PCI in solids with realistic wave functions and decay rates has been developed before [131, 160]. It considers the dynamics of lopsided energy sharing between the photoelectron and an Auger electron in solids. The model is based on an optical response theory, where both the attraction around the core holes and the electron-electron repulsion are considered. Two different models are adopted, which are an *s*-wave and a cubic lattice model [131, 160]. This explains why PCI is strongly affected by the local electronic surroundings near the core-excited atom.

Considerably less information on PCI is reported for condensed matter as well as clusters. There are obvious reasons for this, since the photoelectron signal of the low kinetic energy photoelectron is superimposed to a substantial background of inelastically scattered electrons. This background can be controlled in variable size clusters, where the surface-to-bulk ratio is adjusted as a function of cluster size.

Zero kinetic energy (ZEKE) photoelectron spectra of atomic argon and argon clusters have been investigated before in the Ar $2p$ regime [161]. Photoionization from $2p$-excited argon clusters have been investigated before [68, 162]. At 310 eV photon energy no evidence for PCI has been found [162]. Furthermore, other sources contributing to asymmetric peak shapes besides PCI, which are caused by experimental artifacts from electrostatic electron energy analyzers, have been discussed before for Ar $2p$-excited argon clusters [68]. Simulation on the photoelectron spectra of argon and xenon clusters by using molecular dynamics have been investigated by Amar *et al.* [144]. They found a binding energy shift relative to the isolated atom, which is of the order of -0.5 – -1.5 eV. This due to cluster polarization.

Recently, PCI in condensed neon has been investigated by Romberg *et al.* [163], which is dominated by bulk sites. They found that the inner K-shell ionization threshold of solid neon is equal or slightly larger than that of neon gas at 870.3 eV [164], whereas the value for the surface is lower by 1 eV. Evidently, polarization screening is weak in the bulk of solid neon.

The motivation for the present work is to analyze in small clusters the photoelectron spectra recorded at different excitation energies in the Ar $2p$ continuum. We present results from calculations on Ar $2p$ ionization energies of different geometric sties and compares these to the experimental results. Further, we present in this work results on photoelectron spectra recorded between 255.5 eV and 310.0 eV, in order to find at which photon energy evidence for PCI can be observed in variable size clusters. This allows us to investigate systematically changes in asymmetry as a result of PCI of different geometrical sites, which are separated due to their substantial chemical shifts [68]. The experimental results are assigned by using a simple classical model, which turns out to be suitable, similar to earlier work on atoms [118].
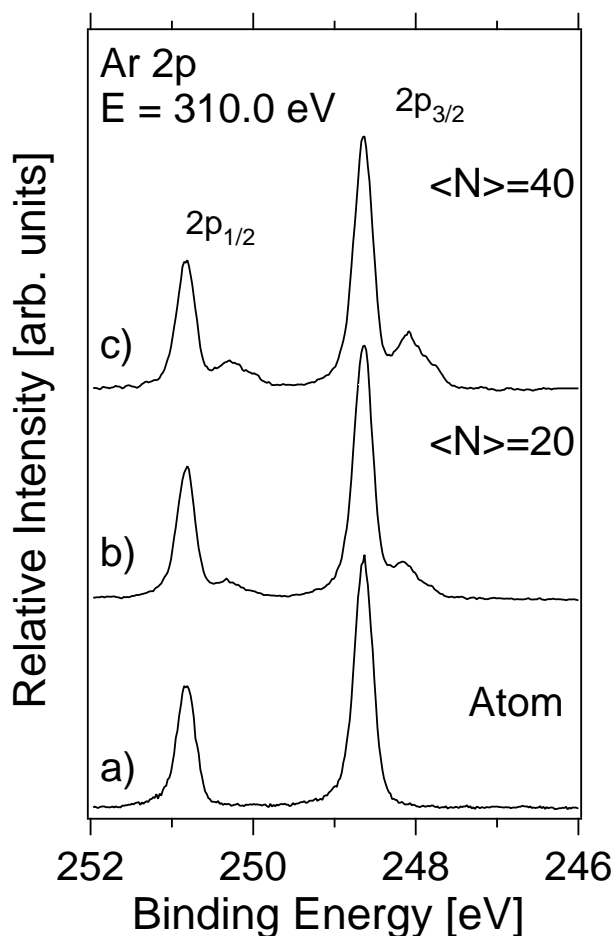
Figure 9.1: Ar $2p$ photoelectron spectra of (a) atomic Ar, (b) from a cluster jet with an average cluster size of $\langle N \rangle = 20$, and (c) a cluster jet with $\langle N \rangle = 40$. The spectra are recorded at $E = 310.0$ eV photon energy.

9.1.1   Experimental results

Two different cluster sizes are investigated: $\langle N \rangle = 20$ and $\langle N \rangle = 40$. Fig. 9.1 shows a comparison between the atomic and cluster photoelectron spectra recorded at 310.0 eV. This photon energy is located about 60 eV above the Ar $2p$ ionization threshold in the Ar $2p$ continuum.

One observes in all spectra shown in Fig. 9.1 a dominant contribution from the atom, since the average cluster size is small so that the jet consists mostly of atoms. This is because mixing ratio of dimers or small clusters is weak compared to the dominant atomic signal in the low $\langle N \rangle$ regime under investigation. The spectral regime that is covered by clusters is broader than the atomic signal. This indicates that the binding energies of different sites in variable size clusters are spread over a larger binding energy regime, as observed in earlier work [68, 143].

A subtraction of the atomic component is shown in Fig. 9.2 ($E = 310.0$ eV). Fig. 9.2 clearly shows that there is a component in cluster spectra that is not shifted relative to the atomic component. It is assigned to dimers, similar to previous work on Kr $3d$
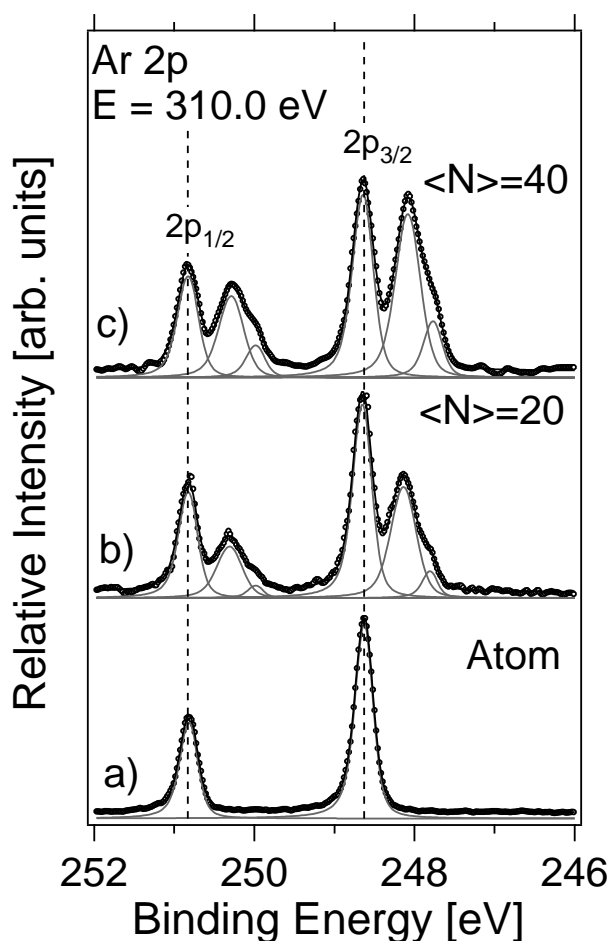
Figure 9.2: Ar 2p photoelectron spectra of (a) atomic Ar, (b) from a cluster jet with an average cluster size of ⟨N⟩ = 20, and (c) a cluster jet with ⟨N⟩ = 40. The spectra were recorded at E = 310.0 eV photon energy. The experimental results (hollow circles) are obtained from a subtraction of the atomic component from the raw data shown in Fig. 9.1. The full lines correspond to a spectral de-convolution, where the sum of all components is indicated by a thick black line. The gray lines correspond to the individual PCI profiles.

photoionization experiments on small Kr clusters [142]. This is also in general agreement with the model calculations outlined above (see Table 7.1 from chapter 7).

Binding energies of surface sites are known to be shifted by ca. 0.5 eV, whereas bulk sites show a shift of about 1 eV, whereas bulk sites show a shift of about -1 eV [68, 130]. This is also observed in this work for surface sites and allows us a simple distinction between different geometric sites in clusters. This is because recent work on small krypton clusters has also shown, that different surface sites, such as corner, edge, and face sites, show slightly different core ionization energies [142]. Similar results are discussed below by using the same approach as in previous work [142].

Additional experiments have been performed at lower excitation energy (255.5 eV), which is close to the Ar 2p ionization thresholds. The results are similar to those obtained from experiments at 310.0 eV, as shown in Figs. 9.3 and 9.4. A comparison of Figs. 9.1 and 9.2 and Figs. 9.3 and 9.4 indicates that all peak shapes become asymmetric, if the

photon energy is close to the Ar $2p$-threshold. This asymmetric broadening already gives evidence for PCI in the raw experimental spectra, similar to earlier work on atoms [96, 114, 118, 119, 126]. Changes in peak shape give information on the PCI process in variable size matter. Furthermore, the core ionization energies cannot be correctly determined from the maxima of the photoelectron bands, if the excitation energy is close to the core ionization energy. This is because the PCI process leads to shifts of the peak maxima to slightly higher binding energies, which are typically shifted by $\sim< 60$ meV relative to excitations far above the core ionization energies (see next sections).

In the following, I will compare the experimental results with the results from model calculations on $2p$ ionization energies of geometric sites in argon clusters from chapter 7. I will discuss suitable PCI profiles of clusters, apply these for spectral de-convolutions of the experimental results shown in Figs. 9.2 and 9.4, and extract from these the core ionization energies and asymmetry parameters of different geometrical sites, which yield a measure for the strength of PCI of cluster-bound atoms. Finally, we derive the energy positions of different surface and bulk components that are used for a comparison with the model calculations.

9.1.2 PCI-line shape analysis

The spectra shown in Figs. 9.2 and 9.4 consist of blended signals. Therefore, it is required to de-convolute the different contributions by using plausible line shapes. The experimental photoelectron spectra of atomic Ar have been fitted by using the model of van der Straten [118], which is expected to be valid even close to the Ar $2p$ threshold. We have also convoluted the line profiles with a Gaussian in order to account for the experimental resolution. Furthermore, in the case of clusters the de-convolution of the experimental spectra also requires to account for changes in the Coulomb potential of the initial and final state. This takes into account the relative permeability of the dielectric medium in the theories of Armen *et al.*[110] and Helenehund *et al.*[114] and using the dielectric constant of solid argon $\varepsilon_r = 1.70$ [117]. For details see chapter 6.

The lifetime of the core hole is assumed to be unchanged for the atom and clusters, corresponding to a Lorentzian width of 118 meV [146]. This is reasonable since the core hole is expected to be negligibly affected by neighbors of the excited atom within a cluster. Gaussian contributions come from the limited experimental resolution of the photoelectron spectrometer and the photon bandwidth, corresponding to a Gaussian width of 50–70 meV. Further, other line broadening mechanisms may contribute to the Gaussian width, such as phonon-broadening, the occurrence of different cluster sizes in the jet, and the different screening properties of the atomic sites in clusters, which are related to the number of nearest neighbors (cf. [142]). The total width of the Gaussian contributions is shown in Table 9.1.

Björneholm *et al.*[68] discussed the variation of the experimental $2p_{3/2}$ binding energies of surface sites in Ar clusters as a result of cluster size dependent changes in the effective numbers of nearest neighbors in surface sites. In their model, the number of the nearest neighbors varies from 5 to 8 for surface sites, which is consistent with commonly assumed cluster geometries with icosahedral or cuboctahedral shape.[130] The present results are in general consistent with previous work of Björneholm *et al.* [68, 130]. However, this work shows that different geometric sites as well as the dimer can be clearly distinguished.
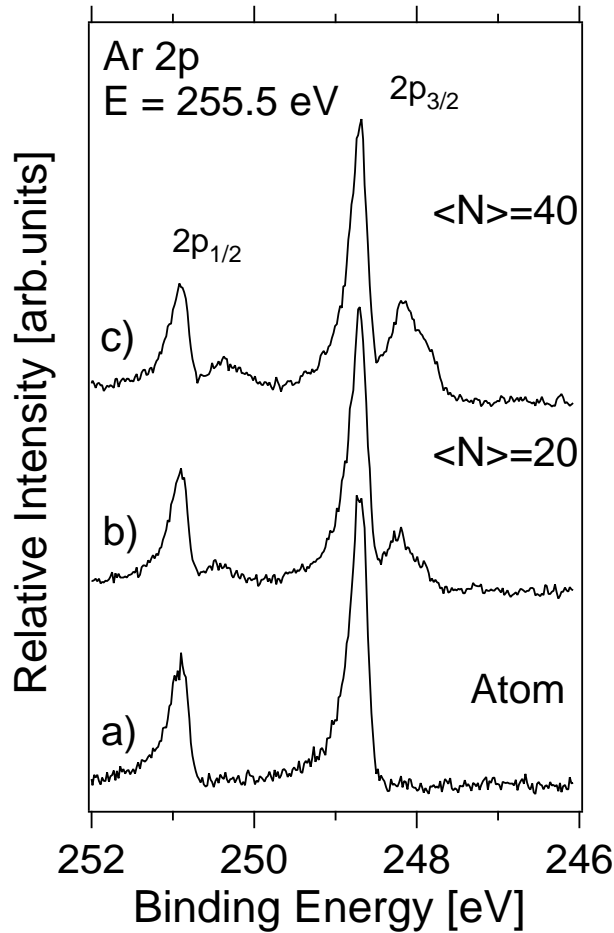
Figure 9.3: Ar $2p$ photoelectron spectra of (a) atomic Ar, (b) from a cluster jet with an average cluster size of $\langle N \rangle = 20$, and (c) a cluster jet with $\langle N \rangle = 40$. The spectra are recorded at $E = 255.5$ eV photon energy.

This is similar to recent work on Kr clusters [142].

The experimental findings show that the Gaussian width of atomic and dimer components is almost the same for both cluster sizes $\langle N \rangle = 20$, $\langle N \rangle = 40$. (Table 9.1a). The shift observed in the surface and sulk sites is due to the combined effect of post collision interaction and the polarization screening. (table 9.2a). The surface component is almost the same for both cluster sizes; an increase for the bulk component for $\langle N \rangle = 40$ is observed.

The fitting parameters of the experimental results are peak intensities, peak positions, and the Gaussian and the Lorentzian line widths. The same widths were used for both spin–orbit components $2p_{3/2}$ and $2p_{1/2}$. Note that the PCI profiles are different for the spin–orbit components, since they occur at different energies above the Ar $2p$ threshold. As a result, there is always higher asymmetry of the $2p_{1/2}$-component (see Table 9.1).

The results of the curve fitting procedure outlined above are compiled in Table 9.1. The total Gaussian width of the atomic and dimer components is found to be of the order of 190 meV at 310.0 eV.

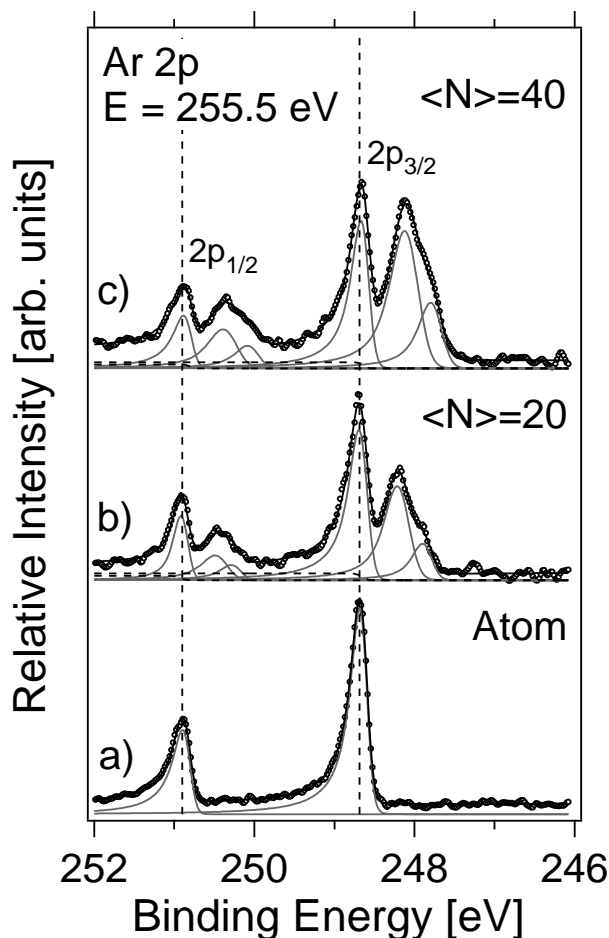Distinct changes in peak shape are observed in the spectra recorded at 255.5 eV,

Figure 9.4: Ar $2p$ photoelectron spectra of (a) atomic Ar, (b) from a cluster jet with an average cluster size of $\langle N \rangle = 20$, and (c) a cluster jet with $\langle N \rangle = 40$. The experimental results (hollow circles) are obtained from the subtraction of the atomic component from the raw data shown in Fig. 9.3. The full lines correspond to a spectral de-convolution, where the sum of all components is indicated by a thick black line. The gray lines correspond to the individual PCI profiles. The long dashed lines correspond to Victoreen functions.

compared to those recorded at 310.0 eV. There is enhanced electron intensity at high binding energies, which corresponds to low kinetic energy electrons (cf. Fig. 9.4, (c)). These occur especially in the case of clusters as a result of inelastic scattering processes. It is known that such processes occur preferably in the bulk interior of clusters [161]. Note that there is also enhanced intensity in the case of the atom in the same binding energy regime (cf. Fig. 9.4(a)). This is likely a result of imperfect energy selection of low kinetic energy photoelectrons. Minor intensity of such low-energy electrons can occur in the Rydberg regime as well as in the Ar $2p$-continuum from double or multiple Auger and resonant shake-off processes [157, 165]. This enhanced intensity of low kinetic energy electrons occurring near threshold may be modeled by a constantly sloped background across the Ar 2p ionization regime [166]. However, it appears to be more realistic to model this process by a step function [161], since there is distinctly lower intensity below

Table 9.1: Gaussian widths and asymmetries ξ obtained from the de-convolution of experimental photoelectron spectra of argon and argon clusters in the Ar $2p$ regime (Ar $2p_{3/2}$ and Ar $2p_{1/2}$): (a) $E_1 = 310.0$ eV (shown in Fig. 9.2) and (b) $E_1 = 255.5$ eV (shown in Fig. 9.4). The Lorentzian width is assumed to be 118 meV in all spectra, which is a result of the core-hole lifetime. The error limits are estimated to be ± 15 meV for Gaussian widths and ± 0.02 for asymmetries.

a) $E_1 = 310.0$ eV

$\langle N \rangle$	Component	Gaussian [meV]	ξ $2p_{3/2}$	ξ $2p_{1/2}$
	Atom	190	0.170	0.196
	Dimer	190	0.142	0.151
20	Surface	298	0.118	0.122
	Bulk	147	0.102	0.109
	Dimer	190	0.141	0.156
40	Surface	300	0.112	0.125
	Bulk	180	0.102	0.113

b) $E_1 = 255.5$ eV

$\langle N \rangle$	Component	Gaussian [meV]	ξ $2p_{3/2}$	ξ $2p_{1/2}$
	Atom	140	0.976	1.329
	Dimer	140	0.971	1.291
20	Surface	230	0.920	1.215
	Bulk	180	0.870	1.192
	Dimer	140	0.971	1.275
40	Surface	290	0.934	1.241
	Bulk	223	0.903	1.176

the $2p$-edge, i.e. in the lower binding energy regime. The ionization cross section above the $2p$-edge is modeled by a Victoreen function for each spin–orbit component [167]. Further, a Gaussian broadening, which corresponds to the instrumental bandwidth of the spectrometer is considered. The sum of these components model the pre-edge background, the location of the edge-jump, and the intensity of low kinetic energy electrons at higher binding energy. A careful analysis of the data shows that the presence of Victoreen functions does not modify the asymmetry parameters, as will be outlined in greater detail below. Moreover, we use the atomic core hole lifetime [146], assuming that this quantity is constant in the atom and in clusters (see above).

The results of the curve fitting procedure outlined above are compiled in Table 9.1. There, it is not attempted to distinguish the different surface sites, rather than to group them together and compare them to bulk sites, similar to earlier work [68, 130, 168]. This implies that there is more broadening of the surface sites than for bulk sites, that occurs especially in the Gaussian broadening (see Table 9.1). The surface component of small clusters ($\langle N \rangle = 20$) is governed by corner sites, whereas at $\langle N \rangle = 40$ edge sites are dominating (cf. Ref. 75, 142. The surface component can, however, be de-convoluted into individual surface sites, as outlined in recent work [142].

Table 9.2: Experimental Ar $2p$ binding energies of atomic argon and shifts of argon clusters in the Ar $2p$ regime given in meV. (a) Atomic Ar $2p$ ionization energies, as deduced from the experimental spectra; (b) absolute shift of the $2p_{3/2}$ spin–orbit component relative to the atomic $2p$ ionization energy; (c) absolute shift of the $2p_{1/2}$ spin–orbit component relative to the atomic $2p$ ionization energy. The values in parentheses correspond to the relative intensities. The error limits are estimated to be ±15 meV.

a) Atom

	Binding Energy [eV]	
Photon Energy [eV]	$2p_{3/2}$	$2p_{1/2}$
310.0	248.620	250.807
255.5	248.659	250.867

b) PCI shifts in clusters at $E = 310.0$ eV

Edge	$\langle N \rangle$	Dimer	Surface	Bulk
$2p_{3/2}$	20	-0.021 (58.4%)	-0.485 (33.6%)	-0.803 (8.0%)
	40	-0.011 (45.4%)	-0.538 (40.6%)	-0.842 (14.0%)
$2p_{1/2}$	20	-0.009 (62.4%)	-0.501 (30.3%)	-0.814 (7.3%)
	40	-0.009 (47.1%)	-0.521 (37.9%)	-0.815 (15.0%)

c) PCI shifts in clusters at $E = 255.5$ eV

Edge	$\langle N \rangle$	Dimer	Surface	Bulk
$2p_{3/2}$	20	-0.003 (53.6%)	-0.477 (33.6%)	-0.772 (12.8%)
	40	-0.006 (42.1%)	-0.548 (39.2%)	-0.849 (18.7%)
$2p_{1/2}$	20	-0.016 (61.7%)	-0.419 (23.8%)	-0.602 (14.6%)
	40	-0.001 (48.8%)	-0.507 (32.5%)	-0.789 (18.7%)

The total Gaussian width of the atomic and dimer components is found to be of the order of 190 meV at 310.0 eV. This quantity is decreased, if lower kinetic energy electrons are analyzed at $E = 255.5$ eV. Therefore, it is anticipated that a substantial portion of the Gaussian width is due to the energy resolution of the electron analyzer. This is also consistent with results from related work on Kr clusters in Kr $3d$ regime [169], where it is also found that the Gaussian width is lowered, if the excitation energy is set close to the threshold.

The Gaussian widths of both atomic and dimer fine structure components are found to be 140 meV at 255.5 eV (cf. Table 9.1(b)). For $\langle N \rangle = 20$ the Gaussian widths of the surface sites is 230 meV and for $\langle N \rangle = 40$ it is increased to 290 meV, whereas the Gaussian widths of the bulk sites vary between 180 meV for $\langle N \rangle = 20$ and 223 meV for $\langle N \rangle = 40$ (cf. Table 9.1). The Gaussian width increases for bulk sites, when the photon energy is lowered to 255.5 eV. This is consistent with results reported by Romberg *et al.* on solid Ar [163]. It is rationalized by phonon coupling and vibrational line broadening. Similarly, the present experimental data contain contributions to the Gaussian width from both the experimental resolution and various broadening mechanisms such as phonons, the distribution of cluster sizes, and the different screening strengths for different positions
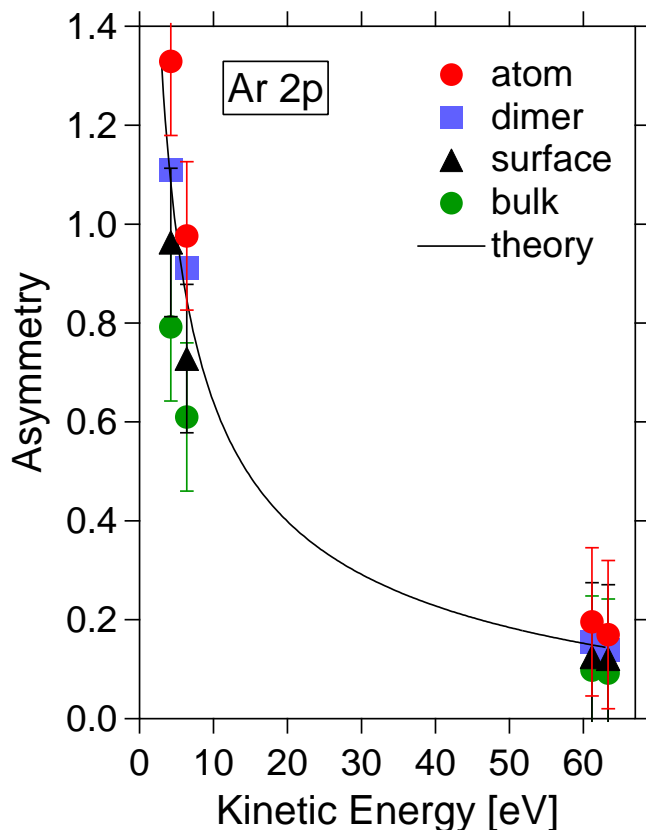
Figure 9.5: The experimental PCI asymmetry as function of the kinetic energy. Hollow symbols correspond to the Ar $2p_{1/2}$ component, full symbols correspond to the Ar $2p_{3/2}$ component. The theoretical curve is shown as a full line.

in the cluster [130].

The PCI line shape formula, which is described above, is based on an effective charge Q, an angle independent quantity [117]. The dynamical charge Q_d in the analytical line shape formula takes into account the "no-passing effect" in PCI during the Auger transition following near threshold photoionization [106, 127]. This was presented in more detail in chapter 6.

The asymmetry parameter of the spin–orbit components is found to be systematically increased for the $2p_{1/2}$-component (see Table 9.1). For a given cluster size there are systematic changes: The asymmetry of the atomic component and the dimer are assumed to be similar to each other. The asymmetry parameter decreases systematically from the atom via surface sites to bulk sites, as shown in Table 9.1. These changes are interpreted by a simple model, taking the electron mean free path in clusters and solid into account. The values of the asymmetry parameter are plotted as function of kinetic energy in Fig. 9.5.

Comparing the spectra at 310.0 eV and 255.5 eV photon energy (cf. Figs. 9.2 and 9.4) we clearly observe that the lines of surface sites are getting asymmetric as the photon energy is lowered. This can be understood using the following oversimplified classical model: In the Ar $2p$ continuum the kinetic energy of the Auger electrons is observed between ca. 150 and 215 eV [170, 171]. Assuming that the kinetic energy of the Auger

electron is ca. 200 eV and the kinetic energy of the photoelectron varies between 1 eV and 60 eV, corresponding to excitation energies between 250 and 310 eV, one can calculate the classical distance where the Auger electron overtakes the photoelectron. One obtains from this simple assumption that overtaking occurs for a 2 eV photoelectron at a distance of ∼6.5 nm from the excited atom. A 5 eV photoelectron is overtaken at 9.6 nm. This distance increases for a 60 eV photoelectron to 57 nm. These distances correspond to 17, 25 and 152 nearest neighbor distances using the lattice constant of solid argon, respectively (3.72 Å [172]). The cluster size regime under investigation has a radius of less than 2–3 nearest neighbor distances. Thus, the average distance the photoelectron travels through the cluster is much smaller than the overtaking distance, so that the classical overtaking would occur in the vacuum, similar to the atom. Outside the cluster screening is not effective. As a result, this contribution cannot influences the PCI line asymmetry, since the energy exchange between the Auger and the photoelectron takes place outside the cluster. The electron mean free path of solid argon has been investigated by Plenkiewicz *et al.* [173]. For electron energies of the order of 4–6 eV, this quantity ranges between 5 and 50 Å. As a result, the probability of photoelectrons undergoing inelastic scattering within the cluster cannot be neglected. Evidently, these scattering processes may also modify the experimental line shapes, leading besides asymmetry to line broadening and enhanced intensity in the 2p continuum. Therefore, line broadening is another issue, that is influenced by the local cluster environment via inelastic scattering processes of the photoelectron and/or Auger electrons. Consequently, it is observed that in the regime of small clusters the line shapes of surface sites are more asymmetric than those of bulk sites. This is clearly evident from the results shown in Table 9.1. Similar results were reported by Kassühlke *et al.* [174], who investigated PCI-induced effects in threshold and near-threshold photoelectron spectra of argon multilayers. Asymmetric line shapes in experimental Ar 2p photoelectron spectra of physisorbed argon on Rb(001) surfaces have been observed [174]. These indicate a larger shift by a factor of three for the Auger lines than observed before for photoelectrons [175].

As the atomic PCI requires the final state ion to remain unscreened, it is surprising that PCI occurs at all in metallic solids [176]. When an Auger process occurs in a solid, screening of the charges can substantially modify the PCI shift. In a metal, all charges are screened by delocalized valence band electrons in a very short distance, which his of the order of an atomic radius. Thus, the long range Coulomb interaction between the charges is significantly reduced. In an insulator, such as argon, where screening is merely efficient, the long range dielectric polarization dominates without charge transfer. Thus, the PCI shift due to the Coulomb interaction can be much larger than in a metal [177, 178].

9.1.3   Comparison with model results

The PCI line shapes for the different components shown in Figs. 9.2 and 9.4 and Table 9.1 are suitable to determine the binding energies of the 2p electrons in Ar clusters. These are compiled in Table 9.2 along with their relative intensities. Table 9.2(a) shows that at 310.0 eV one obtains the atomic 2p binding energies that are comparable with results from previous work [168]. All raw data show that there are slightly asymmetric line profiles already ca. 60 eV above the Ar 2p threshold ($E = 310.0$ eV). We have calculated the PCI shift for 60 eV excess energy, yielding a PCI shift of the order of 30 meV. Near the Ar

2p-threshold ($E = 255.5$ eV) the kinetic energy of the photoelectrons is lowered to 6.42 and 4.22 eV, respectively. This corresponds to a calculated PCI shift for both spin–orbit components of 85 meV and 105 meV, respectively.

Somewhat lower shifts in Ar 2p binding energy are expected to occur for the dimer, as well as the surface and bulk components, which is reflected by a decrease in asymmetry parameter. However, they cannot be compared to reference values since no experimental work on argon clusters is reported to the best of our knowledge, where the excitation energy was chosen high enough to exclude entirely PCI. This is because earlier results reported binding energies that were recorded at considerably lower excitation or similar energy than in this work [68, 130, 143, 161]. From these works, which are in general agreement with the present work, one can derive reliably atom to cluster shifts, but not the absolute binding energy values.

It is expected that PCI tends to decrease the shift in binding energy, since the maxima of photoelectron bands are shifted to higher binding energy. The magnitude of PCI depends on the kinetic energy of the photoelectron. It has been noticed that at high excess energies of the photoelectron the PCI shift deviates from the prediction by a shake-down model [98, 179] or a semiclassical model [95, 96, 170, 176]. Both models give a shift that is proportional to the inverse of the square root of the excess energy.

The PCI shifts of surface and bulk sites are not clearly observed, if one compares the results recorded at 310.0 and 255.5 eV, as compiled in Table 9.2(b) and (c). The surface sites show for the dominant 2$p_{3/2}$-component an almost negligible shift within the error limits (± 15 meV). This may be at least in part rationalized by the decreased asymmetry parameter, indicating that PCI is weaker in surface bound sites. Similar results are obtained from the bulk sites. These are, however, much weaker in intensity in the low $\langle N \rangle$-regime, so that no quantitative conclusions can drawn for this component. The weak 2$p_{1/2}$-component shows at $\langle N \rangle = 20$ large shifts for both the surface and the bulk components at 255.5 eV. This is assumed to be not fully reliable because of the weak intensity of these components.

In conclusion, we have investigated the photoionization and the line shapes of photoelectron spectra of Ar 2p-excited argon clusters. The size regime was set to $\langle N \rangle = 20$ and $\langle N \rangle = 40$, respectively. These clusters consist primarily of surface sites and only to a minor fraction of bulk sites. We have observed a smaller asymmetry in peak shape for surface sites compared to the neat atom. This asymmetry is found to be even smaller for bulk sites, especially when the photon energy is lowered to a regime that is close to the Ar 2p ionization threshold. These results are consistent with the recent work on condensed rare gases [163]. A simple model is developed that is based on the classical overtaking distance of the photoelectron by the Auger electron and changes of the electron mean free path in argon clusters and solid, which qualitatively explain the present results. We note that the present considerations are applicable to all weakly bound atomic and molecular van der Waals systems.

The experimental result suggest that core level photoionization in small clusters shows distinct similarities compared to the free atom, this is especially true since the electronic relaxation via the Auger decay that is essential to PCI comes mostly from the surface region of a clusters. However, a sensitive parameter is the asymmetry, which is shown to decrease from the atom via surface sites to the bulk. Therefore, the present experiments give first evidence for the magnitude of the deviation from PCI models on atomic systems.

In 2p-excited argon clusters, the localized character of the core excitation severely limits the delocalization of the core electron during the excited state lifetime, which is consistent a localized excitation. The weak van der Waals bond in Ar clusters also enhances the localized character of the excitation. There is also weak interaction with distant sites. This is due to the anisotropic charge distribution around the 2p-excited Ar atom, which polarizes the surrounding medium. The energy shift roughly varies linearly with the number of the nearest neighbors. This is consistent with the assignment of the energy shifts due to the confinement of the 2p orbitals by the argon neighbors. The confinement increases with the number of nearest neighbors, distant neighbor shells do not significantly contribute to this confinement. However, we note that the linear variation of the energy shift with the nearest neighbors is a fairly crude approximation and distant neighbor shells appear to contribute in different ways to the energy shift.

Chapter 10

PCI in small Kr clusters

Post collision interaction (PCI) is investigated in free krypton clusters near the Kr $3d$ ionization energy, where the size regime of clusters with an average size ≤ 30 is investigated. It is found that the peak shapes of the $3d$ ionization become asymmetric in the atom and in clusters, but the line shapes of the dimer and different surface sites in the clusters are less asymmetric than the atomic lines at a given photon energy. This behavior is rationalized using a classical PCI model. The results are compared to previous work on condensed rare gases, indicating a similar behavior.

Recently, PCI in condensed rare gases has been investigated, are evidently dominated by bulk sites [163]. Evidently, there are changes in the line shape of PCI profiles, when the absorbing atom has nearest neighbors. This is the motivation for the present work, where we report results on 3d excited krypton clusters. This system has been investigated before, showing site-selective excitation and photoionization [75, 142]. We include these recent results for a comparison in the excitation regime as low as 2.72 eV above the Kr 3d threshold.

10.1 Experimental results and discussion

Fig. 10.1 shows a series of raw photoelectron spectra of atomic Kr $3d$ recorded at different photon energies. Fig. 10.1(a) has been recorded at 140.45 eV, Fig. 10.1(b) at 102.92 eV, Fig. 10.1(c) at 99.8 eV and Fig. 10.1(d) at 97.72 eV. In Kr two strong series of resonances have been observed $3d_{5/2,3/2} \rightarrow np$, $n = 5, 6, \ldots$ [180]. Relaxation of a $3d$ can be classified according to the role played by the Rydberg electron: the principal quantum number, n, of the Rydberg electron may increase (shake up), decrease (shake down) or remain the same (spectator). If the Rydberg electron is excited into the continuum during relaxation then it is said to have been shaken off. Photoionization of the 3d inner shell have been studied by measuring the emitted electrons with energies from 0 to 3 eV and from 0 to 12 eV, respectively by Cubric *et. al* [181].

Fig. 10.2 shows a series of raw photoelectron spectra for a cluster target at $\langle N \rangle = 30$, recorded at different photon energies. Fig. 10.2(a) has been recorded at 140.45 eV, Fig. 10.2(b) at 102.92 eV, Fig. 10.2(c) at 99.8 eV, and Fig. 10.2(d) at 97.72 eV. The raw spectra already show that the peak shapes become increasingly asymmetric as a result of PCI, since these photon energies are close to the Kr 3d ionization energies (93.8 eV for Kr $3d_{5/2}$ and 95.0 eV for Kr $3d_{3/2}$, respectively [145, 146]). The binding energy scale is
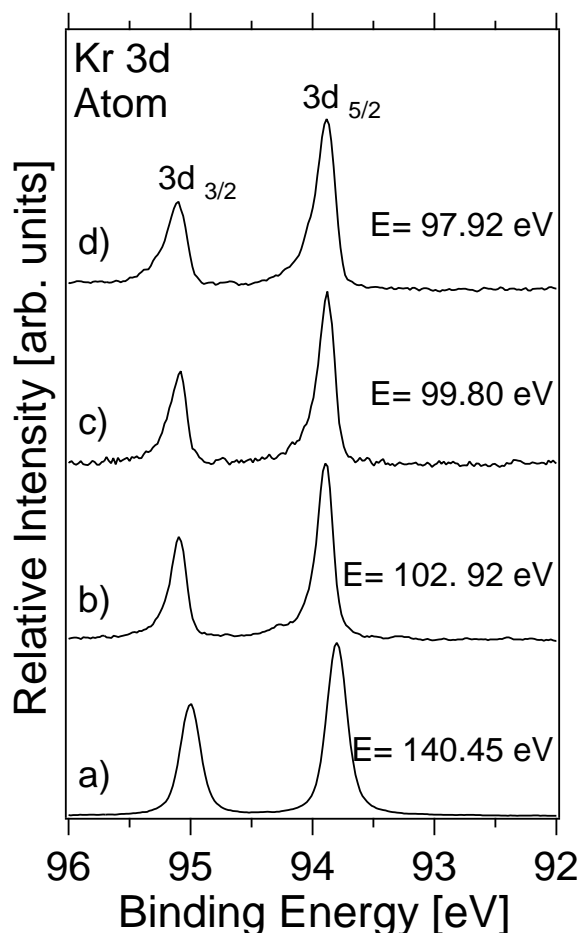
Figure 10.1: Kr 3d photoelectron spectra of raw krypton atoms recorded at different photon energies: a) E=140.45 eV; b) E=102.92 eV; c) E=99.80 eV; d) E=97.72 eV.

established by using Fig. 8 in Ref. 181, so that the shifts due to PCI are already considered in the binding energy scale.

This allows us to observe how PCI influences the peak shape in the spectral regime. In all cases, one observes a dominant contribution from the atom. Careful subtraction of the atomic component from the cluster spectra yields cluster specific information. Interestingly, it was found recently that at the energy position of the atomic peak another contribution is also observed, which was assigned to dimers [142]. Model calculations support this assignment of the experimental near-edge spectra [75]. In contrast, more substantial changes in the Kr 3d ionization energy are observed for the surface and bulk sites of the clusters [145].

This is a result of different polarization screening, allowing the distinction between different surface sites, such as corner, edge, and face sites, similar to site specific changes in near-edge spectra [75]. The polarization screening is strongly dependent on the inter-atomic distance. The strongest contribution comes from the nearest-neighbor atoms. According to Björneholm *et al.* [130], this amounts to two thirds of the total screening, while the remaining one third is contributed by the rest of the solid. For free clusters the polarization screening of surface atoms, which have fewer nearest neighbors than bulk
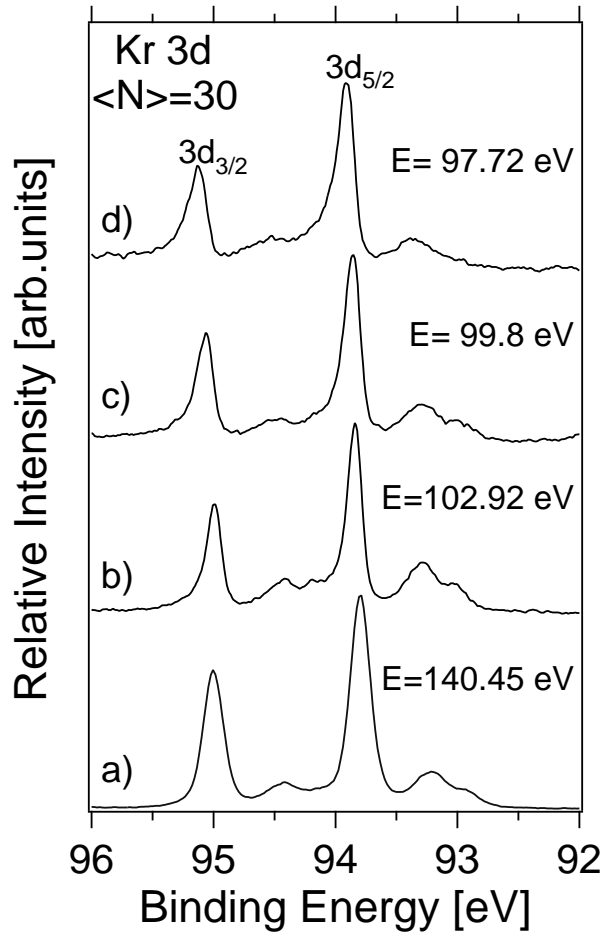
Figure 10.2: Kr 3d photoelectron spectra of raw krypton clusters of average size $\langle N \rangle = 30$ at different photon energies: a) E=140.45 eV; b) E=102.92 eV; c) E=99.80 eV; d) E=97.72 eV.

atoms, is less efficient.

Fig. 10.3 shows the results of the deconvolution of the atomic Kr 3d photoelectron spectra. They were recorded at the same photon energies as that in Fig. 10.3 In the case of the excitation at 140.45 eV, Voigt profiles are suitable, according to the recent result Hatsui *et al.* [142]. The Lorentzian line width is chosen according to the atomic core-hole lifetime. The Gaussian contributions comes from the experimental resolution and various broadening mechanisms such phonon-broadening, the distribution of the cluster sizes, and the different screening for the different positions in the clusters. The widths of the lines are chosen to be identical to that of the bare atom. At lower photon energy, close to the Kr 3d edge, PCI line profiles are used in order to account for the energy-dependent changes in line shape, which are well-known for atomic krypton [181].

The PCI profiles give us a handle how the photoionization dynamics changes in clusters. We summarize in table 10.1 the results of this curve fitting analysis on these spectra for the $3d_{5/2}$ and $3d_{3/2}$ ionization energies. The results are comparable with that from Ref. 182.

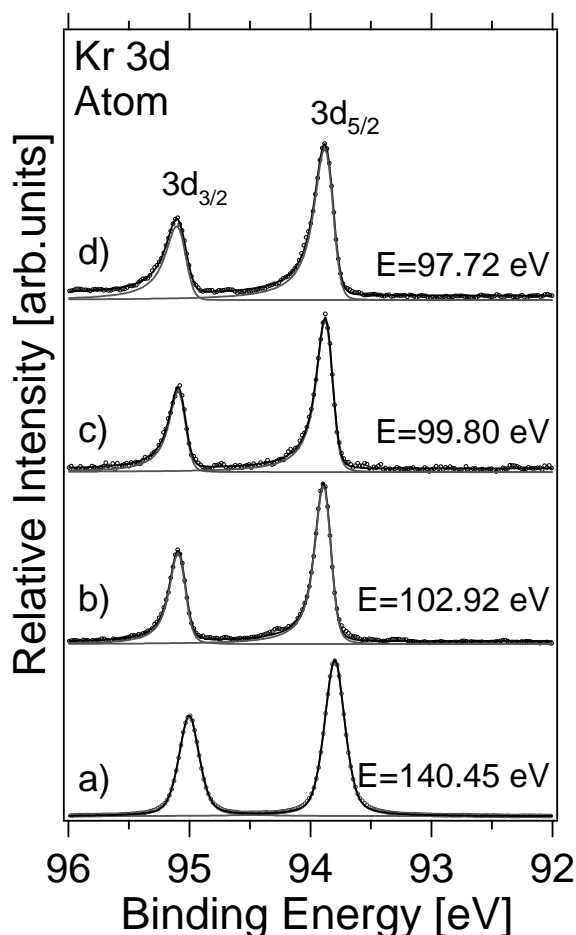A careful subtraction of the atomic component from the raw data is as shown in

Figure 10.3: Kr 3*d* photoelectron spectra of atomic krypton recorded at different photon energies: a) E=140.45 eV; b) E=102.92 eV; c) E=99.80 eV; d) E=97.72 eV. The experimental data are represented by hollow circles. The peak shapes are fitted as indicated in the text (full lines).

Fig. 10.4, where only the dimer and large cluster components remain. Note that the magnitude of bulk sites is negligibly small at ⟨N⟩ = 30, so that the present work is sensitive to the PCI in small clusters consisting essentially of surface sites. There seems to be a difference in the shape depending on the site, where the surface sites are generally less asymmetric than dimer and the free atom. The analysis is performed using the PCI theory of van der Straten *et al.* for ionization near the threshold [118], using a similar approach as Avaldi *et al.* for atomic krypton [182].

The experimental results are fitted by least-squares method using a fitting function which includes the effect of PCI and the limited resolution of the experimental spectra. The fitting parameters are the peak intensity and energy position, the Gaussian and Lorentzian linewidths, the asymmetry parameter, and a linear background. We use the core-hole lifetime of Jurvansuu *et al.* [146], assuming that the core-hole lifetime has not dramatically changed upon cluster formation. Furthermore, we have used a Victoreen function [167] for pre-edge background. The location of the energy set at the edge of the inflection point, the intensity of these components increases with decreasing photon
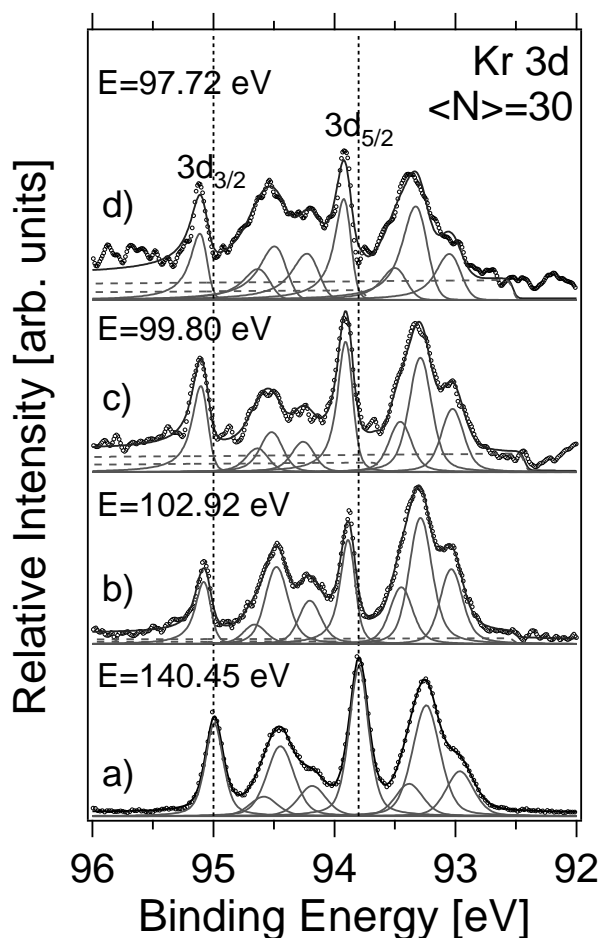
Figure 10.4:   Photoelectron spectra of krypton clusters recorded at $\langle N \rangle = 30$ at different photon energies: a) E=140.45 eV; b) E=102.92 eV; c) E=99.80 eV; d) E=97.72 eV. The experimental results (hollow circles) are obtained by subtracting the atomic component from the raw data. The full lines correspond to a spectral de-convolution, where the sum of all components is indicated by a thick line, dashed lines correspond to Victoreen functions.

energy. (We note that ZEKE [20] spectra of Kr clusters are governed by a high intensity in band the Kr 3d continuum.) Thus, it appears likely that this contribution comes from inelastic scattering processes of photoelectrons in the clusters.

Based on the assumption that the Kr 3d lifetime widths are constant in the current photon energy range, the fit was performed in the same way for atoms and clusters. The Lorentzian contribution was kept fixed during the fitting procedure. For the photoelectrons, it is necessary to include also the contribution for the photon bandwidth. We have used for both spin orbit components the same Gaussian and Lorentzian widths. The surface peaks are indeed broader than the free atomic peaks as we can see the same effect in Xe 4d [183], and this broadening is attributed to the larger variation in type of sites at the surface compared to the bulk peaks. The 50–70 meV contribution from the spectrometer and photon band width should be subtracted.

We will discuss now several important issues that one should consider when applying a

Table 10.1: Gaussian widths and asymmetries obtained from the deconvolution of near-threshold photoelectron spectra near the Kr 3d edge (Fig. 10.3). The Lorentzian width is assumed to be 88 meV in all spectra, which is a result of the core-hole lifetime. The error limit is estimated to be ±10 meV.

Component	140.45 eV	102.92 eV	99.8 eV	97.72 eV
Gaussian width ($3d_{5/2}$ and $3d_{3/2}$):				
Atom	140	96	99	110
Dimer	140	96	99	110
Surface	164	178	190	205
Asymmetry ($3d_{5/2}$):				
Atom	-	0.465	0.593	0.761
Dimer	-	0.389	0.421	0.689
Surface	-	0.125	0.327	0.568
Asymmetry ($3d_{3/2}$):				
Atom	-	0.526	0.656	1.070
Dimer	-	0.419	0.487	0.963
Surface	-	0.229	0.328	0.796

free atom PCI model to the solid. These changes in line shape are as follows: We assume that the electron trajectories are straight lines, though it is known that electron trajectories in a solid are not strictly linear, but rather the electrons can follow complex paths due to elastic and inelastic scattering. Each scattering event can result in the production of secondary electrons. The inelastic mean free path of an inelastically scattered electron is a function of its kinetic energy. PCI data available do not cause any significant deviation from the free atom models. The reasonable agreement between the free atom theoretical and experimental curves suggests that the magnitude of the PCI is mostly associated with the surface excitations. Because PCI depends on the kinematics of emitted particles, the energy distribution of the emitted particles is expected to be different for the free atom compared to the solid state. That means the PCI may be different, depending on the leaving of the free atom of the emitted charges. Moreover, in the case of clusters we have taken into account that the medium is changed, which is more close to the treatment in the solid. The same procedure has been applied to solid neon by Feulner [163] in the classical model.

As the atomic PCI requires the final state ion to remain unscreened, it is surprising that PCI occurs at all in metallic solids [184]. When an Auger process occurs in a solid state environment, screening of the charges can substantially modify the PCI shift. In a metal, all charges are screened by delocalized valence band electrons in a very short distance on the order of an atomic radius, thus the long range Coulomb interaction between charges is significantly reduced. Let assume that the metallic screening proceeds infinitely fast, as the consequence for the excitation to a bound state, photoexcited electron occupies a screening level, and for excitation to a high-lying continuum state, the photoelectron leaves fast but the atom remains neutral by pulling an electron from the conduction band into the screening level. In an insulator whose screening is merely the long range dielectric

Table 10.2: Experimental PCI energy shift for Kr 3d. a) Kr 3d ionization energy relative to the atomic values; b) absolute PCI shift for $3d_{5/2}$ component; c) absolute PCI shift for $3d_{3/2}$ component. The error limit is estimated to be ± 10 meV.

a) PCI shift $3d_{5/2}$

Photon energy [eV]	Binding energy [eV]	Dimer shift [eV]	Corner shift [eV]	Edge shift [eV]	Face, Bulk shift [eV]
140.45	93.799	-0.002	0.430	0.567	0.831
102.92	93.865	-0.019	0.435	0.593	0.853
99.80	93.880	-0.024	0.454	0.622	0.888
97.72	93.901	-0.029	0.480	0.647	0.921

b) PCI shift $3d_{3/2}$

Photon energy [eV]	Binding energy [eV]	Dimer shift [eV]	Corner shift [eV]	Edge shift [eV]	Face, Bulk shift [eV]
140.45	95.002	-0.009	0.427	0.546	0.809
102.92	95.071	-0.025	0.438	0.621	0.908
99.80	95.089	-0.028	0.445	0.602	0.858
97.72	95.094	-0.031	0.422	0.640	0.927

polarization without the charge transfer, the PCI shift due to the Coulomb interaction can be much larger than in a metal. A detailed study of PCI shifts for both spin orbit components is given in the Table 10.2.

10.2   Comparison with experimental results

However, the asymmetric PCI profiles are different, since they are energy dependent and are located at different excitation energies above the 3d thresholds. Looking at the data as a whole, the root-mean-square deviations for the individual fit is about 5 meV. This result gives an indication of the uncertainty within a single fit. The relative intensity of the surface components, corner, edge, face and bulk in the photoelectron spectra of krypton clusters follows the intensity in the core ionization. Comparing the spectra at the kinetic energy of 9.12 eV and 2.72 eV we can see that the surface sites are getting asymmetric in the peak shapes as approaching the threshold.

   This can be understood using the following classical model: In the Kr 3d excitation regime the kinetic energy of the Auger electrons is observed between ca. 50 and 20 eV. Assuming that the kinetic energy of the Auger electron is 50 eV and the kinetic energy of the photoelectron varies between a few meV in the case of ZEKE and 10 eV, one can calculate the classical distance, where the Auger electron overtakes the photoelectron. One obtains from these assumptions that this happens for a 10 meV photoelectron at 5.15 nm. This distance increases for a 1 eV photoelectron to 7.37 nm. A 5 eV photoelectron is overtaken at 15.64 nm. These distances correspond to 13, 19, and 39 nearest neighbor distances using the lattice constant of solid krypton. The implication of this situation is, that the electrons of different kinetic energy undergo inelastic scattering in the cluster
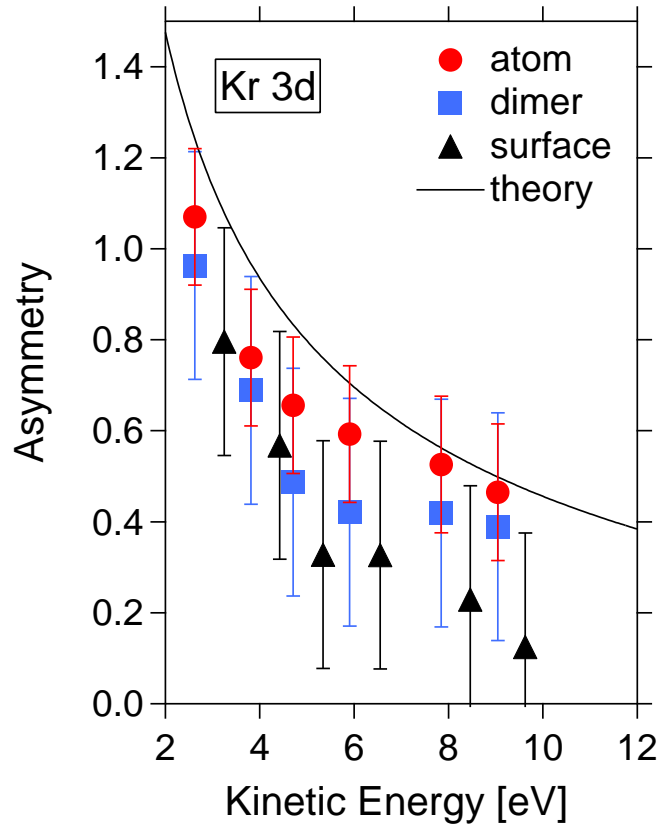
Figure 10.5: The experimental PCI asymmetry as function of the kinetic energy. Empty symbols are for the $3d_{3/2}$ and full symbols are for $3d_{4/2}$. The theoretical curve is shown with a continuous line.

or crystal lattice. The electron mean free path of solid krypton has been investigated by Sanche *et al.* [185, 186]. For electron energies less than 1 eV, the scattering length is greater than 20 nm. This means that the slow electron has a mean free path larger than the classical overtaking point. In contrast, the Auger electrons of ca. 50 eV kinetic energy have a mean free path less than 1 nm, implying that these will be more likely inelastically scattered than the photoelectron. This means that the classical overtaking point is further away than in the corresponding atom. In the case of slow electrons with energies between 1 eV and 3.5 eV, the scattering length is of the same order of magnitude as the overtaking distance and larger than the mean free path of Auger electrons. Above 3.5 eV and 10 eV the mean free path of slow electrons falls below 2 nm, comparable to the scattering length of Auger electrons. It is interesting to note that the present results show a change in the asymmetry of the lineshape, as predicted by Sanche *et al.* [185, 186].

The cluster size regime is not large enough to probe the bulk sites, but already from surface sites one observes that the peak shapes are more symmetric. This is similar to the recent work of Romberg *et al.* [163], who found that there is a narrowing of the PCI-profile in condensed neon compared to the atomic profiles, where exclusively bulk sites dominate.

In conclusion, we have investigated the dynamics of the Kr 3d photoionization in the clusters corresponding to $\langle N \rangle \simeq 30$. These consist primarily of surface sites. We have

observed smaller asymmetry in peak shape at the surface sites when the photon energy is lowered to the Kr 3d ionization threshold. This result is similar to recent work on condensed rare gases as well as a simple model based on the classical overtaking distance in the photoelectron by the Auger electron relative to changes of the electron mean free path in krypton clusters and solid. We note that the present consideration is qualitatively reasonable to all weakly bound atomic and molecular Van der Waals systems.

Chapter 11

ZEKE Photoelectron Spectroscopy of Free Clusters

Zero kinetic energy (ZEKE) photoelectron spectroscopy is based on the measurement of electrons of "zero kinetic energy" (within an energy interval from zero to certain cut-off energy) against excitation wavelength of a tunable light source. For the investigation of a core level excitation and relaxation of free molecules or clusters, using monochromatic soft X-ray synchrotron radiation as excitation source, ZEKE spectroscopy enables one to select and identify the formation of a core hole state at a specific atom in the molecule. Localized site or atom-specific excitation is made possible by chemical shift of the $1s$ electron orbital energies which depends on the different chemical environment of the $1s$ orbital.

The following three $1s$ orbital excitation processes have to be considered:

a) Resonant excitation: excitation from a $1s$ core orbital to a vacant valence orbital below the $1s$ ionization threshold, thus leading to a neutral $1s$ core hole state with an (occupied) excited valence orbital.

b) Direct ionization: excitation from a $1s$ core orbital to the ionization threshold directly producing a free ZEKE electron, thus leading to a singly charged $1s^{-1}$ core hole state with no valence orbital excitation.

c) Ionization with shake-up: excitation from a $1s$ core orbital to the ionization threshold accompanied by the shake-up transition of an electron from an occupied valence orbital to a vacant valence orbital and the emission of a free ZEKE electron, thus leading to a singly charged $1s^{-1}$ core hole state with a valence orbital excitation.

In cases a) and b) excitation processes lead directly to the formation of a ZEKE electron and a singly charged $1s^{-1}$ core hole state. The $1s^{-1}$ core hole is filled with a valence electron and an Auger electron of high kinetic energy is emitted from a valence orbital. Hence, the Auger relaxation processes leave the molecule with a double hole in the valence band. The excitation state of this dication (i.e. the double valence hole electronic configuration) depends on the respective Auger relaxation channel. In contrast to this, the resonance excitation scheme does not produce a ZEKE electron directly but ZEKE electrons can be produced in the relaxation channel. The relaxation channel required for ZEKE electron formation is the three-electron Auger process for which the filling of the

$1s^{-1}$ core hole and the emission of an Auger electron of high kinetic energy is accompanied by the emission of an electron with low kinetic energy (ZEKE electron). The Auger and ZEKE electron can be emitted simultaneously (resonant double autoionization) or sequentially (participator valence Auger decay). Hence, ZEKE electrons are also formed for resonance excitation and as observed for direct and shake-up ionization, the formation of a dication is correlated with the ZEKE electron. The main two-electron Auger-type relaxation process by emission of an Auger electron of high kinetic energy, leads to the formation of a singly charged cation and no ZEKE electron is emitted. Consequently, no co-relaxation exits between a ZEKE electron and the formation of a singly charged system. All three cases (of a ZEKE electron formation) will finally leave the system in a doubly charged state. Such doubly charged molecules are generally unstable and the main decay channel is fragmentation into two or more fragments leading to correlated pairs of singly charged fragment ions.

11.1   Ar $2p$ excited argon clusters

First ZEKE experiments on core-excited clusters yielded a gas-to-solid shift of the Ar $2p_{3/2}$ ionization energy of 1.0±0.1 eV [82]. ZEKE spectra give specific information on the inelastic scattering of photoelectrons in the bulk interior of the clusters. These occur in the Ar $2p$ continuum with strong intensity [82]. First ZEKE experiments were performed with low spectral resolution [82], which did not permit a detailed analysis on changes in inner-shell photoionization dynamics. PCI profiles of surface and bulk sites require high resolution experiments. A detailed analysis of recent results will be given elsewhere [187].

Knop *et al.* [82] has investigated Ar $2p$ ZEKE spectra of atomic and variable size clusters using a combination of time of flight and angular discrimination techniques. They have observed changes in zero-kinetic-energy spectra as a function of average cluster size are interpreted in terms of a lowering of the Ar $2p$ ionization energies in larger clusters. It has not been possible to identify an Ar $2p$ ionization energy for intermediate size clusters or surface atoms because of the limited resolution of the X-ray monochromator used in the ZEKE measurements. The Ar $2p_{3/2}$ ionization energy of solid argon is predicted to be the same as found for the large clusters (247.7±0.1 eV taking into account the estimated PCI lineshape effect [96, 106, 114, 118]). This corresponds to a redshift of 1.0±0.1 eV relative to atomic argon. The ZEKE electron signal at the $4s$ exciton energy and in the far continuum is observed with enhanced intensity in large clusters. This signal is attributed to significant intracluster scattering, which leads to thermalization of the emitted photoelectrons.

The total electron yield (TEY) technique provides spectra which are most representative of the average absorption spectrum since it does not have the mass discrimination which occurs in total and partial ion yield spectra [65]. Small differences occur between the TEY spectra of clusters and the absorption cross section of the solid because of the preferential detection of low energy electrons in TEY. The lowest energy resonance (Ar$2p_{3/2} \rightarrow 4s$; also denoted as $4s_{3/2}$) in the atom ($4s$) is located at 244.390 eV according to high resolution electron energy loss spectroscopy [168]. Rühl and coworkers [65], have reported the energy position of this resonance as a function of cluster size [65]. Three components are identified, corresponding to
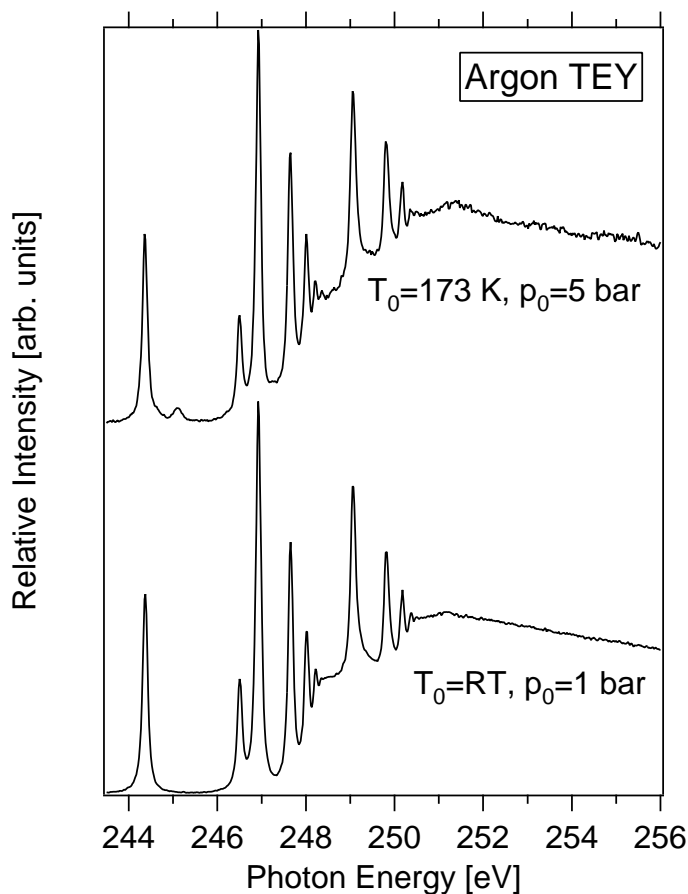
Figure 11.1: Total electron yield (TEY) spectra of Ar atoms and clusters with $\langle N \rangle = 270$ in the Ar $2p$ excitation regime. TEY allow us to determine the energies of the absorption resonances. These correspond to transitions from core levels into unoccupied levels

(i) the atomic component ($4s$) which decreases in intensity with increasing average cluster size since there are fewer atoms in the beam,

(ii) a weak signal around 244.7 eV, most prominent in intermediate cluster sizes, which is attributed to surface excitons in clusters; and

(iii) a "solid-like" component ($4s$) of bulk excitons at 245.16 eV which builds up in intensity as the cluster size is increased and the surface to volume ratio decreases.

TEY spectra of Ar atoms and clusters in the Ar $2p$ excitation regime have been recorded for different expansion conditions (see Fig. 11.1). The figure shows a signal around 245.1 eV which is attributed to bulk excitons in clusters.

Figure 11.1 shows the Ar $2p_{3/2} \rightarrow 3d$ transition and its evolution from the atomic Rydberg state at 246.927 eV [168] towards the corresponding $3d$-exciton in the solid at 247.8 eV [188]. The evolution of the $3d$ spectral component has some similarity to that of the Ar $2p_{3/2} \rightarrow 4s$ transition.

However, the $3d$ spectral changes are clear and resolved by Rühl and coworkers [65] for the isolated Ar $2p_{3/2} \rightarrow 4s$ transition because other transitions, such as the Ar $2p_{1/2} \rightarrow 4s$
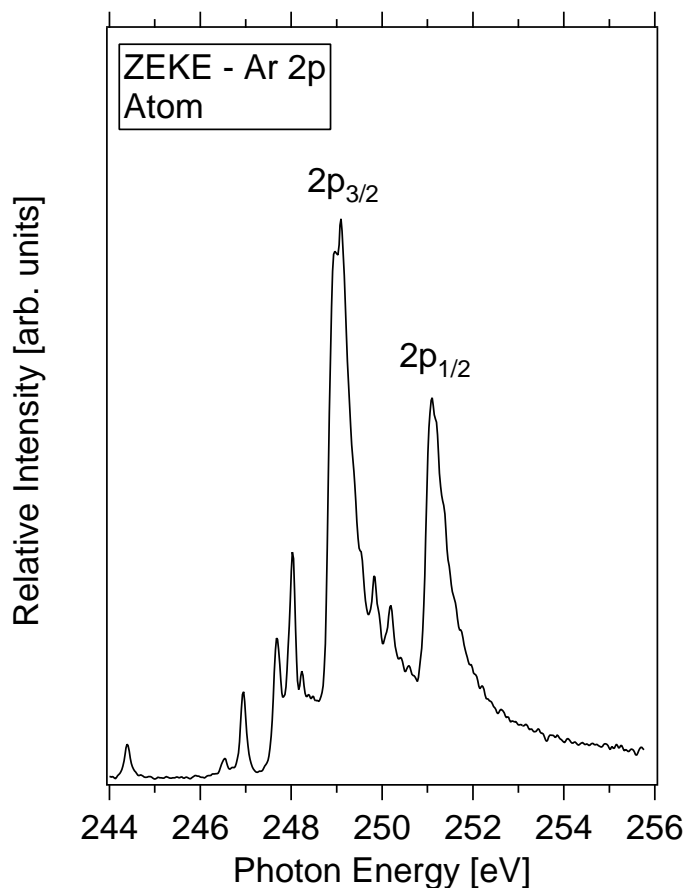
Figure 11.2:   ZEKE photoelectron spectrum of atomic argon in the Ar $2p$ excitation regime.

and Ar $2p_{3/2} \rightarrow 4d$ occur in the vicinity of the Ar $2p_{3/2} \rightarrow 3d$ transition. Fig. 11.1 shows that there is poor alignment of the cluster jet with the photon beam. Therefore, the spectrum essentially shows the atomic lines. From that we can learn how important is the alignment for cluster detection.

The atomic spectrum ZEKE from Fig. 11.2 is characterized by two asymmetric peaks which are a result of direct ionization from the Ar $2p_{3/2}$ and Ar $2p_{1/2}$ levels at 248.93 eV and 251.05 eV, respectively. The maxima are shifted to higher energy compared to ESCA measurements [189]. The peak shapes are asymmetric because of post-collision interaction which transfers kinetic energy from the photoelectron to the Auger electron [105]. As the cluster size is increased the following changes occur:

 (i) direct ionization components at lower energy (248 eV and 250 eV) build up in
      intensity whereas the atomic component loses intensity;

 (ii) the intensity of low-lying exciton states and the Ar $2p$ continuum increases;

 (iii) the exciton bands shift to higher energy as observed in the NEXAFS spectra [65].

The proportion of atoms in the beam and therefore the atomic spectral component decreases as the average cluster size increases. The changes in neutral cluster size can be

followed directly by the shifts of the low lying exciton states. The redshift of the direct Ar 2p ionization energy in clusters is mainly a result of electronic relaxation of the ion caused by polarization of the surrounding neighbors. The surface ionization component in the Ar 2p photoelectron spectra of argon clusters has been observed in recent higher resolution ESCA studies [68]. Two components were observed with binding energies 0.62 eV and 0.95 eV below that of the atomic argon.

The latter value is in excellent agreement with our ZEKE results, consistent with it being assigned as the ionization threshold for the atoms in the bulk of the cluster. Since the general shape of the ZEKE spectrum at $\langle N \rangle > 400$ is similar to the absorption cross section and the total electron yield spectrum of the solid, it is assumed that the lowering of the Ar 2p ionization potential is identical in large clusters and the solid. All this was evaluated by Björneholm *et al.* [68]. The Ar 2p ionization potential in the solid has been determined several times in the past. However, this quantity is difficult to determine precisely because of charging problems with solid samples. Assuming that the post-collision interaction peak shift is the same in clusters and free atoms, the Ar 2$p_{3/2}$ ionization energy of the solid is estimated to be 247.7 eV from the ZEKE spectra of the largest clusters. This value is in excellent agreement with that recently reported from ESCA spectra of the condensed phase [190, 191]. These studies suggest that reliable core ionization energies for condensed phase species can be determined from the ZEKE or ESCA of free clusters.

The ZEKE spectrum shown in Fig. 11.3 contains the signal from the excitations of the well known resonant Rydberg states of the atom ((Ar 2$p_{3/2} \rightarrow 4s$) at 244.39 eV; (Ar 2$p_{1/2} \rightarrow 4s$) at 246.514 eV; (Ar 2$p_{3/2} \rightarrow 3d$) at 246.514 eV; (Ar 2$p_{3/2} \rightarrow 4d$) at 246.927 eV; (Ar 2$p_{3/2} \rightarrow 5d$) at 248.026 eV; (Ar 2$p_{1/2} \rightarrow 3d$) at 249.074 eV; (Ar 2$p_{1/2} \rightarrow 4d$) at 249.819 eV; (Ar 2$p_{1/2} \rightarrow 5d$) at 250.171 eV) [168] and the energy value from Rydberg formula (Ar 2$p_{3/2}$ (248.207 eV, 248.319 eV, 248.392 eV, 248.441 eV, 248.477 eV) and Ar 2$p_{1/2}$ (250.354 eV, 250.467 eV, 250.539 eV, 250.589 eV, 250.625 eV, 250.625 eV). Due to the high density of Rydberg states, we need to calculate their energies. For that we used the Rydberg formula. The quantum defect number determined from a fit of the energies of the first three resolved Rydberg peaks. There is a high density of Rydberg states. Small intensities of low-energy electrons can arise in the Rydberg regime as well as in the Ar 2p continuum from at least double Auger relaxation processes and resonant shake-off which gives rise to low kinetic energy electrons [192].

The maxima of the direct ionization components occur at 248.90 eV (Ar 2$p_{3/2}$) and 250.77 eV (Ar 2$p_{1/2}$) are due to contributions from Rydberg. The values are in agreement with the previous ZEKE work [189] but are slightly higher than the atomic values obtained from ESCA measurements (248.63 eV (Ar 2$p_{3/2}$) IE; 250.78 eV (Ar 2$p_{1/2}$) IE). On the one hand, the difference in the position of ZEKE maxima and the known IE cannot be attributed to a calibration error since the energy scale is set by calibrating the positions of the Ar 2$p_{3/2} \rightarrow 4s$ transition in the total electron yield spectra to it's known value (244.390 eV) [168]. On the other hand, this shift is the effect of post collision interaction (PCI) occurring in the threshold ionization region.

This well known phenomenon at the low excess energies, post-collision interaction, leads to significant transfer of energy from the photoelectron to the Auger electrons, and at higher energies, the PCI function approaches a Voigt shape, but even the highest energy has a noticeable asymmetry in the peaks. At the lowest energies the effects of post
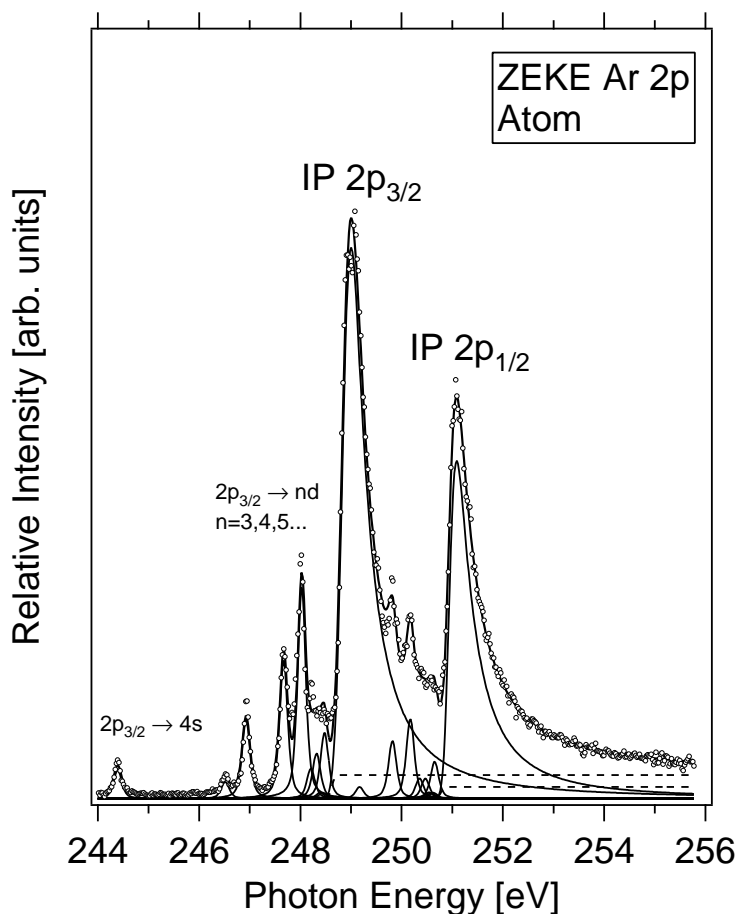
Figure 11.3: ZEKE spectrum of Ar atoms in the Ar $2p$ regime. The experimental results are represented by hollow circles, full lines correspond to individual profiles, where the sum of all components is indicated by a thick black line. The long dashed lines correspond to Victoreen functions.

collision interaction are very pronounced and ZEKE measurements provide a useful test of the PCI theory. If PCI theory is correct, that also provides a sensitive measurement of the core hole lifetime.

The ZEKE spectra have been fit by least-squares using a fitting function that includes the effect of post collision interaction and experimental resolution [193]. This model is based on a semi-classical approximation and takes into account the intermediate state width Γ and the photoexcited electron angular momentum l as parameters. The probability for emission of ZEKE photoelectrons as a function of photon energy is closely tied to the recapture process. A limitation of this model is its neglect of PCI between the photoelectron and Auger electron in cascade steps following the primary excitation Auger decay process [194]. This restriction was discussed in chapter 6 with the general conclusion that the escape distribution can be used for prediction of the Auger intensity but may need modification to describe photoelectron intensity if there are fast cascade Auger steps. The ZEKE probability distribution also must be applied only to cases where cascade PCI effects are negligible.

Three parameters describing a given ZEKE distribution are of interest: peak position, width and asymmetry. The behavior of each of these is explored as a function of the intermediate state width Γ. The peak location, the energy above the threshold at which ZEKE emission reaches a maximum also increases as $\Gamma^{2/3}$. For small Γ these distributions are in good agreement with existing semiclassical theories and indicate that the additional averaging of such distribution that has been proposed [108] is not justified.

In Fig. 11.3 the open circles represent the raw data and the solid lines show the least-squares fits. At high photon energies the important feature of the data is a symmetric tail, and in the fits the Lorentzian width is determined by this tail. This data analysis of the spectra was performed using Voigt line shapes for the low-lying (4s and 3d) Rydberg states of the argon atom. The fits indicate a Lorentzian width of 118 meV and a Gaussian broadening of 123 meV.

In our ZEKE spectrum of atomic argon the $2p_{3/2}$ and $2p_{1/2}$ peaks are fit simultaneously. The different Lorentzian widths were used for two peaks (Ar $2p_{3/2}$ (136 meV) and Ar $2p_{1/2}$ (126 meV)). That is in disagreement with [146].

For the ZEKE spectrum of atomic argon that we have analyzed, the average value of the Lorentzian width is 118 meV, with a root-mean-square deviation of ± 4 meV. The uncertainty reflects only the statistical uncertainty, as given by the least-squares fitting procedure, and does not reflect any contribution from systematic errors. An asymmetric tail on the instrument function would skew the spectra, since the asymmetric tail that is produced by post collision interaction in the spectra and also the instrumental asymmetry would add to this tail.

The PCI profiles are, however, different for the two peaks since they are at different energies above threshold. The ZEKE peak is both broadened and shifted relative to the lower energy. The value of the Gaussian width derived from the fits increases from 123 meV at the lowest energy (Rydberg states) to 296 meV at the highest energy (ionization energy). The asymmetry parameter of the atomic line shape of $2p_{1/2}$ and $2p_{3/2}$ is found to be 3.595 and 3.209, respectively.

In order to account for the incomplete suppression of non-thresholds electrons we have included two additional step functions (Victoreen function [167]), representing the Ar $2p$ continuum ionization signal arising from non-threshold processes. In our ZEKE spectrum of atomic argon the spin-orbit intensity ratio for direct ionization Ar $2p_{3/2}$ and Ar $2p_{1/2}$ is 2:1. ESCA measurements [195] report a value of 2 in agreement with the theoretical value of 1.96 [196]. The asymmetry of the line shapes is determined experimentally by using the kinetic energy of the ZEKE electrons which should be less than the detector window of 0.25 eV (see chapter 5).

The results described above are based on fit to the data in which the instrumental resolution (assumed to be Gaussian) was one of the fitting parameters. It is of interest to compare the Gaussian widths from the resonances to that of the ionization energy. Looking first at ZEKE spectra of argon we can note that the values from the fit are significantly larger that expected. The effect of these differences depends on the spectrometer resolution.

We ask whether the line width of the core-ionized state is different from that of the core-excited state ($2p_{3/2} \rightarrow 4s$). These two values are somewhat different. It is easy to think of reasons why these widths might be different. The presence of the 4s electron in the excited atom opens the additional channels for shake-up, that might expect the
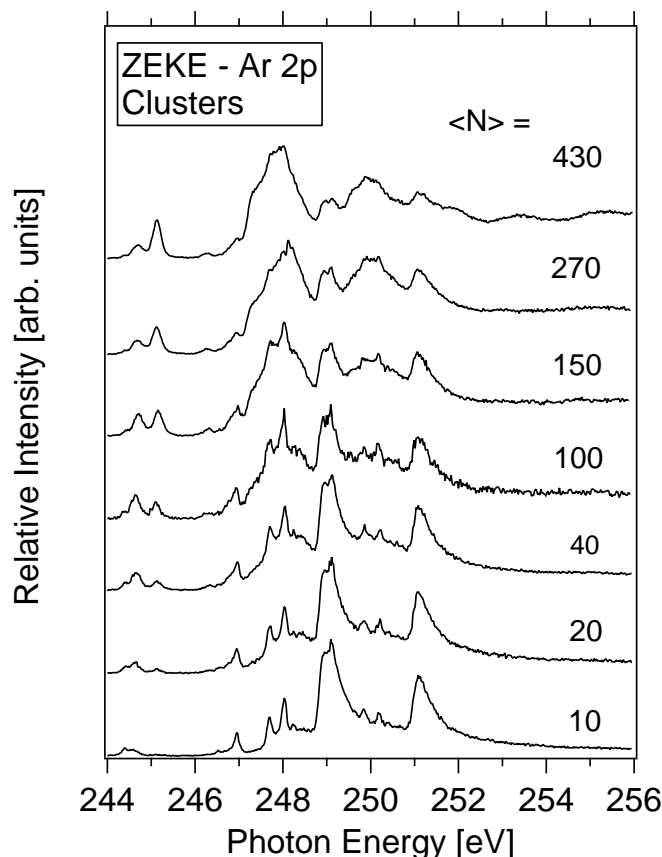
Figure 11.4: ZEKE photoelectron spectra of argon clusters in the Ar $2p$ excitation regime.

presence of the $4s$ electron increase the decay rate and the width.

Figure 11.4 shows ZEKE spectra of free argon clusters as a function of average cluster size. The sensitivity of ZEKE electrons to surface and bulk properties also occurs in the dominant signal of surface bulk exciton e.g. in the Ar $2p_{3/2}$ to $4s$ regime. Cluster formation occurs if the gas has sufficiently cooled down. The size of the clusters is distributed around a mean value, which may be altered by variation of the expansion pressure, the nozzle diameter and the temperature, according to the empirical relation [60] where $\langle N \rangle$ is the cluster average size. In Fig. 11.5 we can see the evolution of ZEKE spectra of argon clusters in the Ar $2p$ regime. The ZEKE spectrum of the atom clearly shows the direct ionization energies (Ar $2p_{3/2}$ and Ar $2p_{1/2}$). This corresponds to the dominant asymmetric peaks near 249 eV and 251 eV. In Fig. 11.5 the surface and bulk excitons in clusters are fitted with Voigt profiles and the two asymmetric peaks which are the result of direct ionization were fitted with PCI profiles. These asymmetric peaks contain surface and bulk components.

We focus our interest on the evolution of the direct photoionization process, which is not clearly visible in the raw cluster spectra, where the atomic contribution has been subtracted (7%). Looking at the cluster spectra one might observe the following changes in the ZEKE spectra:

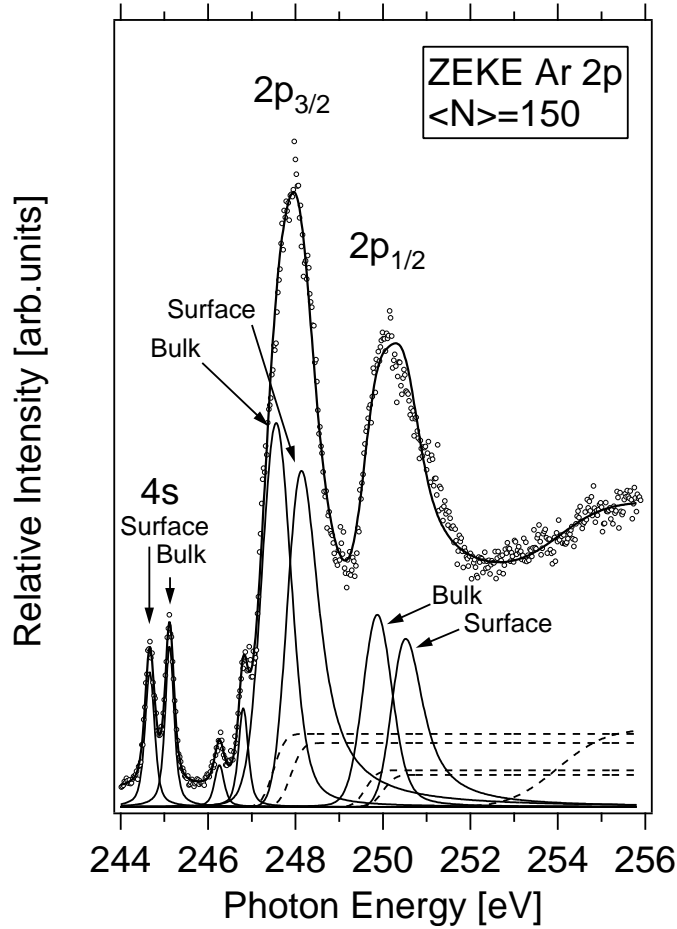(i) the atomic features become weaker in intensity since the mixing ratio between clus-

Figure 11.5: ZEKE spectra of Ar clusters in the Ar 2*p* regime. The experimental results (hollow circles) are obtained from the subtraction of the atomic component from the raw data shown in Fig. 11.4. The full lines correspond to a spectral de-convolution, where the sum of all components is indicated by a thick black line. The thin lines correspond to the individual PCI profiles. The long dashed lines correspond to Victoreen functions.

ters and atoms is increased with $\langle N \rangle$;

(ii) new features occur, which come primarily from direct Ar 2*p* photoionization of surface and bulk sites in clusters;

(iii) the atomic Rydberg states are converted into the corresponding surface and bulk excitons, this is an independent indication for the occurrence of large clusters in the jet,

(iv) new features occur in the Ar 2*p* continuum as a result of single and multiple scattering [82].

We performed a comparative study for each cluster size, but for convenience we discuss only one. Choosing a cluster average size $\langle N \rangle = 150$ atoms (see Tab. 11.1), we present the comparative study of the new features which come from the direct ionization based

Table 11.1: Absolute energy positions and splitting for the Ar $2p$ ZEKE cluster features for a different cluster size. Energies for cluster surface and bulk positions in ZEKE spectrum are given for two groups of ionized states: $2p_{3/2}$ and $2p_{1/2}$. Notations $\delta(a-s)$ and $\delta(a-b)$ and $\delta(a-b)$ correspond to separations between the atomic line and corresponding cluster surface and bulk features; $\delta(s-b)$ is the surface–bulk separation.

Size	Component	Surface	Bulk	$\delta(a-s)$	$\delta(s-b)$	$\delta(a-b)$
40	$2p_{3/2}$	247.903	247.532	1.33	0.43	1.13
	$2p_{1/2}$	249.986	249.774	0.89	0.22	1.01
150	$2p_{3/2}$	247.853	247.535	0.81	0.32	1.12
	$2p_{1/2}$	250.013	249.598	0.83	0.45	1.18
270	$2p_{3/2}$	247.820	247.454	0.93	0.37	1.21

on quantitative least-squares curve fitting analysis of Armen *et al.* [193]. The total Gaussian widths of the surface and bulk direct ionization peaks is 0.786 and 0.489 eV, respectively, while the excitonic structure shows a Gaussian broadening of 0.168 and 0.138 eV, respectively. The asymmetry parameter of the spin–orbit components is found to increase systematically from the $2p_{3/2}$ component to the $2p_{1/2}$ component (2.593 to 0.723). For a given cluster size there are systematic changes. The asymmetry of the atomic component is greater that of the surface component. That means that the asymmetry decreases systematically from the atom via surface sites to bulk sites. These changes can be assigned in the following using a model that considers the electron mean free path (MFP) in clusters and solid. This model was described in chapter 9. Evidently the scattering process may modify the PCI process and lead to broadening of the line shapes and enhanced intensity in the $2p$ continuum, corresponding to the emission of low kinetic energy electrons from clusters.

It is observed that in the regime of small clusters the line shape of the surface sites are more asymmetric than those of the bulk sites [187]. This is similar to recent work of Kassühlke *et al.* [174] who found that PCI-induced effects in threshold and near-threshold photoelectron spectra of Ar multilayers. Further it is known that the broadening and energy shifts are considerably reduced for adlayers of solid Ar on metals [117]. Asymmetric line shapes of Ar $2p$ experimental photoelectron spectra of physisorbed Ar on Rb(001) surfaces [117] indicate a larger shift by a factor of three for the Auger than for the photoemission line shape [175]. We conclude that ZEKE photoelectron spectroscopy of variable size free clusters gives detailed insight into the dynamics of core photoionization processes. In the case of van der Waals clusters one finds exclusively increased contributions from the Gaussian broadening if the cluster is comparable to the atom, the asymmetry of the line shape is larger in the atom and that the decreases systematically via surface to bulk sites.

11.2   Kr $3d$ excited krypton clusters

Electron spectra at the Kr and Xe resonances have been investigated extensively. For Kr [197] the observed variations in valence σ_{ns} and σ_{np} caused by autoionization were small,
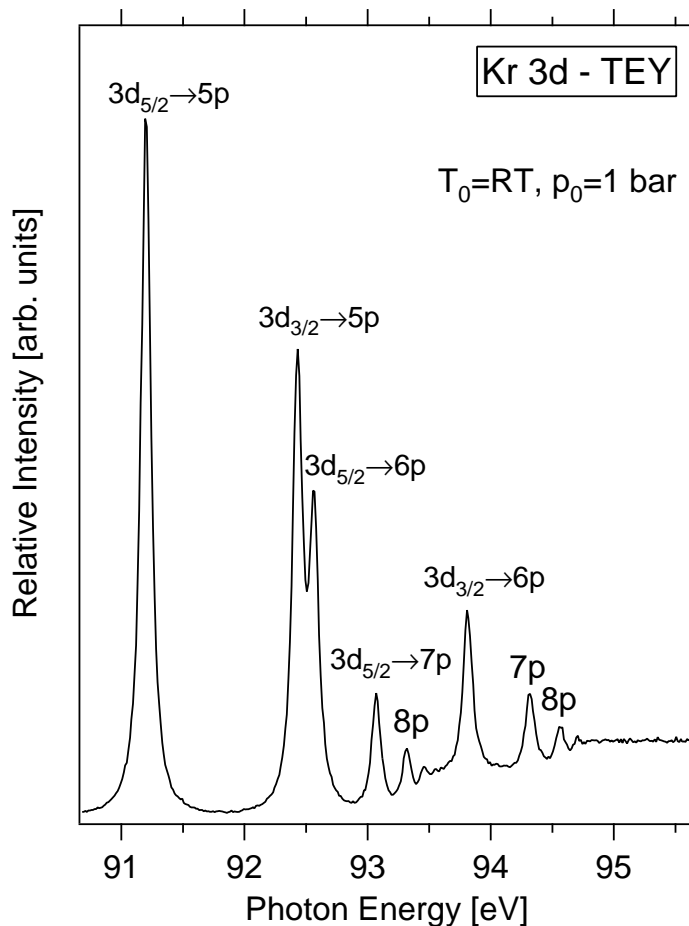
Figure 11.6: Total electron yield (TEY) spectrum of krypton in the vicinity of the $3d$-edge

less than 15%. The electron spectra agree with the expectations of the spectator model with two important exceptions. Firstly, shake-up of the Rydberg electron during Auger-like decay contributes additional peaks, e.g. Kr $3d^{-1}5p \rightarrow$ Kr$^+$ $4p^{-2}6p$ [197, 198, 199, 200]. At the Kr $3d$ threshold, however, Hayaishi et $al.$ [80] surprisingly found no evidence for PCI in the Kr ion cross sections.

The total yield spectrum of krypton at the $3d^{-1}np$ resonance excitation range is depicted in Fig. 11.6. At the $3d_{3/2}^{-1}6p$ resonance an asymmetry can be observed at the high photon energy side. This is most probably due to the $3d_{5/2}^{-1}$ ionization threshold lying almost exactly under the resonance (93.79 eV). The $3d_{3/2}^{-1}6p$ excited state seems to be broader than could be expected from the $3d_{5/2}^{-1}6p$ series. This is also probably due to the underlying $3d_{5/2}^{-1}$ ionization threshold and difficulties in estimating the threshold shape properly.

The threshold photoelectron spectra contain the following features (see Fig. 11.7): a constant level at lower energies from the background and valence shake-off, e.g. Kr + $h\nu$ $\rightarrow$ Kr^{2+} $4p^4$ + $2e^-$, and a constant signal above the thresholds, which is higher as a result of double Auger events, e.g. Kr$^+$ $3d^{-1}$ $4p^6 \rightarrow$ Kr^{3+} $4p^3$ + $2e^-$. Strong, nearly Lorentzian peaks are observed at resonances below threshold from the shake-off decay of the excited
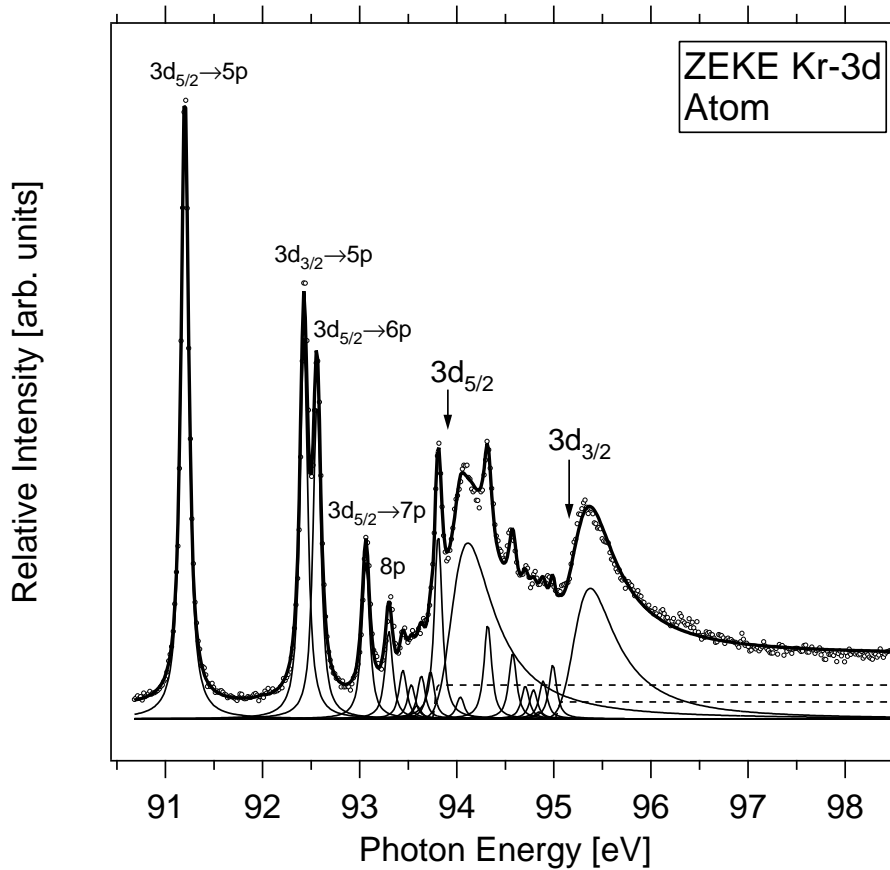
Figure 11.7: ZEKE spectrum of Kr atoms in the Kr $3d$ regime. The experimental results are represented by hollow circles, full lines correspond to individual profiles, where the sum of all components is indicated by a thick black line. The long dashed lines correspond to Victoreen functions.

state, e.g. Kr $3d^{-1}\,5p \to$ Kr$^{2+}\,4p^4 + 2e^-$. These resonant shake-off transitions resemble the double Auger events above threshold. Finally, at the inner-shell thresholds, there are peaks due to near 0 eV kinetic energy photoelectrons, e.g. Kr $+ h\nu \to$ Kr$^+\,3d^{-1}$ $+ e^-$, which are broadened and shifted to higher photon energy $h\nu$ by the post-collision interaction (PCI) between the slow photoelectron and the faster Auger electron.

There are three possible shake-off decay paths from the $3d^{-1}5p$ resonant state of Kr in which (i) two valence electrons are ejected, (ii) the Rydberg electron is ejected along with a valence electron and (iii) the Rydberg electron and two valence electrons are ejected. For path (i), the same orbitals nl are involved as in double Auger above threshold ionization, e.g. Kr$^+$ 3d$^{-1} \to$ Kr$^{3+}\,4p^{-3}$. The double Auger signal intensity is divided by the intensity of the threshold peaks, Kr $\to$ Kr$^+\,3d^{-1}$.

The ZEKE spectra of atomic Kr have been fitted by least-squares using a fitting function that includes the effect of post collision interaction and experimental resolution [193]. Three parameters describing a given ZEKE distribution are of interest: peak position, width and asymmetry. The behavior of each of these is explored as a function of intermediate state width Γ, as in the case of Ar.
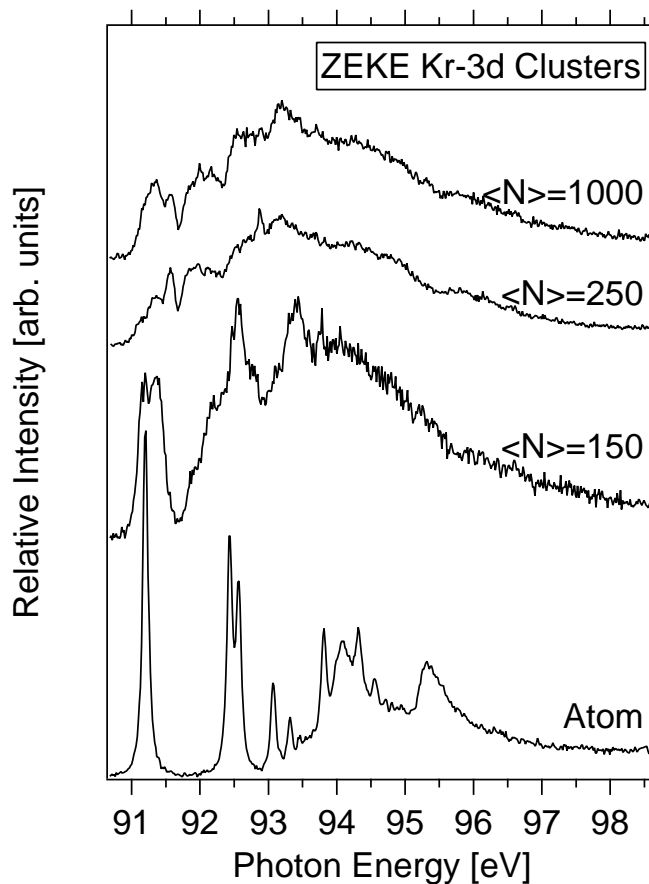
Figure 11.8: Series of ZEKE photoelectron spectra of atomic krypton and krypton clusters in the Kr 3*d* excitation regime.

In Fig. 11.7 the open circles represent the raw data and the solid lines show the least-squares fits. At high photon energies the important feature of the data is a symmetric tail, and in the fits the Lorentzian width is determined by this tail. This data analysis of the spectra was performed using Voigt line shapes for the low-lying (5p and 6p) Rydberg states of the Kr atom. The fits indicate a Lorentzian width of 88 meV and a Gaussian broadening of 30 meV. The 3d thresholds have been fitted with a PCI profile of a Gaussian width of 370 meV. The Lorentzian width was kept the same as for the Rydberg states. The 3d ionization threshold is shifted to lower energy by 110 meV ($3d_{5/2}$ IP=93.810 eV, $3d_{3/2}$ IP=95.012 eV). As in the Ar case, the asymmetry is different between the two components, for $3d_{3/2}$ it is 3.744 and for $3d_{5/2}$ it is 3.724, with a root-mean-square deviation of 4 meV.

For the sake of brevity the presentation of the calculated energies by using the Rydberg formula and quantum defect numbers will be omitted. However, they are nevertheless present in the fitted spectrum, as seen in Fig. 11.7.

Small intensities of low-energy electrons can arise in the Rydberg regime as well as in the 3d continuum, at least double relaxation process and resonant shake-off which give rise to low kinetic energy electrons [157, 165]. However, it appears to be more realistic to model this by a step function. Therefore we have chosen a Victoreen function [167] for each spin–orbit component. This models the pre-edge background, the location of the

edge jump, and the intensity of low kinetic energy electrons. A careful analysis of the data shows that the presence of the Victoreen function does not modify the asymmetry parameter.

Clusters are prepared in a supersonic jet expansion of neat krypton, where cluster sizes up to 1000 atoms per cluster are obtained by expanding neat krypton through a 50 μm nozzle at stagnation temperatures down to -120 °C and stagnation pressures of 5 bar. Total electron yield spectra are obtained using a channeltron multiplier which is mounted in 1 cm distance from the cluster beam. ZEKE photoelectrons are measured by delaying the X-ray light pulse before extracting the ZEKE photoelectrons with a small voltage pulse of typically 6 V/cm [201].

A series of total electron yield spectra of krypton clusters is given by Knop *et al.* [75]. Cluster specific resonances occur at average cluster sizes $\langle N \rangle > 150$. This is well-visible in the regime between 91.3 eV and 92.3 eV which is almost transparent in the atom. Intense bulk exciton bands are dominating the TEY spectra of large clusters. These bands occur at 91.6 eV and 92.9 eV. The bulk excitons are observed for cluster sizes which are larger than 250 atoms, because of the increasing bulk to surface ratio. Surface excitons remain weak in total electron yield spectra, since their contribution is small relative to unclustered atoms in spectra containing only small clusters. This is also true for large cluster conditions, where most of the atoms are bound in the bulk. The spectrum recorded at $\langle N \rangle = 1000$ shows still an appreciable contribution of the atomic component. This is because the cross section of the atomic lines is by factor of four larger than the bulk exciton lines [202]. If a contribution of 7% of the atomic component is subtracted, one obtains a spectrum which is quite similar to the absorption cross section of the solid [202]. Evidently, the TEY detector also accepts electrons from the surroundings of the cluster beam, which contains mostly atoms. Differences occur in the regime of surface excitons (91.36 eV and 92.61 eV) which are still visible in the cluster spectrum in contrast to the condensed phase absorption cross section.

Fig. 11.8 shows a series of ZEKE photoelectron spectra of krypton clusters. These spectra are recorded at decreased spectral resolution because of the low signal strength of ZEKE photoelectrons. The atomic spectrum shows intense resonances at 94.1 eV and 95.35 eV, which do not occur in the TEY spectrum. These are a result of the direct Kr $3d$ photoionization process (Kr $3d_{5/2}$ and Kr $3d_{3/2}$). The maxima are shifted to higher energy compared to ESCA data because of the post-collision interaction effect [157]. As the cluster size is increased one observes a complicated evolution of the ZEKE signal. Differences with respect to the TEY spectra occur in terms of the more efficient suppression of atomic contributions. This is a result of the smaller acceptance angle of the ZEKE photoelectron spectrometer compared to TEY detector. The ZEKE spectrum recorded at $\langle N \rangle = 1000$ is dominated by bulk exciton transitions. Most probably, the Kr $3d$ ionization energies are considerably redshifted in large clusters (91.9 eV and 93.1 eV), which are in a similar energy regime as obtained for condensed krypton [117].

11.3   Ne 1s excited neon clusters

Fir. 11.9 shows the gas phase spectrum of neon electron yield is in good agreement with the existing result [203]. Two sharp peaks at 867.1 and 868.8 eV in gaseous Ne correspond to the $1s \rightarrow 3p$ and $1s \rightarrow 4p$ transitions, respectively. Ionization potential of 1s electron
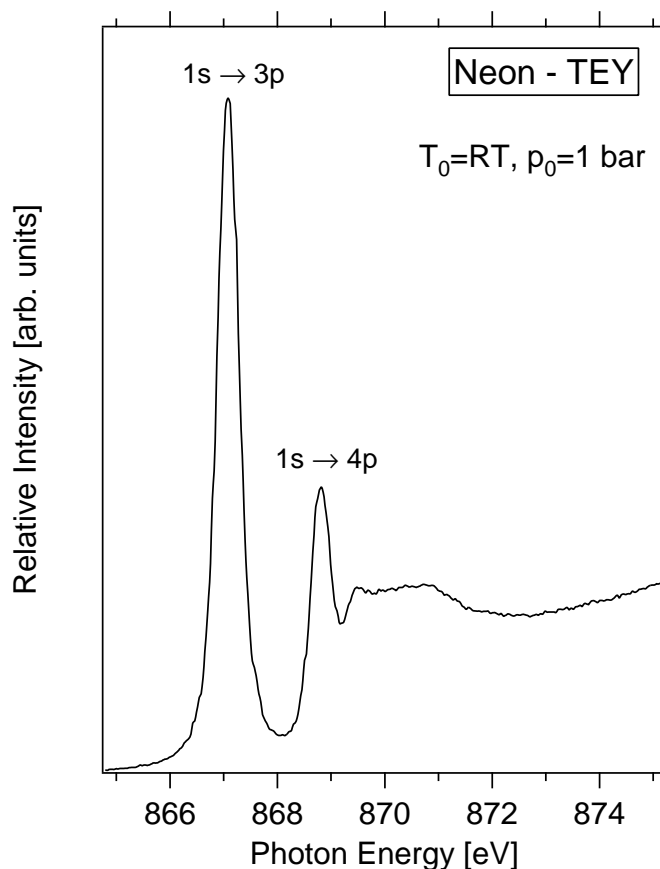
Figure 11.9:   Total electron yield (TEY) spectrum of krypton in the vicinity of the Ne 1s-edge

in gaseous Ne, 870.2 eV, is deduced from the two peak positions with the Rydberg formula and agrees well with the value of 870.21 eV obtained from a high-resolution K-emission spectrum [204]. The spectrum of solid Ne has close resemblance with that of gaseous Ne, that is, two sharp peaks are observed at 868.3 and 869.6 eV corresponding to the sharp peaks in gaseous Ne. When the sample is solidified, the two sharp peaks shift to high energy side by 0.8–1.2 eV and the separation between the first and second peaks decreases (1.7–1.3 eV), which are due to solid state effect. The peaks seem to be due to the excitonic transitions because of then sharpness. The observed band width (FWHM) of the $1s \rightarrow 3p$ resonance line in gaseous Ne is 0.63 eV, while its theoretical (radiative + Auger) width is estimated to be 0.37 eV [163].

The ZEKE spectrum from Fig. 11.11 is dominated by a rather broad structure peaking at 870.446 eV, far beyond the nominal threshold at 870.17 eV [205]. This peak corresponds to direct photoionization from the Ne 1s core level. The shift away from threshold and the peak shape in general is principally determined by the PCI effect: electrons which are photoemitted at threshold leaving an ion with a core vacancy are recaptured by the ion after the Auger emission. Electrons which are emitted with some kinetic energy loose almost all this energy during the Auger decay are detected in the ZEKE spectrometer. The peak shape is determined by the various decay channels and the lifetime of the core
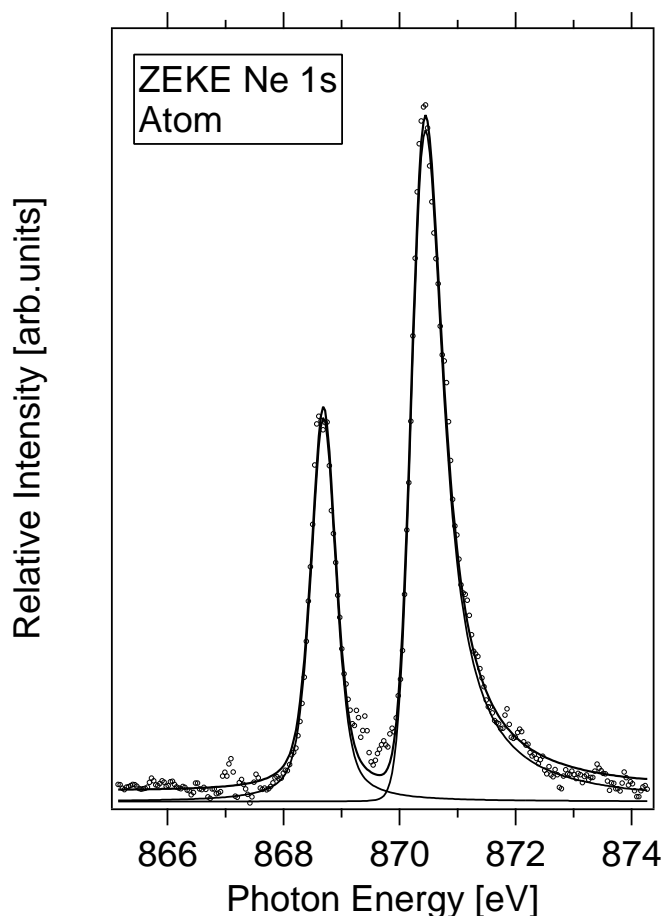
Figure 11.10: ZEKE spectra of Ne atoms in the Ne 1s regime. The experimental results are represented by hollow circles, full lines correspond to individual profiles, where the sum of all components is indicated by a thick black line. The $1s \rightarrow 4p$ transitions are fitted with Voigt profiles.

hole ion.

These simulations were made using the PCI theory as formulated by Armen *et al.* [193] for ionization near threshold. The procedure used was as follows. For each photon energy, the "nominal" kinetic energy of the photoelectron was calculated, then using this energy the shift in the Auger electron peak was determined. From the shift in the Auger spectrum the photoelectron energy was recalculated using conservation of energy. A similar procedure has been used by Avaldi *et al.* [182]. The important parameters in this type of simulation are the kinetic energy of the Auger electron and the lifetime of the core hole state undergoing the Auger decay. According to the literature [206] more than 90% of the neon core hole ions decay via single Auger decay.

The deconvolution of the raw ZEKE spectra is shown in Fig. 11.10. The life time of the core-hole is assumed to be unchanged for the atom and clusters. It is considered by a Lorentzian with a width of 270 meV [207]. Gaussian contributions come from the experimental resolution and various broadening mechanisms, such as phonon broadening, the distribution of different clusters in the jet, and the different screening for the different
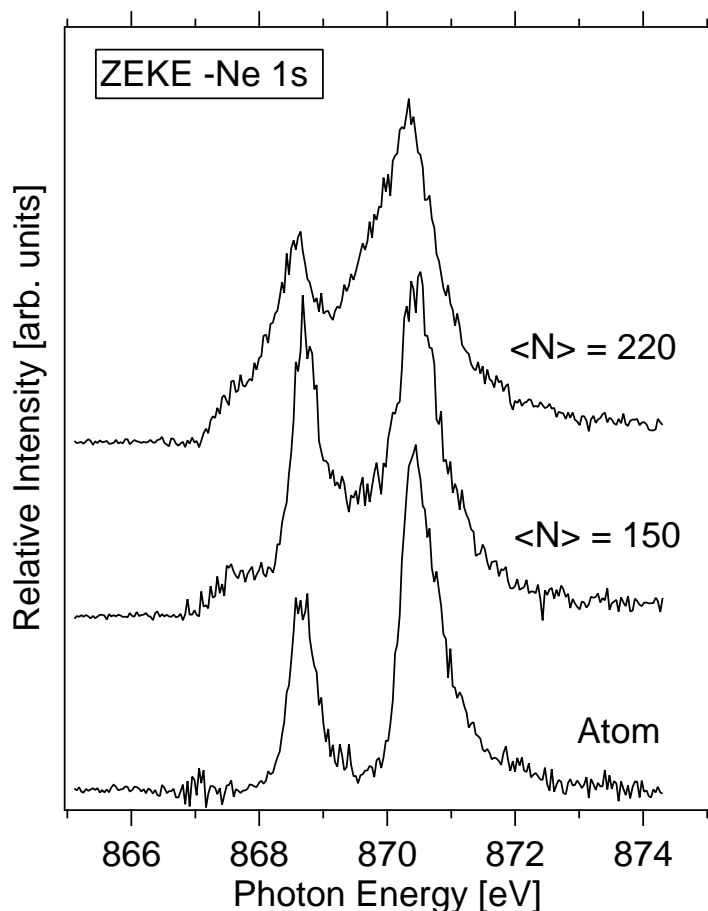
Figure 11.11: Series of ZEKE photoelectron spectra of atomic neon and neon clusters in the Ne 1*s* excitation regime.

positions in clusters. The main peak in Fig. 11.10 has been fitted by using a PCI profile [193] with a Gaussian width of 406 meV and an asymmetry of 1.069, and the $1s \rightarrow 4p$ transition has been fitted with a Voigt profile of Gaussian width of 345 meV. The $1s \rightarrow 3p$ transition is found at 868.69 eV and the ionization threshold is at 870.37 eV. This values are in agreement with refs. [164, 207, 208].

Fig. 11.12 shows the evolution of the Ne 1*s* spectra with different cluster sizes. Here $\langle N \rangle$ is the average size of clusters in the beam and is estimated from empirical scaling laws [51]. For the smallest clusters the structures are rather broad but they get increasingly sharper as the clusters reach an average size of about 220. For the largest clusters the structures of the spectrum of solid Ne [209] are clearly discernable. This implies that the clusters are solid with a substantial amount of order beyond the first coordination shell, and probably have and fcc structure. For the smaller clusters the second coordination shell predicts it's existence for surface atoms, even though most atoms in small clusters are located in the surface. For solid Ne the amplitude of zero point vibration amounts to almost 10% of the interatomic distance [210]. For bulk solids an amplitude larger than 10% is normally taken as typical for liquid (Lindemann criterion). Since the small clusters to have high degree consist of atoms located at the surface where the vibrational
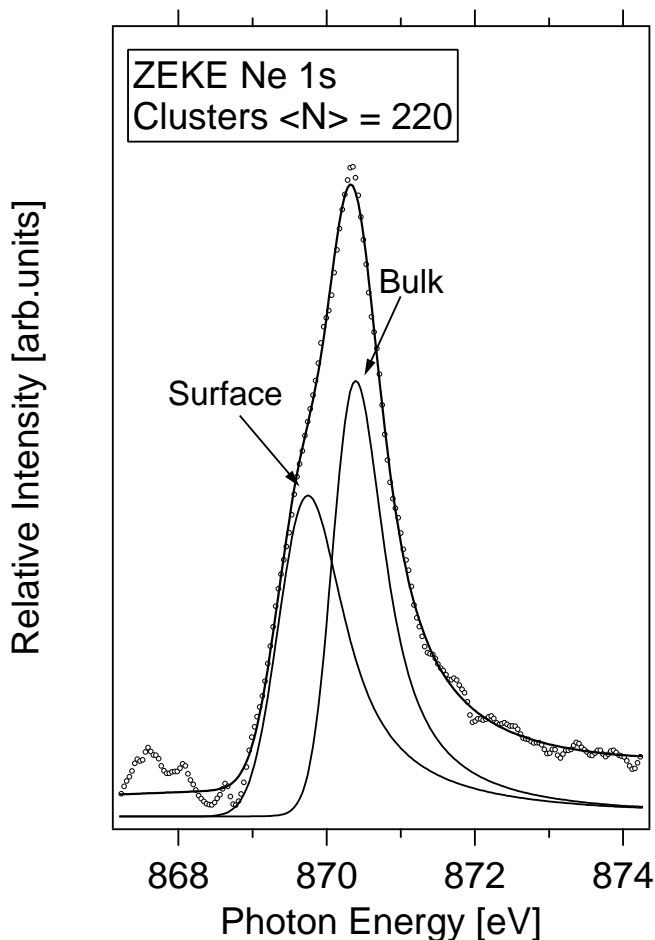
Figure 11.12: ZEKE spectra of Ne clusters in the Ne 1s excitation regime. The experimental results (hollow circles) are obtained from the subtraction of the molecular component from the raw data shown in Fig. 11.10. The full lines correspond to a spectral de-convolution, where the sum of all components is indicated by a thick black line. The thin lines correspond to the individual PCI profiles.

amplitude may be considerably larger, it is likely that the small clusters exhibit a liquid-like behavior. As the clusters get larger, the fraction of atoms at the surface decreases.

We note that Fredermann *et al.* [78] give the fist value corresponding to the surface excitation which may place at 867.6 eV. They note that the 3p bulk excitation seems to be largely unaffected by the overall cluster size indicating that indeed only the cluster environment determines the transition. A similar relative shift from the free atom to the surface and bulk has been observed for Ar where the surface states are found at about 40% of the bulk shift [68]. That means the 1s $\rightarrow$ 3p surface transition shows a strong variation with the cluster size. It is interesting to note that the behavior of the 1s $\rightarrow$ 3p transition because the radius of an excited orbital depends strongly on the principal quantum number and this may provide the opportunity to study effects due to the respective sizes of the excited orbital and the cluster as a whole. A nearest neighbor distance of 3.1 Å in a solid shows that the wavefunctions are likely modified in the cluster,

the orbital may well extend beyond the second coordination shell.

The band calculation shows that the minimum of the first conduction band in solid Ne is Γ_1 which has s-like character [211]. The transition from the 1s state to the s-like minimum of the conduction band is symmetry forbidden. Therefore in the band picture the sharp peaks in the solid Ne are attributed to the $n = 1$ and $n = 2$ excitons (Wannier exciton) associated with the transitions to the second conduction band which has p-like character. On the other hand, the close resemblance in peak position between the solid and gaseous Ne suggests that the two sharp peaks in solid Ne are due to the local excitation of Ne atom (Frenkel exciton). For the excitons in the fundamental absorption of solid Ne, an intermediate type picture had been suggested [212] and then more satisfactory description in terms of the Wannier model was given except for $n = 1$ exciton [213].

Due to the PCI core ionization threshold peaks are broadened and the ionization potential corresponds to the onset rather than the maximum of the peak [96]. The onset of the threshold distribution is 870.2 eV corresponding to the threshold electrons for 1 eV kinetic energy corresponding to the bottom of the conduction band at 869.3 eV for a kinetic energy of 0 eV corresponding to the ionization threshold for surface atoms [214]. The spacing of 0.9 eV between the onset of the surface and bulk emissions is slightly smaller than the electron affinity of 1 eV. This might reflect a less effective polarization screening of the core-hole at the surface due to the incomplete shell of the next neighbors as compared to the bulk. The PCI profile of the surface sites show a Gaussian width of 0.721 eV with an asymmetry of 1.092 in contrast with the bulk sites which give a Gaussian width of 556 meV and an asymmetry of 0.832. Compared with the Ar 2p and Kr 3d excitations, the asymmetry parameter gets lower for the 1s electrons than for 2p or 3d electron. We shall see next how the molecular nitrogen will give us a hint about the K-shell excitation near the threshold.

11.4   N$_2$ 1s excited nitrogen clusters

Resonances below the core ionization threshold of small molecules are usually attributed to one-hole one-electron excitations, i.e. core-to-valence and core-to-Rydberg excitations. However, the electronic decay spectrum of N$_2$ has revealed resonances below the N 1s threshold which do not stem from singly excited states [215]. These resonances were assigned to core-hole double excitations, where the excitation of the N 1s electron is accompanied by a simultaneous excitation of a valence electron. The existence of such states in the region of the core-to-Rydberg transitions has been predicted by Arneberg *et al.* [216]. Whereas double excitations in the continuum are easily observed in the normal X-ray absorption spectrum of N$_2$ [217], the doubly excited states below threshold are much more difficult to detect since they are obscured by the more intense core-to-Rydberg transitions.

The occupied orbitals of N$_2$, are $(1\sigma_g)^2$ $(1\sigma_u)^2$ $(2\sigma_g)^2$ $(2\sigma_{u*})^2$ $(1\pi_u)^4$ $(2\sigma_g)^2$, $^1\Sigma_g^+$. First absorption spectra were reported by Nakamura *et al.* [218] and Bianconi *et al.* [219]. Electron-energy-loss spectra were measured by Wright *et al.* [220]. The first photoelectron spectrum originates from Gelius [221]. The absorption, ion yield and EEL spectra are dominated by the $\sigma_u 1s \rightarrow \pi_g 2p$ $(^1\pi_u)$ transition [222]. With increasing energy, it is followed by a Rydberg series and the broad σ_u shape resonance.

Fig. 11.13 shows the total electron yield of the N$_2$ molecule. Comparing the spectrum
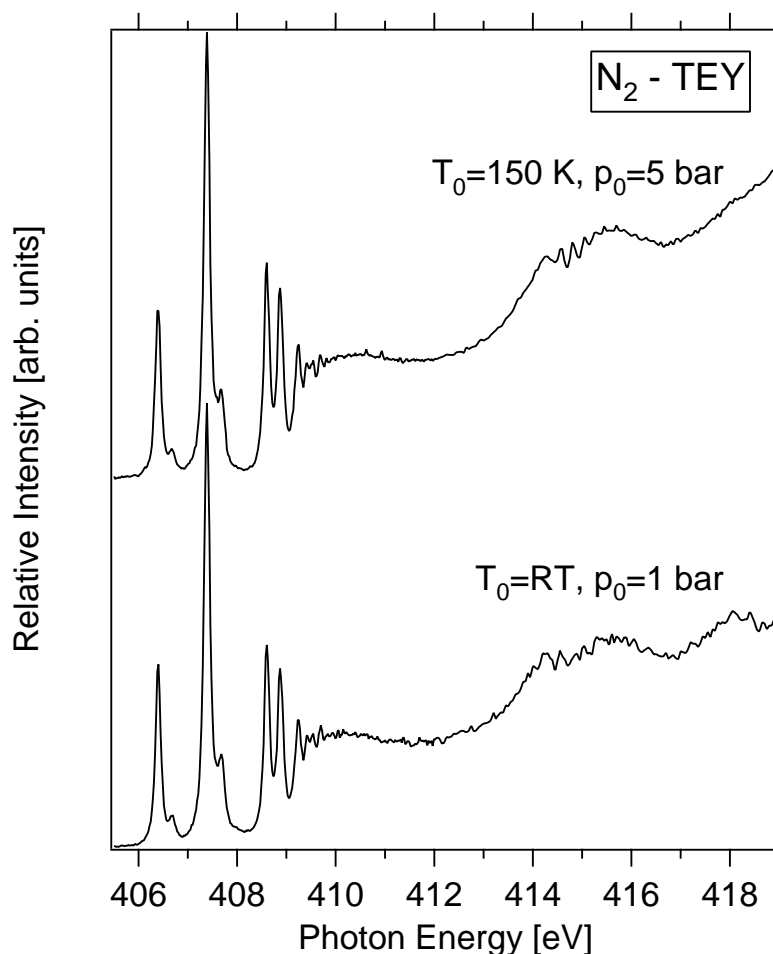
Figure 11.13:   Total electron yield (TEY) spectrum of molecular N_2 $1s$-edge.

at 1 bar of N_2 to that of 5 bar, we see that they look the same, because N_2 at 5 bar does not form clusters. This bonding situation is directly reflected by its K-shell spectrum. The lowest energy resonances around 9 eV below the IP arises from the transition of the $1s$ electron to the N–N anti-bonding $1\pi_g^*$ orbital and the highest energy resonances around 9 eV above the IP is due to a transition to the N–N σ_u^* anti-bonding orbital [223]. The weak structures below the IP are Rydberg resonances which, in general, can be identified by their characteristic term values, i.e., their separation from the IP [224]. The structure near 5 eV above the IP is the multi-electron excitation feature [225, 226].

At incident photon energies above the main-line threshold, not only satellites contribute to the continuum absorption spectrum, but also shape resonances and discrete multielectron resonances. In a threshold photoelectron spectrum, we observe the presence of Rydberg states together with ZEKE electrons, so that each main line gives one peak followed by its correlation satellite peaks. Also, although perhaps less obviously, discrete resonances, both above and below the main line threshold energy, produce ZEKE electrons by the decay of the excited state through an Auger-like process, in which two or more electrons are ejected at once (double Auger decay). The great intensity of these peaks in the ZEKE spectrum may arise through energy sharing between the two emitted
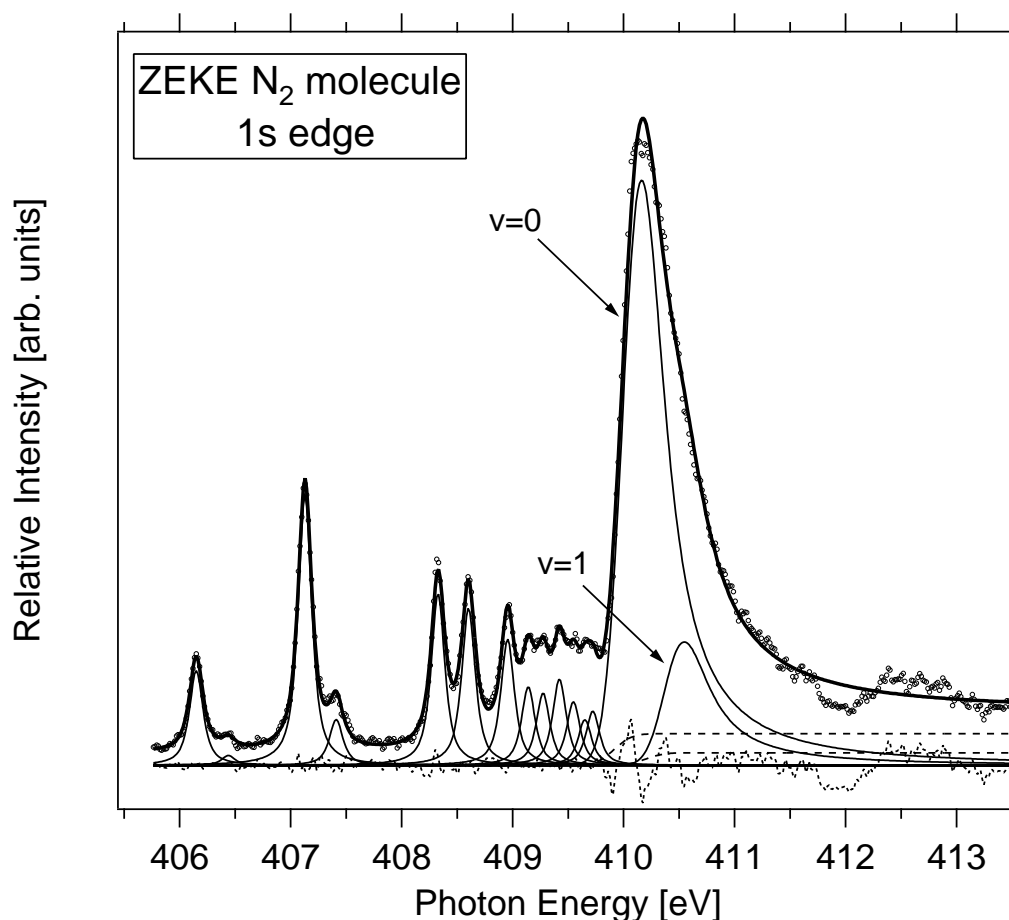
Figure 11.14: ZEKE spectrum of N$_2$ atoms in the N$_2$ 1s regime. The experimental results are represented by hollow circles, full lines correspond to individual profiles, where the sum of all components is indicated by a thick black line. The 1$s \to 4p$ transitions are fitted with Voigt profiles. The long dashed lines correspond to Victoreen functions.

electrons in a way that favors low-energy electrons. Another channel that is expected to yield ZEKE electrons is the decay of states reached by direct ionization, through shake-off processes.

Transitions through the above channels should lead to a ZEKE spectral response that reflects much of the absorption spectrum. However, intensity increases due to classical one-electron shape resonances, in particular, photoionization channels would not be prominent in the ZEKE signal. Rather, peaks that are prominent in the ZEKE spectrum above the main-line ionization threshold, if not due to correlation satellite state thresholds, should be assigned to doubly excited states. Thus, ZEKE spectra can be used, with caution, to distinguish between shape resonances, which yield primarily single, higher-energy electrons, and doubly excited states, which decay by multielectron processes [227]. However, caution is required, because the ZEKE signal may rise slightly at the shape resonance energy due to a double Auger decay.

The ZEKE spectrum of molecular nitrogen in the regime of the N 1s edge is shown in Figure 11.15. It is in agreement with the ZEKE spectrum published earlier [165] The
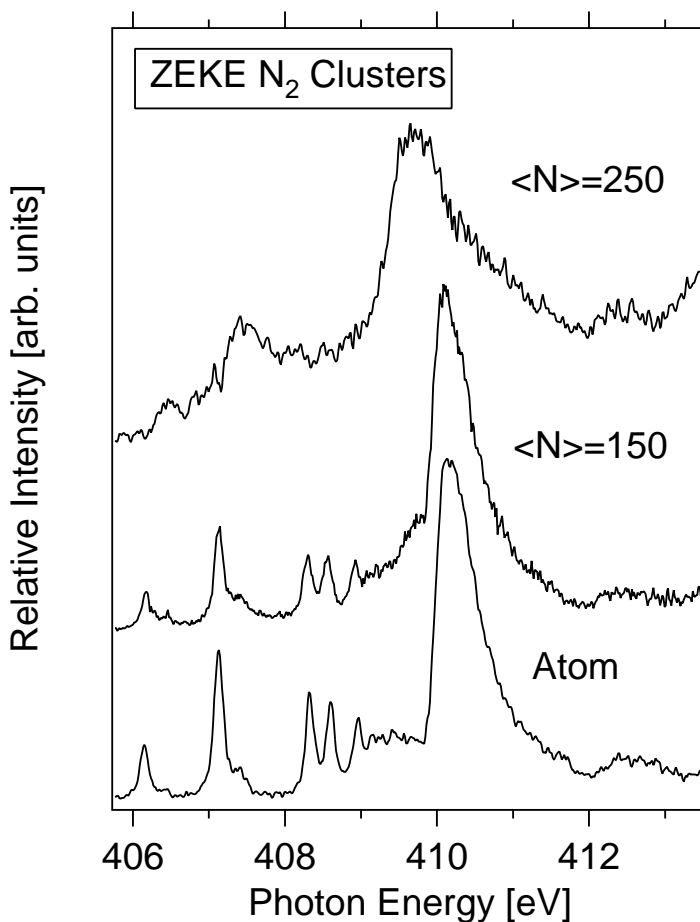
Figure 11.15: Series of ZEKE photoelectron spectra of molecular N_2 and N_2 clusters in the N $1s$ excitation regime.

spectrum shows contributions from resonant excitations of the N $1s \rightarrow \pi^*$ transition at 400.96 eV as well as an intense maximum from the direct ionization process at 409.9 eV. Small changes occur in the ZEKE spectrum when clusters are present in the beam. The molecular spectrum can be described by a single Gaussian centered at 409.96 eV whereas the spectrum containing clusters shows an additional component redshifted by 0.6 eV which is assigned to the threshold ionization signal of nitrogen clusters. This result is in agreement with the redshift of 0.85 eV between the first ionization energy of the molecule and the dimer [228].

We have measured two different cluster sizes $\langle N \rangle = 150$ and $\langle N \rangle = 250$, which are dominated by an intense N $1s \rightarrow \pi^*$ resonance.

The $1s$ main line peaks, because of their asymmetric profiles, were fitted with a Armen's formula [193]. This is the result of post collision interaction (PCI), which is well characterized in atoms. This causes an abrupt change in the potential of both electrons, increasing the kinetic energy of the Auger electron and decreasing the kinetic energy of the photoelectron. This resulted in a significantly larger intensity for this peak than a simple Gaussian function and shifted the maximum peak intensity to higher photon energy. The $1s$ ionization threshold (mainline) appears in the ZEKE spectra as an intense
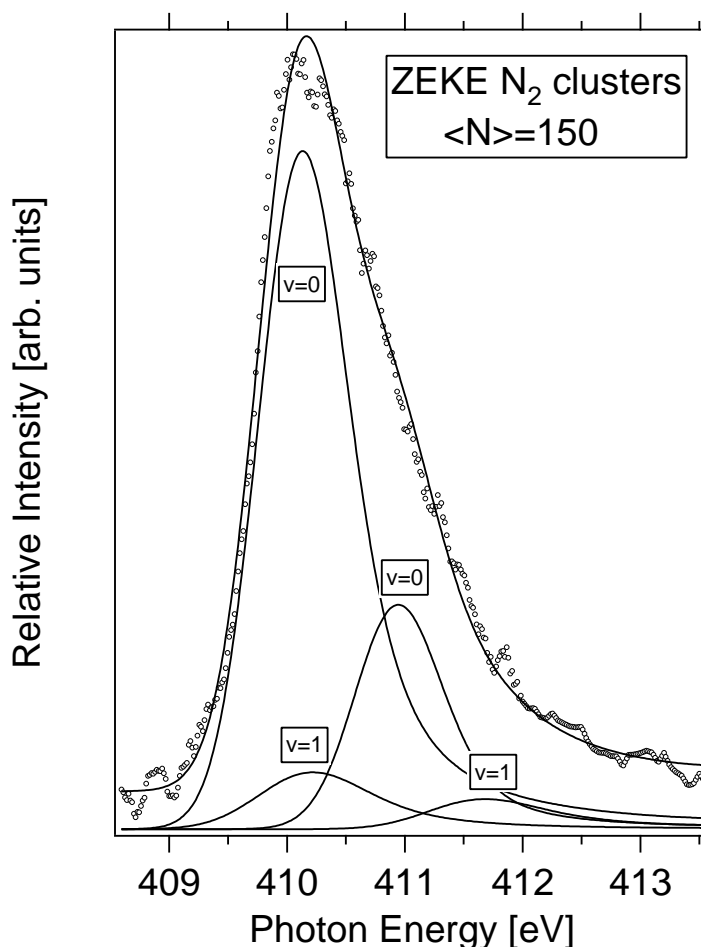
Figure 11.16:   ZEKE spectra of N$_2$ clusters in the N 1s excitation regime. The experimental results (hollow circles) are obtained from the subtraction of the molecular component from the raw data shown in Fig. 11.14. The full lines correspond to a spectral de-convolution, where the sum of all components is indicated by a thick black line. The thin lines correspond to the individual PCI profiles.

peak with vibrational structure. At higher photon energies there is additional structure corresponding to two-electron transitions in the-neutral. These peaks are more prominent in the photoabsorption spectra.

Fig. 11.14 shows the mainline peak and it's vibrational structure. The solid line is a least squares fit to the data, and the dashed lines show the individual vibrational peaks. In contrast to the excited states of the neutral molecule, peaks which correspond to an ionization threshold exhibit post-collision interaction (PCI), which broadens the peaks asymmetrically and shifts the maxima to higher photon energy. This is caused by the interaction of the photoelectron with the Auger electron.

The Gaussian widths for all Rydberg peaks is 60 meV. For N$_2$ the Lorentzian linewidth was determined to be 120 meV. However, the vibrational spacing, and the instrumental broadening is not strong for overlapping functions [193]. The peak positions determined from the spectrum are 410.066 eV for $v = 0$ and 410.339 eV for $v = 1$ and the Franck-

Condon factors, determined using the algorithm of Nicholls [229], are 0.86 and 0.24. The difference in the N $1s$ ionization threshold for IP=409.9 eV [230] compared with that from present results of 410.066 eV is due to the PCI shift, which close to the threshold is more accentuated than far away from the threshold. The results are comparable with those of Medhurst *et al.* [226]. The Gaussian widths of the two vibrational peaks which come from direct ionization are 281 meV with an asymmetry parameter of 0.98 for $v = 0$ and of 1.57 for $v = 1$.

Fig. 11.16 shows the cluster spectrum of the N_2 with the cluster size of 150 atoms. The molecular contribution from the raw cluster spectrum has been subtracted. The spectra are similar to the molecular one, but a redshift of 0.1 eV compared to the isolated molecule is observed. If the cluster size is increased to 250 atoms the redshift is stronger, 0.6 eV compared to the isolated molecule. I will give details about the deconvolution of the mean cluster size of 150 atoms because the substraction of the atomic contribution was more easily done. Future work is planned on cluster sizes $\langle N \rangle = 250$ atoms. Fig. 11.16 has been fitted with the PCI line shape of Armen *et al.* [193]. Details of the line shape is given in a separate chapter.

The N $1s$ photoemission given by Kassühlke *et al.* [214] give an IP of the N $1s$ ionization threshold in solid of 408.85 eV. This is about 1 eV less than the gas phase [40], and in good agreement with the value of 409.4 eV obtained for nitrogen dimers [228] where different values are obtained compared to core ionization thresholds. In the spectrum in Fig. 11.16 the ionization threshold for $v = 0$ of the surface is 409.799 eV and for $v = 1$ is 410.105 eV. The shift is caused by the PCI effect. These results are quite different from those of Kassühlke *et al.*, but we are investigating smaller N_2 clusters and the shift compared to the isolated molecule is expected to be smaller. The second vibrational band in cluster, which may be attributed to the bulk, for $v = 0$ the IP is 410.694 eV and for $v = 1$ it is 411.000 eV. As we can see, the vibrational splitting which was obtained from the fitting of the molecular spectrum is in good agreement with the cluster spectrum. In all fitting line shapes the Lorentzian was kept constant and equal to the natural life time of the N $1s$ core-hole. As in the molecular spectrum, we observe an increase in the Gaussian broadening, which is for $v = 0$ and $v = 1$ 0.461 meV for surface components and 0.396 meV for bulk components. The asymmetry of the surface is 1.2, compared to the bulk value of 0.89. This tells us that the peak shape of the N $1s$ ionization becomes asymmetric in the clusters but the line shape of the surface sites in the cluster is less asymmetric than that of bulk sites. If we compare the results for the atomic and molecular line shapes we can talk about $2p$ and $3d$ excitations, which give higher asymmetry compared with the $1s$ excitation where the asymmetry parameter of the line shape is smaller.

Solid Ar, Kr and Ne are van der Waals bonded insulators and rare gas clusters are important model systems in cluster physics. In conclusion we have investigated the dynamics of the Ar $2p$, Kr $3d$, Ne $1s$ and N $1s$ photoionization in clusters, corresponding to different cluster sizes. These clusters consist of surface and bulk sites. We have observed a smaller asymmetry in the peak shape at the surface sites, and even smaller for bulk sites for a kinetic energy around 60 meV. These results are similar to the work on condensed rare gases and photoemission results on non-resonant processes, which will be discussed in the next chapter. We note that the present consideration is qualitatively reasonable for all weakly bound molecular and van der Waals systems.

Chapter 12

Radiative Decay of Core-Hole State: Ar $2p$

This chapter will investigate the emission of ultraviolet fluorescence radiation from variable size argon clusters. The fluorescence excitation spectra reveal strong fluorescence intensity in the Ar $2p$-continuum, but no evidence for the occurrence of discrete low-lying core-exciton states in the near-edge regime. This finding is different from the absorption and photoionization cross section of argon clusters and the solid. The results are consistent with the formation of singly charged, excited moieties within the clusters, which are assigned as sources of the radiative emission in the 280 nm regime. A fast energy transfer process (interatomic Coulombic decay (ICD)), which has been proposed by recent theoretical work, is assigned to be primarily the origin of these singly charged, excited cations besides intra-cluster electron impact ionization by the Auger electrons. Our findings give first possible experimental evidence for ICD after excitation in the core level regime [231].

Before going on, I would like to ask the question: what is the probability for Ar to emit X-ray fluorescence? I hope that by the end of this chapter, the answer will be obvious.

12.1 Experimental results: Fluorescence excitation in Ar clusters

Rühl and coworkers [89] have investigated the third continuum of $2p$-excited Ar clusters by dispersed fluorescence spectroscopy. The motivation for the present work [231] is to re-examine the emission of UV radiation by Ar $2p$-excitation of variable size argon clusters. In our published paper [231] new insights into the relaxation process occurring in $2p$-excited Ar clusters are presented.

The results are assigned in terms of plausible relaxation processes occurring in the 2p-excitation regime. A comparison with recent work on radiative relaxation of argon aggregates indicates that predominantly singly charged moieties give rise to the emission of 250-300 nm radiation [29]. This implies that charge separation mechanisms are active, which occur after electronic relaxation of the core hole. Besides electron impact ionization within clusters caused by Auger electrons, the interatomic Coulombic decay (ICD) mechanism proposed in theoretical work [25], appears to be a plausible way to rationalize the experimental findings. The ICD-mechanism corresponds to an ultrafast energy trans-
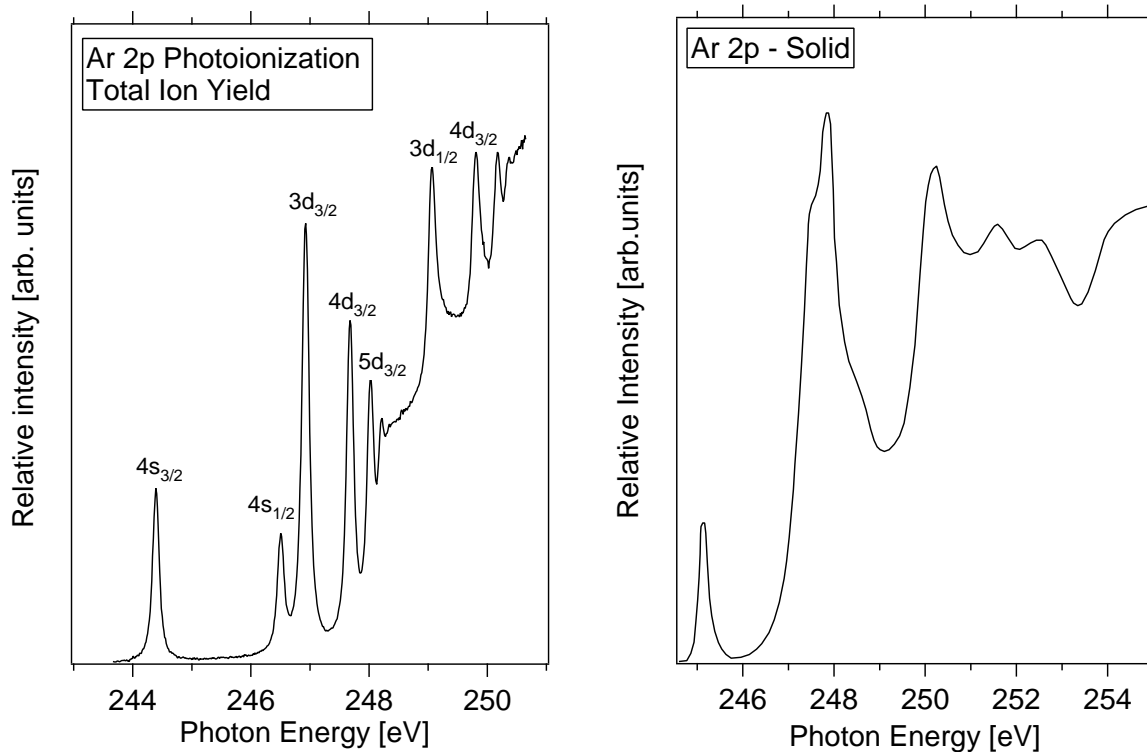
Figure 12.1: Comparison of the Ar $2p$ spectra of (a) atomic and (b) solid argon [232]. (a) The total ion yield (TIY) of argon atoms near the Ar $2p$ threshold reveals a series of Rydberg transitions that converge to the $^2P_{3/2}$ and $^2P_{1/2}$ thresholds.

fer process within clusters that is proposed to occur in the core level regime [30]. The present results indicate that this mechanism fully explains the dominant occurrence of excited singly charged moieties in core ionization continua, which decay via the emission of fluorescence radiation in the ultraviolet regime [231].

Fig. 12.1(a) shows the total cation yield of atomic argon in the $2p$ excitation regime [168, 218]. Fig. 12.1(b) presents the $2p$ spectra of crystalline argon solid [232]. The total photoionization cross-section, which is a sum of the partial cross section of Ar^+, Ar^{2+} and Ar^{3+} charged states, near the L threshold of argon is shown in Fig. 12.1. The single photoionization cross-section of singly charged Ar^+ near the L threshold shows prominent peaks in the resonance states of the Rydberg series, $2p^{-1}ns$ and $2p^{-1}nd$. The background continuum below the resonance region is caused by the other M-shell ionization. The double and triple photoionization cross-sections, Ar^{2+} and Ar^{3+} remain low below the L threshold and then a gradual rise is observed near the L threshold. It is well known that the Rydberg states strongly affect the formation of the multiply charged ions as well as singly charged ions. Therefore, one or two electron shake-off in the Auger process takes place not only above the L threshold but also in the Rydberg states.

In the excitation to the Rydberg states, intermediate ionic states, for instance, something like $2p^{-1}3s^{-1}nl$, are caused by the decay from the $2p$ hole state, $2p^{-1}nl$. On the other hand, in the excitation of the background continuum around the resonance states, similar intermediate ionic states may be considered to be the main products and then
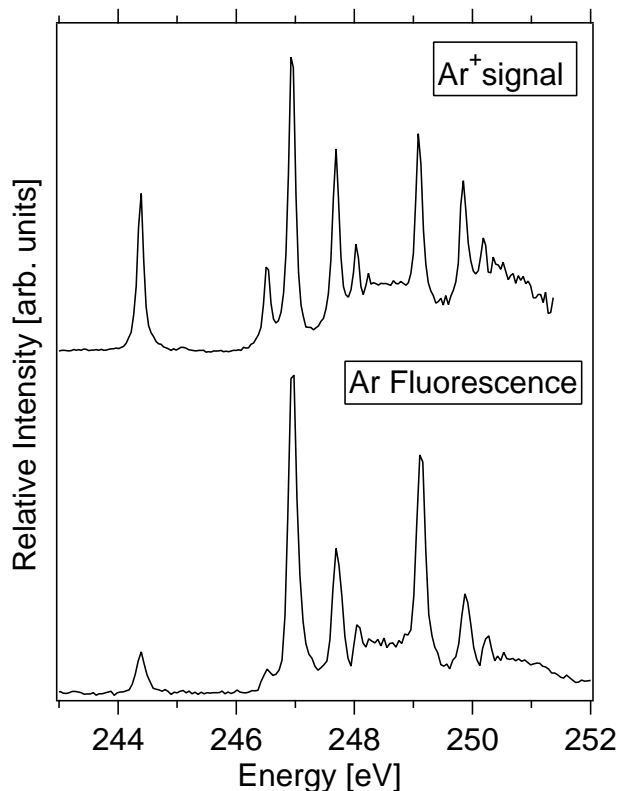
Figure 12.2: The visible fluorescent radiation emitted as a function of the incident photon energy is compared with the Ar$^+$ signal. There is a small continuous background in each spectrum that is produced by direct ionization and/or excitation of the Ar valence electrons. The 4s level can fluoresce only in the vacuum ultraviolet region [233]. Thus the small visible signal observed must be caused by shake-up of 4s–5s as predicted by theory [234].

multiply charged ions are formed as in the case of excitation to the Rydberg states.

The visible fluorescent radiation emitted as a function of the incident photon energy is compared with the Ar$^+$-ion signal in Fig. 12.2. There is a small continuous background in each spectrum that is produced by direct ionization and/or excitation of the Ar valence electrons. The similarity between the two spectra above the $^2P_{1/2}$ limit leaves little doubt that the Ar$^+$ continuum is created by electron capture into Ar$^+$ satellite states that subsequently fluoresce in the visible and vacuum UV spectral regions. The 4s level can fluoresce only in the vacuum ultraviolet region [235]. Thus the small visible signal observed must be caused by shake-up of 4s–5s, as predicted by theory [35].

The total fluorescence yield is similar in shape to the Ar$^+$ yield. Both spectra (Fig. 12.2) show intense maxima in the pre-edge regime corresponding to excitations into $2p^{-1}nl$ Rydberg states. The signals drop in the Ar 2p photoionization continuum, since Auger relaxation produces primarily Ar^{2+}. Post-collision interaction explains the finding that Ar$^+$ can be found above the Ar 2p ionization thresholds [65, 80, 89, 89, 105]. The shapes of the fluorescence excitation spectra also indicate that Ar$^+$ is predominantly the source of UV/VIS fluorescence near the Ar 2p edge. This is consistent with the well-known result that the Ar$^+$ yield and the photoabsorption cross section are different in shape [65, 168].
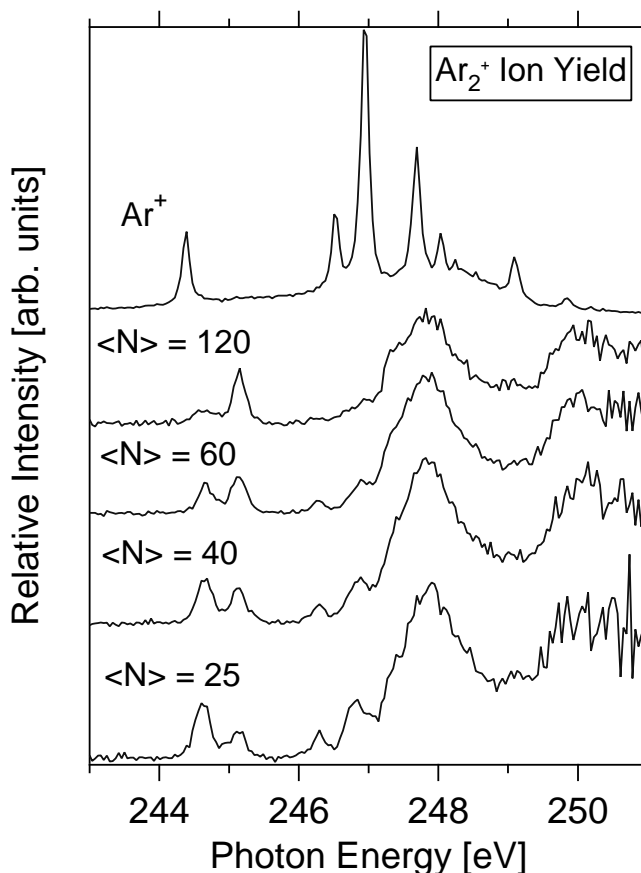
Figure 12.3:   The dimer cation yield shows intense resonances in the near-edge regime which are characteristically blueshifted and broadened relative to the atomic Rydberg transition. This can be attributed to the presence of surface and bulk excitons.

However, it cannot be completely excluded that fluorescence of excited Ar^{2+} occurs in the $2p$ near-edge regime. This requires fluorescence light detection at shorter and longer wavelengths than detected in the present work [236, 237, 238]. A comparison of the Ar^+ yield with the total fluorescence yield shows that the intensity of the $2p_{3/2}^{-1}4s$ resonance ($E = 244.390$ eV) is lower in the total fluorescence yield than in the Ar^+ yield [65].

Note, as in the Ar^+ and fluorescence spectra (Fig. 12.5), there is a small continuous Ar^{2+} signal caused by direct double ionization of the Ar valence shell. The cross section of this continuum steadily decreases as a function of photon energy from its maximum at about 100 eV [239, 240].

Figure 12.3 shows the argon dimer cation (Ar_2^+) yield in variable size argon clusters ranging from 120 to 25 atoms using the $\langle N \rangle$ calibration from reference [60]. This cation yield shows intense resonances in the near-edge regime, which are characteristically blueshifted and broadened relative to the atomic transitions [21, 65, 68]. Singly charged fragments have been investigated before [21]. We observe for the lowest energy features a dominant contribution of $4s$-bulk excitons occurring at 245.15 eV and a weak signal from $4s$-surface excitons at 244.65 eV. The corresponding transition occurs in the atom at 244.390 eV [168] (cf. Fig. 12.3). The origin of these energy shifts has been discussed

extensively before [68], so that Figure 12.3 essentially serves for a comparison with the series of fluorescence excitation spectra of variable size argon clusters and as an independent proof for the proper operation of the jet and the formation of clusters.

The clearest changes are observed for the $2p_{3/2} \rightarrow 4s$ transition, which is split into two separate components at somewhat higher energy (see Fig. 12.3). The low-energy component dominates at small cluster sizes, whereas the higher one gradually becomes more prominent with increasing cluster size. The lowest of the lines is observed to shift to higher energy to 244.58 eV (+0.19 eV, values in brackets give the shift relative to the atomic $2p_{3/2} \rightarrow 4s$ transition) for the average cluster size to 244.70 eV (+0.31 eV) for the average cluster size. No comparable shift is observed for the high-energy line, which has an energy of 245.14 eV (+0.75 eV) varying less than ± 0.01 eV over the whole size range. The $2p_{3/2} \rightarrow 4s$ transition energy as a function of cluster size is shown in Fig. 12.3. Some geometric considerations are helpful for the interpretation of the spectra from the Fig. 12.3. As the cluster size increases, the fraction of atoms located at the cluster surface will gradually decrease, whereas the bulk fraction will increase. The coordination of the individual argon atoms will also change, from 0 for the isolated atom to 8 or 9 for an atom in the surface of solid argon and 12 for an atom located in the bulk. In the atom, the final $2p_{3/2}^{-1}4s$ Rydberg state has an appreciably larger spatial extent than the ground state, but unlike in more strongly bonded systems such as semiconductors and metals, hybridization with orbitals on the neighboring atoms is practically negligible in this case.

Fluorescence excitation spectra of variable size clusters are shown in Fig. 12.4. The average cluster size ranges from $\langle N \rangle = 20$ to $\langle N \rangle = 120$. We have subtracted the atomic contribution from the total fluorescence yield of argon clusters 12.4 by using the atomic fluorescence yield. The difference spectra are shown in Fig. 12.6. Subsequently all spectra are normalized to the photon flux of the soft X-ray monochromator, so that only contributions from clusters remain. Evidently, the spectra suffer from low signal strength and thus a limited signal to noise ratio, since they were recorded with the same spectral resolution as the atomic spectra. This was necessary in order to prove whether discrete resonances from exciton states occur in fluorescence excitation spectra in the Ar $2p$ near-edge regime. This indicates that the fluorescence intensity increases substantially with the cluster size $\langle N \rangle$. The experimental results on fluorescence yields of variable size clusters shown in Fig. 12.6 indicate that there are distinct differences compared to the spectra shown in Fig. 12.3 and 12.2. The cluster size dependence of the fluorescence excitation spectra indicates that there is hardly any signal detected at $\langle N \rangle = 20$, corresponding to a stagnation temperature of -25°C at 5 bar stagnation pressure. A weak fluorescence signal is observed at $\langle N \rangle = 25$ with two weak steplike onsets at photon energies of 248 eV and 250 eV. At $\langle N \rangle = 40$ these are slightly redshifted to 247.3 eV and 249.4 eV, respectively, and there is weak fluorescence intensity above the background level at photon energies above 246 eV. Moreover, there is a broad resonance between 254 eV and 259 eV, which has been observed before [65, 89]. The spectrum recorded at $\langle N \rangle = 60$ is similar in shape. The clearest spectral dependence of the fluorescence is observed at $\langle N \rangle = 120$. The step-like onset energies are also observed at 247.3 eV and 249.4 eV and there is an onset above the background noise level at 246.6 eV. These results indicate that there is almost no evidence for contributions to the fluorescence from variable size clusters from low-lying surface and bulk exciton states, which are superimposed to the step-like structures.

The Ar $2p$ ionization energies in clusters are known to shift to lower energy as a
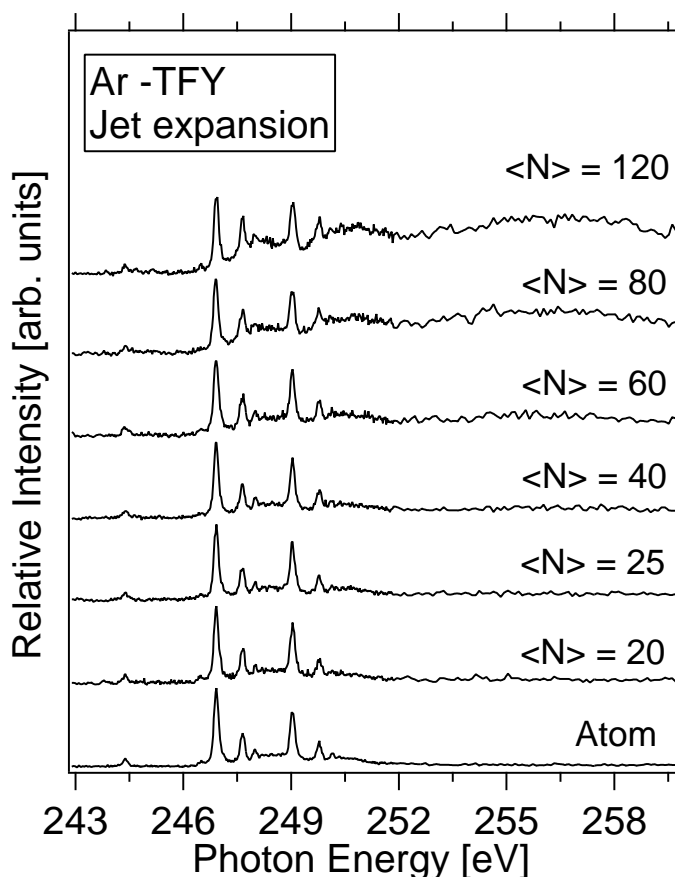
Figure 12.4: The fluorescence yield of a supersonic jet expansion of argon at different average cluster sizes $\langle N \rangle$. Cluster fluorescence occurs mainly in the Ar 2p continuum, indicating that double or multiple ionization leads to the emission of fluorescence photons from clusters.

function of cluster size as a result of polarization screening [68, 130]. Evidence for this assignment comes on the one hand from the energy difference between both step-like features, which are separated by the spin-orbit splitting of 2.1 eV [82]. On the other hand, the energy position of the step-features is similar to the onset of direct $2p$ photoionization from bulk sites, as published by Björneholm *et al.* [68]. However, a close inspection of the values derived from Ref. [68] indicates that the step-like onsets already occur at the low energy part of the features that are observed in photoelectron spectra, i.e. somewhat below the vertical core ionization energies of bulk sites. This is expected for a threshold signal which extends into the regime below a vertical transition. In the case of small clusters the onsets of the fluorescence yield occur at somewhat higher energies, which are assigned to weak fluorescence from surface sites. The size evolution of the signal strength indicates that radiative relaxation comes preferably from bulk sites of large clusters. This interpretation is also in agreement with the occurrence of the broad continuum feature between 254 eV and 259 eV, which is found in total electron yields of large clusters [65].

The wavelength range of fluorescence radiation that contributes to the excitation spectra is shown in Fig. 12.7. It consists of a broad resonance located in the wavelength regime
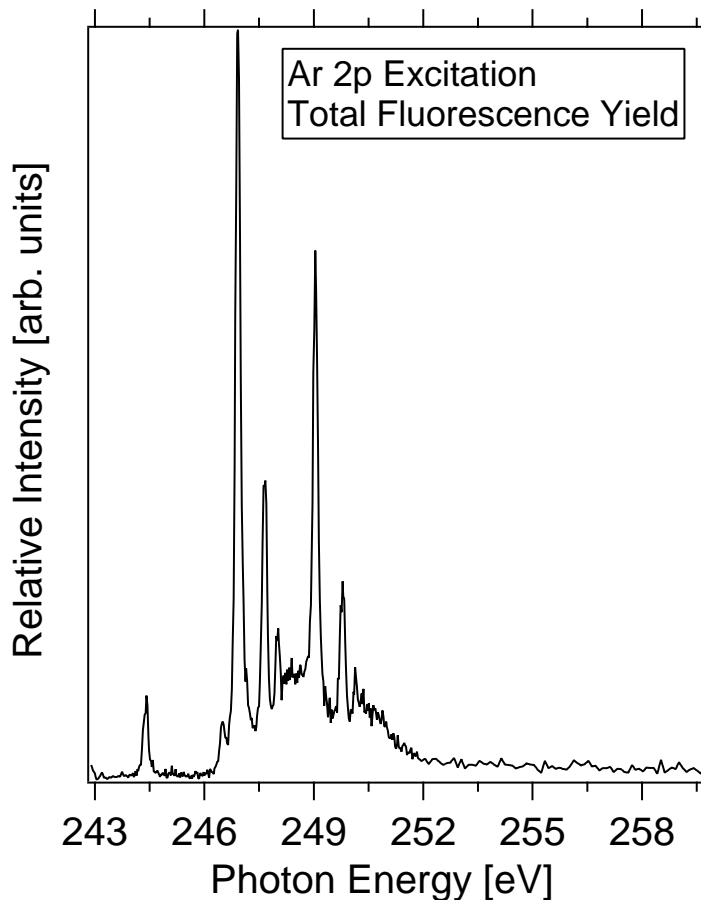
Figure 12.5: The total fluorescence yield (TFY) of argon atoms near the Ar $2p$ threshold. It is similar to the Ar$^+$ yield. The atomic fluorescence vanishes in the Ar $2p$ continuum as a result of the dominant normal Auger effect.

between 250 nm and 300 nm. The spectrum shown in Fig. 12.7 indicates that there are indeed no discrete features resulting from atomic lines in the spectral regime under investigation. But there is a remarkable difference in comparison with the previous work, where a broad double-hump feature was observed with maxima at 200 nm and 270 nm, respectively [89]. The short wavelength feature near 200 nm is not observed in the present work. A plausible explanation for this difference is found by the fact that different experimental set-ups are used. The previous one was optimized for the spectral regime around 200 nm [89], whereas the present one looses substantially detection sensitivity with decreasing wavelength [68]. Thus, we expect that the transmission drops significantly below 250 nm and only the long wavelength feature is detected. The results on fluorescence excitation spectra indicate, however, that the observed energy dependence of the fluorescence yield is comparable to previous work [89].

Ogurtsov and co-workers [241] indicates that the fluorescence near 200 nm is clearly due to singly charged argon, which follows from the low excitation energies in the outer shell excitation regime, where double ionization cannot occur [241]. This result is in agreement with work of Amirov *et al.*, who developed a model in order to rationalize the emission of continua of UV-radiation [242]. Specifically, it was proposed that the continua
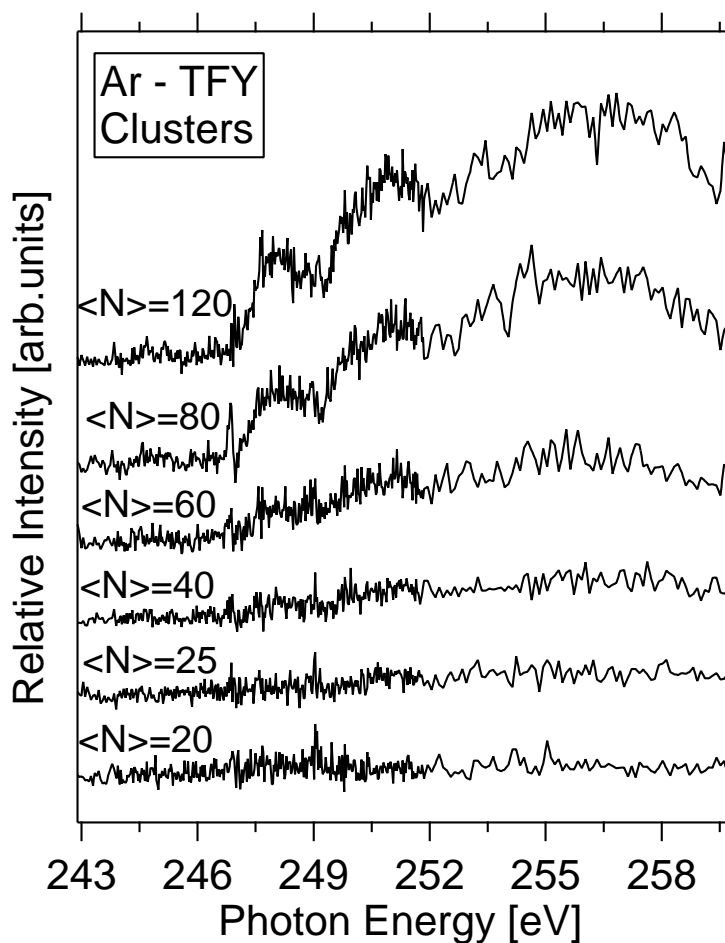
Figure 12.6: Total fluorescence of argon clusters, where the atomic contribution has been subtracted. The spectra show that the formation of excitons in clusters gives rise to the emission of fluorescence photons. These result indicate that there is almost no evidence for contribution to the fluorescence from variable size clusters from low-lying surface and bulk exciton states, which are superimposed to the step-like structure.

can be attributed to transitions from low lying Rydberg states of singly charged dimer cations to low repulsive states.

The fluorescence observed in the present work [231] indicates that this process occurs almost exclusively in the $2p$-continuum. The fact that there is hardly any evidence for UV-fluorescence from clusters in the pre-edge regime already indicates that the process is initiated by the production of the $2p$-core hole and the ejection of the core electron into the $2p$-continuum. It is clear that this process is tightly related to double or even multiple ionization of clustered atoms, that are preferably located in the bulk of the clusters. Further support for this interpretation comes from the step-like onset of the fluorescence excitation spectra, since resonant excitations into low-lying near-edge exciton states lead preferably to singly charged products via spectator autoionization. It is, however, not clear that necessarily doubly charged atoms are the origin of the fluorescence photons in clusters. Previous work of Rühl *et al.* [89] was in line with the model of Langhoff, who
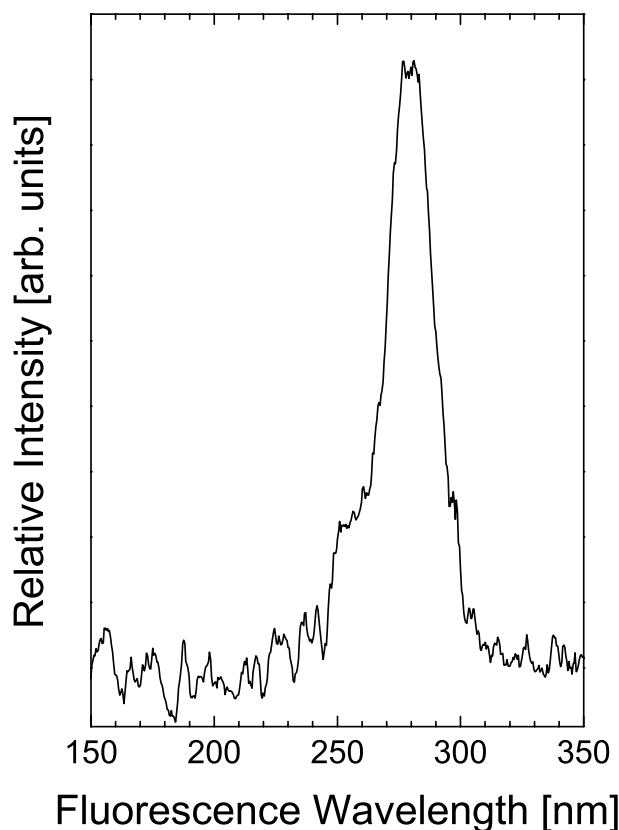
Figure 12.7:   Dispersed fluorescence spectrum recorded using undispersed, quasi-monochromatic undulator radiation at $E = 263$ eV. The sensitivity of the detector drops at wavelengths below 250 nm, indicating that the signal shown in this regime is essentially due to background noise. Clusters are formed at a stagnation pressure of 5 bar and a stagnation temperature of -100°C, corresponding to an average cluster size $\langle N \rangle \geq 80$.

considered the formation of charge transfer excimers [233, 243].

More recent theoretical work by Cederbaum and co-workers predicts that there are efficient, ultrafast energy transfer processes active in inner-valence shell excited clusters, which take place in the femtosecond time regime [25, 26, 27, 244, 245]. These are termed interatomic Coulombic decay (ICD), illustrated schematically in Fig. 3.3 in chapter 3. The lifetime of these multiply charged states is significantly reduced for bulk sites compared to dimers. Related work predicts that ICD is not only present in inner-valence-excited, but also in core-excited clusters [30]. This implies that ICD will follow the Auger decay, which is localized to the excited atom. The ICD lifetime is expected to drop with the number of nearest neighbors of the excited center [27, 30, 244], implying that bulk sites are most sensitive to this ultrafast process. Experimental proof for the occurrence of ICD has been given recently, which also includes short lifetimes of the order of a few femtoseconds [246, 247, 248].

Previous work by Santra and Cederbaum on core-excited neon dimers as a simple model system indicates that more than 20% of all dications that are produced by the Auger process will undergo ICD forming a trication [30]. The doubly charged species are calculated to be inner-valence shell excited. Considering the reduced ICD lifetime of

bulk sites mentioned above [30, 244], the importance of ICD increases with cluster size. A consequence of ICD is that sites next to the core-excited atom undergoing the Auger decay become singly charged, and the net charge of the cluster becomes at least +3. The charges located on different atoms, as a result of the ICD mechanism, will repel each other. This may even lead to fission [22], if doubly charged clusters contain less than 91 atoms [249] or triply charged ones less than 226 atoms [250].

One may consider that the Auger electron can also be inelastically scattered at neighboring sites within the cluster. The process can also occur in the femtosecond time regime. This process will also lead to triple or multiple ionization of clusters, similar to ICD. Such electron impact ionization of the nearest neighbor shell within a cluster or a solid will preferably occur in large clusters and solids, where inelastic scattering is most efficient for sites deep in the bulk. This is unlike ICD, which is mostly sensitive to the nearest neighbor shell [30, 244]. Thus, in ICD the shells of further distant sites are less important than in inelastic scattering. As a result, ICD is dominating for bulk sites of small clusters, i.e. the cluster size regime under investigation.

De-excitation processes of core-excited atoms and molecules lead to the formation of excited cations, which are stabilized by the emission of fluorescence radiation in the ultraviolet/visible regime. In these systems the Auger effect is most efficient for the formation of excited, singly charged species, which are stabilized via the emission of fluorescence radiation [36, 91]. In the case of weakly bound clusters, there is the additional ICD process following the Auger decay, leading to charge de-localization via an energy transfer. As a result, singly charged, excited moieties in clusters are formed, which cannot be stabilized via the emission of electrons. Their radiative de-excitation is assumed to be observed in the present experiments. Moreover, the Auger decay may also lead to the formation of excited dications, which are expected to emit radiation, but likely in a different wavelength regime. The central question is in which wavelength regime singly or doubly charged moieties within a cluster decay via the emission of ultraviolet radiation.

In contrast, long wavelength radiation, observed in the present experiments around 280 nm is most likely due to the emission from excited, singly charged sites. These sites are assigned to be preferably formed via ICD in the cluster size regime under investigation using the present experimental results. This result provides evidence that fluorescence spectroscopy is a sensitive probe for the predicted ICD mechanism of core-excited clusters.

Chapter 13

Size-dependent Core-to-Rydberg Excitations: N_2

Van der Waals systems, such as nitrogen, are a key part of chemical physics of clusters, because they can be studied both experimentally and theoretically in a wide size range, reaching from a few to several thousands of molecules. In particular, they provide prototype species to study the mechanisms leading from molecular to bulk properties.

Focusing on molecular nitrogen clusters in the small-size regime is very useful in itself, as very scarce data are known on these systems to date. This is unlike the information that is available on molecular and bulk nitrogen. Three forms of solid nitrogen can be found, the most stable is the cubic α phase. A hexagonal β phase appears above 36 K. Finally, a third γ phase is stable at high pressures. The β phase melts at 63.1 K at atmospheric pressure [251].

A few experimental investigations on the structure of finite-size $(N_2)_n$ clusters have been carried out in the past decades. An electron diffraction study has been reported by the Orsay group, giving evidence of structural similarities between the diffraction patterns of Ar and N_2 clusters [252, 253]. According to previous results on argon [254], the polyicosahedral structure was attributed to small-size N_2 clusters, whereas large-size clusters displayed a crystalline cubic structure.

Using unrelaxed cluster models in the cubic α phase, it was possible to derive information about large molecular nitrogen clusters: the presence of defects in the cubic structure, the amplitude of molecular librational motions larger than in the bulk cubic solid, and the correlated motions of nearest-neighbor molecules. Intermediate size N_2 clusters, have not been considered as realistic cluster models [255]. Very large N_2 clusters, with an estimated size of more than 3×10^4 molecules, have been studied by Beck and coworkers using stimulated Raman spectroscopy [256]. These authors were able to probe, in the jet expansion the freezing of liquid-N_2 droplets leading to solid clusters of the (high-temperature) hexagonal β phase. In a electron diffraction work performed on growing clusters [257], Kovalenko and co-workers detected the $\alpha - \beta$ phase transition occurring when the cluster size was about 1.5×10^4 molecules.

From the theoretical point of view, only little attention has been paid to the structure of $(N_2)_n$ clusters up to now. Using two different model potentials, both Rodríguez and co-workers [258] and Bertolus and co-workers [259] have shown that there were large similarities between the geometry of the molecular centers of mass in the $(N_2)_n$ cluster

and the structure of Ar$_n$, in the size range $n \leq 13$. Recently, we have used the same potential-energy function as Bertolus *et al.* [259] to investigate clusters containing as much as 55 molecules [260]. A similar conclusion was reached concerning the similarities between N$_2$ and Ar. Just above 13 molecules, (N$_2$)$_n$ clusters tend to add molecules over the icosahedral surface, thus maximizing the number of nearest neighbors. This construction scheme leads to the polyicosahedra which were already observed in argon clusters [254]. As the number of external molecules increases, the inner part of the cluster becomes more and more distorted, and starts to reorganize in icosahedral layers, as observed in argon clusters [59] near the size 55. Despite these strong similarities, some quantitative differences were also observed. The main result of all these numerical works is that (N$_2$)$_n$ clusters exhibit local or global icosahedral symmetry for all sizes in the range $n \leq 55$, except at $n = 38$, where the structure is a truncated octahedron. As in the case of rare-gas atomic clusters [261, 262], this should not be taken as evidence for the general trend of an increasing stability of the bulk geometry, but only as a peculiar, pathological feature of the potential-energy surface at this size. Contrary to (CO$_2$)$_n$ clusters [263], icosahedral structures have greater stability than cubic structures up to the size 55, where the double-layer Mackay icosahedron is found.

Resonances below the core ionization threshold of small molecules are usually attributed to one-hole one-electron excitations. However, the electronic decay spectrum of N$_2$ has revealed resonances below the N $1s$ threshold which do not stem from singly excited states [215]. These resonances were assigned to core-hole double excitations, where the exciton of the N $1s$ electron is accompanied by a simultaneous excitation of a valence electron. The existence of such states in the region of core-to-Rydberg transitions has been predicted by Årneberg *et al.* [216].

Core level excitation of isolated molecules is governed by core-to-valence and Rydberg transitions [264]. When a molecule is bound in van der Waals clusters or in the condensed phase, the core-to-valence transitions are slightly modified by the surroundings of the absorbing site, which is a result of the strong localization of the electronic transitions [1]. This leads to small spectral shifts, which are of the order of a few meV [20]. These spectral shifts have been assigned in terms of dynamic stabilization, which primarily occurs in clusters containing molecules of high symmetry [265].

The conversion of atomic Rydberg states into the corresponding core excitons has been investigated in the past for rare gas clusters as well as the corresponding condensed gases [68, 202]. The conversion of molecular Rydberg states into the corresponding core excitons as well as core-to-valence transitions have also been investigated in the past, where the spectra of the gas phase species were compared to the condensed molecules [266]. The detailed understanding of such spectral changes requires high resolution experiments, which have become available more recently [214]. The motivation of the present work [11] is to investigate theoretically and experimentally the origin of the spectral shifts which are related to the cluster size.

13.1   Theoretical calculations

Molecular nitrogen clusters were modeled using the Böhm-Ahlrichs intermolecular potential [267], previously employed in bulk [267] and finite-size systems [251, 259, 268, 269] studies. It consists of atom-atom repulsion-dispersion forces of the Buckingham form
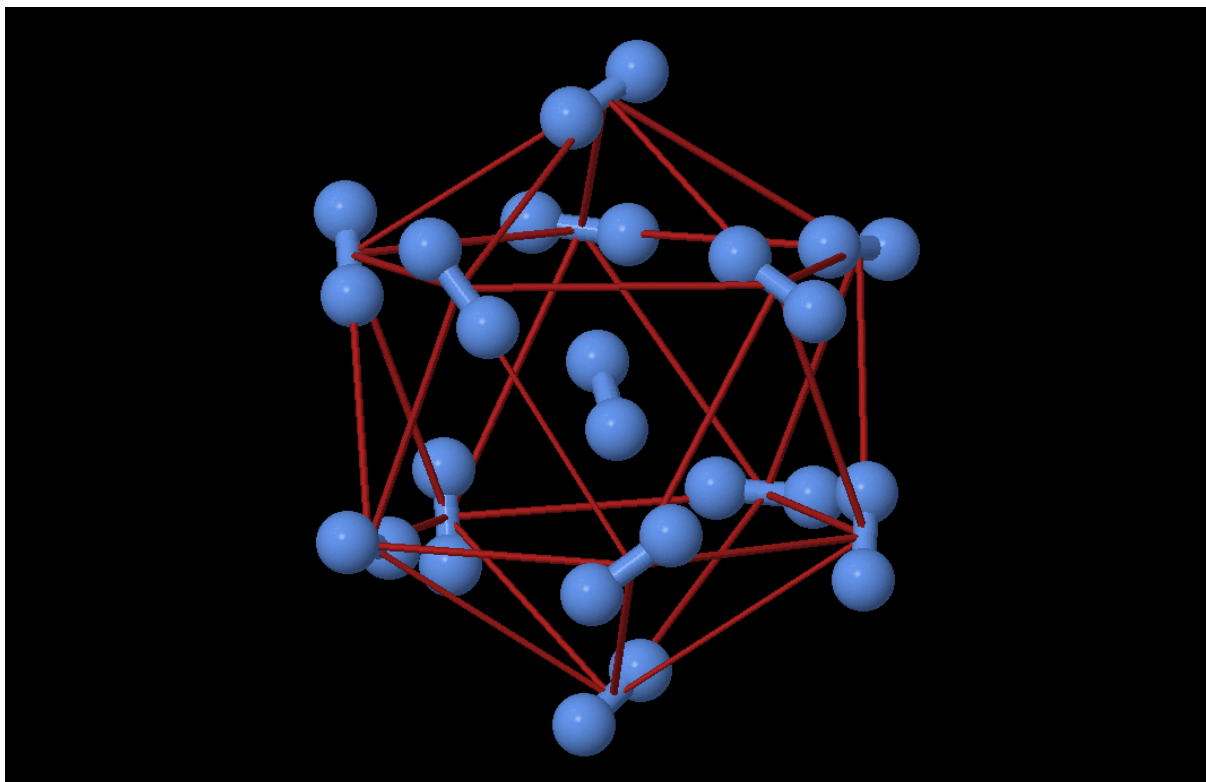
Figure 13.1: Geometry of the icosahedral $(N_2)_{13}$ cluster.

$V(r) = A \exp(-\alpha r) - C/r^6$, plus an electrostatic interaction term between partial charges located on the N–N axes. The parameters are taken as $A = 125502.7$ kJ/mol, $\alpha = 3.461136$ Å^{-1}, and $C = 1641.2749$ kJÅ^6/mol. Two positive charges of $+0.373e$ are located at ± 0.847 Å on the molecular axis with respect to the center of mass, and two negative charges $-0.373e$ are located at ± 1.044 Å. The fixed distance between the two nitrogen atoms is equal to 1.094 Å.

The electrostatic repulsion is partly related to the quadrupole-quadrupole interaction. It is mainly taken into account even in self consistent field (SCF) level calculations. The dispersion force is considered by MP2 calculations where $(N_2)_{13}$ cluster is fully optimized by using the Gaussian03 program [138] with a 3-21G* basis set, yielding at the end of the geometry optimization an icosahedral geometry.

Geometry optimization of the $(N_2)_{13}$ consists of 12 molecules from the first shell around a single central molecule. The first shell is characterized by oriented molecules, which represent "inner-surface sites" and "outer-surface sites". The inner-surface sites consist of five molecules. These are somewhat closer to the center of the cluster than the other seven molecules, which form the outer-surface sites.

Ab initio quantum mechanical calculations are carried out by using the GSCF3 code [270, 271] on molecular N_2 and $(N_2)_{13}$. The N $1s$ excited states are obtained from the improved virtual orbital or static exchange (STEX) method [272, 273, 274], which are applied to the fully relaxed SCF potentials for the localized N $1s$ ionized states for all atoms in N_2 and $(N_2)_{13}$. The primitive basis functions given by Huzinaga *et al.* [275], N(73/7) are used as [721/52] for neutral nitrogen atoms and [4111111/31111] for ionized
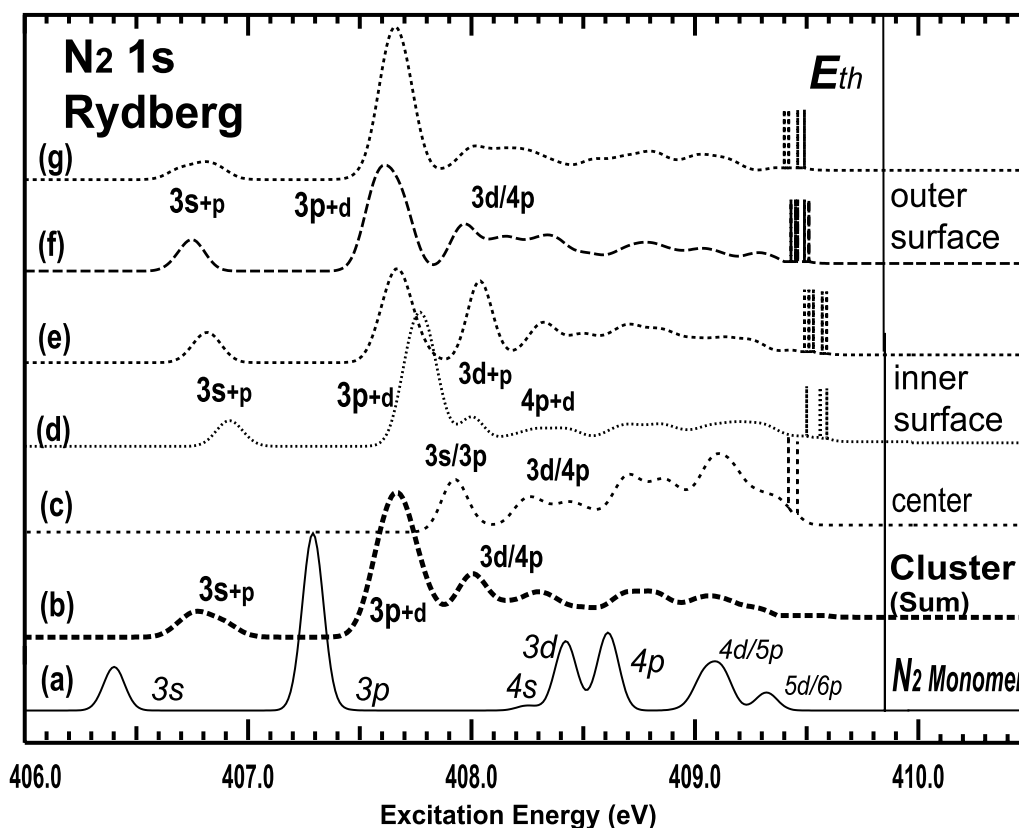
Figure 13.2: Calculated N $1s$ →Rydberg/exciton region in molecular and clustered nitrogen: (a) molecular spectrum; (b) sum of the individual components of $(N_2)_{13}$ in icosahedral geometry, where the components are shown in (c)-(g); (c) central nitrogen molecule; (d) and (e) inner-surface molecules; (f) and (g) outer-surface molecules. The vertical lines correspond to the N $1s$ ionization energies E_{th} in the free molecule (long vertical line) and in clustered molecules (short vertical lines), respectively.

N. The basis set of neutral N does not have polarization functions. Therefore, redshifts of the N $1s$ ionization threshold E_{th} of the excited atom may be underestimated by the present basis set, where E_{th} is stabilized by the polarization effect of the surrounding neutral molecules in cluster.

Figure 13.2 shows the calculated N $1s$ photoabsorption spectrum of molecular N$_2$ and a $(N_2)_{13}$ cluster, which are based on the STEX approach [272, 273, 274, 276]. Fig. 13.2(a) corresponds to the spectrum of free N$_2$ which is similar to the experimental spectrum, and showing only slight deviations in transition energy. The calculated N $1s$-ionization energy E_{th} is 409.84 eV for the isolated N$_2$ molecule. Figures 13.2(c)-13.2(g) correspond to the spectral components of $(N_2)_{13}$, where Fig. 13.2(b) is the weighted sum of the absorbing atoms. The center of the cluster contains one molecule, which is surrounded by a shell of 12 nearest neighbors. As a result, both atoms of the central molecule have the same local environment. This central molecule is suitable to simulate bulk properties of nitrogen clusters as well as the condensed phase. Figure 13.2(d) corresponds to five nitrogen atoms near the center of the cluster, i.e. these belong to the molecules that represent the inner-surface sites. These atoms are located in the regime between 3.1 and
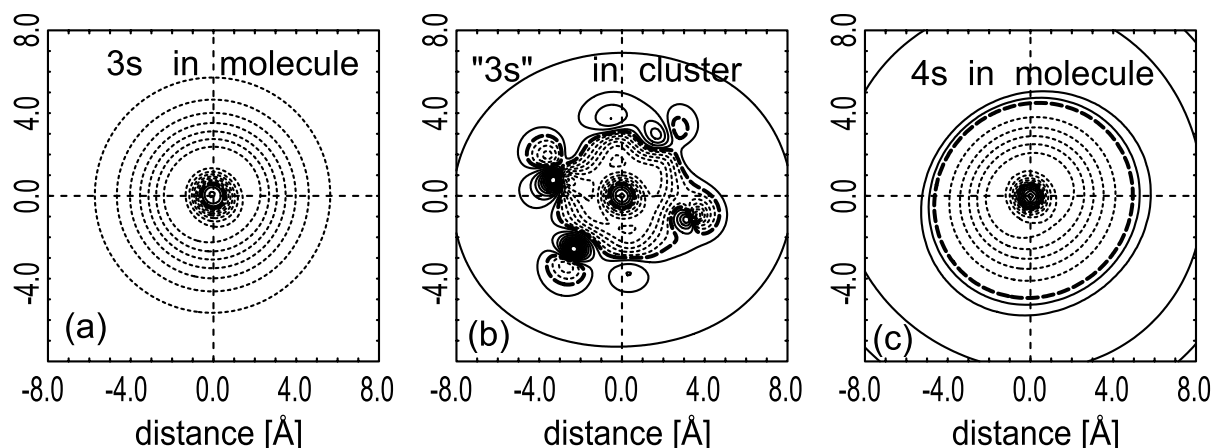
Figure 13.3: Two-dimensional contour maps of the $3s$ and $4s$ orbitals in molecular and clustered nitrogen $[(N_2)_{13}]$: (a) $3s$ Rydberg orbital of molecular N_2. The central nitrogen molecule in a $(N_2)_{13}$ cluster is shown in an appropriate intersection with one core hole atom, where the surrounding 12 molecules are removed; (b) $3s$ orbital of the central molecule in a $(N_2)_{13}$ cluster with optimized geometry in the same orientation as shown in (a); (c) $4s$ Rydberg orbital molecular N_2 in the same orientation as shown in (a). Full and dotted lines correspond to positive and negative phases. Thick dashed lines correspond to nodes. The outermost node lies outside of the plotted range.

3.2 Å from the middle of the central nitrogen bond. The calculated spectrum of the other group of five inner-surface atoms is shown in Fig. 13.2(e), these atoms belong to the same molecules that are plotted in Figure 13.1, but they are found at a distance between 3.5 and 3.9 Å from the center of the cluster. Fig. 13.2(f) represents the absorption of seven nitrogen atoms from the outer surface of the cluster, which are found in the range from 3.2 to 3.6 Å from its center. Finally, Fig. 13.2(g) represents the group of seven atoms which are bound to the sites plotted in Fig. 13.2(f). These are located 3.7 to 4.0 Å from the center, they also belong tho the outer-surface of the cluster.

These calculations show clearly that the lowest energy Rydberg exciton states (N $1s \rightarrow 3s\sigma$) is sensitive to the geometrical site and there are contributions from the final $3p$ state in clusters. The central molecule has no distinct $3s$ core exciton state, but there is a weak $3s$ contribution, which is embedded in the strong N $1s \rightarrow 3p\pi$ region.

Fig. 13.2 also indicates that the spectral evolution is more complicated in the N $1s \rightarrow 3p\pi$ regime than near the lowest energy resonance, since there are contributions from $3p + d$ final states, in which the $3p$ states have some $3d$ contributions due to the lower symmetry. The outer-surface states are blueshifted with respect to the $3p\pi$-Rydberg state by 330 and 380 meV. The center of the cluster shows a blueshift of almost 500 meV, this is even larger for the central molecule where a blueshift of 630 meV is found from the calculated spectra (see Fig. 13.2(c)). The surface sites contribute to the steep increase of the absorption cross section of the N $1s \rightarrow 3p\pi$ band. The asymmetry and peak shape of this spectral feature in small clusters is due to the substantial redshift of the N $1s \rightarrow 3d\pi$ transitions as well as the N $1s \rightarrow 4p\pi$ transition in clusters relative to the corresponding molecular transitions as shown in Fig. 13.2. Also there is a larger shift for outer-surface
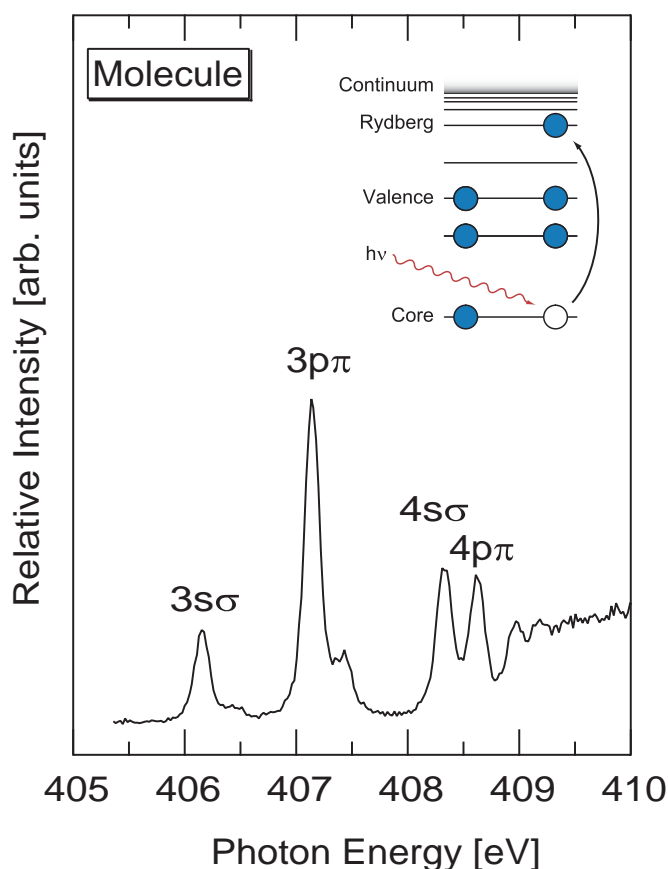
Figure 13.4:   N $1s$-Rydberg regime of molecular nitrogen.

sites than for the inner-surface sites. The central molecule shown in Fig. 13.2(c) has a much smaller redshift of 170 meV.

In Figure 13.3 are shown two dimensional contour maps of the $3s$ and $4s$ Rydberg orbitals in molecular nitrogen (see fig. 13.3(a) and 13.3(c)). The calculations are performed by using the molecular orientation of the central molecule in $(N_2)_{13}$, where the molecules from the first shell are removed from the central molecule which is core excited.

The optimized geometry of $(N_2)_{13}$ is used to calculate the contour plot show in Fig. 13.3(b). This indicates that the "$3s$" state shown in Fig. 13.3(b) is no more the original molecular $3s$ state of spherical shape with two nodes in the radial direction [cf. Fig. 13.3(a)]. It is rather like a $4s$ state with 3 nodes [cf. Fig. 13.3(c)], as can be easily seen from the contour orbital maps shown in Fig. 13.3. This massive destabilization of the $3s$ state shown in Fig. 13.3(b) is characteristic for bulk sites in condensed nitrogen clusters. The $3s$ state shows with an increasing number of nearest neighbors a blueshift, where the smallest spectral shift is found for the outer-surface sites.

13.2   Experimental results

Figure 13.6 shows a comparison of the experimental cluster and solid nitrogen spectra, which have been recorded in the N $1s$-Rydberg regime (405-410 eV). Fig 13.4 shows
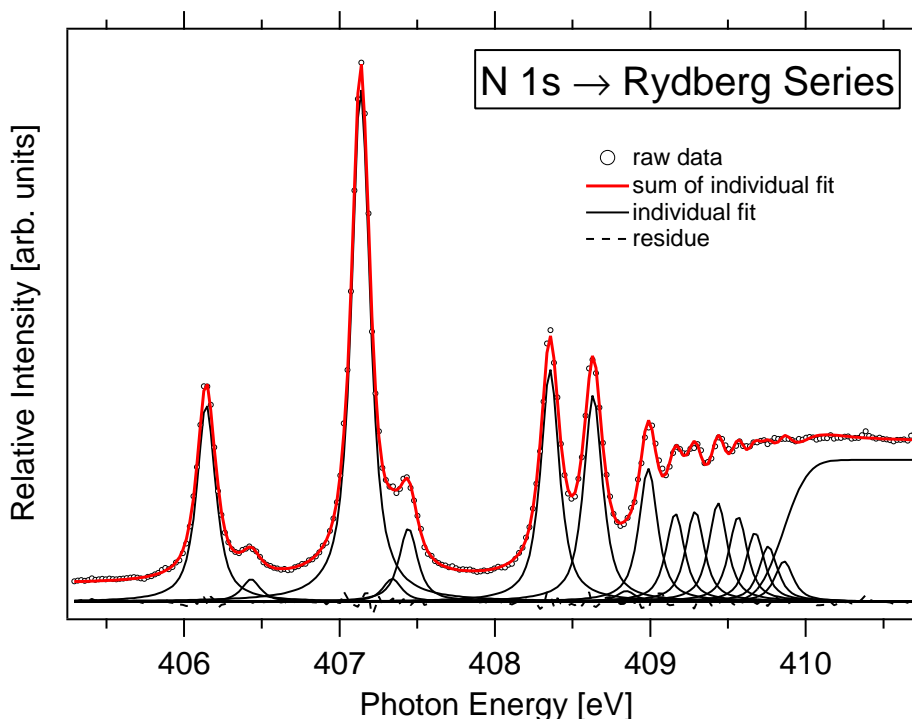
Figure 13.5: N 1s-Rydberg regime of molecular nitrogen. Individual transitions are fitted with Voigt profiles.

the molecular properties. It has been recorded by measuring the N$^+$ yield as a function of the photon energy, similar to previous work, where the N 1s $\rightarrow$ π* transition was investigated [74]. The molecular spectrum has mostly been recorded as a reliable reference for the energy positions of the molecular Rydberg transitions and to determine the energy resolution of the soft X-ray monochromator. The peak shapes of the molecular Rydberg transitions are represented by Voigt profiles, where a Lorentzian width of 118$\pm$5 meV and a Gaussian width of 65$\pm$5 meV (which represents the experimental resolution) are used (see Fig. 13.5).

Two photoion yield spectra of $(N_2)_2^+$ clusters shown in Fig. 13.6 correspond to cluster sizes of $\langle N \rangle$ = 10 and $\langle N \rangle$ = 150. Near the threshold of cluster formation ($\langle N \rangle$ = 10) it is most interesting to investigate the conversion of molecular Rydberg states into the corresponding cluster excitons, as discussed in previous work on variable size atomic clusters [68, 75].

The most intense feature at $\langle N \rangle$ = 10 occurs at $\sim$407.35 eV (see Fig. 13.6). It is tentatively assigned to the surface excitons of the N 1s $\rightarrow$ 3$p\pi$ transition where the corresponding molecular Rydberg state is found at 407.115 eV [40, 277, 278, 279]. The spectrum recorded at $\langle N \rangle$ = 150 is similar in overall shape to that measured near the threshold of cluster formation at $\langle N \rangle$ = 10. However, there are distinct changes as $\langle N \rangle$ is increased. There is also a slight blueshift of both prominent features by about 100 meV, indicating that there are cluster size effects in both bands discussed above. The feature near 407.35 eV builds up in intensity as $\langle N \rangle$ is increased, which indicates that large clusters containing a significant amount of bulk sites also absorb in this spectral regime. This is
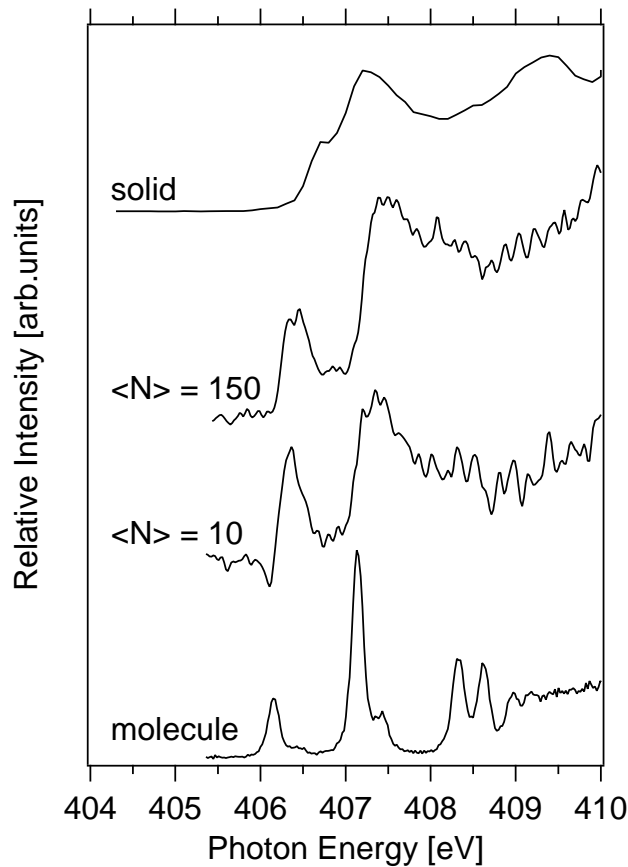
Figure 13.6: N 1s-excitation in the Rydberg regime of molecular nitrogen, variable size nitrogen clusters of $\langle N \rangle = 10$ and $\langle N \rangle = 150$, and condensed nitrogen.

in agreement with the result of the condensed state phase absorption. It also shows a resonance at almost the same photon energy (see Fig. 13.6). Moreover, continuous spectral intensity increases above ~ 408 eV and there are two weak, but distinct resonances at 408.12 and 408.42 eV, respectively, which occur at $\langle N \rangle = 150$. More details are give in ref. [11].

The plot on the top of Fig. 13.6 corresponds to the absorption spectrum of condensed nitrogen, obtained from partial electron yields [279] and is used for a comparison with variable size clusters. Moreover, we observe a distinct shoulder of the low energy feature centered at 406.93 eV. These features have been observed before [214]. The broad feature near 409.45 eV is found in a spectral regime that is slightly above the N 1s-ionization energy E$_{th}$, which is found at 408.85±0.15 eV for condensed nitrogen [214]. The 1s ionization energy is decreased by ~ 1.1 eV relative to the isolated molecule (cf. Ref. 40), which is mostly a result of polarization screening [68]. We expect that the density of states is increased near the N 1s ionization threshold which explains the experimental findings.

The experimental results are assigned in comparison to ab initio calculations which have been shown in the previous section. The present results clearly show that there are specific properties in molecular van der Waals clusters, which do not exist in atomic van der Waals clusters. This concerns the molecular orientation within the cluster, which

strongly affects the inner-shell absorption properties in the Rydberg-excitation regime. It is shown that inner- and outer-surface sites give rise to distinct energy shifts of the low lying surface core excitons. It is assumed, however, that the experimental spectra represent an average over various cluster sizes and molecular orientations in weakly bound clusters, so that it appears to be remarkable that model simulations on the ab initio level are suitable to model successfully the experimental spectra, by using just a single cluster shape.

Conclusions

The studies presented in this thesis deal with resonant and non-resonant excitation of free variable size clusters using synchrotron radiation in the soft X-ray regime.

The post collision interaction (PCI) effect is investigated in free variable size krypton and argon clusters near the Kr $3d$ and Ar $2p$ ionization energies. The core ionization energies of surface and bulk sites in variable size clusters can be clearly distinguished. This is mostly due to the polarization screening. It is found that the asymmetry, which is a consequence of PCI, is characteristically smaller for clusters than for isolated atoms. Moreover, there is less asymmetry for bulk sites than for surface sites in variable size rare gas clusters. We assign the results in terms of mechanisms that are based on quantum mechanical models of post collision interaction.

Complementary experiments on the photoionization of free van der Waals clusters are performed by using zero kinetic energy (ZEKE) photoelectron spectroscopy in the Ar $2p$-, Kr $3d$-, Ne $1s$-, and N_2-regimes. The experimental approach is also suitable to detect cluster size dependent changes in electronic structure. This also allows us to study post collision interaction in variable size clusters. The parameters of the PCI profiles deduced for ZEKE experiments indicate that there are no significant changes in core ionization dynamics compared to near-threshold experiments.

Results from model calculations in Kr $3d$ ionization energy indicate that different geometric sites can be clearly distinguished from each other by their substantial shift in Kr $3d$ ionization energy, though the dimer shows almost the same Kr $3d$ ionization energy as the free atom. A comparison with the experimental results indicates that there is resemblance with the model calculations, even though close-lying ionization energies are blended and require deconvolutions of the experimental spectra. It is evident from the present work that one can observe distinct shifts in core ionization energies in van der Waals clusters that are formed in wide size distributions of a jet expansion.

The emission of ultraviolet fluorescence radiation from variable size argon clusters is investigated with high spectral resolution in the Ar $2p$-excitation regime. The fluorescence excitation spectra reveal strong fluorescence intensity in the Ar $2p$-continuum, but no evidence for the occurrence of discrete low-lying core-exciton states in the near-edge regime. This finding is different from the absorption and photoionization cross sections of argon clusters and the solid. The dispersed fluorescence shows a broad molecular band centered near 280 nm. The present results are consistent with the formation of singly charged, excited moieties within the clusters, which are assigned as sources of the radiative relaxation in the 280 nm regime. A fast energy transfer process (interatomic Coulombic decay, ICD) is assigned to be primarily the origin of these singly charged, excited cations besides intra-cluster electron impact ionization by Auger electrons. Our findings give possibly the first experimental evidence for ICD in the core level regime.

Free, variable size nitrogen clusters are investigated in the N $1s$ excitation regime in comparison with the free molecule and solid nitrogen. The conversion of Rydberg states into core excitons, surface and bulk, was studied. The experimental results are simulated by *ab initio* calculations using $(N_2)_{13}$ as a reasonable prototype cluster structure that allows us to simulate both surface and bulk properties in comparison with the isolated molecule. The present results clearly show that there are specific properties, such as molecular orientation, in molecular van der Waals clusters, which do not exist in atomic van der Waals clusters. It is shown that inner and outer surface sites give rise to distinct energy shifts of the low lying surface core excitons.

Zusammenfassung

In der vorliegenden Dissertation wurden Experimente zur resonanten und nicht-resonanten Anregung von Clustern variabler Größe durchgeführt. Hierzu kam Synchrotronstrahlung im weichen Röntgenbereich zum Einsatz.

Der "Post-Collision Interaction"-Effekt (PCI) wurde im Detail am Beispiel von Krypton- und Argon-Clustern im Bereich der Kr $3d$- und Ar $2p$-Anregung studiert. Es lassen sich die Ionisierungsenergien von Atomen, die an der Oberfläche bzw. im Volumen gebunden sind, klar unterscheiden. Dies ist aufgrund der unterschiedlichen Polarisationsabschirmung möglich, die zu einer Verschiebung der Innerschalen-Ionisierungsenergien führt. Die Linienformen der Photoelektronenbanden werden asymmetrisch, wenn die Anregungsenergie geringfügig über der Ionisierungsenergie liegt. Dies lässt sich auf den PCI-Effekt zurückführen. Es wird beobachtet, dass die Asymmetrie vom isolierten Atom über Oberflächenatome zu den im Volumen gebundenen Atomen abnimmt. Diese Veränderung der Linienformen wird mit Hilfe von Mechanismen, die auf Grundlage von quantenmechanischen Modellen basieren, interpretiert.

Komplementäre Experimente wurden an Argon- und Neon-Clustern zur Nullvolt-Photoelektronen-Spektroskopie (ZEKE) durchgeführt (Anregung der Ar $2p$-Kante, Kr $3d$-Kante, N_2 $1s$ und Ne $1s$-Kante). Auch mit diesem Ansatz lassen sich größenabhängige Veränderungen der elektronischen Struktur in Clustern sowie die Bedeutung des PCI-Effektes bestimmen. Ein Vergleich dieser Resultate mit der Anregung, die nahe der Ionisationsschwelle liegt, zeigt, dass es zu keiner signifikanten Veränderung der Ionisationsdynamik als Funktion der Anregungsenergie kommt.

Berechnungen zur Ioniserungsenergien von Krypton-Clustern im Bereich der Kr $3d$-Anregung zeigen, dass sich einzelne geometrische Orte klar in ihrer Ionisierungsenergie unterscheiden. Das Krypton-Dimer zeigt allerdings fast dieselbe $3d$-Ionisierungsenergie wie das freie Atom. Der Vergleich mit den experimentellen Resultaten zeigt, dass eine gute Übereinstimmung zwischen Modell und Experiment besteht. Allerdings müssen die experimentellen Spektren entfaltet werden, da die relativen Verschiebungen der Ionisierungsenergien zu gering sind und die Rumpflochlebensdauer zu einer Verbreiterung der Banden führt. Die Resultate belegen, dass sich ausgezeichnete Werte für Rumpfniveau-Ionisierungsenergien bestimmen lassen, obwohl die Cluster in breiten Größenverteilungen vorliegen. Dies lässt sich durch die ortsspezifische Photoionisation erklären.

Die Emission von Fluoreszenzstrahlung im ultravioletten Spektralbereich nach Rumpfniveauanregung wurde im Fall von $2p$-angeregten Argon-Clustern untersucht. Die hochaufgelösten Spektren zeigen hohe Intensität im $2p$-Kontinuum, jedoch keinen Hinweis auf signifikante Beiträge im Bereich der Rumpfniveau-Excitonen. Dieses Ergebnis unterscheidet sich vom Absoprtions- und Photoionisationsquerschnitt von Argon-Clustern sowie festem Argon. Die dispergierte Fluoreszenz liefert eine intensive Bande bei 280 nm. Dieses

Resultat lässt sich mit der Fluoreszenz von einfach geladenen, angeregten Argon-Clustern erklären. Die Bildung von einfach geladenen Ionen nach primärer Doppelionisation im Ar $2p$-Kontinuum wird durch einen schnellen Energietransfer-Prozess (Interatomic Coulombic Decay, ICD) erklärt. Er läuft nach der Rumpfniveauanregung ab und liefert, neben der Elektronenstoßionisation durch schnelle Auger-Elektronen, einfach geladene Clusterfragmente, die nachfolgend strahlend relaxieren. Dieses Ergebnis ist als erster Hinweis darauf zu werten, dass der ICD-Prozess auch im Bereich der Innerschalenanregung auftritt.

Freie Stickstoff-Cluster variabler Größe wurden im Bereich der N $1s$-Anregung untersucht. Hier stand die Umwandlung der Rydberg-Zustände in die entsprechenden Oberflächen- und Volumen-Excitonen in Fokus der Studien. Die Resultate wurden mit denen zu freiem und kondensiertem Stickstoff verglichen. Die experimentellen Resultate lassen auch einen Vergleich mit *ab initio* Rechnungen zu, wofür $(N_2)_{13}$ als Prototyp-Cluster genutzt wurde, da hier sowohl oberflähen – als auch volumengebundene Moleküle auftreten. Diese Resultate zeigen signifikante Unterschiede im Vergleich zu atomaren Clustern. Es zeigt sich, dass die molekulare Orientierung die Lage der Excitonenbanden beeinflusßt. Ebenso treten signifikante Energieverschiebungen relativ zum isolierten Molekül auf, die sich durch Absorption von Zentren erklären lassen, die entweder auf der inneren bzw. äußeren Oberfläche der Cluster gebunden sind.

Outlook

Before ending this thesis, I would like to take the opportunity to think about what could be done in the future.

One of the challenges of the future work is related to the development of stable and intense cluster sources that are compatible with the environment of synchrotron radiation research. The control of structural properties, especially if the clusters are size-selected and deposited on substrates, are expected to be of outstanding interest to future developments of matter. The present work was strongly stimulated by new experimental opportunities that arise from state-of-art light sources such as high brightness synchrotron radiation sources from storage ring facilities, including free electron lasers that are expected to reach the soft x-ray regime. Concerning resonant Auger electron spectroscopy on uncondensed molecules and the corresponding molecular cluster systems fundamental a question of interest could be: What happens to the dynamics of the cluster formation? In addition to that, combined synchrotron-laser two-photon experiments should be very challenging to be performed as well on cluster systems, as this is currently a completely untouched research field.

We have now entered the attosecond world, but we will need a better guidebook to help us find our way around it. What sort of experiments are possible with attosecond pulses? At these timescales, chemistry is essentially frozen in time, so the only dynamics to be studied are those of electrons, as they are much lighter and faster than nuclei. Most femtochemistry measurements are based on the pump-probe method: one pulse sets the system into motion, and a second one probes it after a controlled delay. But this approach is not possible with attosecond pulses: they are just too weak.

Acknowledgments

This is going to be long. I am indebted for an enormous number of things to my supervisor. Over the almost three years I spent as a graduate student in the Eckart's group. I have received an education much more diverse than I had expected. I started in the belief I would get trained in clusters physics and possibly in creative thinking. I have been trained in working hard, not giving up but giving in – from time to time. As a graduate student I was not only being trained, I was allowed to simply explore and discover my own strengths and weaknesses. I was free to find out what I wanted. I am very grateful for this time, which gave room for forming me as a person and as a scientist. Eckart has spent a lot of time teaching me many things. What would I have done without you?

Thank you for having the patience and energy to put up with me throughout these years. All I know about the experiments which we have performed together, I owe to Eckart and Roman. I thank Eckart for all what I was able to experience and enjoy in all these years and for things which did not happen in the lab.

For an equally large number of things I would like to thank Nobu. I had the great opportunity to collaborate with Nobu during my Ph.D studies. I would like to thank to Nobu who had patience for me to explain how things work in GSCF3. I am very grateful for this. Thank you for spending time with me during my visit in Okazaki where I had a good time.

I would like to thank Roman for several nice beamtime when we have been sharing shifts together, for making my eyes sensible for ZEKE spectra. It was a special beamtime for me. Roman was like a supervisor for me without whom this would not have been started, and certainly not finished. Thank you!

I am also grateful to Michael Meyer, who have teached me how things are going in fluorescence experiments. Thank you for the fruitful beamtimes which we have shared together.

To Olle Björneholm and Svante Svensson I want to say thank you for inviting me to MAX-lab, for a nice beamtime together with Marcus, Henrik Andreas, Torbjön, and Maxim.

At BESSY in Berlin I found many friends during the last three years: Kai Godehusen, Ralph Püttner, Olaf Schwarzkopf and Uwe Hergenhan.

I'd like to thank Uwe for our discussion on the PCI project. Your advice have been valuable for me. Kai and Olaf are gratefully acknowledged for past and present beamline managers, for having done an excellent job in keeping UE52-SGM and U49-PGM smoothly running. The same holds for the staff at BESSY-II in Berlin. Thanks a lot!

I have had the opportunity to discuss physics with people outside of the team at conferences and similar occasions: Nobu, Uwe, Olle, Svante, Michael, Thomas, Maxim, Dennis Lindle, Pascal Lablanquie, Edwin Kukk have all taken their time for discussions

Bibliography

[1] H. Haberland. *Clusters of Atoms and Molecules*, volume I and II. Springer, Berlin, 1994, 1995.

[2] W. Eberhardt. *Applications of Synchrotron Radiation*. Springer, Berlin, 1995.

[3] J. Stöhr. Nexafs spectroscopy. In *Springer Ser. Surf. Sci.*, volume 25. Springer, Berlin, 1992.

[4] J. Wörmer, M. Joppien, G. Zimmerer, and T. Möller. *Phys. Rev. Lett.*, 67:2053, 1991.

[5] J. Wörmer, R. Karnbach, M. Joppien, and T. Möller. *J. Chem. Phys.*, 104:8269, 1996.

[6] L.N. Mazalov, F.Kh. Gel'mukhanov, and V.M. Chermoshentsev. *J. Struct. Chem.*, 15:975, 1974.

[7] J.L. Dehmer and D. Dill. *Phys. Rev. Lett.*, 35:213, 1975.

[8] V.I. Nefedov. *J.Struct.Chem.*, 11:272, 1970.

[9] A. Föhlisch, J. Hasselström, P. Bennidi, N. Wassdahl, O. Knris, A. Nilsson, L. Triguero, M. Nyberg, and L.G.M. Pettersson. *Phys. Rev. B*, 61:10229, 2000.

[10] P. Auger. *J. Phys. (PARIS)*, VI:205, 1925.

[11] R. Flesch, N. Kosugi, I.L. Bradeanu, J.J. Neville, and E. Rühl. *J. Chem. Phys.*, 121:8343, 2004.

[12] Y. Kawazoe, T. Kondow, and K. Ohno, editors. *Clusters and Nanomaterials*. Springer, Berlin, 2002.

[13] H.L. Davis, J. Jellinek, and R.S. Berry. *J. Chem. Phys.*, 86:6456, 1987.

[14] J. Jortner. *Ber. Bunsenges. Phys. Chem.*, 88:188, 1984.

[15] J. Jortner. *Z. Phys. D*, 24:247, 1992.

[16] H. Koizumi S. Sugano. *Microcluster Physics*. Springer, Berlin, 1998.

[17] J. Jortner. *J. Chim. Phys.*, 92:205, 1995.

[18] P.-G. Reinhardt and E. Suraud. *Introduction to cluster dynamics.* Wiley-VCH, 2004.

[19] R.L. Johnston. *Atomic and molecular clusters.* Taylor & Francis, 2002.

[20] E. Rühl. *Int. J. Mass. Spectroscom.*, 229:117, 2003.

[21] E. Rühl, C. Schmale, H.W. Jochims, E. Biller, M. Simon, and H. Baumgärtel. *J. Chem. Phys.*, 95:6544, 1991.

[22] E. Rühl, C. Heinzel, H. Baumgärtel, M. Lavollée, and P. Morin. *Z. Phys. D*, 31:245, 1994.

[23] R. Casero, J. Saenz, and J. Soler. *Phys. Rev. A*, 37:1401, 1988.

[24] A. De Fanis, M. Oura, N. Saito, M. Machida, M. Nagoshi, A. Knapp, J. Nickles, A. Czasch, R. Dörner, Y. Tamenori, H. Chiba, M. Takahashi, J.H.D. Eland, and K. Ueda. *J. Phys. B*, 37:L235–42, 2004.

[25] L.S. Cederbaum, J. Zobeley, and F. Tarantelli. *Phys. Rev. Lett.*, 79:4778, 1997.

[26] J. Zobeley, L.S. Cederbaum, and F. Tarantelli. *J. Phys. Chem. A*, 103:11145, 1999.

[27] R. Santra, J. Zobeley, L.S. Cederbaum, and N. Moiseyev. *Phys. Rev. Lett.*, 85:4490, 2000.

[28] J. Zobeley, R. Santra, and L.S. Cederbaum. *J. Chem. Phys.*, 115:5076, 2001.

[29] J. Wieser, A. Ulrich, A. Fedenev, and M. Salvermoser. *Opt. Commun.*, 173:233, 2000.

[30] R. Santra and L.S. Cederbaum. *Phys. Rev. Lett.*, 90:153401, 2003.

[31] H. Aksela, S. Aksela, H. Pulkkinen, G.M. Bancroft, and K.H. Tan. *Phys. Rev. A*, 37:1798, 1988.

[32] J.A. de Gouw, J. van Eck, J. van der Weg, and H.G.M. Heideman. *J. Phys. B*, 28:1761, 1995.

[33] J.A. de Gouw, J. van Eck, J. van der Weg, and H.G.M. Heideman. *J. Phys. B*, 25:2007, 1992.

[34] J. Mursu, H. Aksela, O.-P. Sairanen, A. Kivimäki, E. Nommiste, A. Ausmees, S. Svensson, and S. Aksela. *J. Phys. B*, 29:4387, 1996.

[35] M. Meyer, E.V. Raven, B. Sonntag, and J.E. Hansen. *Phys. Rev. A*, 43:177, 1991.

[36] R. Flesch, H.W. Jochims, J. Plenge, and E. Rühl. *Phys. Rev. A*, 61:062504, 2000.

[37] M. Meyer, J. Lacoursiére, M. Simon, P. Morin, and M. Larzillière. *Chem. Phys.*, 187:143, 1994.

[38] U. Becker and D.A. Shirley, editors. *VUV and Soft X-Ray Photoionization*. Plenum, New York, 1996.

[39] P. Glans, P. Skytt, K. Gunnelin, J.-H. Guo, and J. Nordgren. *J. Electron Spectrosc. Relat. Phenom.*, 82:193, 1996.

[40] C.T. Chen, Y. Ma, and F. Sette. *Phys. Rev. A*, 40:6737, 1989.

[41] M. Neeb, J.-E. Rubensson, M. Biermann, and W. Eberhardt. *J. Phys. B*, 29:4381, 1996.

[42] W. Eberhardt, E.W. Plummer, I.-W. Lyo, R. Carr, and W.K. Ford. *Phys. Rev. Lett.*, 58:207, 1987.

[43] M.N. Piancastelli, A. Kivimäki, B. Kempgens, M. Neeb, K. Maier, U. Hergenhahn, A. Rüdel, and A.M. Bradshaw. *J. Electron Spectrosc. Relat. Phenom.*, 98-99:111, 1999.

[44] W. Eberhardt, J. Stöhr, J. Feldhaus, E.W. Plummer, and F. Sette. *Phys. Rev. Lett.*, 51:2370, 1983.

[45] H. Ågren. *J. Chem. Phys.*, 75:1267, 1981.

[46] R. Fink. *J. Electron Spectrosc. Relat. Phenom.*, 76:295, 1995.

[47] E.E. Koch, editor. *Handbook on synchrotron radiation*. North Holland, 1983.

[48] A. Hofmann. *Nucl. Instr. Meth.*, 152:17, 1978.

[49] C.J. Kim. *Nuclear Instruments and Methods*, 219:425, 1984.

[50] H. Winick. Synchrotron radiation sources: a primer. In *Series on Synchrotron Radiation Techniques and Applications*, volume 1. World Scientific, London, 1994.

[51] O.F. Hagena. *Surf. Sci.*, 106:101, 1981.

[52] W.A. de Heer. *Rev. Mod. Phys.*, 65:611, 1993.

[53] P. Milani and S. Iannotta. *Cluster Beam Synthesis of Nanostructured Materials*. Springer, Berlin, 1999.

[54] H. Pauly. *Atom, Molecule, and Cluster Beams*, volume I and II. Springer, Berlin, 2000.

[55] R.A. Larson, S.K. Ncoh, and D.R. Herschbach. *Rev. Sci. Instr.*, 45:1511, 1984.

[56] O.F. Hagena. *Phys. Fluids*, 17:894, 1974.

[57] O.F. Hagena. *Z. Phys. D*, 4:291, 1987.

[58] J. Wörmer, V. Guzielski, J. Stapelfeldt, G. Zimmerer, and T. Möller. *Phys. Scr.*, 41:490, 1990.

[59] J. Farges, M.F. de Feraudy, B. Raoult, and G. Torchet. *J. Chem. Phys.*, 84:3491, 1986.

[60] R. Karnbach, M. Joppien, J. Stapelfeldt, J. Wörmer, and T. Möller. *Rev. Sci. Instrum.*, 64:2838, 1993.

[61] U. Buck and H. Meyer. *Phys. Rev. Lett.*, 52:109, 1984.

[62] A. Knop and E. Rühl. In T. Kondow, K. Kaya, and A. Terasaki, editors, *Structure and Dynamic of Clusters*, page 235. Academic Press, Tokyo, 1996.

[63] C. Ellert, M. Schmidt, C. Schmitt, T. Reiners, and H. Haberland. *Phys. Rev. Lett.*, 75:1731, 1995.

[64] W. Miehle, O. Kandler, T. Leisner, and O. Echt. *J. Chme. Phys.*, 91:5940, 1989.

[65] E. Rühl, C. Heinzel, A.P. Hitchcock, and H. Baumgärtel. *J. Chem. Phys.*, 98:2653, 1993.

[66] E. Rühl, C. Heinzel, A.P. Hitchcock, H. Schmelz, C. Reynaud, H. Baumgärtel, W. Drube, and R. Frahm. *J. Chem. Phys.*, 98:6820, 1993.

[67] E. Rühl, C. Heinzel, H. Baumgärtel, W. Drube, and A.P. Hitchcock. *Jap. J. Appl. Phys.*, 32:791, 1993.

[68] O. Björneholm, F. Federmann, F. Fössing, and T. Möller. *Phys. Rev. Lett.*, 74:3017, 1995.

[69] E. Rühl, P.G.F. Bisling, B. Brutschy, and H. Baumgärtel. *Chem. Phys. Lett.*, 126:232, 1986.

[70] W. Kamke, B. Kamke, H.U. Kiefl, and I.V. Hertel. *J. Chem. Phys.*, 84:1325, 1986.

[71] M. Lewerenz, B. Schilling, and J.P. Toennies. *Chem. Phys. Lett.*, 206:381, 1993.

[72] A.A. Vostrikov, D.Y. Dubov, and I.V. Samoilov. *Tech. Phys.*, 39:1267, 1994.

[73] M. Simon, T. LeBrun, P. Morin, M. Lavollée, and J.L. Maréchal. *Nucl. Intrum. Meth. B*, 62:167, 1991.

[74] R. Flesch, A.A. Pavlychev, J.J. Neville, J. Blumberg, M. Kuhlmann, W. Tappe, F. Senf, O. Schwarzkopf, A.P. Hitchcock, and E. Rühl. *Phys. Rev. Lett.*, 86:3767, 2001.

[75] A. Knop, B. Wassermann, and E. Rühl. *Phys. Rev. Lett.*, 80:2302, 1998.

[76] S. Kakar, O. Björneholm, J. Weigelt, A.R.B. de Castro, L. Tröger, R. Frahm, T. Möller, A. Knop, and E. Rühl. *Phys. Rev. Lett.*, 78:1675, 1997.

[77] W.C. Wiley and I.H. McLaren. *Rev. Sci. Instrum.*, 26:1150, 1955.

[78] F. Federmann, O. Björneholm, A. Beutler, and T. Möller. *Phys. Rev. Lett.*, 73:1549, 1994.

[79] M.J. van der Viel and G. Wiebes. *Physica*, 53:225, 1971.

[80] R. Hayaishi, Y. Morioka, Y. Kageyama, M. Watanabe, I.H. Suzuki, A. Mikuni, G. Isoyama, S. Asaoka, and M. Nakamura. *J. Phys. B*, 17:3511, 1984.

[81] E. Rühl, A. Knop, A.P. Hitchcock, P.A. Dowben, and D.N. McIlroy. *Surf. Rev. Lett.*, 3:557, 1996.

[82] A. Knop, H.W. Jochims, A.L.D. Kilcoyne, A.P. Hitchcock, and E. Rühl. *Chem. Phys. Lett.*, 223:553, 1994.

[83] D.N. McIlroy, P.A. Dowben, A. Knop, and E. Rühl. *J. Vac. Sci. Technol. B*, 13:2142, 1992.

[84] C.M. Teodorescu, D. Gravel, E. Rühl, T.J. McAvoy, J. Choi, D. Pugmire, P. Pribil, J. Coos, and P.A. Dowben. *Rev. Sci. Instrum.*, 69:3805, 1998.

[85] K. Müller-Dethlefs and E.W. Schlag. *Ann. Rev. Phys. Chem.*, 42:109, 1991.

[86] T. Baer, W.B. Peatman, and E.W. Schlag. *Chem. Phys. Lett.*, 4:243, 1969.

[87] H.W. Jochims, E. Rühl, and H. Baumgätel. *Z. Naturforsch.*, B44:13, 1989.

[88] D.A. Dahl. Simion for the personal computer in reflection. *Int. J. Mass Spectrom.*, 200:3, 2000. source: Scientific Instrument Services, Inc., Ringoes, NJ, www. simion. com.

[89] E. Rühl, C. Heinzel, and H.W. Jochims. *Chem. Phys. Lett.*, 211:403, 1993.

[90] A. Marquette, M. Gisselbrecht, W. Benten, and M. Meyer. *Phys. Rev. A*, 62:22513, 2000.

[91] A. Marquette, M. Meyer, F. Sirotti, and R.F. Fink. *J. Phys. B*, 32:L325, 1999.

[92] F.H. Read. In J.S. Risley and R. Geballe, editors, *The Physics of Electronic and Atomic Collisions*, page 176. Univ. of Washington Press, 1975.

[93] M.J. van der Viel, G.R. Wight, and R.R. Tol. *J. Phys. B*, 9:L5, 1976.

[94] R. Morgenstern, A. Niehaus, and U. Thielmann. *Phys. Rev. Lett.*, 37:199, 1976.

[95] R. Morgenstern, A. Niehaus, and U. Thielmann. *J. Phys. B*, 10:1039, 1977.

[96] A. Niehaus. *J. Phys. B*, 10:1845, 1977.

[97] F.H. Read. *J. Phys. B*, 10:L207, 1976.

[98] G.C. King, F.H. Read, and R.C. Bradford. *J. Phys. B*, B8:2210, 1975.

[99] F.H. Read. *Rad. Research*, 64:23, 1975.

[100] T.A. Carlson and M.O. Krause. *Phys. Rev. Lett.*, 17:1079, 1966.

[101] J.A.R. Samson, W.C. Stolte, X.Z. He, J.N. Cutler, and D. Hansen. *Phys. Rev. A*, 54:2099, 1996.

[102] J. Tulkki, T. Åberg, S.B. Whitfield, and B. Crasemann. *Phys. Rev. A*, 41:181, 1990.

[103] Y. Lu, W.C. Stolte, and J.A.R. Samson. *Phys. Rev. A*, 58:2828, 1998.

[104] T. Hayaishi, E. Murakami, A. Yagishita, F. Koike, Y. Morioka, and J.E. Hansen. *J. Phys. B*, 21:3203, 1988.

[105] W. Eberhardt, S. Bernstorff, H.W. Jochims, S.B. Whitfield, and B. Crasemann. *Phys. Rev. A*, 38:3808, 1988.

[106] A. Russek and W. Mehlhorn. *J. Phys. B*, 19:911, 1986.

[107] J.C. Levin, C. Biedermann, N. Keller, L. Liljeby, R.T. Short, and I.A. Stellin. *Phys. Rev. Lett.*, 65:989, 1990.

[108] T D. Thomas, R.I. Hall, M. Hochlaf, H. Kjeldsen, F. Penent, P. Lablanquie, M. Lavollée, and P. Morin. *J. Phys. B*, 29:3245, 1996.

[109] P. Lablanquie, S.A. Sheinerman, F. Penent, T. Aoto, Y. Hikosaka, and K. Ito. *J. Phys. B*, 38:L9, 2005.

[110] G.B. Armen, J. Tulkki, T. Åberg, and B. Crasemann. *Phys. Rev. A*, 36:5606, 1987.

[111] S.A. Sheinerman, W. Kuhn, and W. Mehlhorn. *J. Phys. B*, 27:5681, 1994.

[112] F. Koike. *J. Phys. Soc. Jpn.*, 57:2705, 1988.

[113] F. Koike. *Phys. Lett. A*, 193:173, 1994.

[114] K. Helenelund, S. Hedman, L. Asplund, U. Gellius, and K. Siegbahn. *Physica Scripta*, 27:245, 1983.

[115] M. Gell-Mann and M.L. Goldberger. *Phys. Rev.*, 91:398, 1953.

[116] G. Breit and H.A. Bethe. *Phys. Rev.*, 93:888, 1954.

[117] W. Berthold, F. Rebentrost, P. Feulner, and U. Höfer. *Appl. Phys. A*, 78:131, 2004.

[118] P. van der Straten, R. Morgenstern, and A. Niehaus. *Z. Phys. D*, 8:35, 1987.

[119] V. Schmidt. *Rep. Prog. Phys.*, 55:1483, 1992.

[120] D. Čubric, A.A. Wills, E. Sokell, J. Comer, and M.A. Macdonald. *J. Phys. B*, 26:4425, 1993.

[121] J.A. de Gouw, J. van Eck, A.C. Peters, J. van der Weg, and H.G.M. Heideman. *J. Phys. B*, 28:2127, 1995.

[122] G.B. Armen, S.H. Southworth, J.C. Levin, U. Arp, T. LeBrun, and M.A. Macdonald. *Phys. Rev. A*, 56:R1079, 1997.

[123] J. Tulkki, G.B. Armen, T. Åberg, B. Crasemann, and M.H. Chen. *Z. Phys. D*, 5:241, 1987.

[124] T. Åberg. *Phys. Scr.*, 21:495, 1980.

[125] G.B. Armen, T. Åberg, J.C. Levin, B. Crasemann, M.H. Chen, G.E. Ice, and G.S. Brown. *Phys. Rev. Lett.*, 54:1142, 1985.

[126] M.Yu. Kuichev and S.A. Sheinerman. *Sov. Phys. JETP*, 63:986, 1986.

[127] M. Borst and V. Schmidt. *Phys. Rev. A*, 33:4456, 1986.

[128] G.B. Armen, S.L. Sorensen, S.B. Whitfield, G.E. Ice, J.C. Levin, G.S. Brown, and B. Crasemann. *Phys. Rev. A*, 35:3966, 1987.

[129] G.N. Ogustrov. *J. Phys. B*, 16:L745, 1983.

[130] O. Björneholm, F. Federmann, F. Fössing, T. Möller, and P. Stampfli. *J. Chem. Phys.*, 104:1846, 1996.

[131] K. Iwano and K. Nasu. *J. Phys. Soc. Japan*, 64:3537, 1995.

[132] D.M. Coward and S.M. Thurgate. *J. Electron Spectrosc. Relat. Phenom.*, 107:193, 2000.

[133] V.M. Mikushkin, A.V. Zakharevich, I.I. Pavletsov, S.E. Sysoev, V.V. Shnitov, M.Yu. Kuchiev, and S.A. Sheinerman. *JETP Letters*, 58:891, 1993.

[134] D.A. Shirley. *Phys. Rev. A*, 7:1520, 1973.

[135] O. Gunnarsson and K. Schönhammer. *Phys. Rev. B*, 22:3710, 1980.

[136] W. Sandner and M. Völkel. *Phys. Rev. Lett.*, 62:885, 1989.

[137] G.J. Martyna and B.J. Berne. *J. Chem. Phys.*, 90:3744, 1989.

[138] M.J. Frisch, G.W. Trucks, H.B. Schlegel, G.E. Scuseria, M.A. Robb, J.R. Cheeseman, J.A. Montgomery, Jr., T. Vreven, K.N. Kudin, J.C. Burant, J.M. Millam, S.S. Iyengar, J. Tomasi, V. Barone, B. Mennucci, M. Cossi, G. Scalmani, N. Rega, G.A. Petersson, H. Nakatsuji, M. Hada, M. Ehara, K. Toyota, R. Fukuda, J. Hasegawa, M. Ishida, T. Nakajima, Y. Honda, O. Kitao, H. Nakai, M. Klene, X. Li, J.E. Knox, H.P. Hratchian, J.B. Cross, V. Bakken, C. Adamo, J. Jaramillo, R. Gomperts, R.E. Stratmann, O. Yazyev, A.J. Austin, R. Cammi, C. Pomelli, J.W. Ochterski, P.Y. Ayala, K. Morokuma, G.A. Voth, P. Salvador, J.J. Dannenberg, V.G. Zakrzewski, S. Dapprich, A.D. Daniels, M.C. Strain, O. Farkas, D.K. Malick, A.D. Rabuck, K. Raghavachari, J.B. Foresman, J.V. Ortiz, Q. Cui, A.G. Baboul, S. Clifford, J. Cioslowski, B.B. Stefanov, G. Liu, A. Liashenko, P. Piskorz, I. Komaromi, R.L. Martin, D.J. Fox, T. Keith, M.A. Al-Laham, C.Y. Peng, A. Nanayakkara, M. Challacombe, P.M.W. Gill, B. Johnson, W. Chen, M.W. Wong, C. Gonzalez, and J.A. Pople. Gaussian 03, Revision C.02. Gaussian, Inc., Wallingford, CT, 2004.

[139] P.R. Herman, P.E. LaRocque, and B.P. Stoicheff. *J. Chem. Phys.*, 89:4535, 1988.

[140] R.A. Aziz and H.H. Chen. *J. Chem. Phys.*, 67:5719, 1977.

[141] R.C. Weast. *Handbook of Chemistry and Physics.* Chemical Rubber Company, Boca Raton, FL, 66 edition, 1986.

[142] T. Hatsui, H. Setoyama, N. Kosugi, B. Wassermann, I.L. Bradeanu, and E. Rühl. 2005.

[143] M. Tchaplyguine, R. Feifel, R.R.T. Marinho, M. Gisselbrecht, S.L. Sorensen, A. Naves de Brito, N. Mårtensson, S. Svenson, and O. Björneholm. *Chem. Phys.*, 289:3, 2003.

[144] F.G. Amar, J. Smaby, and T. Preston. *J. Chem. Phys.*, 122:244717, 2005.

[145] M. Tchaplyguine, R.R.T. Marinho, M. Gisselbrecht, J. Schultz, N. Mårtensson, S.L. Sorensen, A. Naves de Brito, R. Feifel, G. Öhrwall, M. Lundwall, S. Svenson, and O. Björneholm. *J. Chem. Phys.*, 120:345, 2004.

[146] M. Jurvansuu, A. Kivimäki, and S. Aksela. *Phys. Rev. A*, 64:012502, 2001.

[147] M.R. Hoare. *Adv. Chem. Phys.*, 40:49, 1979.

[148] R.E. Benfield. *J. Chem. Soc. Farraday Trans.*, 88:1107, 1992.

[149] B.W. van de Waal. *Z. Phys. D*, 20:249, 1991.

[150] B.W. van de Waal. *J. Chem. Phys.*, 98:4909, 1993.

[151] B.W. van de Waal. *Phys. Rev. Lett.*, 76:1083, 1996.

[152] B. Daniels, G. Shirane, B.C. Frazer, H. Umebayashi, and J.A. Leake. *Phys. Rev. Lett.*, 18:548, 1967.

[153] G.J. Martyna and B.J. Berne. *J. Chem. Phys.*, 90:3744, 1989.

[154] K.P. Huber and G. Herzberg. *Molecular Spectra and Molecular Structure*, volume 4. Van Nostrand, New York, 1979.

[155] R.C. Weast, editor. *Handbook of Chemistry and Physics.* Chemical Rubber Company, Boca Raton, FL, 69 edition, 1988.

[156] M.Yu. Kuchiev and S.A. Sheinermann. *Sov. Phys.-USP*, 35:569, 1989.

[157] P.A. Heimann, D.W. Lindle, T.A. Ferrett, S.H. Liu, L.J. Medhurst, M.N. Piancastelli, D.A. Shirley, U. Becker, H.G. Kerkhoff, B. Langer, D. Szostak, and R. Wehlitz. *J. Phys. B*, 20:5005, 1987.

[158] L. Avaldi, G. Dawber, R. Camilloni, G.C. King, M. Roper, M.R.F. Siggel, G. Stefani, and M. Zitnik. *J. Phys. B*, 327:3453, 1994.

[159] H. Kjeldsen, T.D. Thomas, P. Lablanquie, M. Lavollée, F. Penent, M. Hochlaf, and R.I. Hall. *J. Phys. B*, 29:1689, 1996.

[160] K. Iwano and K. Nasu. *J. Electron Spectrosc. Relat. Phenom.*, 79:237, 1996.

[161] A. Knop, H.W. Jochims, A.L.D. Kilcoyne, A.P. Hitchcock, and E. Rühl. *Chem. Phys. Lett.*, 223:553, 1994.

[162] R. Feifel, M. Tchaplyguine, G. Öhrwall, M. Salonen, M. Lundwall, R.R.T. Marinho, M. Gisselbrecht, S.L. Sorensen, A.N. de Brito, L. Karlsson, N. Martensson, S. Svensson, and O. Bjorneholm. *J. Eur. Phys. D*, 30(3):343–51, 2004.

[163] R. Romberg, B. Kassuhlke, P. Wiethoff, D. Menzel, and P. Feulner. *Chem. Phys.*, 289:69–79, 2003.

[164] L.J. Saethre, T.D. Thomas, and L. Ungier. *J. Electron Spectrosc. Relat. Phenom.*, 33:381, 1984.

[165] W. Habenicht, K. Müller-Dethlefs, and E.W. Schlag. *J. Electron Spectrosc. Relat. Phenom.*, 52:697, 1990.

[166] M. Lundwall, M. Tchaplyguine, G. Öhrwall, A. Lindblad, S. Peredkov, T. Rander, S. Svensson, and O. Björneholm, 2005. doi:10.1016/j. susc.2005.07.007.

[167] J.A. Victoreen. *J. Appl. Phys.*, 19:855, 1948.

[168] G.C. King, M. Troc, F.H. Read, and R.C. Bradford. *J. Phys. B*, 10:2479, 1977.

[169] I.L. Bradeanu, H. Setoyama, T. Hatsui, N. Kosugi, and E. Rühl. Post collision interaction of free van der waals clusters. in manuscript, 2005.

[170] H. Hanashiro, Y. Suzuki, T. Susaki, A. Mikuni, T. Takayanagi, K. Wakiya, H. Suzuki, A. Danjo, T. Hino, and S. Ohtani. *J. Phys. B*, 12:L775, 1979.

[171] R. Hoogewijs, L. Fiermans, and J. Vennik. *Surf. Sci.*, 69:273, 1977.

[172] W. Malzfeldt, W. Niemann, P. Rabe, and R. Haensel. *Springer Proceedings in Physics*, 2:445, 1984.

[173] P. Plenkiewicz, J.-P. Jay-Gerin, B. Plenkiewicz, and G. Perluzzo. *Solid Stat. Comm.*, 57:203, 1985.

[174] B. Kassuhlke, R. Romberg, P. Averkamp, and P. Feulner. *Phys. Rev. Lett.*, 81:2771, 1998.

[175] G. Rocker, P. Feulner, R. Scheuerer, L. Zhu, and D. Menzel. *Phys. Scripta*, 41:1014, 1990.

[176] M.K. Bahl, R.L. Watson, and K.J. Irgollic. *Phys. Rev. Lett.*, 42:165, 1979.

[177] Y. Takata, T. Hatsui, and N. Kosugi. *J. Electron Spectrosc. Relat. Phenom.*, 101-103:443, 1999.

[178] A. Kakizaki, T. Kinoshita, T. Ishii, T. Kashiwakura, T. Okane, S. Suzuki, S. Sato, and Y. Isikawa. *J. Phys. Soc. Japan*, 62:3327, 1993.

[179] F.H. Read. *J. Phys. B*, 10:L207, 1977.

[180] K. Codling and R.P. Madden. *Phys. Rev. Lett.*, 12:106, 1964.

[181] D. Čubrić, A.A. Wills, J. Comer, and M.A. MacDonald. *J. Phys. B*, 25:5069, 1992.

[182] L. Avaldi, R.I. Hall, G. Dawber, P.M. Rutter, and G.K. King. *J. Phys. B*, 24:427, 1991.

[183] G. Öhrwall, M. Tchaplyguine, M. Gisselbrecht, M. Lundwall, R. Feifel, T. Rander, J. Schulz, R.R.T. Marinho, A. Lindgren, S.L. Sorensen, S. Svensson, and O. Björneholm. *J. Phys. B*, 36(19):3937–3949, 2004.

[184] M.K. Bahl, R.L. Watson, and K.J. Irgollic. *Phys. Rev. Lett.*, 42:165, 1978.

[185] E. Keszei, R. Marsolais, M. Deschênes, T. Goulet, L. Sanche, and J.-P. Jay-Gerin. *J. Electron Spectrosc. Relat. Phenom.*, 49:175–182, 1989.

[186] A.D. Bass and L. Sanche. *Radiat. Environ. Biophys.*, 37:243, 1998.

[187] I.L. Bradeanu, R. Flesch, and E. Rühl. Zero kinetic energy photoelectron spectroscopy of ar clusters. manuscript in preparation, 2005.

[188] R. Scheuerer, P. Feulner, and G. Rocker. In G. Betz and P. Varga, editors, *Desorption Induced by Electronic Transitions, DIET IV*, page 235. Springer, Berlin, Heidelberg, 1990.

[189] L. Pettersson, J. Nordgren, L. Selander, C. Nordling, K. Siegbahn, and H. Ågren. *J. Electron Spectrosc. Rel. Phenom.*, 27:29, 1982.

[190] W. Wurth, G. Rocker, P. Feulner, R. Scheuerer, L. Zhu, and D. Menzel. *Phys. Rev. B*, 47:6697, 1993.

[191] A. Nilsson, O. Björneholm, B. Hernnas, A. Sandell, and N. Martensson. *Surf Sci. Lett.*, 293:L835, 1993.

[192] P.A. Heimann, D.W. Lindle, T.A. Ferrett, S.H. Liu, L.J. Medhurst, M.N. Piancastelli, D.A. Shirley, U. Becker, H.G. Kerkhoff, B. Langer, D. Szostak, and R. Wehlitz. *J. Phys. B*, 20:5005, 1987.

[193] G.B. Armen and J.C. Levin. *Phys. Rev. A*, 56:3734, 1997.

[194] T. Hayaishi, E. Murakami, Y. Morioka, E. Shigemasa, A. Yagishita, and F. Koike. *J. Phys. B*, 27:L115, 1994.

[195] K. Siegbahn, C. Nordling, G. Johansson, J. Hedman, P.-F. Heden, K. Hamrin, U. Gelius, T. Bergmark, L.O. Werme, R. Manne, and Y. Baer. *ESCA applied to free molecules*. North-Holland, Amsterdam, 1969.

[196] W.B. Peatman, G.B. Kasting, and D.J. Wilson. *J. Electron Spectrosc. Rel. Phenom.*, 7:233, 1975.

[197] D.W. Lindle, P.A. Heimann ans T.A. Ferrett, M.N. Piancastelli, and D.A. Shirley. *Phys. Rev. A*, 45:4605, 1987.

[198] V. Schmidt, S. Krummacher, F. Wuilleumier, and P. Dhez. *Phys. Rev. A*, 24:1803, 1981.

[199] H. Aksela, S. Aksela, K.H. Tan, G.M. Bancroft, and H. Pulkkinen. *Phys. Rev. A*, 33:3867, 1986.

[200] H. Aksela, S. Aksela, H. Pulkkinen, G.M. Bancroft, and K.H. Tan. *Phys. Rev. A*, 33:3876, 1986.

[201] E. Rühl. Core level excitation of clusters. In T. Kondow and F. Mafune, editors, *Advanced Series in Physical Chemistry*, volume 13, pages 189–237. World Scientific, Singapore, 2003.

[202] R. Haensel, N. Kosuch, U. Nielsen, U. Rössler, and B. Sonntag. *Phys. Rev. B*, 7:1577, 1973.

[203] F. Wuilleumier. *J. Phys. (Paris), Colloq. C4, Suppl. 10*, 32:88, 1971.

[204] H. Ågren, J. Nordgren, L. Selander, C. Nordling, and K. Siegbahn. *J. Electron Spectrosc. Relat. Phenom.*, 14:27, 1978.

[205] M. Coreno, L. Avaldi, R. Camilloni, K.C. Prince, M. de Simone, J. Karvonen, R. Colle, and S. Simonucci. *Phys. Rev. A*, 59:2494, 1999.

[206] B. Kanngießer, M. Janiz, S. Brünken, W. Benten, C. Gerth, K. Godehusen, K. Tiedtke, P. van Kampen, A. Tutay, P. Zimmermann, V.F. Demekhin, and A.G. Kochur. *Phys. Rev. A*, 62:014702, 2000.

[207] J.-E. Rubensson, M. Neeb, A. Bringer, M. Biermann, and W. Eberhardt. *Chem. Phys. Lett.*, 257:447, 1996.

[208] A.P. Hitchcock and C.E. Brion. *J. Phys. B*, 13:3269, 1980.

[209] A. Hiraya, K. Fukui, P.K. Tseng, T. Murata, and M. Watanabe. *J. Phys. Soc. Jpn.*, 60:1824, 1991.

[210] H.R. Glyde. In M.L. Klein and J.A. Vanables, editors, *Rade Gas Solids*, volume I. Academic Press, London, 1976.

[211] W.B. Fowler. *Phys. Rev.*, 132:1591, 1963.

[212] R. Haensel, G. Keitel, E.E. Koch, N. Kosuch, and M. Skibowski. *Phys. Rev. Lett.*, 25:1281, 1970.

[213] D. Pudewill, F.J. Himpsel, V. Saile, N. Schwentner, M. Skibowski, and E.E. Koch. *Phys. Status Solidi (b)*, 74:485, 1976.

[214] B. Kassühlke, P. Averkamp, S. Frigo, P. Feulner, and W. Berthold. *Phys. Rev. B*, 55:10854, 1997.

[215] M. Neeb, A. Kiwimäki, B. Kempgens, H.M. Köppe, and A.M. Bradshaw. *Phys. Rev. Lett.*, 76:2250, 1996.

[216] R. Arneberg, H. Ågren, J. Müller, and R. Manne. *Chem. Phys. Lett.*, 91:362, 1982.

[217] C.T. Chen, Y. Ma, and F. Sette. *Phys. Rev. A*, 45:2915, 1992.

[218] M. Nakamura, M. Sasanuma, S. Sato, M. Watanabe, H. Yamashita, Y. Iguchi, A. Ejiri, A. Nakai, S. Yamaguchi, T. Sagawa, Y. Nakai, and T. Oshio. *Phys. Rev. Lett.*, 21:1303, 1968.

[219] A. Bianconi, H. Petersen, F.C. Brown, and R.Z. Bachrach. *Phys. Rev. A*, 17:1907, 1978.

[220] G.R. Wright, C.E. Brion, and M.J. van der Wiel. *J. Electron Spectrosc. Relat. Phenom.*, 1:457, 1972.

[221] U. Gelius. *J. Electron Spectrosc. Relat. Phenom.*, 5:985, 1974.

[222] T.N. Rescigno and A.E. Orel. *J. Chem. Phys.*, 70:3390, 1979.

[223] A.P. Hitchcock and C.E. Brion. *J. Electron Spectrosc. Relat. Phenom.*, 18:1, 1980.

[224] M.B. Robin. *Higher Excited States of Polyatomic Molecules*, volume 1. Academic Press, New York, 1974.

[225] J.K. Dehmer and D. Dill. *J. Chem. Phys.*, 65:5327, 1976.

[226] L.J. Medhurst, T.A. Ferrett, P.A. Heimann, D.W. Lindle, S.H. Liu, and D.A. Shirley. *J. Chem. Phys.*, 89:6096, 1988.

[227] M.N. Piancastelli, D.W. Lindle, T.A. Ferrett, and D.A. Shirley. *J. Chem. Phys.*, 86:2765, 1987.

[228] C.Y. Ng. *Adv. Chem. Phys.*, 52:263, 1983.

[229] R.W. Nicholls. *J. Chem. Phys.*, 74:6980, 1981.

[230] W.J. Jolly, K.D. Bomben, and C.J. Eyermann. *At. Data. Nucl. Data Tab.*, 31:433, 1984.

[231] I.L. Bradeanu, R. Flesch, M. Meyer, and H.W. Jochims und E. Rühl. *Eur. Phys. J. D*, 2005. DOI: 10.1140/epjd/e2005-00223-5.

[232] R. Haensel, G. Keitel, N. Kosuch, U. Nielsen, and P. Schreiber. *J. Phys. (Paris) C*, 4:236, 1971.

[233] H. Langhoff. *Opt. Commun.*, 68:31, 1988.

[234] C. Cachoncinlle, J.M. Pouvesele, G. Durand, and F. Spiegelmann. *J. Chem. Phys.*, 96:6093, 1992.

[235] J.A.R. Samson, Y. Chung, and E.-M. Lee. *Phys. Lett. A*, 127:171, 1988.

[236] A.R. Striganov and N.S. Sventitskii. *Tables of Spectral Lines of Neutral and Ionized Atoms*. Plenum, New York, 1968.

[237] G.S. Rostovikova, V.P. Samoilov, and Y.M. Smirnov. *Opt. Spectrosc.*, 35:222, 1973.

[238] J.E. Hansen and W. Persson. *J. Phys. B*, 20:693, 1987.

[239] N. Saito and I.H. Suzuki. *Int. J. Mass Spectrom.*, 115:157, 1992.

[240] D.M.P. Holland, K. Codling, J.B. West, and G.V. Marr. *J. Phys. B*, 12:2465, 1979.

[241] A.N. Ogurtsov, E.V. Savchenko, J. Becker, M. Runne, and G. Zimmerer. *J. Lumin.*, 76:478, 1998.

[242] A.K. Amirov, O.V. Korshunov, and V.F. Chinnov. *J. Phys. B*, 27:1753, 1994.

[243] H. Langhoff. *J. Phys. B*, 27:L709, 1994.

[244] R. Santra, J. Zobeley, and L.S. Cederbaum. *Phys. Rev. B*, 64:245104, 2001.

[245] R. Santra and L.S. Cederbaum. *Phys. Rep.*, 368:1, 2002.

[246] S. Marburger, O. Kugeler, U. Hergenhahn, and T. Möller. *Phys. Rev. Lett.*, 90:203401, 2003.

[247] T. Jahnke, A. Czasch, M.S. Schöffler, S. Schössler, A. Knapp, M. Käsz, J. Titze, C. Wimmer, K. Kreidi, R.E. Grisenti, A. Staudte, O. Jagutzki, U. Hergenhahn, H. Schmidt-Böcking, and R. Dörner. *Phys. Rev. Lett.*, 93:163401, 2004.

[248] G. Öhrwall, M. Tchaplyguine, M. Lundwall, R. Feifel, H. Bergersen, T. Rander, A. Lindblad, J. Schulz, S. Peredkov, S. Barth, S. Marburger, U. Hergenhahn, S. Svensson, and O. Björneholm. *Phys. Rev. Lett.*, 93:173401, 2004.

[249] P. Scheier and T.D. Märk. *J. Chem. Phys.*, 86:3056, 1987.

[250] P. Scheier and T.D. Märk. *Chem. Phys. Lett.*, 136:423, 1987.

[251] J.-B. Maillet, A. Boutin, S. Buttefey, F. Calvo, and A.H. Fuchs. *J. Chem. Phys.*, 109:329, 1998.

[252] J. Farges, M.-F. de Feraudy, B. Raoult, and G. Torchet. *Ber. Bunsenges. Phys. Chem.*, 88:211, 1984.

[253] G. Torchet, J. Farges, M.-F. de Feraudy, and B. Raoult. *Ann. Phys. (Paris)*, 14:245, 1989.

[254] J. Farges, M.-F. de Feraudy, B. Raoult, and G. Torchet. *J. Chem. Phys.*, 78:5067, 1983.

[255] T.A. Scott. *Phys. Rep.*, 27:85, 1976.

[256] R.D. Beck, M.F. Hineman, and J.W. Nibler. *J. Chem. Phys.*, 92:7068, 1990.

[257] S.I. Kovalenko, D.D. Solnyshkin, E.A. Bondarenko, E.T. Verkhovtseva, and V.V. Eremenko. *J. Cryst. Growth*, 191:553, 1998.

[258] I. Rodríguez, A.J. Acevedo, and G.E. López. *Mol. Phys.*, 90:943, 1997.

[259] M. Bertolus, V. Brenner, P. Millié, and J.-B Maillet. *Z. Phys. D*, 39:239, 1997.

[260] F. Calvo, G. Torchet, and M.-F. de Feraudy. *J. Chem. Phys.*, 111:4650, 1999.

[261] J.P.K. Doye, D.J. Wales, and R.S. Berry. *J. Chem. Phys.*, 103:4234, 1995.

[262] J.P.K. Doye, D.J. Wales, and M.A. Miller. *J. Chem. Phys.*, 109:8143, 1998.

[263] G. Torchet, M.-F. de Feraudy, A. Boutin, and A.H. Fuchs. *J. Chem. Phys.*, 105:3671, 1996.

[264] A.P. Hitchcock and D.C. Mancini. *J. Electron Spectrosc. Relat. Phenom.*, 67:1, 1994.

[265] A.A. Pavlychev, R. Flesch, and E. Rühl. *Phys. Rev. A*, 70:015201, 2004.

[266] R.A. Rosenberg, P.J. Love, P.R. La Roe, V. Rehn, and C.C. Parks. *Phys. Rev. B*, 31:2634, 1985.

[267] H.-J. Böhm and R. Ahlrichs. *Mol. Phys.*, 55:1159, 1985.

[268] J.-B. Maillet, A. Boutin, and A.H. Fuchs. *Phys. Rev. Lett.*, 76:4336, 1996.

[269] F. Calvo, A. Boutin, and P. Labastie. *Eur. Phys. J. D*, 9:189, 1999.

[270] N. Kosugi and H. Kuroda. *Chem. Phys. Lett.*, 74:490, 1980.

[271] N. Kosugi. *Theor. Chim. Acta*, 72:149, 1987.

[272] W.J. Hunt and W.A. Goddard. *Chem. Phys. Lett.*, 3:414, 1969.

[273] H. Ågren, V. Carravetta, O. Vahtras, and L.G.M. Pettersson. *Chem. Phys. Lett.*, 222:75, 1994.

[274] S. Iwata, N. Kosugi, and O. Nomura. *Jpn. J. Appl. Phys.*, 17-S2:109, 1978.

[275] S. Huzinaga, J. Andzelm, M. Klobukowski, E. Eadzio-Andzelm, Y. Sakai, and H. Tatewaki. *Gaussian Basis Sets for Molecular Calculations*. Elsevier, Amsterdam, 1984.

[276] L.G.M. Pettersson, T. Hatsui, and N. Kosugi. *Chem. Phys. Lett*, 311:299, 1999.

[277] J. Adachi, N. Kosugi, E. Shigemasa, and A. Yagishita. *Chem. Phys. Lett.*, 309:427, 1999.

[278] K. Lee, D.Y. Kim, C.-I. Ma, and D.M. Hanson. *J. Chem. Phys.*, 100:8550, 1994.

[279] N. Kosugi. *J. Electron Spectrosc. Relat. Phenom.*, 137-140:351, 2004.

Erklärung

Hiermit erkläre ich an Eides statt, dass ich die Dissertation "Photoionization and Excitation of Free Variable Size van der Waals Clusters in the Inner Shell Regime" selbständig angefertigt und keine anderen als die von mir angegeben Quellen und Hilfsmittel benutzt habe.

Ich erkläre außerdem, dass diese Dissertation weder in gleicher oder anderer Form bereits in einem anderen Prüfungsverfahren vorgelegen hat.

Ich habe früher außer den mit dem Zulassungsgesuch urkundlich vorgelegten Graden keine weiteren akademischen Grade erworben oder zu erwerben versucht.

Würzburg, den   Unterschrift
                                                 Ioana Bradeanu

Ioana Lavinia Bradeanu

e-mail: ioana.bradeanu@mail.uni-wuerzburg.de

Address

Gertrud-von-le-Fort Str. 4, App. 33

D-97074 Wrzburg, Germany

Tel: +49 931 9916491

Date of birth: 3rd of July 1973

Education

1980 – 1988: Primary and secondary school, mathematics and informatics in secondary school, Bucharest

1988 – 1992: High School of Mathematics and Informatics, Tudor Vianu, Bucharest

1993 – 1997: Bachelor of Science in Physics, Faculty of Physics, University of Bucharest
Report title: "Applications of Fourier analysis in solid state physics"
Supervisor: Prof. Dr. Adrian Dafinei

1997 – 1999: Master's Degree in Physics, University of Bucharest, Faculty of Physics
Report title: "Modeling electron beam induced current (EBIC) in silicon / porous silicon structures"
Supervisor: Prof. Dan Brancus

March 1998 – June 1998: TEMPUS scholarship performed at the Condensed Mater Theory Group, Uppsala University, Sweden

2001 – 2002: CAPES scholarship performed at Instituto de Fisica Teorica, Universidade Estadual Paulista, São Paulo SP, Brazil
Research: Bose-Einstein condensation: stationary and time-evolution problems of single and coupled condensates under the action of a trap
Supervisor: Prof. S. Adikari

2002 – 2003: Ph.D student with Niedersächsische Stipendium, Osnabrück University, Fachbereich Physik, Germany
Ph.D program: Synthesis and characterization of surfaces and interfaces assembled from clusters and molecules, Research: Size transition in metal clusters
Supervisor: Prof. Dr. Eckart Rühl

2003 – present: Ph.D student, Würzburg University, Institut für Physikalische Chemie, Würzburg, Germany
Research: Resonant and non-resonant excitation of atoms, molecules, and free clusters
Supervisor: Prof. Dr. Eckart Rühl